

©2007

Yigit Karpat

ALL RIGHTS RESERVED

PREDICTIVE MODELING AND OPTIMIZATION IN HARD TURNING:
INVESTIGATIONS OF EFFECTS ON CUTTING TOOL MICRO-GEOMETRY

by

YİĞİT KARPAT

A dissertation submitted to the
Graduate School-New Brunswick
Rutgers, The State University of New Jersey
in partial fulfillment of the requirements

for the degree of

Doctor of Philosophy

Graduate Program in Industrial and Systems Engineering

written under the direction of

Dr. Tuğrul ÖZEL

and approved by

New Brunswick, New Jersey

October, 2007

ABSTRACT OF THE DISSERTATION

PREDICTIVE MODELING AND OPTIMIZATION IN HARD TURNING: INVESTIGATIONS OF EFFECTS ON CUTTING TOOL MICRO-GEOMETRY

By Yiğit KARPAT

Dissertation Director:
Dr. Tuğrul ÖZEL

Hard turning, which is turning of hardened parts into finished components, offers distinct advantages to manufacturers. It is favorable in terms of cost because it has the potential to eliminate the grinding process. Complex surfaces can be machined with a single machine. It is an environmentally friendly process because no cutting fluid is used. Its major drawback is rapid tool wear due to high temperatures and high stresses at the tool rake and flank faces. Short tool lives of expensive Polycrystalline Cubic Boron Nitride (PCBN) type of cutting tools hinder the economic advantage of hard turning. This research focuses mainly on the effects of cutting tool micro geometry on hard turning process. The goal is to develop a methodology for the selection of cutting tool micro geometry and machining parameters for hard turning process. To this end, existing analytical and experimental modeling techniques used in modeling of hard turning will be improved and new methodologies will be proposed.

In this research, firstly, we have developed a predictive analytical force, stress and thermal model for machining with worn tools by modifying Oxley's machining theory.

The proposed model combines a work material based deformation model with a moving band heat source model and predicts stresses and temperature distributions on the tool for tool wear modeling. Secondly, we have developed a methodology based on slip-line field analysis and experimental observations to identify tool-chip interface friction in order to investigate the influence of various edge preparations on machining performance. The ideal cutting conditions for a given edge preparation is obtained. Thirdly, we have established physics based models by utilizing 2-D and 3-D finite element methods (FEM) to analyze machining with advanced cutting tool micro geometry in order to improve the tool design for better tool life. Experimental investigations have shown that the cutting tools with advanced edge geometries perform better than uniform edge geometries. Lastly, we have introduced a multi-objective optimization methodology to select optimum machining parameters in the presence of conflicting objectives to assist in decision-making for process planning.

ACKNOWLEDGEMENTS

This study would not have been completed without the help of several people. I would like to take this opportunity to express my gratitude to:

My advisor, Dr. Tugrul Özel, for his mentorship, guidance and help at every stage of my doctoral study at Rutgers University. I am grateful to him for his constant encouragement and belief in my work.

My committee members: Dr. T. Boucher, Dr. A. Cuitino, and Dr. E. Elsayed for their suggestions and constructive advice.

The Rutgers University Industrial and Systems Engineering Department for offering fellowships and teaching assistantships throughout my studies.

Bill Schaffer and John Sockman of Conicity Technologies for supporting our research.

Helen Pirello and Cyndi Ielmini for administrative support and Joe Lippencott for his assistance during the experimentation stages of my work.

Special thanks to all my friends who made my life much more fun in New Brunswick. I will always remember them.

Edward, Patricia, and Stu Kennedy for treating me as a member of their family and making me feel at home.

Colleen B. Kennedy for her love, endless support and understanding.

Finally, I am indebted to my parents, Nakiye and the late Cevdet Karpas, my brother Hakan and his family, Naz and Munire. I will never forget their sacrifices.

TABLE OF CONTENTS

	Page
Abstract of Dissertation	ii
Acknowledgements	iv
Table of Contents	v
List of Tables	ix
List of Illustrations	xi
List of Symbols	xx
Chapter 1 Introduction	1
1.1 Tool Wear	4
1.2 Surface Integrity	7
1.3 Tool Edge Preparation	8
1.4 Motivation	10
1.5 Objectives of the Study	14
1.6 Organization of the Dissertation	18
Chapter 2 Experimental Modeling and Optimization of Cutting Conditions	
In Hard Turning	20
2.1 Introduction	20
2.2 Effects of Machining Factors on Hard Turning	21
2.3 Neural Network Modeling	30
2.4 Multi-Objective Optimization of Hard Turning	39
2.5 Particle Swarm Optimization and Multi Objective Particle Swarm Optimization	42

2.6 Swarm-Intelligent Neural Network System	50
2.7 Conclusions and Discussions	59
Chapter 3 Predictive Analytical and Thermal Modeling of Orthogonal Cutting Process	62
3.1 Introduction	62
3.2 Analytical Modeling of the Cutting Process	64
3.3 Analytical Thermal Modeling of the Cutting Process	72
3.4 Solution of the Combined Thermal and Analytical Modeling of the Cutting Process	76
3.5 Model Validation and Results	87
3.6 Effect of Tool Flank Wear On Tool Forces, Stresses and Temperature Distributions	82
3.7. Thermal Modeling of the Cutting Process for Worn Tools	91
3.7.1 Modeling of Temperature Rise in the Chip	94
3.7.2 Modeling of Temperature Rise in the Tool	94
3.7.3 Modeling of Temperature Rise on the Workpiece	97
3.8 Solution for Temperature Distributions	100
3.9. Prediction of Temperature Distributions	102
3.9.1 Effect of Tool Flank Wear on Temperature Distributions	102
3.10 Conclusions and Discussions	108
Chapter 4 Analytical and Thermal Modeling of High-Speed Machining with Chamfered Tools	110
4.1 Introduction	110

4.2 Slip-Line Modeling for Machining with Chamfered Tools Considering Dead Metal Zone	114
4.3 Experimental Setup and Results	122
4.4 Identification of Slip-Line and Friction Factors	126
4.5 Thermal Modeling of Chamfered Tools for Orthogonal Machining	131
4.5.1 Modeling of Temperature Rise in the Chip Due to Shear Plane Heat Source	132
4.5.2 Modeling of Temperature Rise in the Chip Due to Frictional Heat Sources	135
4.5.3 Modeling of Temperature Rise in the Tool Due to Stationary Heat Sources	137
4.6 Results and Model Validation	139
4.6.1 Temperature Distributions along the Tool Chamfer and Rake Face	140
4.6.2 Comparison of Calculated Temperature Fields with FEA	145
4.7. Conclusions	152
Chapter 5 Mechanics of High Speed Cutting with Curvilinear Edge Tools	154
5.1 Introduction	154
5.2 Slip Line Modeling for Machining with Round Edged Tools	159
5.3 Experimental Plan	161
5.4 Finite Element Analysis	170
5.5 Conclusion	187
Chapter 6 Design and Analysis of Variable Micro-Geometry Cutting Tools	189
6.1 Introduction	189

6.2 Mechanics of 3-D Turning	190
6.3 Advanced Cutting Tool Micro-Geometry Design	193
6.4 Experimental Procedure	198
6.5 3D Finite Element Analysis	204
6.6 Tool Wear Analysis Using 3-D FEA	213
6. 7 Conclusions	215
Chapter 7 Achievements and Future Work	216
Appendix	221
References	226
Curriculum Vita	237

LIST OF TABLES

	Page
Table 2.1 Experimental factors and levels	24
Table 2.2 ANOVA table for Ra surface roughness in finish hard turning of AISI H13 using CBN tools.	25
Table 2.3 ANOVA table for VB tool flank wear in finish hard turning of AISI H13 using CBN tools	26
Table 2.4. An example training procedure for selecting number of neurons in hidden layer.	34
Table 2.5 Summary of the experimental results	52
Table 2.6 Some selected optimal machining parameters from Pareto Front.	56
Table 2.7 Some selected optimal machining parameters	59
Table 3.1: Cutting conditions for AISI 1045 steel ($w=2$) (Ivester et al. (2000)) (*model predictions)	81
Table 3.2: Force and temperature predictions for AISI 1045 steel	81
Table 3.3: Predicted normal stress distribution parameters for machining AISI 1045 steel	83
Table 4.1. Heat intensities at various locations around cutting zone.	140
Table 5.1 Cutting conditions used in experiments and simulations.	161
Table 5.2 Comparison of identified slip-line angles of honed and waterfall hone edge preparations for $V=125$ m/min	167
Table 5.3 Comparison of identified slip-line angles of honed and waterfall hone edge preparations for $V=175$ m/min.	168

Table 5.4 Predicted and measured cutting forces and chip thicknesses	184
Table 6.1 Cutting conditions used in experiments and simulations	199
Table 6.2 The effect of friction factor on process outputs	205
Table 6.3 Chip diameter and pitch measurements	209

LIST OF ILLUSTRATIONS

	Page
Figure 1.1 Figure 1.1 A typical hard turning process.	4
Figure 1.2 Tool wear patterns in hard turning.	6
Figure 1.3 Tool edge preparations for a triangular insert.	9
Figure 1.4 Summary of inputs and expected outputs from a simulation system.	11
Figure 2.1 Cutting with various edge geometry CBN tools	22
Figure 2.2 Feed-forward neural network architecture	31
Figure 2.3 Neural network model for tool wear and surface roughness prediction.	35
Figure 2.4 An example of training results for selecting number of neurons in hidden layer	35
Figure 2.5 Comparison of predicted surface roughness and tool wear using neural network vs regression model.	36
Figure 2.6 Comparison of surface roughness and tool wear predictions and measurements.	37
Figure 2.7 Development of tool wear and surface roughness with respect to circumferential machined distance.	38
Figure 2.8 Pareto front illustrated with solid line for a min-min problem (Hu and Eberhardt (2002)).	46
Figure 2.9 Concept of dynamic neighborhood in the solution space.	46
Figure 2.10 Selection pbest according to Pareto Dominance principle.	48
Figure 2.11 Swarm Intelligent Neural Network System (SINNS).	51
Figure 2.12 Neural network model used in SINNS for surface roughness and tool	

wear predictions.	51
Figure 2.13. The Pareto front of non-dominated solutions for machining parameter using chamfered inserts.	53
Figure 2.14 The Pareto front of non-dominated solutions for machining parameters using honed inserts.	54
Figure 2.15. The Pareto front of non-dominated solutions with MRR for machining parameters using chamfered inserts.	55
Figure 2.16. The Pareto front of non-dominated solutions with MRR for machining parameters using a honed inserts.	55
Figure 2.17 Tool life curves for CBN tools under different machining conditions. Data from Mamalis et al. (2005)	57
Figure 2.18 Pareto Front of the max-max optimization problem	58
Figure 3.1. Simplified deformation zones in orthogonal cutting	65
Figure 3.2. Forces acting on the shear plane and the tool with resultant stress distributions on the tool rake face	68
Figure 3.3 Modified Hahn's model for an oblique band heat source in a semi-infinite medium	73
Figure 3.4. Heat intensity model along the rake face of the tool	75
Figure 3.5. Flow chart for computing average temperatures	78
Figure 3.6. Flow chart of the computational algorithm	79
Figure 3.7. Comparison of the predictions of the cutting force (a), and thrust force (b) with experimental data from (Ivester et al. (2000))	82
Figure 3.8. Predicted stress distributions on the tool rake face for machining AISI	

1045 steel.	83
Figure 3.9. Temperature distributions for AISI 1045 at conditions in Test #1	84
Figure 3.10. Temperatures along the tool-chip interface for test condition #1 for AISI 1045	85
Figure 3.11. Heat partition ratio along the tool chip interface for test condition #1 for AISI 1045	85
Figure 3.12. Comparison of temperature distributions (a) Predicted (b) Measured (Davies et al., (2005))	86
Figure 3.13. Forces acting on the shear plane, the rake and on the worn faces of the tool.	88
Figure 3.14. (a) Heat sources in worn tool thermal modeling and (b) coordinate systems for chip, tool and workpiece.	92
Figure 3.15 Thermal modeling of rubbing heat source on the tool rake and flank faces.	95
Figure 3.16. Thermal modeling of primary heat source on the workpiece side	98
Figure 3.17. Thermal modeling of rubbing heat source on the workpiece side	99
Figure 3.18. Predicted temperature distributions for AISI-1045 steel (a) 0.15 mm and (b) 0.32 mm of flank wear	103
Figure 3.19. Change in the heat partition coefficients B_1 and B_2 with increasing flank wear.	105
Figure 3.20. Change in the maximum temperatures with increasing flank wear.	105
Figure 3.21. (a) Temperature distributions along the tool-chip interface, (b) temperature distributions along the tool-workpiece interface for AISI 1045 steel.	106

Figure 3.22. (a) Heat partition ratio along the tool-chip interface, (b) Heat partition ratio along the tool-workpiece interface for AISI-1045 steel.	107
Figure 3.23. Temperature distributions in the chip, tool and workpiece with the non-linear heat partition ratio assumption for $V/B=0.32$ mm for AISI-1045 steel.	108
Figure 4.1 Dead metal zone when machining austenitic stainless steel with a chamfered tool with 60° rake angle at cutting speed 45 m/min (Zhang et al. (1991)).	112
Figure 4.2 The slip-line model (a) and its hodograph (b).	114
Figure 4.3 (a) Normal and shear stress distribution on the chamfer tool, (b) Force equilibrium at the chamfer face.	121
Figure 4.4 Experimental set-up for orthogonal turning.	122
Figure 4.5 SEM image of the chamfered insert at 50 times magnification.	123
Figure 4.6 Measured: (a) forces, (b) force ratio, (c) cut chip thickness.	124
Figure 4.7 SEM images of the chips collected during experiments.	125
Figure 4.8 Identified dead metal zone angle (α) and Slip Line Field Angle (θ) for $V=125$ m/min $t_u=0.1$ mm, (b) $t_u=0.15$ mm, (c) $t_u=0.18$ mm.	127
Figure 4.9 Variation of rake face friction factor with uncut chip thickness and cutting speed.	128
Figure 4.10 Distribution of normal stresses for $V=125$ m/min on the rake face of the tool.	129
Figure 4.11 Percentage of resultant force exerted on the chamfer face	130
Figure 4.12 Heat sources in thermal modeling of orthogonal cutting with a chamfered tool	132

Figure 4.13 Shear plane heat source.	133
Figure 4.14 Thermal modeling of primary heat source on the workpiece side	134
Figure 4.15 Thermal modeling of DMZ heat source on the workpiece side	135
Figure 4.16 (a) Frictional heat source along tool chip interface and (b) non-uniform heat intensity.	136
Figure 4.17 Thermal modeling on the tool side; (a) rake face, (b) chamfer face.	138
Figure 4.18 Temperature distribution at the (a) rake and (b) chamfer interfaces for $t_u=0.1$ mm	141
Figure 4.19 Temperature distribution along the (a) rake and (b) chamfer interfaces for $V=125$ m/min and various uncut chip thickness values.	142
Figure 4.20 Temperature distribution along the (a) rake and (b) chamfer interfaces for $V=175$ m/min and various uncut chip thickness values	143
Figure 4.21 Heat partition along rake face for $t_u=0.15$ mm.	144
Figure 4.22 Simulated chip formation for the cutting conditions of $V=125$ m/min, $t_u=0.1$ mm and $V=175$ m/min, $t_u=0.15$ mm.	146
Figure 4.23 Velocity field for the cutting conditions of $V=125$ m/min, $t_u=0.1$ mm and $V=175$ m/min, $t_u=0.15$ mm.	146
Figure 4.24 Isotherms obtained from analytical method for (a) $V=125$ m/min, $t_u=0.1$ mm, and (b) $V=175$ m/min, $t_u=0.1$ mm. (All temperatures are in °C)	148
Figure 4.25 Temperature distributions in the workpiece (a) $V=175$ m/min, $t_u=0.1$ mm (b) $V=125$ m/min, $t_u=0.1$ mm. (All temperatures are in °C)	149
Figure 4.26 Temperature distributions in the workpiece (a) $V=175$ m/min, $t_u=0.18$ mm and (b) $V=175$ m/min, $t_u=0.15$ mm. (All temperatures are in °C)	150

Figure 4.27 Temperature distributions in the workpiece (a) $V=125$ m/min, $t_u=0.18$ mm and (b) $V=125$ m/min, $t_u=0.15$ mm. (All temperatures are in °C)	151
Figure 4.28 Maximum temperatures under the dead metal zone T_{AD} .	152
Figure 5.1 Waterfall hone ($r_\varepsilon-r_\varepsilon/2$) and honed (r_ε) type of edge preparations.	158
Figure 5.2 SEM images of (a) waterfall hone and (b) honed edge preparations	158
Figure 5.3 Slip-line model for machining with (a) honed and (b) waterfall hone type of edge preparations.	159
Figure 5.4(a, b) Measured cutting (F_c) and thrust forces (F_t): (a) $V=125$ m/min F_c , (b) $V=175$ m/min F_c	162
Figure 5.4(c, d) Measured cutting (F_c) and thrust forces (F_t): (c) $V=125$ m/min F_t , (d) $V=175$ m/min F_t .	163
Figure 5.5. (a) Comparison of force ratio for waterfall and honed edge preparations (b) Force ratio (F_c/F_t) versus ratio of uncut chip thickness to edge radius	165
Figure 5.6. Variation of rake face friction factors with respect to ratio of uncut chip thickness to edge radius.	166
Figure 5.7 Length of front surface of the DMZ and tool chip contact length for various uncut chip thickness values at $V=125$ m/min.	169
Figure 5.8 Friction definition used in finite element simulations.	171
Figure 5.9 (a) Strains and temperatures on the machined workpiece surface, (b) Tool tip temperatures and maximum effective stresses at the cutting condition $V=175$ m/min, $t_u=0.15$ mm.	173
Figure 5.10 Tool temperature distributions for $V=175$ m/min, $t_u=0.15$ mm: (a)	

Hone 40 μm , (b) Hone 50 μm , (c) WF 20-40 μm , (d) WF-25-50 μm , (e) WF 30-60 μm . 176

Figure 5.11 Effective stress distributions in honed and waterfall hone tools for $V=175$ m/min, $t_u=0.15$ mm: (a) Hone 40 μm , (b) Hone 50 μm , (c) WF 20-40 μm , (d) WF-25-50 μm , (e) WF 30-60 μm . 177

Figure 5.12 Strain distributions in honed and waterfall hone tools for $V=175$ m/min, $t_u=0.15$ mm: (a) Hone 40 μm , (b) Hone 50 μm , (c) WF 20-40 μm , (d) WF-25-50 μm , (e) WF 30-60 μm . 178

Figure 5.13 Tool temperature distributions for $V=125$ m/min, $t_u=0.1$ mm: (a) Hone 40 μm , (b) Hone 50 μm , (c) WF 20-40 μm , (d) WF-25-50 μm , (e) WF 30-60 μm . 179

Figure 5.14 Effective stress distributions in honed and waterfall hone tools for $V=125$ m/min, $t_u=0.1$ mm: (a) Hone 40 μm , (b) Hone 50 μm , (c) WF 20-40 μm , (d) WF-25-50 μm , (e) WF 30-60 μm . 180

Figure 5.15 Strain distributions in honed and waterfall hone tools for $V=125$ m/min, $t_u=0.1$ mm: (a) Hone 40 μm , (b) Hone 50 μm , (c) WF 20-40 μm , (d) WF-25-50 μm , (e) WF 30-60 μm . 181

Figure 5.16 Effective stress distributions in honed tool 40 μm at $V=125$ m/min: (a) $t_u=0.075$ mm, (b) $t_u=0.1$ mm, (c) $t_u=0.125$ mm. 182

Figure 5.17 Dead metal zone formation for honed and waterfall edge preparations: (a) Hone 40 $V=125$ m/min, $t_u=0.1$ mm, (b) WF 30-60 $V=125$ m/min, $t_u=0.1$ mm, (c) WF 30-60 $V=175$ m/min, $t_u=0.15$ mm 183

Figure 5.18 Chip formation for honed edge preparations for $V=125$ m/min, $t_u=0.1$

mm: (a) Hone 40 μm , (b) Hone 50 μm	185
Figure 5.19 Chip formation for waterfall hone edge preparations for $V=125$	
m/min, $t_u=0.1$ mm: (a) WF 20-40 μm , (b)WF 25-50 μm	185
Figure 5.20 Chip formation for waterfall hone edge preparation for $V=125$ m/min,	
$t_u=0.1$ mm with two magnification levels	186
Figure 5.21 Chip formation for honed and waterfall edge preparations for $V=175$	
m/min, $t_u=0.15$ mm: (a) Hone 50 μm , (b)WF 25-50 μm , (c) WF 30-60 μm	186
Figure 6.1 Mechanics of 3-D turning. (Altintas (2000))	191
Figure 6.2 Chip load in typical turning operation with a corner radius tool.	191
Figure 6.3 Variation of uncut chip thickness	192
Figure 6.4 Uniform vs. variable edge design on a tool insert	198
Figure 6.5 The tip of the variable hone micro-geometry insert	187
Figure 6.6 Flowchart of advanced cutting tool micro-geometry design.	189
Figure 6.7 Images of PCBN inserts at 50 times magnification obtained with	
scanning electron microscopy: a) chamfered, b) uniform honed with 50 μm radius,	
c) variable hone with 10 to 50 μm edge dimensions.	198
Figure 6.8 Measured cutting forces at the cutting condition of	
$V=125$ m/min, $f=0.15$ mm/rev, $d=1$ mm	200
Figure 6.9 Measured cutting forces at the cutting condition of	
$V=125$ m/min, $f=0.1$ mm/rev, $d=1$ mm.	201
Figure 6.10 Measured cutting forces at the cutting condition of	
$V=175$ m/min, $f=0.1$ mm/rev, $d=1$ mm	202
Figure 6.11 Measured cutting forces at the cutting condition of	

$V=175\text{m/min}$, $f=0.1\text{ mm/rev}$, $d=0.5\text{mm}$	203
Figure 6.12 Measured cutting forces at the cutting condition of	
$V=175\text{m/min}$, $f=0.15\text{ mm/rev}$, $d=0.5\text{mm}$	203
Figure 6.13 Comparison of measured and simulated forces for various micro- geometry inserts	206
Figure 6.14 Temperature distributions simulated for machining with (a) variable honed inserts $r_\epsilon=10\text{ }\mu\text{m}$ - $50\text{ }\mu\text{m}$, (b) uniform honed $r_\epsilon=50\text{ }\mu\text{m}$ and (c) uniform chamfered	207
Figure 6.15 Photographs of collected chips: (a) Uni. Hone $50\mu\text{m}$, (b) Var Hone $50\text{ }\mu\text{m}$, (c) Uni. Waterfall Hone $25:50\text{ }\mu\text{m}$, (d) Variable Waterfall $25:50\text{ }\mu\text{m}$, (e) Uni. Waterfall Hone $30:60\text{ }\mu\text{m}$, (f) Chamfered	208
Figure 6.16 Temperature distributions in the chip and workpiece	210
Figure 6.17 Effective strain distributions at the cutting zone for uniform honed and variable honed inserts	211
Figure 6.18 SEM images of chip shapes produced by (a) uniform chamfered, (b) uniform honed and (c) variable hone inserts.	212
Figure 6.19 Tool wear simulations for machining with (a) honed inserts, (b) uniform chamfered and (c) variable honed.	214

LIST OF SYMBOLS

Chapter 2.

VB	Flank wear (mm)
KT	Crater Wear (mm)
f	Feed rate (mm/rev)
d	Depth of cut (mm)
V	Cutting Speed (m/min)
H	Hardness
L	Cutting Length (mm)
E	Edge Preparation
c_i	Coefficients of regression model
R_a	Surface roughness (μm)
p_i	Input to neural network
w_{ij}	Weight term in neural network model
b_i	Bias term in neural network model
$f(x)$	Objective function
$g(x)$	Constraint
$h(x)$	Equality type constraints
x	Decision variable
v	Objective function parameter

φ	Objective function parameter
W	Sum of squares of neural network weights
p_{best}	Personal best position in the swarm
g_{best}	Global best position in the swarm
N	Rotational speed (rpm)

Chapter 3.

A	Plastic equivalent strain in Johnson-Cook constitutive model, (MPa)
a_i	Thermal diffusivity of the medium i
B	Strain related constant in Johnson-Cook constitutive model, (MPa)
$B(x)$	Heat partition fraction
C	Strain-rate sensitivity constant in Johnson-Cook constitutive model
F_c, F_t	Cutting and thrust force components, (N)
K_0	Zero order Bessel function of the second kind
m	Thermal softening parameter in Johnson-Cook constitutive model
n	Strain-hardening parameter in Johnson-Cook constitutive model
q	Heat intensity
T_M	Temperature rise, (°C)
T_m	Melting temperature of the work material, (°C)
T_0	Initial work material temperature, (°C)
t_u, t_c	Uncut and cut chip thickness, (mm)
w	Width of cut, (mm)
α	Tool rake angle, (degree)

ϕ	Shear angle, (degree)
τ	Frictional shear stress, (N/mm ²)
λ_t	Thermal conductivity, (W/m °C)
ρ	Prow angle, (degree)
δ	Proportion of the thickness of the secondary zone to the chip thickness
a	Power exponent of the normal stress distribution on the tool rake face
C_0	Strain rate constant proposed by Oxley
F_F, F_N	Frictional and normal force components at tool rake face, (N)
F_S, F_{NS}	Shear force and normal to the shear force components at AB, (N)
k_{AB}	Shear flow stress on AB, (N/mm ²)
k_{chip}	Shear flow stress in chip at tool-chip interface, (N/mm ²)
l_{AB}	Length of the primary shear zone, (mm)
l_c	Length of tool-chip contact, (mm)
l_p	Length of sticking region, (mm)
p_A, p_B, p_M, p_N	Hydrostatic stresses at the points A, B, M , and N , (N/mm ²)
T_{AB}	Average temperature along AB, (°C)
T_{int}	Average temperature along tool-chip interface, (°C)
V, V_S, V_C	Cutting velocity, shear velocity, and chip velocity, (m/sec)
$\bar{\epsilon}_{AB}, \bar{\epsilon}_{int}$	Effective strain at AB and tool-chip interface, (mm/mm)
$\dot{\bar{\epsilon}}_0$	Reference strain rate, (s ⁻¹)
$\dot{\bar{\epsilon}}_{AB}, \dot{\bar{\epsilon}}_{int}$	Effective strain rate at AB and tool-chip interface, (s ⁻¹)
$\bar{\gamma}_{AB}, \bar{\gamma}_{int}$	Effective shear strain at AB and tool-chip interface, (mm/mm)
$\dot{\bar{\gamma}}_{AB}, \dot{\bar{\gamma}}_{int}$	Effective shear strain-rate at AB and tool-chip interface, (s ⁻¹)

μ_e	Coefficient of friction in the elastic contact region of tool-chip interface
$\bar{\sigma}_{AB}$	Effective flow stress at AB, (N/mm ²)
σ_N	Normal stresses acting on tool-chip interface, (N/mm ²)
$\sigma_{N\max}$	Maximum normal stresses acting on tool-chip interface, (N/mm ²)
τ_{int}	Frictional shear stress at tool-chip interface, (N/mm ²)
X, Y, Z	Coordinates (mm)

Chapter 4

γ_1, γ_2	Rake and chamfer angle, (degree)
$\zeta_1, \zeta_2, \zeta_3$	Slip-line angles, (degree)
θ, δ	Slip-line central fan angles, (degree)
P_E	Hydrostatic pressure at point E (N/mm ²)
α	Dead metal zone angle, (degree)
m_1, m_2, m_3	Friction factors
ϕ	Shear angle, (degree)
ρ	Prow angle, (degree)
Δ	Slip line angle, (degree)
t_u, t_c	Uncut and cut chip thickness, (mm)
F_c, F_t	Cutting and thrust force components, (N)
σ_D, σ_F	Normal stresses acting on tool-chip interface, (N/mm ²)
τ	Shear stress (N/mm ²)
k	Shear flow stress, (N/mm ²)

T_M	Temperature rise, (°C)
q	Heat intensity
V, V_{shear}, V_{ch}	Cutting velocity, shear velocity, and chip velocity, (m/sec)
K_0	Zero order Bessel function of the second kind
a_i	Thermal diffusivity of the medium i
w	Width of cut, (mm)
A	Plastic equivalent strain in Johnson-Cook constitutive model, (MPa)
B	Strain related constant in Johnson-Cook constitutive model, (MPa)
C	Strain-rate sensitivity constant in Johnson-Cook constitutive model
m	Thermal softening parameter in Johnson-Cook constitutive model
n	Strain-hardening parameter in Johnson-Cook constitutive model
X, Y, Z	Coordinates (mm)

Chapter 5.

r_ϵ	Edge radius (mm)
γ_2	Rake angle, (degree)
θ, δ	Slip-line central fan angles, (degree)
P_E	Hydrostatic pressure at point E (N/mm ²)
α	Dead metal zone angle, (degree)
m_1, m_2, m_3	Friction factors
ϕ	Shear angle, (degree)
ρ	Prow angle, (degree)
Δ	Slip line angle, (degree)

t_u, t_c	Uncut and cut chip thickness, (mm)
F_c, F_t	Cutting and thrust force components, (N)
τ	Shear stress (N/mm ²)
k	Shear flow stress, (N/mm ²)
A	Plastic equivalent strain in Johnson-Cook constitutive model, (MPa)
B	Strain related constant in Johnson-Cook constitutive model, (MPa)
C	Strain-rate sensitivity constant in Johnson-Cook constitutive model
m	Thermal softening parameter in Johnson-Cook constitutive model
n	Strain-hardening parameter in Johnson-Cook constitutive model

Chapter 6

f	Feed rate (mm/rev)
d	Depth of cut (mm)
V	Cutting Speed (m/min)
F_c	Cutting force (N)
F_t	Thrust force (N)
F_z	Feed force (N)
C_s	Side rake angle (deg)
Ω	Sweep angle (deg)
R	Cutting tool nose/corner radius (mm)
t_Ω	Uncut chip thickness corresponding to angle Ω (mm)
r_ϵ	Edge radius (mm)
A	Plastic equivalent strain in Johnson-Cook constitutive model, (MPa)

B	Strain related constant in Johnson-Cook constitutive model, (MPa)
C	Strain-rate sensitivity constant in Johnson-Cook constitutive model
m	Thermal softening parameter in Johnson-Cook constitutive model
n	Strain-hardening parameter in Johnson-Cook constitutive model
VB	Flank wear (mm)
c_i	Coefficients of tool wear rate model
T	Temperature (C)
V_s	Sliding velocity
σ_n	Normal stresses acting on tool-chip interface, (N/mm ²)
λ	Ratio of uncut chip thickness to edge radius

CHAPTER 1

INTRODUCTION

In order to remain competitive in today's market, manufacturers should enhance the quality of their products and reduce costs while meeting strict customer requirements. Metal cutting is still the core of manufacturing industry and it is predicted to remain so for the upcoming years. Thus, recent research in manufacturing science community has been mainly focused on increasing efficiency by fully utilizing the resources. It has been shown that, actual machining times are actually much shorter than the non-productive times spent on loading/unloading, transferring etc. the parts. Therefore, if two or more consecutive operations can be performed on a single machine, it would decrease the production time and eliminate accuracy related problems due to re-clamping.

A recently developed machining technology called "Hard Turning", machining of hardened parts into finished components, constitutes a good example for the integration of multiple processes into a single process. Hard turning offers the opportunity of eliminating grinding process, which is usually applied after turning in order to obtain a good surface finish. If the migration of processing from grinders to lathes can be achieved, cost of machining can be reduced because less floor space will be required, overall investment will be lower, complex contours can be machined, material removal rate will be 4-5 times greater, and configuration changes will be made faster. Recent advances in cutting tool technology and introduction of high quality lathes into the

market have made the hard turning a viable technology. The ability of manufacturing complex geometries in one machine and still obtaining comparable surface finish as in grinding has made hard turning a favorable choice. Besides, since no or minimum quantity of cutting fluid is used in hard turning, it is also preferable from ecological point of view.

Since hardened parts are machined in hard turning, cutting tools are subjected to high stresses and temperatures therefore tool wear is an important issue. In order to resist tool wear under these harsh cutting conditions, cutting tool material should have high hardness, high toughness, chemical stability, high thermal conductivity and low thermal expansion coefficients. Cubic boron nitride (CBN) tools which possess most of the above given qualities are usually used in hard turning. Other than CBN tools, cermet or ceramic tools are also used. CBN tools are comprised of a polycrystalline layer of CBN crystals and a tungsten carbide substrate which are bonded together. CBN inserts are produced through powdered metal processes. Wafers are cut into slices and brazed to a carbide insert, and then edge preparation is performed. The CBN content, grain size and distribution and composition of the binder material greatly influence the performance of the CBN tool. Many studies showed that CBN tools with lower CBN content perform better in hard turning applications. While low CBN content provides improved edge wear; high CBN content offers higher strength. Hard turning is a technology-driven process therefore its success depends on machine and workholding technology. In combination with CBN cutting tools, the development of high precision lathes which have better spindle systems and higher structural stiffness, improved the outcome of hard

turning process significantly. As mentioned before, the elimination of the usage of cutting fluids is the advantage of hard turning. CBN tools have made dry or near dry cutting possible because they are durable enough to resist heat generated during cutting, in addition to that the application of cutting fluids to cutting zone make them vulnerable to thermal shocks which may cause sudden breakages. Elimination of the cutting fluids, which include chemical elements harmful to human health, is important in terms of cost, environmental, and health issues.

The selection of cutting conditions in hard turning is very important and directly affects the performance of the hard turning process. For example; increasing cutting speed, increases the temperatures at shear zone and tool-chip interface which softens the hardened steel being cut due to material's thermal softening behavior, thus reduced cutting forces are observed. Furthermore, low thermal conductivity of the CBN tools assures that the heat generated is taken away and dissipated with the chips. However, high cutting temperatures strongly influence the tool wear, workpiece surface integrity and chip formation mechanism. A typical hard turning process with red hot chips indicating the high cutting temperatures at the cutting zone is shown in Fig. 1.1.



Figure 1.1 A typical hard turning process.

In order to promote hard turning to a wider range of applications, some challenging issues are needed to be solved. These are addressed below:

1.1 Tool Wear

Tool wear is an important problem for hard turning because it not only affects the economic advantage of hard turning, also affects the surface quality of the workpiece. The friction mechanism and heat generated between tool, chip and workpiece determines the tool wear. The cost of CBN tools are high compared to conventional cutting tools and the downtime during tool change has an additional cost which may hinder the economic advantage of the process. In order to replace hard turning with grinding, the relationships between surface quality, dimensional accuracy and tool wear should be very well analyzed. The tool performance is mainly influenced by factors such as: workpiece material and hardness, cutting conditions (cutting speed, feed rate and depth of cut), tool

material composition, tool geometry (rake angle) and tool edge preparation (i.e. micro-geometry of the tool tip). Increasing tool wear yields unsatisfactory surface finish and increased power consumption. The main mechanisms of tool wear for CBN tools can be explained as below:

1. Abrasion wear: Caused by sliding motion between chips and the tool rake face, and also by friction between the tool flank and workpiece. Strain hardened particles of the work material and/or hard tool grain particles rub the tool rake and flank face and cause abrasion wear.
2. Adhesion wear: Adhesive wear is caused by the fracture of micro welds which are formed between asperities of tool and workpiece materials due to high pressure and temperature.
3. Chemical wear: This type of wear is caused due to chemical reaction between CBN's chemical composition and workpiece materials. As an example, since it tends to accelerate chemical wear, ductile iron is not suitable for CBN machining.
4. Thermal Fatigue Wear: It is usually seen in interrupted machining where cycling of heating and cooling stages results in thermal cracks and therefore tool breakage.

It must be noted that some of these wear mechanisms are cutting condition dependent and they may become more or less dominant under different cutting conditions. Depending on the area where tool wear occurs, three types of tool wear pattern can be identified: Flank wear (VB), crater wear (KT) and chipping. Flank wear (VB) occurs between the tool

and the workpiece because of rubbing action. In real life applications maximum permissible value of flank wear (VB_{max}) is usually used as a decision factor on tool life since it is easy to measure flank wear than crater wear. It also has the biggest influence on the surface quality of the finished component. Crater wear (KT) occurs on the rake face of the tool because of chemical interaction between tool material and workpiece. Crater wear changes the contact conditions on the tool-chip interface by altering effective tool rake angle which leads to a change in cutting characteristics. A developed crater wear zone usually causes sudden tool breakage because it weakens the cutting edge. Chipping results from broken small pieces of the tool and reduced by increasing the toughness of the tool. The trailing edge of the cutting tools which corresponds to the area where minimum uncut chip thickness is machined is also subjected to plastic deformations. The tool wear problem around that area can be solved by employing cutting tools with “engineered” micro geometry. The tool wear patterns are shown in Fig. 1.2.

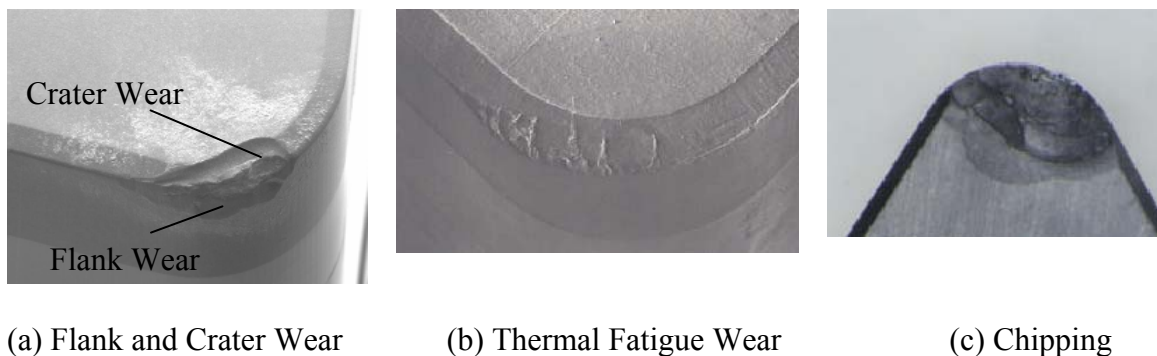


Figure 1.2 Tool wear patterns in hard turning.

1.2 Surface Integrity

Hard turning processes have strong impact on the surface integrity. Surface integrity requirements can be categorized as geometrical surface integrity (surface roughness, dimensional accuracy) and physical surface integrity (residual stresses, microstructure changes). Surface roughness, which is maybe the most important customer requirement, is greatly affected by the selection of cutting conditions, tool edge geometry, and tool wear. Surface roughness is measured by calculating the height differences of the valleys on the surface profile. It directly affects the mechanical performance of the finished component since the fatigue behavior is related to depth of these valleys which are also known as notches. Hard turning and grinding processes produce different surface structures. Hard turning process can produce surface superior than grinding as long as cutting conditions are properly selected and machining is performed with an unworn tool.

Residual stresses are the stresses which remain in the part after machining. The residual stress values in the workpiece are mainly influenced by tool tip and tool workpiece interaction as well as the friction between the surfaces. Edge geometry of the cutting tools is an important factor on the machined surface integrity. Worn tools cause undesirable tensile residual stresses and increasing tool wear value pushes those residual stresses into deeper regions in the sub layer of the workpiece. Plastic deformation and thermal effects are crucial factors and should be considered in residual stress modeling. Residual stresses affect the fatigue behavior of the part under actual working conditions.

Other than residual stresses, the formation of white layers, which appears as a white layer at the surface of the material under metallographic examination, characterizes the surfaces produced by hard cutting process. White layer formation is also seen in grinding applications. White layers are generated depending on the thermal and mechanical loads that the machined surface is subjected to. White layers can be caused either due to severe plastic deformation that causes rapid grain refinement or due to rapid heating to austenite temperatures and fast cooling (quenching). White layer formation can be avoided by carefully selecting cutting parameters.

1.3 Tool Edge Preparation

The contact conditions between tool and workpiece are dependent on edge preparation which plays an important role on the performance of the cutting, integrity of the machined surfaces and the tool life. In order to improve the overall quality of the finished component, tool edge geometry should be carefully designed or selected. Design of cutting edge may affect the chip formation mechanism and therefore help reducing cutting forces and increasing tool life. As an emerging machining technique, hard turning sets high standards for cutting tool edge design since the uncut chip thickness and the tool edge dimensions are in the same order of magnitude. It has been reported by many researchers that cutting edge design affects the outcome of the machining processes in terms of forces generated, surface roughness, residual stresses and tool life. It is known that sharp tools are not durable enough for most of the machining operations; therefore, tool manufacturers introduced different types of tool edge preparations such as

chamfered, double chamfered, chamfer + hone, honed, and waterfall hone edge designs in order to reduce edge related problems such as chipping and breakage. Different types of edge preparations are shown in Fig. 1.3.

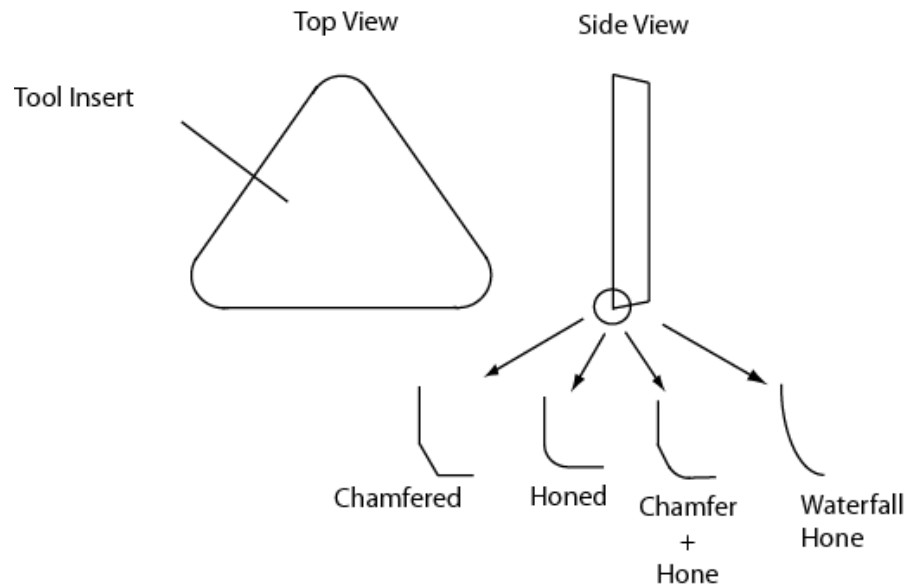


Figure 1.3 Tool edge preparations for a triangular insert.

The purpose of edge preparation is to increase tool tip strength. It is easier to coat edge preparation cutting tools with a protective material. Edge preparation affects the cutting dynamics. Chip formation mechanism is also affected by edge preparation. In current hard turning practice, chamfered tools are usually used in rough turning and hard turning; honed tools are usually employed in finish hard turning. These edge preparations can be obtained through processes such as grinding, brushing, and blasting. Recently, new technological advancements in brushing materials (i.e. the Nylon Abrasive Filament brush) and the introduction of CNC controlled honing machines enabled the production of more precise edges.

The new trend in tool edge design is towards designing application specific or custom geometries. In advanced tool designs, instead of tools with uniform edge preparation all along the cutting edge, variable geometry edge design are used. As an example, in the case of 3D cutting, where the thickness of the chip varies from a maximum value, which is equal to the feed rate, to a minimum value on the tool's corner radius, the ideal tool edge preparation should possess a variable edge configuration which is different at the primary cutting edge than at the tool's corner radius. Proper tool edge preparation for the process in hand can be designed only when tool-chip friction and heat generation mechanisms at the tool-chip and tool-workpiece interfaces are understood. Availability of metal cutting simulation tools which are capable of predicting the outcome of the process accurately is believed to help understanding the mechanics of cutting and enable optimization of the cutting conditions during process planning stage, and designing tool edge micro-geometry. This constitutes the motivation of this research which is explained in detail below.

1.4 Motivation

Current body of research has been concentrated on modeling the machining processes and developing simulation tools, which eliminates the necessity of extensive experimentation process currently used in industry, to understand the mechanics of metal cutting and to model the relationships between process inputs and outputs. If the effects of cutting conditions and cutting tool micro geometry on the tool life and surface integrity can be determined by using a predictive model, optimum cutting conditions and/or

optimum cutting tool micro geometry can be obtained without any experimentation. Therefore, the main goal is the development of predictive models which will yield accurate prediction of cutting forces, stresses and temperature distributions in the tool, chip and workpiece in response to given cutting conditions (cutting speed, feed rate, depth of cut), workpiece material, tool material, and tool edge preparation. A predictive model should make use of physics based material constitutive models which explain the behavior of the material depending on applied strains, strain rates and temperatures and material's thermal properties. Thermal properties of the cutting tool must also be considered in the model. An ideal simulation model is expected to yield fast and accurate results which would allow the user to observe the influence of changing cutting conditions, tool type, and workpiece material on the process outputs. Process outputs such as forces, stresses and temperatures can be further employed to determine tool wear, tool life, and residual stresses. The inputs of a simulation model and expected outputs are summarized in Fig. 1.4.

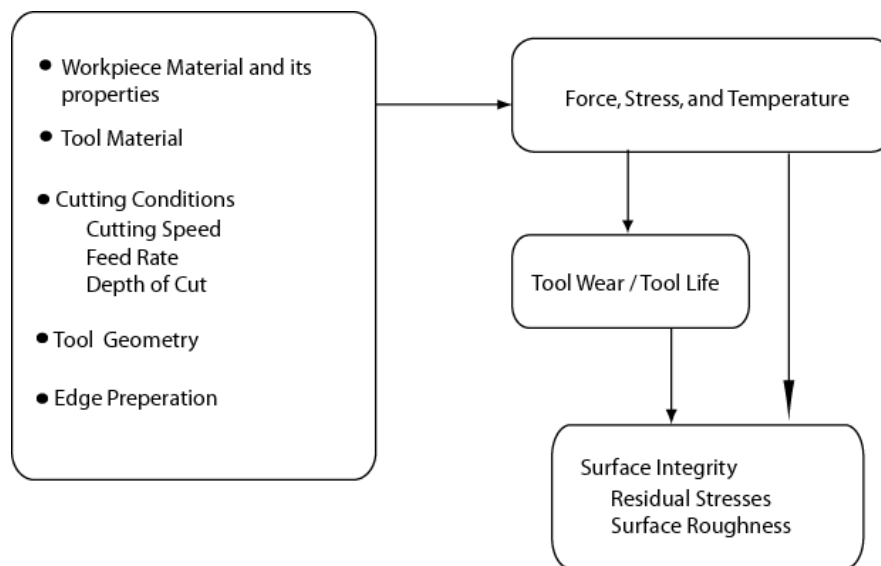


Figure 1.4 Summary of inputs and expected outputs from a simulation system.

Although there are many methodologies which can be used to establish the relationships between process inputs and outputs there is no single methodology which can perform the above defined task reliably due to highly non-linear nature of metal cutting operations. These major methodologies with their pros and cons are explained below.

1. Analytical Modeling: Most of the analytical models are based on Merchant's (1944) basic model where the chip is considered to be in equilibrium between resultant forces acting from the workpiece and the tool. Since Merchant's model (1944) requires the information such as shear angle of the primary shear zone and friction conditions between tool and chip to calculate forces, it can not be used as a predictive model. Oxley (1989) proposed a predictive analytical model by observing material flow around the cutting edge by using visio-plasticity technique. Oxley's (1989) method utilizes a material model and minimum energy principle to predict cutting forces. An empirical formula is also given to predict temperatures at the cutting zone. Oxley's (1989) predictive model is proposed for sharp tools; since it does not consider edge effects it can not be directly used for tools with edge preparation. In order to explain complex material flow around the cutting edge of the tool, slip-line field analysis has been used by many researchers (Lee and Shaffer (1951), Shi and Ramaligam (1991), Waldorf (1996), Fang (2003, 2005), Fang and Wu (2005), etc). Slip-line field analysis assumes constant plastic material flow around the cutting edge and requires experimental orthogonal cutting data in order to deduce information about cutting mechanics. It must be noted that, there are other views in literature about chip formation

mechanisms. Another school of researchers believe that the fracture of workpiece material ahead of the tool must also be considered in chip formation (Astakhov (1999), Atkins (2003)). It has been shown that the effect of fracture can be neglected when machining large uncut chip thicknesses (Shaw (1954)).

2. Mechanistic Modeling: Cutting forces can be predicted by using this method based on the assumption that cutting forces are related to the uncut chip area and specific cutting energy. It requires extensive experimentation to calculate coefficients in the model (Budak and Altintas (1993), Fu et al. (1984), etc.). This methodology lacks providing physical process information because the model does not depend on material. After calculating necessary coefficients, three dimensional cutting forces can be easily calculated by using this methodology.
3. Finite Element Modeling: Finite element techniques use small mesh representations of the material and cutting tool which are based on continuity principles (Ceretti et al. (2000), Guo and Dornfeld (1998), Guo and Liu (2002), Ohbuchi and Obikawa (2003), Özel and Altan (2000), etc.). When material constitutive model, tool-friction conditions, and thermal properties of the workpiece and tool are defined properly, finite element analysis provides the most information about the process. Friction conditions must be modeled carefully since it determines the outcome of the simulation. Machining process with finite element analysis can be modeled as; rigid-plastic or elastic-plastic; Eulerian (fixed mesh) or Lagrangian (mesh flow with the material); using adaptive meshing or not. Cutting edge of the tool poses difficulties in terms of generating meshes in Lagrangian approach. In order to correct highly distorted elements around the

cutting edge, techniques such as mesh rezoning and dynamic remeshing are utilized. Another approach is to use node separation principles to simulate material separation which requires a separation line to determine material separation. That approach is criticized as being not based on physics of machining. Computation times, sensitivity to material constitutive models and friction definitions, and some instability problems with meshing are the drawbacks of finite element modeling.

4. Experimental Modeling: Relationships between outputs and inputs can be obtained by using design of experiments principles. Process outputs such as surface roughness and residual stresses can be modeled by experimental modeling since they are influenced by hard-to-model factors (Chou et al. (2002), Feng and Wang (2002), Feng and Wang (2003), Özel and Karpaz (2005), etc). In order to obtain reliable models, large numbers of experiments should be performed. Regression and neural network based models are usually employed to establish the relationships between inputs and outputs.

1.5 Objectives of the Study

The scope of this study is conventional and hard turning processes. The overall objective is to gain science-based understanding of the material removal process and develop a predictive modeling framework for optimal selection of machining parameters and tool geometry. In this study, analytical and finite element modeling techniques are used together to study tool-chip friction, temperatures and tool stresses. A predictive

analytical method based on Oxley (1989) machining model is proposed and extended to machining with worn tools. Analytical thermal modeling is integrated into Oxley (1989) model to obtain temperature distributions in the workpiece, chip and the cutting tool. The effects of edge preparation are studied by using slip-line field analysis and orthogonal cutting tests which yield information about tool-chip friction. The findings of slip-line field analysis are employed in finite element simulations in order to eliminate trial and error stage in finite element simulations. The simulation results are used to explore the machining characteristics of various edge preparations and suitable cutting conditions. Finally, a methodology to design advanced cutting tool micro-geometry is proposed. Bar turning experiments and 3D finite element simulations are conducted to validate the results.

Mechanistic modeling approach was not considered in this study since it is not a physics-based model. In spite of all efforts, reliable predictions of surface roughness and tool life is still not possible by using analytical or finite element models. Therefore, modeling of tool wear/tool life and surface roughness will be obtained by experimental methods. These obtained models are integrated into an optimization scheme to calculate optimum cutting conditions with respect to various objective functions. Experimental models used in the optimization scheme can be replaced with analytical models once reliable analytical models are available. The specific objectives of this study can be summarized as:

(a) Propose a methodology for the optimization of cutting conditions in the presence of multiple objectives for hard turning process by using experimental modeling: The conflicting objectives in machining such as increasing tool life and increasing material removal rate are considered in optimization. The relationships between machining parameters and process outputs are modeled by utilizing modular neural networks. Multi-objective particle swarm optimization method is employed to solve some multi-objective optimization case studies where the objectives are treated separately in order to obtain a set of solution consisting of optimum cutting conditions. It is believed that using optimized cutting conditions may result in substantial cost savings in metal cutting industry.

(b) Better understanding of tool-chip friction by utilizing slip-line field theory: Tool-chip friction plays an essential role in understanding complex material flow around the cutting edge when tools with edge preparation are used. Theory of plasticity based slip-line field analysis is used to study tool-chip friction for cutting tools with edge preparation. Tool-chip friction of various edge preparations under different cutting conditions is evaluated and characteristics of these edge preparations are explained. Identified friction information is used in finite element analysis to validate the findings of slip-line field analysis and obtain additional information about the process. Dead metal zone phenomenon, which is common when machining with negative rake angle tools, is also investigated.

(c) Improving predictive workpiece material model based analytical modeling: In order to be able to model tool wear analytically, stress and temperature distributions on the cutting tool must be determined. Oxley's (1989) predictive machining model uses empirical thermal models and a primitive friction model, which yields only average temperatures and stresses at the tool-chip interface. An analytical thermal model which considers non-linear heat intensity at the tool chip interface will be integrated into the Oxley's (1989) predictive machining model. In addition to that, modifications to the existing predictive machining model such as calculation of sticking and slipping zones on the secondary shear zone are introduced. The effects of tool wear on temperature distributions are investigated by using proposed worn tool analytical thermal model that provides valuable workpiece temperature distribution information which can be used in analytical residual stress models. The analytical thermal model for worn tools is modified to calculate temperature distributions when machining with chamfered tools. It must be noted that analytical models yield steady state temperature distributions during machining in a very short calculation time.

(d) Propose a systematic approach for advanced cutting tool edge micro-geometry design:

A systematic approach, which makes use of the tool-chip friction information obtained and 3D finite element analysis is introduced to design advanced cutting tool micro-geometry. The effectiveness of new cutting edge designs will be demonstrated by bar turning tests.

1.6 Organization of the Dissertation

The organization of the dissertation is detailed below:

In Chapter 2, an experimental analysis of hard turning is performed. The factors affecting hard turning are identified using design of experiments approach. In light of these results, the relationships between cutting conditions and process outputs are obtained by using neural network modeling. Optimum cutting conditions when multiple conflicting objectives present are obtained by using an evolutionary multi-objective optimization.

In Chapter 3, a modification to Oxley's predictive machining theory is proposed and it is extended for worn tools. An analytical thermal model based on oblique moving heat source is presented and integrated into modified Oxley's predictive machining model. That model is extended for worn tools to predict non-uniform heat partition and temperature distributions. The thermal effects of machining with worn tools are investigated.

Chapter 4 is devoted to chamfered edge design tools. Cutting mechanics of chamfered tools is studied by using slip-line field theory. Orthogonal cutting experiments are performed to identify slip-line angles and therefore tool-chip friction. An analytical thermal model, which makes use of identified slip-line parameters, for chamfered tools are proposed. Proposed analytical thermal model enables the calculation of temperatures

at cutting zone in a very short time. The temperature distributions are compared and validated with those obtained by finite element simulations.

Chapter 5 investigates the tool-chip friction phenomena when machining with curvilinear edge cutting tools again by using slip-line field analysis and orthogonal cutting experiments. Temperature and stress distributions are obtained by using finite element simulations and effects of micro-geometry on process outputs are analyzed. The influence of edge preparation on chip formation is studied. The findings of Chapters 3, 4 and 5 constitute a base for advanced cutting tool micro geometry design for 3-D turning operation.

In Chapter 6, the comparison of using cutting tools with uniform and advanced micro-geometries is studied. Cutting tool micro-geometry effects are investigated by using 3D finite element simulations and bar turning experiments. A methodology for advanced cutting tool design is proposed.

In Chapter 7, achievements of this study are summarized and future research directions are discussed.

CHAPTER 2

EXPERIMENTAL MODELING AND OPTIMIZATION OF CUTTING CONDITIONS IN HARD TURNING

2.1 Introduction

In machining of parts, surface roughness is one of the most important customer requirements. Surface roughness is mainly a result of process parameters such as tool geometry (i.e. nose radius, edge geometry, rake angle etc.) and cutting conditions (feed rate, cutting speed, depth of cut etc.). In finish hard turning, tool wear becomes an additional parameter affecting surface quality of finished parts. In current hard turning practice, industry chooses the correct tool geometry less than half of the time, uses proper machining parameters only about half of the time, and uses cutting tools, especially Cubic Boron Nitride (CBN), to their full life capability only one third of the time. These sub-optimal practices cause loss of productivity. Improvements to the current process planning for finish hard turning are needed to improve cost effectiveness and productivity. This can be achieved by developing predictive models using experimental data and using these models to optimize the cutting conditions. In optimization of metal cutting problems, usually competing/conflicting objectives such as increasing tool life and increasing material removal rate exist. Furthermore, it is important to give manufacturers different alternative solutions which can be applied under different circumstances. In light of these facts, the optimization of hard turning problem is considered as a multi objective optimization problem. A recently developed optimization

algorithm called Particle Swarm Optimization is used due to its simplicity and success in multi objective optimization problems.

2.2 Effects of Machining Factors on Hard Turning

There are numerous machining factors that affect surface quality in hard turning using CBN cutting tools, but their effects have not been adequately quantified. Experimental approaches to identify important factors in hard turning have been used by many researchers. In recent studies, Chou et al.(1997, 2002), Thiele et al. (1999, 2000), and Özel et al. (2005) among others performed experiments on hard turning of various steels using CBN tools and identified the factors affecting surface roughness, tool wear, cutting forces and surface integrity.

Workpiece hardness and microstructure has a profound effect on the cutting life of the CBN tools (Barry and Byrne (2001), Toenshoff et al. (1995, 2000), Matsumoto et al. (1999), and Thiele et al. (1999)). It is known that a suitable CBN tool grade must be matched for different workpiece materials to get favorable surface finishes. It is also known that the surface roughness decreases with increasing hardness.

CBN cutting tools demand prudent design of tool geometry (Narutaki and Yamane (1979), Hodgson et al. (1981), Chryssolouris (1982)). CBN tools are subjected to high cutting forces and temperatures therefore, proper edge preparation is required to increase the strength of cutting edge and attain favorable surface characteristics on

finished metal parts. CBN cutting tools designed for hard turning feature negative rake geometry and an edge preparation (chamfered, honed, chamfer and hone, etc.) as shown in Fig. 2.1.

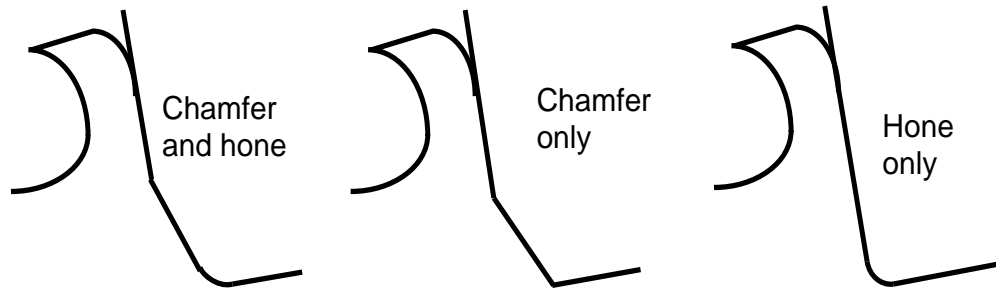


Figure 2.1 Cutting with various edge geometry CBN tools

Edge geometry of the CBN tool is an important factor affecting surface quality. However, performance observations on edge preparations are mixed. Hodgson et al. (1981) reported that the chamfered cutting edge of CBN tools results in a significant reduction in tool life and they usually develop notch wear. Koenig et al. (1984) suggested that the chamfer is unfavorable in terms of attainable surface finish compared to honed edges. Chou et al. (1997) tested three types of edge preparation for CBN in finish turning of hardened steels. The results indicated that the honed cutting edge has worse performance than the other two, based on tool flank wear and part surface finish. In light of these observations, it is clear that suitable edge preparation for a given cutting condition may change depending on the cutting condition. The importance of edge geometry implies additional importance to tool wear. As tool wears out, its edge geometry may change and thus affect the part surface quality. The effect of edge preparation on surface integrity has been studied by many researchers. Theile et al. (2000) showed that cutting edge geometry has significant impact on surface integrity and residual stresses in finish hard turning and

large hone radius tools produced more compressive stresses, but left “white-layers”, which is caused either due to severe plastic deformation that causes rapid grain refinement or due to rapid heating to austenite temperatures and fast cooling, on the surface. Koenig et al. (1984) also reported that an increase in feed rate raises the compressive residual stresses and deepens the affected zone. Tool nose radius has an inverse relationship with surface quality thus nose radius cannot be made very large although it increases the strength of the tool tip. The geometrical design of the workpiece is an important factor for selecting tool nose geometry. Small features cannot be machined by large tool nose radius cutting tools.

Performance of CBN cutting tools is highly dependent upon the cutting conditions i.e. cutting speed, feed, and depth of cut. Thiele et al. (1999) used a 3-factor full factorial design to determine the effects of workpiece hardness and tool edge geometry on surface roughness in finish hard turning using CBN tools. They performed three replicates of each factor level combination in order to account for variability in the process. They used analysis of variance (ANOVA) to discern differences in surface quality between various runs. They found that edge geometry and feed rate have an impact on surface quality. Their ANOVA results showed that the interaction between the hardness and edge geometry, and the interaction between hardness and feed rate were significant. Chou et al. (2002) utilized a similar approach to determine the influence of various parameters to surface roughness and flank wear in finish hard turning. They considered the effect of – cutting speed, CBN content percentage, and length of the cut. As a result, all the factors are found to be significant on tool wear and surface roughness in hard turning.

In this study, experimental observations on low CBN content inserts with two distinct edge preparations and through-hardened AISI H13 steel bars were investigated. The honed inserts with a radius of 0.01 mm, and chamfered inserts with 0.1 mm chamfer height and 20° chamfer angle are used. All inserts have 1.19 mm nose radius. The experimental conditions are summarized in Table 2.1. A total of 256 tests were conducted with replications. Each replication represents 25.4 mm cutting length in axial direction.

Table 2.1 Experimental factors and levels

Level	HRC	Edge geometry	V(m/min)	f(mm/rev)
Low	51.3	honed	100	0.1
High	54.7	chamfered	200	0.2

Longitudinal turning of hardened steel bars was conducted on a rigid, high-precision, production type CNC lathe (Romi Centur 35E) at a constant depth of cut at 0.254 mm. Surface roughness and tool wear measurements were conducted after machining axial cutting length of 25.4 mm (1 inch) up to 406.4 mm (16 inches) during each factor-level combination. The surface roughness was measured with a Taylor-Habson Subtronic 3+ profilometer and Mitutoyo SJ-digital surface analyzer. The surface roughness values were recorded at eight equally spaced locations around the circumference to obtain data for each factor level combination. CBN inserts were examined using a tool-maker microscope to measure flank wear depth and detect undesirable features on the edge of the cutting tool by interrupting finish hard turning process. Tables 2.2 and 2.3 present ANOVA results for finish hard turning of AISI H13 steel using CBN tools.

Table 2.2 ANOVA table for R_a surface roughness in finish hard turning of AISI H13 using CBN tools.

Source	DF	MS	F-ratio	p-value
H	1	0.02859	0.5802	0.448
V	1	2.58310	52.415	0.000
E	1	0.05681	1.1528	0.286
F	2	5.66360	114.93	0.000
L	15	0.02060	0.4180	0.970
H*V	1	0.55220	11.206	0.001
H*E	1	1.23390	25.036	0.000
H*f	1	0.00289	0.0584	0.810
H*L	15	0.03242	0.6578	0.817
V*E	1	0.97134	19.710	0.000
V*f	1	0.52002	10.552	0.002
V*L	15	0.04579	0.9291	0.536
E*f	1	0.32329	6.5601	0.012
E*L	15	0.04004	0.8126	0.661
f*L	21	0.03627	0.7360	0.784
Error	81	0.04928		
Total	173			

Table 2.3 ANOVA table for VB tool flank wear in finish hard turning of AISI H13 using CBN tools.

Source	DF	MS	F-ratio	p-value
H	1	0.02725	55.127	0.0000
V	1	0.02277	46.066	0.0000
E	1	0.00097	1.9648	0.1648
F	2	0.02534	51.256	0.0000
L	15	0.01489	30.124	0.0000
H*V	1	0.00014	0.2751	0.6014
H*E	1	0.00045	0.9169	0.3412
H*f	1	0.00253	5.1164	0.0264
H*L	15	0.00134	2.7104	0.0021
V*E	1	0.02646	53.532	0.0000
V*f	1	0.00175	3.5405	0.0635
V*L	15	0.00046	0.9231	0.5424
E*f	1	0.00283	5.7336	0.0190
E*L	15	0.00039	0.7918	0.6830
F*L	21	0.00156	3.1508	0.0001
Error	81	0.00049		
Total	173			

From the ANOVA for surface roughness, factors such as Hardness (H), Length (L), and interaction terms H*f, H*L, V*L, E*L, f*L are found to be statistically less significant on generation of surface roughness. For the tool flank wear progress interaction terms such as H*V, H*E, V*L, E*L are found to be insignificant. . In order to keep the model simple second order interactions were not included in the regression model.

Relationships between tool wear, surface roughness and machining parameters can be modeled by using experimental data. Regression models or neural network models have been used for this purpose in the literature (Fang and Safi-Jahanshahi (1997), Feng and Wang (2002)). In this study, an exponential model (Eq. 2.1) for both surface roughness and tool flank wear is suggested considering finish hard turning process using CBN tools. In the model, surface roughness and flank wear depth is considered to be a function of work material hardness (H), edge preparation (E), cutting speed (V), feed rate (f), and cutting length (L).

$$R_a = c_0 H^{c_1} E^{c_2} V^{c_3} f^{c_4} L^{c_5} \quad (2.1)$$

By using the experimental data, coefficients of the model can be calculated as in Eq. (2.2) and (2.3).

$$R_a = 1.0632 H^{0.5234} E^{0.1388} V^{-0.0229} f^{1.0198} L^{0.0119} \quad (2.2)$$

$$VB = 2.562 \times 10^{-8} H^{2.9656} E^{0.1074} V^{-0.0562} f^{-0.2618} L^{0.5420} \quad (2.3)$$

It has been reported in many studies that, neural networks, thanks to their capability of modeling non-linear relationships, outperforms regression models. Elanayar and Shin (1995) proposed a model, which approximates flank and crater, wear propagation and their effects on cutting force by using radial basis function neural networks. A wide range of tool monitoring techniques utilizing neural networks has been reviewed by Dimla et al. (1997). They concluded that neural networks are adequate for tool wear monitoring. Ghasempoor et al. (1999) proposed a tool wear classification and continuous monitoring neural network system for turning by employing recurrent neural network design. Liu and Altintas (1999) derived an expression to calculate flank wear in terms of cutting force ratio and other machining parameters. The calculated flank wear, force ratio, feed rate and cutting speed are used as an input to a neural network to predict the flank wear in the next step. Özel and Nadgir (2002) developed a back-propagation neural network model to predict tool wear on chamfered and honed CBN cutting tools for a range of cutting conditions. Sick (2002) demonstrated a hybrid technique, which combines a physical model describing the influence of cutting conditions on measured force signals with neural model describing the relationship between normalized force signals and the wear of the tool. Time-delay neural networks are used in his studies. Scheffer et al. (2003) developed an online tool wear monitoring system for hard turning by using a similar approach proposed by Ghasempoor et al. (1999). They combined the static and dynamic neural networks as a modular approach. The static neural networks are used to model flank and crater wear and trained off-line. The dynamic model is trained on-line to estimate the wear values by minimizing the difference between on-line measurements and the output of the static networks that enables the prediction of wear

development on-line. Choudry and Bartarya (2003) compared the design of experiments and neural networks techniques for predicting tool wear. They established the relationships between temperature and tool flank wear. They concluded that neural networks perform better than design of experiments technique.

On the other hand, there are very few publications appeared in the literature for predicting surface roughness utilizing neural network modeling. In an earlier work, Azouzi and Guillot (1997) examined the feasibility of neural network based sensor fusion technique to estimate the surface roughness and dimensional deviations during machining. This study concludes that depth of cut, feed rate, radial and z-axis cutting forces are the required information that should be fed into neural network models to predict the surface roughness successfully. In addition to those parameters, Risbood et al. (2003) added the radial vibrations of the tool holder as additional parameter to predict the surface roughness. During their experiments they observed that surface finish first improves with increasing feed but later it starts to deteriorate with further increase of feed. Tsai and Wang (2001) compared six types of neural network models and a neuro-fuzzy network in predicting surface roughness. Their study revealed that multilayer feed-forward neural network with hyperbolic tangent-sigmoid transfer functions performed better among feed-forward neural network models. Recently, Benardos and Vosniakos (2003) made an extensive literature review on predicting surface roughness in machining and confirmed the effectiveness of neural network approach. Feng and Wang (2003) compared regression models with a feed-forward neural network model by using experimental data obtained for traditional turning of aluminum 6061-T6 and AISI 8620

steel. Their results indicated that backpropagation neural network modeling provided better predictions for all of the cutting conditions that they are trained for. A short information on neural networks is given below.

2.3 Neural Network Modeling

Neural networks are nonlinear mapping systems consisting of neurons (processing units), which are linked by weighted connections. Neural networks have user-defined inputs and produce an output which reflects the information stored in connections during training. A neural network consists of at least three layers; input, hidden and output layer. As an example, the output expression of a 3-4-1 feed-forward neural network (Fig 2.2) with sigmoid activation functions in the hidden layer and linear activation function in the output layer in terms of its weight and bias terms is given in Eq. (2.4). Learning in neural networks, that is the calculation of the weights of the connections, is achieved by minimizing the error between the output of the neural network and the actual output over a number of available training data as given in Eq. (2.5).

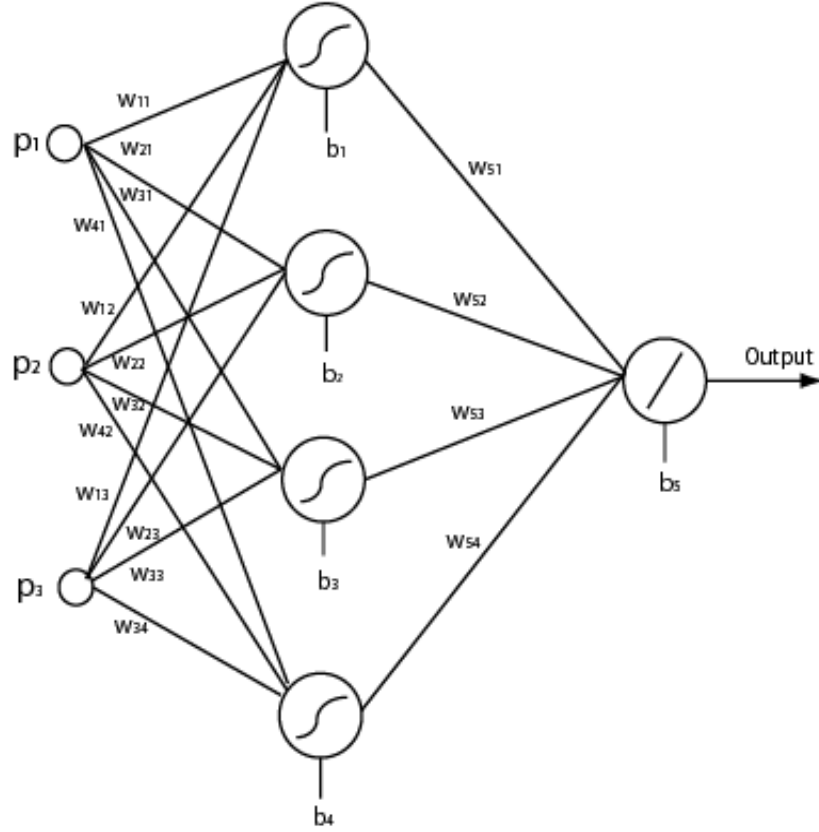


Figure 2.2 Feed-forward neural network architecture.

$$Output_{NN} = \left(\text{tansig} \left(\begin{bmatrix} w_{11} & w_{12} & w_{13} \\ w_{21} & w_{22} & w_{23} \\ w_{31} & w_{32} & w_{33} \\ w_{41} & w_{42} & w_{43} \end{bmatrix} \times \begin{bmatrix} p_1 \\ p_2 \\ p_3 \end{bmatrix} + \begin{bmatrix} b_1 \\ b_2 \\ b_3 \\ b_4 \end{bmatrix} \right) \times \begin{bmatrix} w_{51} & w_{52} & w_{53} & w_{54} \end{bmatrix} \right) + b_5 \quad (2.4)$$

$$SSE_{Error} = \sum_{i=1}^k \left[(\text{Output}_{\text{actual}})_i - (\text{Output}_{NN})_i \right]^2 \quad (2.5)$$

Backpropagation is the most commonly used method to calculate values for the weight and bias terms of the neural network model. In the backpropagation method, all weights are adjusted according to the calculated error term using steepest descent method. This

procedure is repeated many times until the sum squared error term reaches an acceptable level.

The structure of the neural network, normalization of input-output pairs, and appropriate selection of the number of hidden layers and the number of neurons in each hidden layer has a strong influence on the performance of the trained neural network. In this study, the non-linear *tanh* activation functions are used in the hidden layer and input data are normalized in the range of $[-1, 1]$. The weights and biases of the network are initialized to small random values to avoid immediate saturation in the activation functions. Throughout this study, the data set is divided into two sets: Training and test sets. Neural networks are trained by using a training data set, and their generalization capacity is examined by using test sets. The training data is never used in the test data. When the number of training data is limited, instead of backpropagation, more advanced training algorithms such as Bayesian regularization, which is also employed in this study, are more appropriate. The basic assumption in Bayesian regularization is that the true underlying function between input-output pairs should be smooth and this smoothness can be obtained by keeping network weights small and well distributed within the neural network. This is achieved by constraining the size of the network weights which is referred to as regularization which adds additional terms to the objective function

$$F = \phi.(SSE_{error}) + \nu.W \quad (2.6)$$

where SSE_{error} is the sum of squared errors (performance index) which was defined in Eq. (2.5), W is the sum of squares of the network weights, ϕ and ψ are objective function parameters. This modification in performance index will result in a neural network with smaller weights and biases which will force its response to be smoother and decrease the probability of overfitting. The weights and biases are assumed to be random variables with specific distributions. The regularization parameters are related to the unknown variances associated with these variables. If $\phi \gg \psi$, the objective function will try to minimize the network error or else ($\phi \ll \psi$) the objective function will drive weights to smaller values at the expense of network errors. Training with Bayesian regularization yields important parameters such as sum of square errors (SSE), sum of squares of weights (SSW) and number of effective parameters used in neural network, which can be used to eliminate guesswork in selection of number of neurons in hidden layer. Number of neurons to be used in the hidden layer of a neural network is critical in order to avoid overfitting problem, which hinders the generalization capability of the neural network. Number of hidden layer neurons is usually found with trial and error approach. In this study, a systematical approach is adapted by using the output parameters of Bayesian regularization algorithm. The basic idea is to obtain approximately the same number of effectively used parameters (NOEP) over the trials. This assumes that the resultant neural network has enough number of parameters to represent the training set. In the mean time, the consistency of sum of squared errors (SSE) and sum of network weights (SSW) is maintained. An example of this procedure is given in Table 2.4 for training neural network for flank wear and surface roughness prediction.

Surface roughness and tool wear are predicted with a feed-forward multilayer neural network as shown in Fig. 2.3 by using direct process parameters tool edge geometry, Rockwell-C hardness of workpiece, cutting speed, feed rate and cutting length as inputs to neural network. This neural network is trained with 173 data points. It is tested on 36 data points which are randomly chosen from different cutting conditions from the data set consists of 209 data points. As seen from Table 2.4, network structure 5-15-2 is chosen after the observation of consistent number of effective parameters and error terms. The output parameters of training with Bayesian regularization with respect to epoch number are given in Fig. 2.4. It can be seen that training of neural networks can be achieved quickly.

Table 2.4. An example for selecting number of neurons in hidden layer.

	SSE	SSW	NOEP	Rms Error VB	Rms Error Ra
Structure 5-13-2					
Trial 1	3.33	28.04	81 (106)	8.77	7.70
2	3.26	28.98	83 (106)	9.32	8.44
3	3.38	26.36	81 (106)	8.63	7.74
4	3.43	26.82	78 (106)	9.65	8.42
5	3.43	27.02	79 (106)	9.62	8.66
6	3.26	31.11	84 (106)	8.02	8.29
				Avg 9.01	Avg 8.20
Structure 5-15-2					
Trial 1	3.00	36.14	92 (122)	7.98	7.77
2	3.11	33.93	91 (122)	8.66	7.84
3	2.99	35.34	92 (122)	7.71	8.08
4	3.12	31.15	91 (122)	9.02	7.92
5	3.02	34.77	91 (122)	8.24	7.9
6	3.05	34.84	91 (122)	7.96	8.48
				Avg 8.26	Avg 7.98

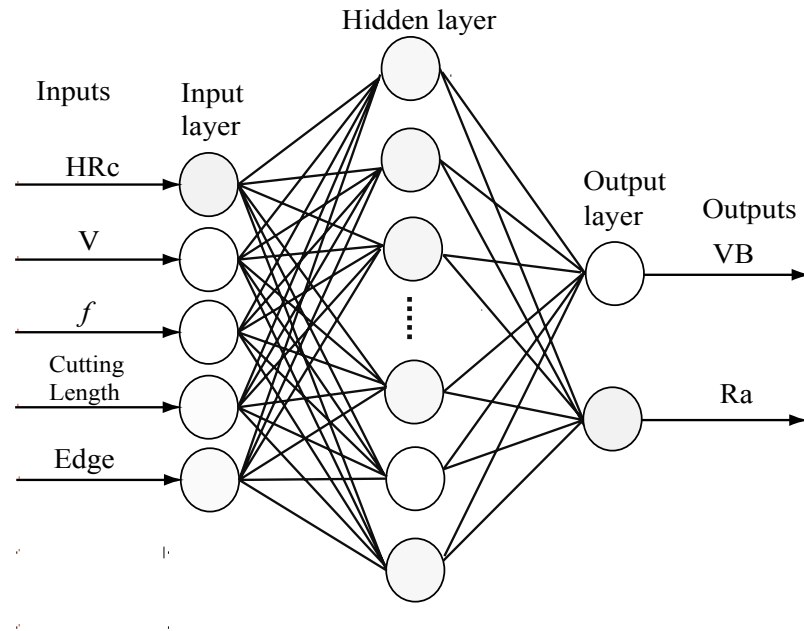


Figure 2.3 Neural network model for tool wear and surface roughness prediction.

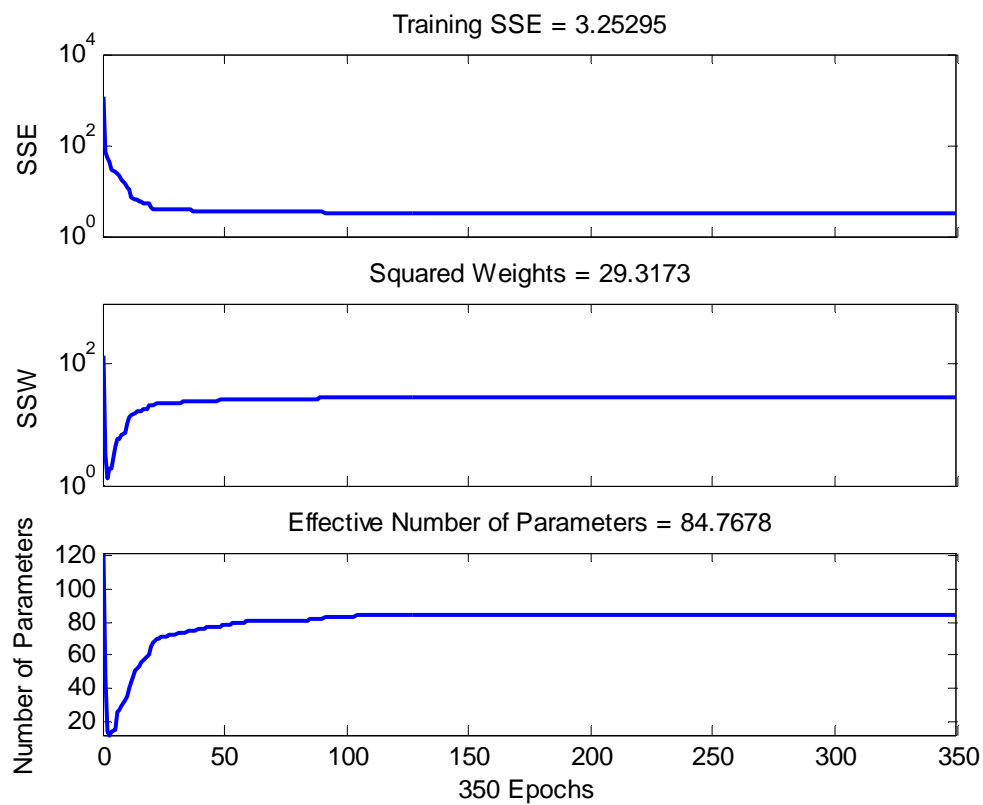


Figure 2.4 An example of training results for selecting number of neurons in hidden layer.

Comparison of sum of square errors of neural network predictions, regression model, and measurements can be seen in Fig 2.5.

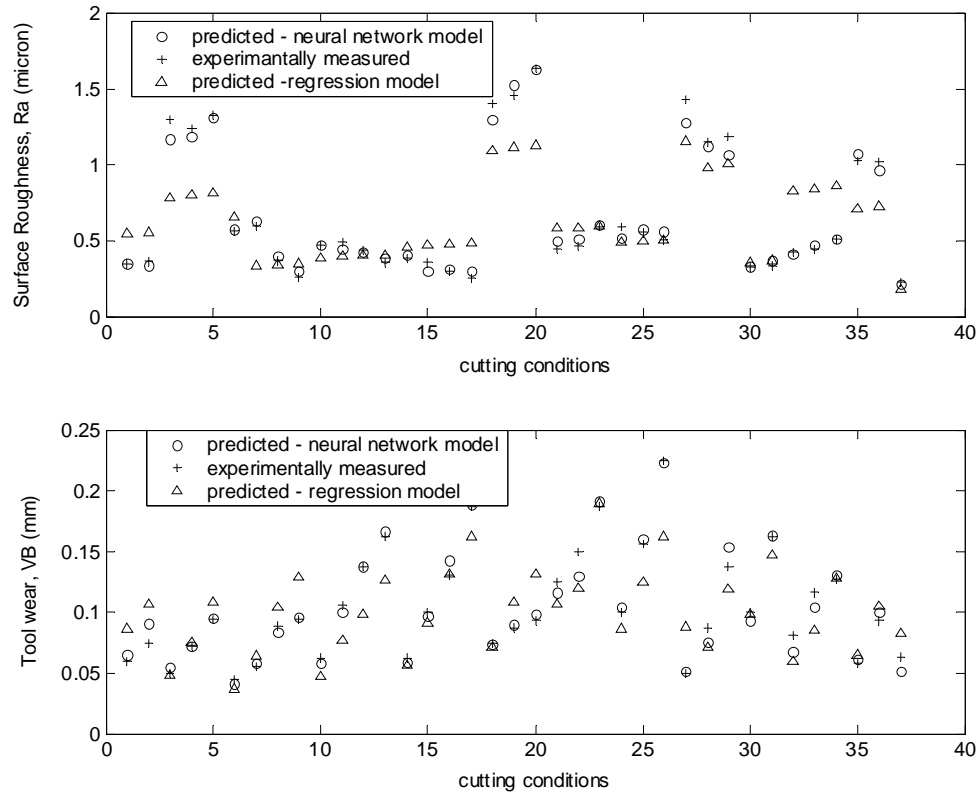


Figure 2.5 Comparison of predicted surface roughness and tool wear using neural network vs. regression model.

According to above given results, predictions with neural networks outperform the prediction resulted from regression-based models. Tool wear development and surface roughness predictions with respect to cutting length are given in Fig. 2.6. As expected, tool wear increases with cutting distance and neural network model does a good job predicting the tool wear development. As for surface roughness, which is affected by

many factors, the neural network model is able to capture the trend with respect to axial cutting distance.

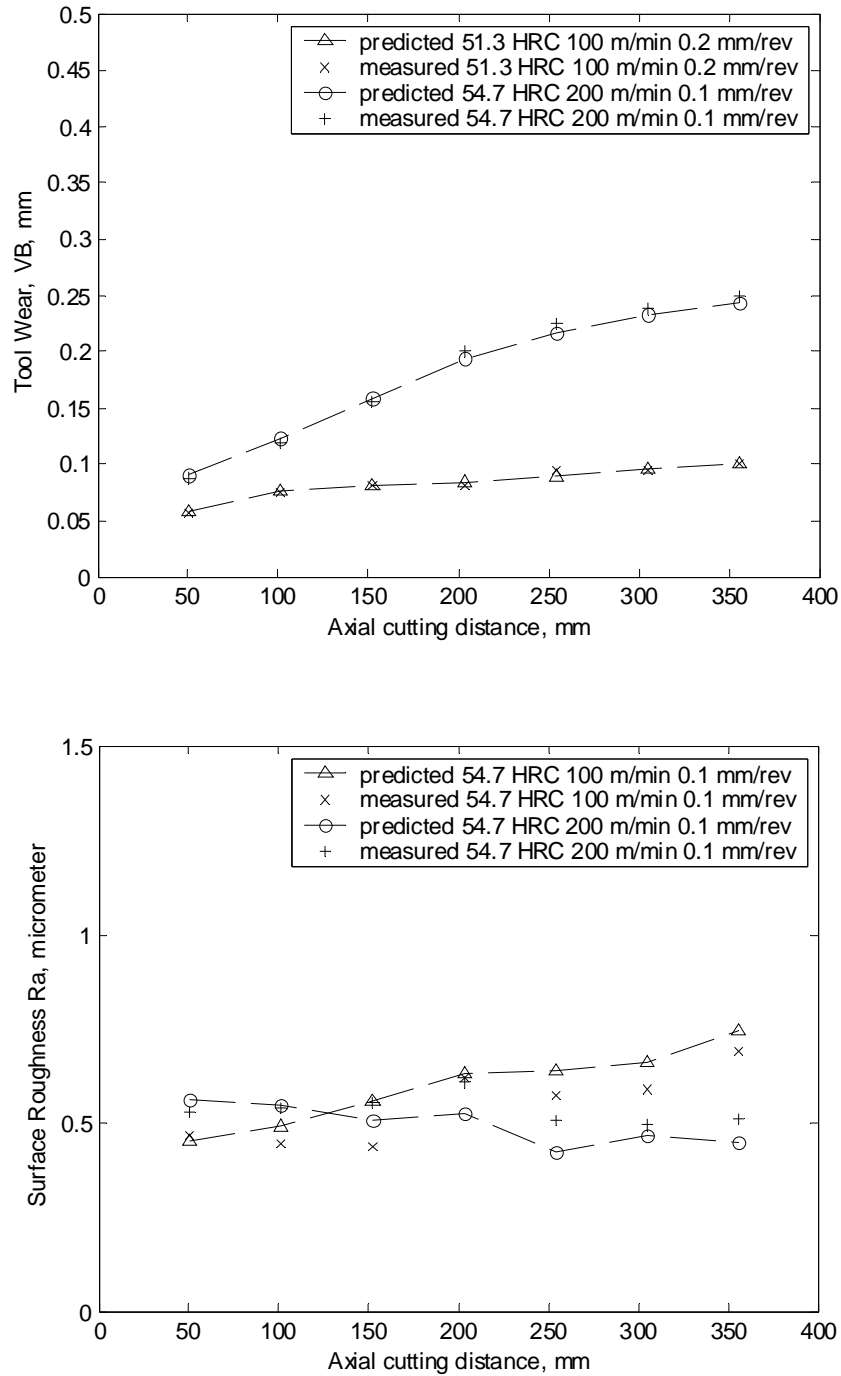


Figure 2.6 Comparison of surface roughness and tool wear predictions and measurements.

Prediction simulations are performed with respect to axial cutting distance to demonstrate the tool wear and surface roughness development in finish hard turning. As expected, tool wear values increase with increasing cutting distance, cutting speed and workpiece hardness. In surface roughness simulations, it is observed that decreasing feed rate and increasing cutting speed improves surface finish quality. However, it should be noted that increasing cutting speed adversely affects tool wear and decreasing feed rate may hinder productivity. In some cutting conditions, as in Fig. 2.7, surface roughness improved with increasing tool wear due to sharpening effect of tool wear on cutting edges, therefore attention should be paid to the relation between tool wear and surface roughness.

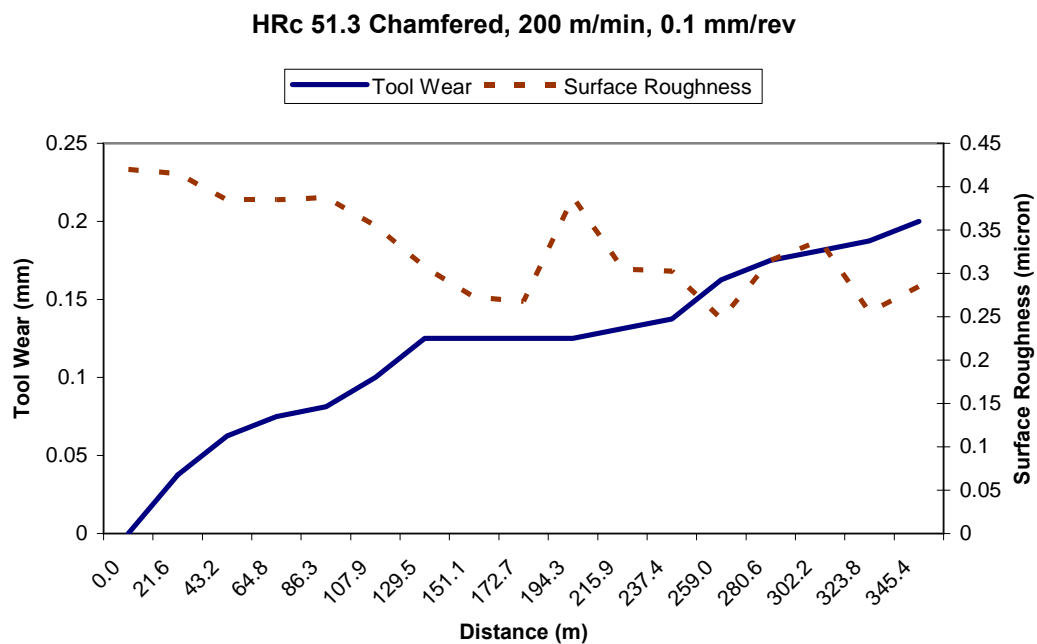


Figure 2.7 Development of tool wear and surface roughness with respect to circumferential machined distance.

Having obtained a model which can predict tool wear and surface roughness depending on the cutting conditions, attempts toward finding optimum cutting conditions can be made. Since more than one objective exists in hard turning such as increasing material removal rate and decreasing surface roughness, our interest is multi objective optimization of hard turning.

2.4 Multi Objective Optimization of Hard Turning

The general formulation of multi-objective optimization problems can be written in the following form:

$$\begin{aligned} &\text{Minimize (or maximize) } \mathbf{f}(\mathbf{x}) = \{f_1(\mathbf{x}), f_2(\mathbf{x}), f_3(\mathbf{x}), \dots, f_k(\mathbf{x})\} \\ &\text{subject to } g_j(\mathbf{x}) \leq b_j \text{ for } j = 1, 2, \dots, m \\ &\text{and } h_j(\mathbf{x}) = b_j \text{ for } j = m + 1, \dots, m + p \end{aligned}$$

In this formulation; $f_i(\mathbf{x})$ denotes the i^{th} objective function, $g_i(\mathbf{x})$ and $h_i(\mathbf{x})$ indicate inequality and equality type of constraints and the decision variables (machining parameters) are shown with the vector \mathbf{x} , where $\mathbf{x} = (x_1, x_2, \dots, x_n) \in \mathbb{R}^N$. The ultimate goal is simultaneous minimization or maximization of given objective functions. When, as in most cases, some of the objective functions conflict with each other there is no exact solution but many alternative solutions. This family of potential solutions cannot improve all objective functions simultaneously. This is called Pareto optimality (Pareto, (1896)) and the related definitions are given below.

Definition 1: Pareto Optimal. Consider a point \mathbf{x}^* in the feasible solution space, \mathbf{X} , $\mathbf{x}^* \in \mathbf{X}$. The point (a set of decision variables) is Pareto optimal if and only if there does not exist another point, $\mathbf{x} \in \mathbf{X}$, that satisfies $\mathbf{f}(\mathbf{x}) < \mathbf{f}(\mathbf{x}^*)$ and $f_i(\mathbf{x}) < f_i(\mathbf{x}^*)$ for at least one function.

In other words, this definition states that, for a minimization problem, there is no other point which can cause a decrease in one objective function value without causing a simultaneous increase in at least one of the other objective function values.

Definition 2: Dominated and Non-Dominated Points. A vector of objective functions, $\mathbf{f}(\mathbf{x}^*)$, is non-dominated if and only if there does not exist another vector, $\mathbf{f}(\mathbf{x})$, that satisfies $\mathbf{f}(\mathbf{x}) \leq \mathbf{f}(\mathbf{x}^*)$ with at least one $f_i(\mathbf{x}) < f_i(\mathbf{x}^*)$. Otherwise, $\mathbf{f}(\mathbf{x}^*)$ is dominated.

Definition 3: Pareto Front. The set $\mathbf{X}^* = \{\mathbf{x}_1^*, \mathbf{x}_2^*, \dots, \mathbf{x}_n^*\}$, which is composed of all the non-dominated Pareto optimal solutions that comprise the Pareto front of non-dominated solutions.

There are many ways to solve multi-objective optimization problems. A summary of these methods can be found in Marler and Arora (2004). The most common method is to combine all the objectives into a single objective function by multiplying each objective function by weight functions which represent the relative importance among the objectives. However, choosing proper weights can be a problem, and they are usually selected arbitrarily. The Pareto optimal non-dominated solution set avoids this problem

and may provide numerous prospective solutions (sets of machining parameters) for the decision maker (manufacturer) during process planning.

Since neural network models are used to model the relationships, conventional gradient-based multi objective optimization techniques are not suitable therefore meta-heuristic search algorithms are often employed in these cases. Stochastic and population based search algorithms are suitable for finding approximate Pareto optimal solutions for multi-objective functions. Many genetic algorithms (GA) based approaches have been proposed to solve multi-objective optimization problems for machining processes, e.g. Cus and Balic (2003), and Saravanan et al. (2002). The PSO has reportedly performed as well as GAs on many test problems (Zitzler et al. 2003), and it is an efficient and general method to locate the Pareto front of the multi-objective optimization problems. The PSO has been applied successfully to predicting surface roughness in end milling by El-Mounayri et al. (2003) and optimization of cutting conditions for NC end milling by Tandon et al. (2002).

In obtaining optimal solutions for these multi-objective problems, a number of heuristic algorithms including genetic algorithms (GA), evolutionary algorithms (EA) and simulated annealing (SA), as well as a recently developed optimization algorithm called particle swarm optimization (PSO) have been used. The PSO is a population based search algorithm, which was inspired by the social behavior of bird flocks as originally developed by Eberhart and Kennedy (1995). The PSO operates on a population of potential solutions rather than a single individual solution. Conventional optimization

techniques, such as gradient-based methods, do not function effectively solving true multiple objective functions without reducing the objectives into a single function and handling it accordingly. Many researchers such as Coello and Lechuga (2002) find the PSO as an efficient alternative over other search algorithms when dealing with multi-objective optimization problems.

In this study, the particle swarm optimization method was used to solve the multi-objective optimization problem. The multiple objectives are used to obtain a group of optimal process parameters which minimize surface roughness values and maximize the productivity at the same time. The PSO algorithm is relatively easy to implement and has fewer parameters to adjust when compared to other evolutionary algorithms. The information sharing mechanism among the particles in PSO is significantly different than the information sharing among the chromosomes in GAs. In GAs, the entire group moves towards an optimal solution area. However, in PSO only the global best or local best solution is reported to the other particles in a swarm. Therefore, evolution only looks for the best solution and the swarm tends to converge to the best solution quickly and efficiently.

2.5 Particle Swarm Optimization (PSO) and Multi Objective Particle Swarm Optimization (MOPSO)

PSO is a population based stochastic optimization technique developed by Eberhart and Kennedy (1995) inspired from social behavior of bird flocks. The PSO is

initialized with a population of random solutions and this initial population evolves over generations to find optima. In PSO, different from genetic algorithms, each particle in the population has a velocity, which enables it to fly through the problem space. Therefore, each particle is represented by a position and a velocity vector. Dimensions of position and velocity vectors are defined by the number of decision variables in the optimization problem. Modification of the position of a particle is performed by using its previous position information and its current velocity. According to the value of the objective function, each particle knows its best position ever (personal best, $pbest$) and the best position achieved in the group (group best, $gbest$) among all personal bests. For a single objective problem, the result of the optimization problem will be the position vector of $gbest$. These principles can be formulated as:

$$v_i^{k+1} = wv_i^k + c_1rand_1(pbest_i - x_i^k) + c_2rand_2(gbest_i - x_i^k) \quad (2.7)$$

where

v_i^k : velocity of agent i at iteration k
 x_i^k : current position of agent i at iteration k
 $pbest_i$: personal best of agent i
 $gbest$: best position in the neighborhood
 $rand$: random number between 0 and 1
 w : weighting function
 c_j : learning rate $j=1,2$

$$x_i^{k+1} = x_i^k + v_i^{k+1} \quad (2.8)$$

The first term on the right hand side of Eq. (2.7) is the previous velocity of the particle.

Weighting function w is set at a large value at the beginning of the search and decreased

to a smaller value over the iterations to confine the search in a smaller region in later iterations, or it could be selected randomly. The second and third terms are used to change the velocity of the particle according to $pbest$ and $gbest$ values. The random numbers used in the velocity update step give the PSO a stochastic behavior. The iterative approach of PSO can be described as follows:

Step 1: Initial position and velocities of agents are generated. The current position of each particle is set as $pbest$. The $pbest$ with best value is set as $gbest$ and this value is stored. The next position is evaluated for each particle by using Eq. (2.7) and (2.8).

Step 2: The objective function value is calculated for new positions of each particle. If an agent achieves a better position, the $pbest$ value is replaced by the current value. As in Step 1, $gbest$ value is selected among $pbest$ values. If the new $gbest$ value is better than the previous $gbest$ value, the $gbest$ value is replaced by the current $gbest$ value and stored.

Step 3: Steps 1 and 2 are repeated until the iteration number reaches a predetermined iteration number.

The velocity update step in the PSO is stochastic due to the random numbers generated, which may cause an uncontrolled increase in velocity and therefore instability in the search algorithm. In order to prevent this, velocities are limited to the dynamic range of the particle on each dimension.

The formulation of the PSO given with Eq. (2.7) and (2.8) corresponds to the global version of the PSO. In addition, a local version of the PSO algorithm also exists. In the local version, particles have information only of their own and their nearest neighbor best (*lbest*) *gbest* is then replaced by *lbest* in the algorithm.

The above given version and variations of PSO are not suitable for solving multi-objective optimization problems since there is no absolute global minimum (or maximum) in multi-objective problems. Therefore, the algorithm needs some modifications to locate the Pareto front in multi-objective optimization problems. Hu and Eberhart (2002) proposed Dynamic Neighborhood-Particle Swarm Optimization (DN-PSO) for this purpose. In this approach, instead of defining one global best for the whole population, neighborhoods are defined for each particle and local *gbests* are found within these neighborhoods. Fig. 2.8 shows a two-dimensional objective function space in a min-min problem. The Pareto front is the boundary of the objective value region, which is the lower left side of the objective function space for min-min problems. The objective of the proposed algorithm is to drop those solutions onto the boundary line indicated by a solid line.

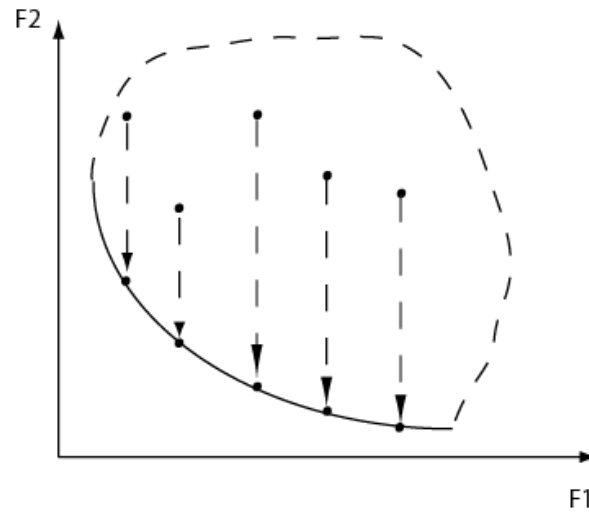


Figure 2.8 Pareto front illustrated with solid line for a min-min problem (Hu and Eberhardt (2002)).

For this purpose, the first objective function is fixed to define neighborhoods and the second objective function is used in optimization.

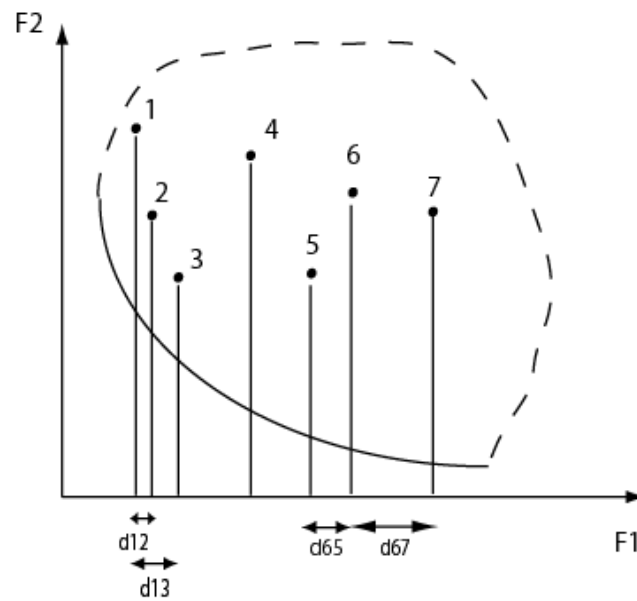


Figure 2.9 Concept of dynamic neighborhood in the solution space.

According to the DN-PSO algorithm; (1) the distances between the current particle and other particles are calculated in terms of the first objective function, (2) based on these distances, the nearest m (neighborhood size) particles are found, (3) the local best particle among neighbors is selected in terms of the second objective function as illustrated in Fig. 2.9.

The neighborhood size can be selected as $m=2$. As an example, for a particle whose objective function values correspond to point 6 in the objective function space, the nearest neighbors in terms of the first objective function are points 5 and 7. Since point 5 has a lower objective function value in terms of the second objective function, point 5 is selected as a local *gbest* for point 6. Similarly, point 3 is selected as the local *gbest* for point 1. This procedure is repeated for all particles and local *gbests* for each particle are found. Since after the each iteration the positions of the particles change (also their objective values), neighborhoods are defined dynamically at each step.

Another important term *pbest*, which is the best position in the memory of a particle, is updated according to Pareto dominance principle. The new *pbest* should simultaneously improve both objective functions as shown in Fig. 2.10.

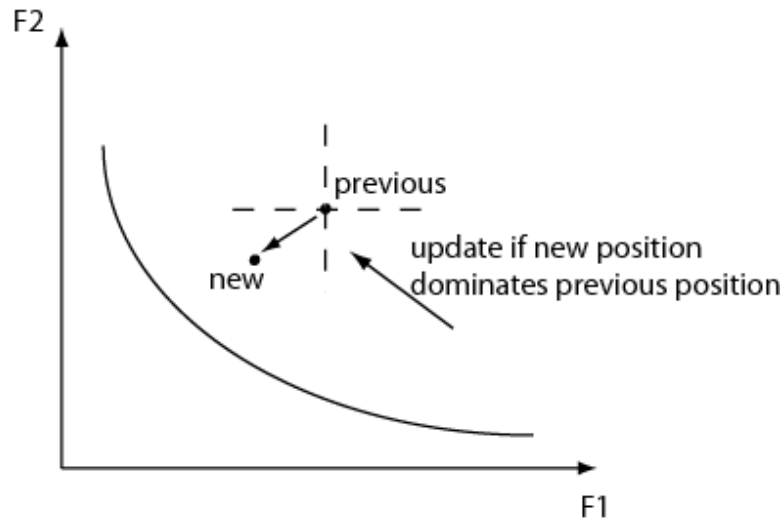


Figure 2.10 Selection pbest according to Pareto Dominance principle.

The DNPSO methodology proposed by Hu and Eberhardt (2002) can only be applied to multi-objective problems with two dimensions. It presents a simple and a novel approach to locate the Pareto front but usually does not yield a well-distributed Pareto front because the algorithm was not designed to promote diversity during search.

For cases where more than two objective functions exist, different algorithms have been proposed by Coello et al. (2004), Fieldsend and Singh (2002), Mostaghim and Teich (2003), Villalobos et al. (2005) and Benitez et al. (2005). Recently proposed algorithms make use of constrained or unconstrained archives, which store the non-dominated solutions found during search. Each member of the non-dominated archive can be a potential global guide for any particle in the swarm but the main problem is how to choose the right one.

In order to overcome this difficulty while obtaining a well-distributed Pareto front, Coello et al. (2004) used an external repository that contains the non-dominated

solutions and divides the objective space into grids (hypercubes). Each non-dominated solution, depending on its objective function value, is assigned into the closest grid. During the selection of gbest, grids which contain fewer numbers of non-dominated solutions are selected with a random approach so that particles are directed to search in these areas. Although very successful results are obtained, this methodology is susceptible for problems with different objective function scaling.

In this study, the methodology proposed by Benitez et al. (2005) is adopted. In their study, the selection of global guides (gbest) is based on Pareto dominance. An external archive is again used to store the non-dominated solutions found by the algorithm and its size is not restricted. When new non-dominated solutions are found, they are entered into the archive and existing members of the archive are deleted if they are dominated by the new solutions. The idea is to select a global guide for a particle from the archive members that dominate that particle. One particle can be dominated by more than one non-dominated solution. The selection can be made randomly or a promotion value can be assigned to each non-dominated solution which increases with the number of iterations. An archive member with high promotion value is more likely to be picked as a global guide. When an archive member is selected its promotion value is reset to zero. In addition, the archive members in densely populated regions are assumed to be more likely to dominate more particles than the archive members in sparsely populated regions.

In the PSO, weighting function w and learning rates c_1 and c_2 need to be adjusted. The values of these parameters are adapted from Hu and Eberhart (2002) where weight w was chosen as $(0.5 + (\text{Rand}[0,1]/2))$ and learning rates were taken as 1.49445. In order to make particles explore a wider area, c_2 parameter is taken as zero until the size of the external archive reaches 50. By doing so, there will be many potential guides when it comes to selecting guides for each particle. Since the PSO and its extensions to multi-objective optimization are relatively new, development of better methodologies is an ongoing research area.

2.6 Swarm-Intelligent Neural Network System (SINNS)

In order to obtain a family of solutions that will provide useful information to the user during the selection of machining parameters, trained neural network models should be integrated with the multi-objective particle swarm optimizer. For this purpose, Swarm Intelligent Neural Network System (SINNS) is proposed. The architecture of SINNS is shown in Fig. 2.11.

Single or multiple neural network models are grouped together under the neural network model (Fig. 2.12) and its output is fed into the multi-objective particle swarm optimizer where the objective functions and constraints are defined. As a result, the Pareto front corresponding to the objective functions is produced. There is no other user intervention in the system. The cutting speed, feed rate and cutting distance are the inputs of the neural network model. It must be noted that, tool wear is used as an inputs to the surface

roughness neural network model due to the fact that increasing tool wear affects surface roughness.

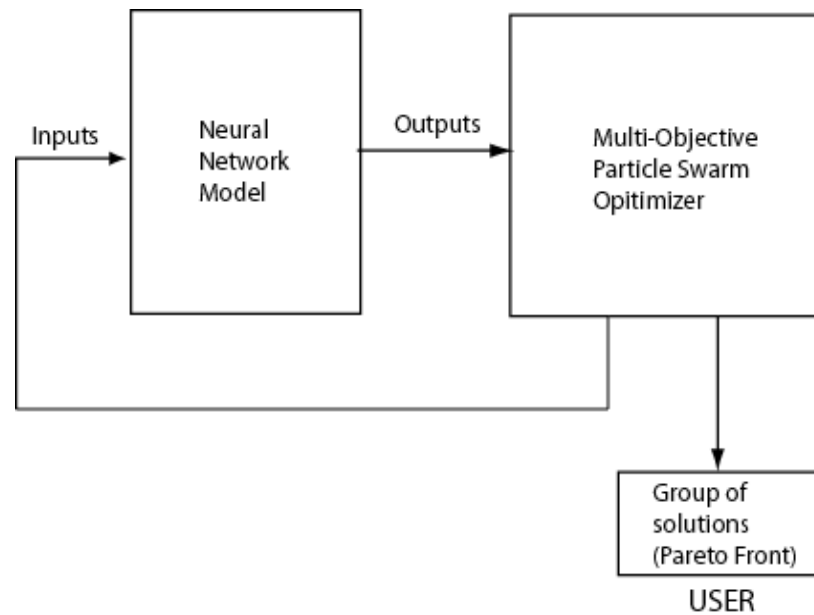


Figure 2.11 Swarm Intelligent Neural Network System (SINNS).

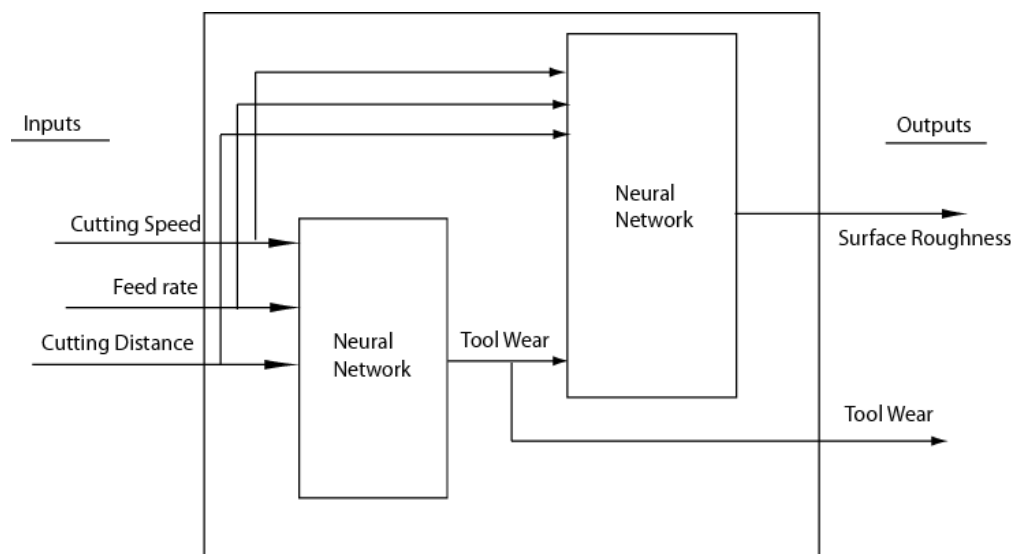


Figure 2.12 Neural network model used in SINNS for surface roughness and tool wear predictions.

Summary of the experimental results used while training these neural networks is given in Table 2.5. The workpiece hardness is not taken as an input in this study; it is assumed that the AISI H13 workpiece has hardness value of 54.7 HRC.

Table 2.5 Summary of the experimental results

Honed Inserts				Chamfered Inserts			
Cutting Speed (m/min)	Feed Rate	Tool Wear (mm)	Surface Rough. (μm)	Cutting Speed (m/min)	Feed Rate (mm/rev)	Tool Wear (mm)	Surface Roughness (μm)
100	0.1	0.13	0.38	100	0.1	0.2	0.5
200	0.1	0.16	0.33	200	0.1	0.25	0.54
100	0.2	0.13	0.42	100	0.2	0.25	1.25
200	0.2	0.13	1	200	0.2	0.15	1.15
200	0.05	0.15	0.25	N/A			

The following optimization problem can be defined for chamfered and honed tools separately as below and used in multi-objective particle swarm optimizer in SINNS architecture. Decision variables cutting speed V and feed rate f are constrained within the ranges of the experiments. In Eq. (2.9), L is the length of the shaft, and N is the rotational speed of the spindle. In order to handle constraints, a simple modification to the particle swarm optimization algorithm is sufficient.

$$\begin{aligned}
 f_1 &= \text{minimize (Surface roughness)} \\
 f_2 &= \text{minimize } \left(\text{Machining Time} = \frac{L}{f \times N} \right) \\
 \text{subject to} \\
 100 \text{ m/min} &\leq V \leq 200 \text{ m/min} \\
 0.05 \text{ mm/rev} &\leq f \leq 0.2 \text{ mm/rev (Honed inserts)} \\
 0.1 \text{ mm/rev} &\leq f \leq 0.2 \text{ mm/rev (Chamfered inserts)}
 \end{aligned} \tag{2.9}$$

The additional rules that should be implemented in MOPSO algorithm are: (1) Particles should be initiated within feasible region. (2) When updating memories, only the particles within feasible region should be kept in memory. MOPSO optimization algorithm combined with constraints was converted into a code in Matlab software. The results obtained for chamfered and honed tools are shown in Fig. 2.13 and 2.14.

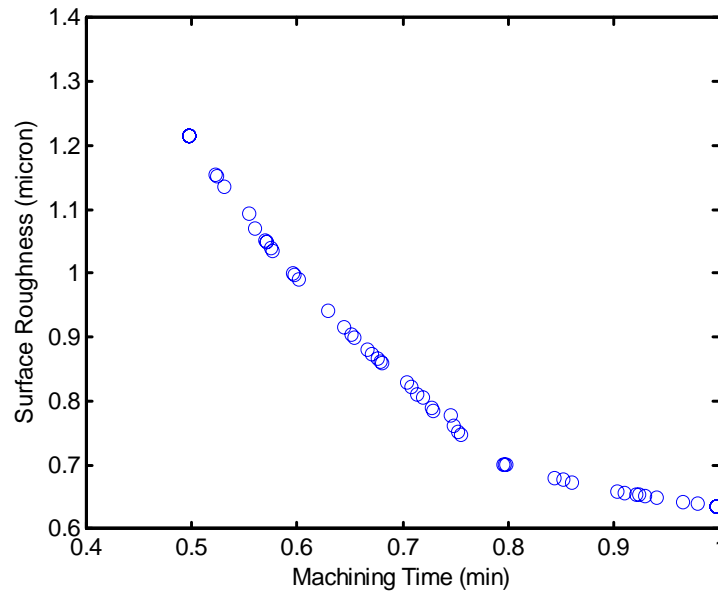


Figure 2.13 The Pareto front of non-dominated solutions for machining parameter using chamfered inserts.

Since the selection of feed rate influences surface roughness and machining time conversely, minimization of surface roughness and minimization of machining time are contradicting objectives. In order to obtain a good surface finish, feed rate should be reduced, which then increases the machining time. Therefore, a compromise between surface roughness and machining time should be made. According to some candidate solutions listed in Table 2.5, machining time can be reduced more than one minute with a 0.1 micron sacrifice in surface roughness estimation by setting the cutting conditions to $V=200\text{ m/min}$ and $f=0.125\text{ mm/rev}$ instead of $V=100\text{ m/min}$ and $f=0.1\text{ mm/rev}$.

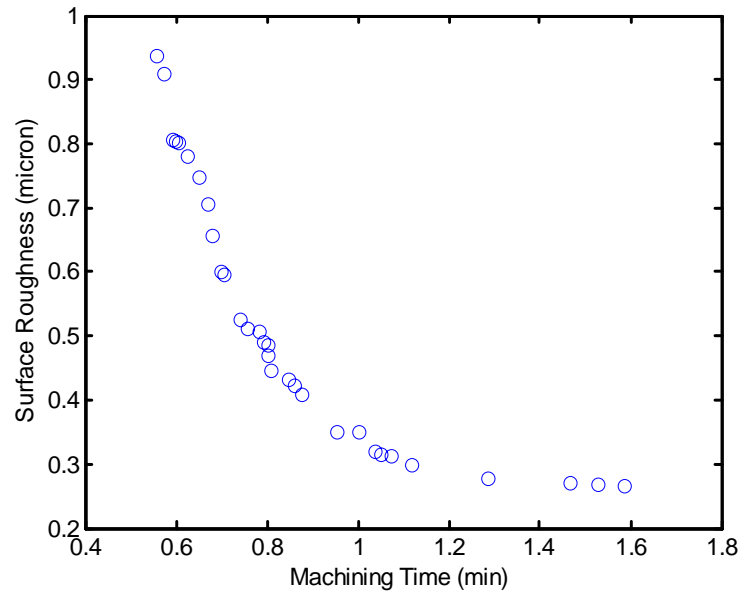


Figure 2.14 The Pareto front of non-dominated solutions for machining parameters using honed inserts.

As for honed edge, since lower feed rate experiments were performed during experimentation, better surface roughness values were obtained. Similarly, at the cost of increasing surface roughness slightly shorter machining times can be obtained by

adopting optimum cutting conditions given in Table 2.5. Fig. 2.15 and 2.16 demonstrate an, increasing trend in material removal rate, an important productivity indicator.

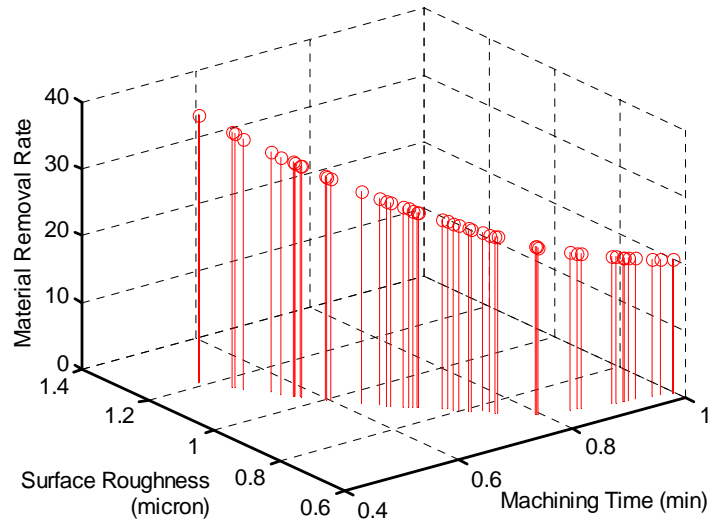


Figure 2.15 The Pareto front of non-dominated solutions with MRR for machining parameters using chamfered inserts.

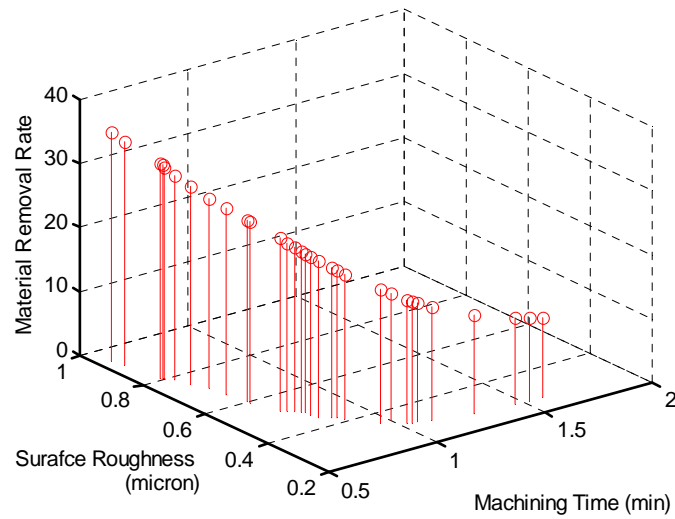


Figure 2.16 The Pareto front of non-dominated solutions with MRR for machining parameters using a honed inserts.

Some of the optimal cutting speed, feed rate pairs from the Pareto fronts with corresponding surface roughness and machining times are shown in Table 2.6.

Table 2.6 Some selected optimal machining parameters from Pareto Front.

Honed Inserts				Chamfered Inserts			
Cutting Speed (m/min)	Feed Rate (mm/rev)	Mach Time (min.)	Surface Roughness (μm)	Cutting Speed (m/min)	Feed Rate (mm/rev)	Mach Time (min.)	Surface Roughness (μm)
200	0.05	1.58	0.26	100	0.1	1.99	0.61
197.7	0.094	1.07	0.31	200	0.125	0.79	0.70
184.8	0.12	0.84	0.43	192.8	0.147	0.70	0.83
163.4	0.18	0.64	0.74	200	0.175	0.57	1.05
178.7	0.2	0.55	0.93	200	0.2	0.49	1.21

As another case study, where the objective is to maximize multiple objectives is given next. This example also demonstrates the unique tool life behavior of CBN cutting tools. The tool life expressions developed for conventional tools does not apply to CBN tools. In a recent work by Mamalis et al. (2005), tool life tests of CBN tools when machining 100Cr6 steel (62 HRC) has been reported. In this study, the experimental data given in Mamalis et al. (2005) is used to design a neural network model which predicts tool life according to given cutting speed, feed rate and depth of cut values. A neural network with two hidden layers and sigmoid transfer functions 3-4-2-1 is chosen and trained with Bayesian regularization. The experimental values obtained at feed rate of 0.075 mm/rev and depth of cut of 0.1 mm are excluded from the data set during training.

The comparison of predicted and actual data together with other experimental values is shown in Fig. 2.17. As in the previous case study, the neural network model is inserted in SINNS to obtain the Pareto front between tool life and material removal rate. Since it is desirable to maximize both tool life and material removal rate, necessary modifications in the MOPSO algorithm should be performed.

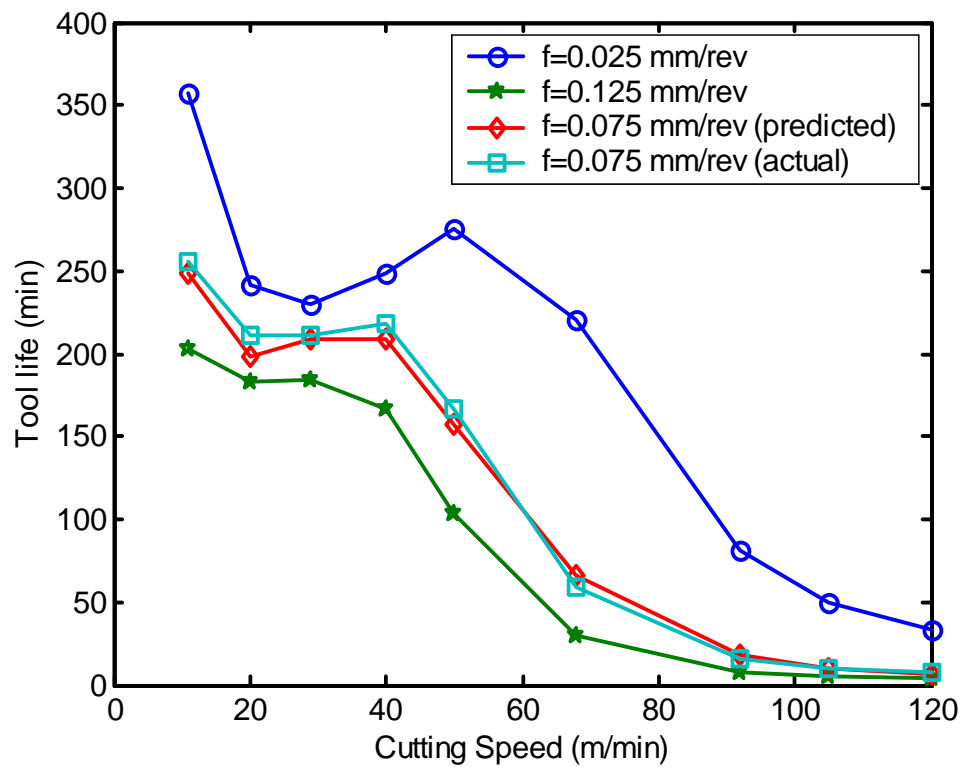


Figure 2.17 Tool life curves for CBN tools under different machining conditions. Data from Mamalis et al. (2005)

The optimization problem can be defined as:

$$f_1 = \text{maximize (Tool life)}$$

$$f_2 = \text{maximize (Material removal rate} = V \times f \times d)$$

subject to

$$11 \text{ m/min} \leq V \leq 120 \text{ m/min}$$

$$0.025 \text{ mm/rev} \leq f \leq 0.125 \text{ mm/rev}$$

$$0.05 \text{ mm} \leq d \leq 0.25 \text{ mm}$$

where V is cutting speed, f is feed rate and d is depth of cut. The Pareto front can be seen in Fig. 2.18. Some of the optimal cutting conditions are listed in Table 2.7.

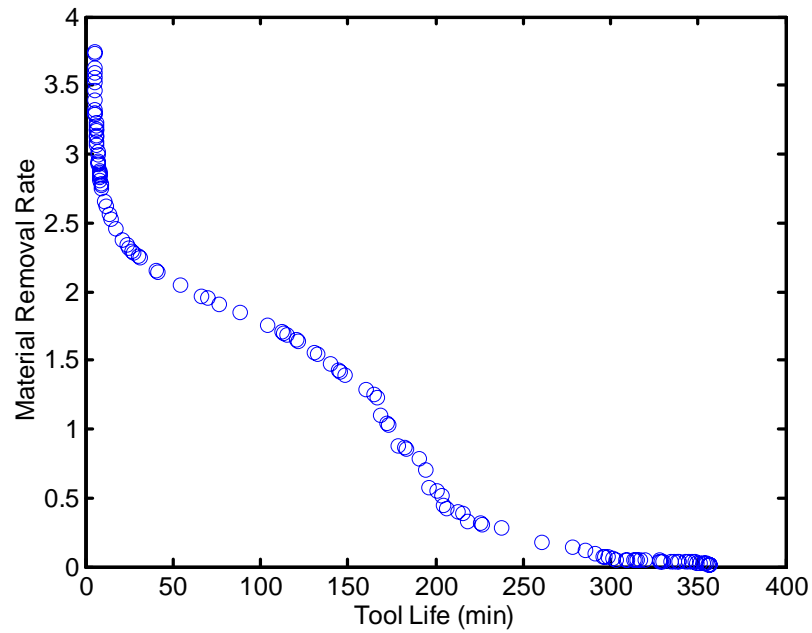


Figure 2.18 Pareto Front of the max-max optimization problem

Table 2.7. Some selected optimal machining parameters

Feed Rate (mm/rev)	Depth of Cut (mm)	Cutting Speed (m/min)	Tool Life (min.)	MRR (mm ³ /min)
0.025	0.05	11	356	0.01375
0.037	0.168	48.4	235	0.305
0.084	0.198	35.11	193.26	0.589
0.116	0.25	37.7	171.1	1.101
0.125	0.25	57.4	98.4	1.79
0.125	0.25	120	4.69	3.75

2.7 Conclusions and Discussions

The objective of this chapter was; (1) to introduce the factors affecting surface roughness and tool wear, (2) to develop a predictive tool wear and surface roughness models based on neural networks, (3) to use these models in an optimization scheme to calculate optimum cutting conditions in the presence of multiple objectives.

Firstly, analysis of variance (ANOVA) is used to investigate the factors affecting tool wear and surface roughness in hard turning. Neural network and regression models which make use of these factors were developed by using experimental data. The effectiveness of neural network and regression models were tested on test data which was excluded from experimental data during training. Test data was randomly selected from experimental data set. As a result, developed neural network models are found to perform

better on our experimental data. However this does not mean that neural networks are always better than regression models. In fact, due to their simplistic representation of input-output relationships regression models are widely used and preferred in practical applications in industry.

Secondly, a procedure to formulate and solve optimization problems for multiple and conflicting objectives that may exist in finish hard turning processes using neural network modeling together with particle swarm optimization technique is introduced. The representative multiple objectives for hard turning are defined to obtain a group of optimal process parameters for two different case studies. The Swarm Intelligent Neural Network System (SINNS) is proposed in order to obtain a family of solutions that provides useful information to the user during the selection of machining parameters. As a result, a Pareto-optimal front is calculated representing machining parameters yielding to a certain merit of interest such as material removal rate, surface roughness, tool life etc. that can be selected by the user according to production requirements. The results indicate that the proposed particle swarm intelligence-based algorithm for solving the multi-objective optimization problem with conflicting objectives is both effective and efficient, and can be integrated into an intelligent machining system for solving more complex machining optimization problems.

It must be noted that in experimental design, the number of experimental data and selection of training and testing data sets are very important and the selection procedure is random. In order to obtain a good experimental model of a process, large number of

experiments should be performed. Considering the number of factors and the cost of experimentation, experimental modeling approach is definitely not the ideal method. The experimental model in SINNS methodology can easily be replaced with analytical predictive models as long as predictive analytical model produces results in a short time.

CHAPTER 3

PREDICTIVE ANALYTICAL AND THERMAL MODELING OF ORTHOGONAL CUTTING PROCESS

3.1. Introduction

Modeling metal cutting processes with the aid of plasticity theory has been of great interest to researchers. One of the most significant contributions to the field is the parallel-sided shear zone theory introduced by Oxley and co-workers (1989) to predict cutting forces and process outputs in orthogonal cutting. Oxley's (1989) machining theory uses the dependence of material flow upon strain, strain rate and temperature to obtain the shear angle and other outputs of interest by considering the workpiece material properties, tool geometry and cutting conditions. Oxley's work was primarily focused on primary shear zone where the hydrostatic pressures at the primary shear zone were investigated by using visio-plasticity technique. In Oxley's work, temperature calculations at the cutting zone and friction modeling at the tool-chip interface was modeled by using simplistic and empirical models.

The objective of this study is to obtain cutting forces, stress distributions on the tool rake face and temperature distributions in the deformation zones by implementing more advanced modeling techniques. These models include, improved friction modeling at the secondary shear zone, analytical thermal model which will enable the calculation temperature rise at any point in the chip, workpiece and cutting tool, and a material

model which considers strain, strain rate and temperature effects, into Oxley's (1989) predictive machining model.

As a result of the proposed approach, normal and frictional shear stress distributions, lengths of sticking and sliding zones along the tool-chip interface which will be utilized later to model non-uniform heat intensity as the heat source in the secondary shear zone are obtained. Stress distributions at tool-chip interface and temperature distributions in the workpiece and cutting tool are important to model tool wear mechanisms and the integrity of the finished surface.

In machining of metals, the deformation process is concentrated in a very small zone and the temperatures generated in the deformation zone affect both the tool and the workpiece. The heat energy generated in the primary shear zone softens the materials, and the heat generated at the tool-chip interface affects the friction conditions. Many analytical models have been proposed to predict temperature distributions in the deformation zones. Pioneering studies were performed by Hahn (1951), Trigger and Chao (1951), Chao and Trigger (1953), Loewen and Shaw (1954), Leone (1954), Boothroyd (1963) and recently by Komanduri and Hou (2001 a, b, c) and Huang and Liang (2003).

In our proposed model, Johnson-Cook (J-C) (1983) work material model is used as an engine which produces flow stress information which makes our model physics-based. Therefore, all the predictions will be material dependent. The effects of different

materials can be studied. The J-C work material model describes the flow stress of the material by considering strain, strain rate and temperature effects as given in Eq. (3.1).

$$\bar{\sigma} = \left[A + B(\bar{\varepsilon})^n \right] \left[1 + C \ln \left(\frac{\dot{\bar{\varepsilon}}}{\dot{\bar{\varepsilon}}_0} \right) \right] \left[1 - \left(\frac{T - T_0}{T_m - T_0} \right)^m \right] \quad (3.1)$$

The constants A , B , C , n and m of the model are obtained experimentally by Split Hopkinson Pressure Bar (SHPB) tests conducted at various ranges of strain, strain-rate and temperatures.

3.2 Analytical Modeling of the Cutting Process

A simplified illustration based on experimental observations of the plastic deformation for the formation of a continuous chip when machining a ductile material is given in Fig.3.1. Oxley (1989) assumed that the primary zone is a parallel-sided shear zone and the secondary deformation zone adjacent to the tool-chip interface causes further plastic deformation by the intense contact pressures and frictional forces. Based on Oxley's model, the average value of the shear strain rate along AB is:

$$\dot{\gamma}_{AB} = C_0 \frac{V_S}{l_{AB}} \quad (3.2)$$

This equation basically represents the major contribution of Oxley (1989) which states that shear zone is not a single line but a zone and its thickness is controlled by the

parameter C_0 which represents the ratio of the thickness of the primary zone to the length of plane AB . This parameter is cutting condition dependent and must be calculated using the iterative approach. This approach will be explained later in the text.

The shear velocity V_s along the shear plane is:

$$V_s = \frac{V \cos \alpha}{\cos(\phi - \alpha)} \quad (3.3)$$

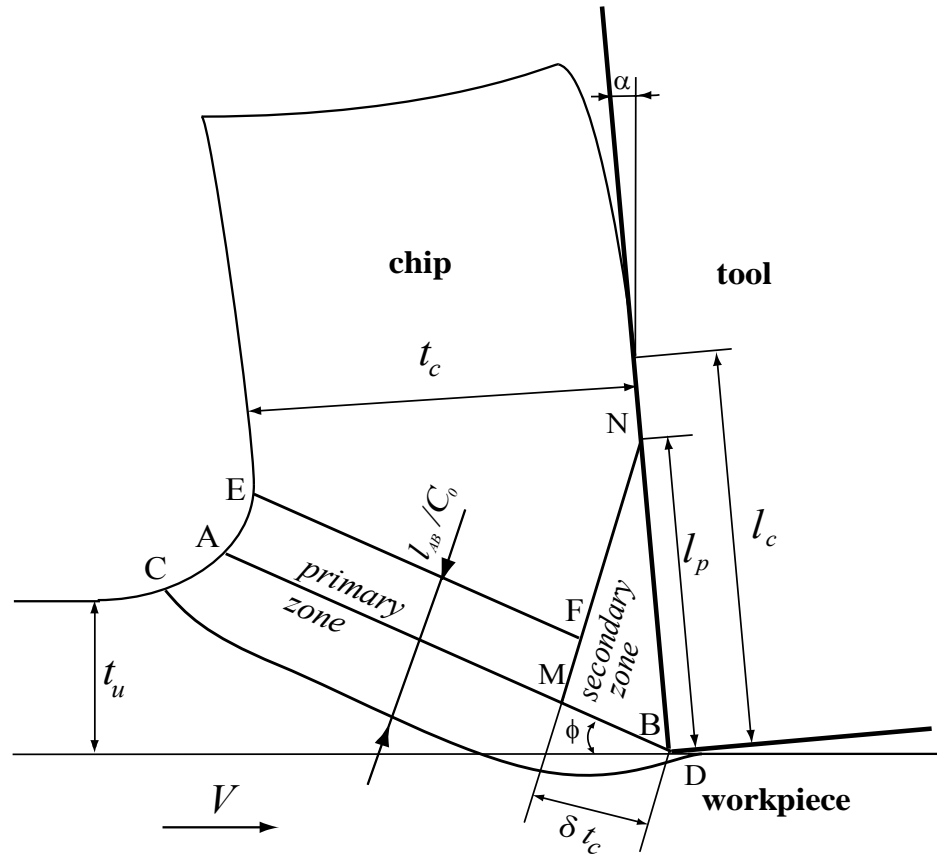


Figure 3.1 Simplified deformation zones in orthogonal cutting

Given by Eq.(3.4), l_{AB} is the length of primary zone AB , and can be calculated from geometry as:

$$l_{AB} = \frac{t_u}{\sin(\phi)} \quad (3.4)$$

Cut chip thickness can be estimated from Eq. (3.5) for a given shear angle ϕ as:

$$t_c = \frac{t_u \cos(\phi - \alpha)}{\sin(\phi)} \quad (3.5)$$

and the average strain in the middle of the primary shear zone is given as in Eq. (3.6):

$$\bar{\varepsilon}_{AB} = \frac{\cos \alpha}{2\sqrt{3} \sin \phi \cos(\phi - \alpha)} \quad (3.6)$$

In the primary zone, the flow stress on plane AB can be calculated by using Eq. (3.1) as a function of calculated strain, strain rate and temperatures. The average value of shear stress at AB according to the Von Mises criterion can be calculated as:

$$k_{AB} = \sigma_{AB} / \sqrt{3} \quad (3.7)$$

Once the shear flow stress is known, the shear force along AB may then be calculated as:

$$F_s = \frac{k_{AB} t_u w}{\sin \phi} \quad (3.8)$$

The hydrostatic pressures at A and B as calculated through viscoplasticity analysis are:

$$p_A = k_{AB} \left[1 + 2 \left(\frac{\pi}{4} - \phi \right) \right] \quad (3.9)$$

$$p_B = k_{AB} \left(2 \tan \theta - \left(1 + 2 \left(\frac{\pi}{4} - \phi \right) \right) \right) \quad (3.10)$$

The angle between the resultant force and the direction of the primary shear zone θ can be obtained using the known pressure distribution and shear stress along the shear plane.

$$\theta = \tan^{-1} \left(1 + 2 \cdot \left(\frac{\pi}{4} - \phi \right) - \frac{dk}{d\gamma} \frac{C_0 \gamma_{AB}}{k_{AB}} \right) \quad (3.11)$$

where

$$\frac{dk}{d\gamma} = \frac{\partial k}{\partial \varepsilon} \frac{\partial \varepsilon}{\partial \gamma} + \frac{\partial k}{\partial T} \frac{\partial T}{\partial \gamma} + \frac{\partial k}{\partial \dot{\varepsilon}} \frac{\partial \dot{\varepsilon}}{\partial \gamma} \quad (3.12)$$

and after necessary differentiations Eq. (3.13) is obtained.

$$\begin{aligned} \frac{dk}{d\gamma} = & \frac{1}{3} \left(B n \varepsilon_{AB}^{n-1} \right) \left(1 + C \ln \left(\frac{\dot{\varepsilon}_{AB}}{\dot{\varepsilon}_0} \right) \right) \left(1 - \left(\frac{T_{AB} - T_0}{T_m - T_0} \right)^m \right) \\ & + \frac{1}{\sqrt{3}} \left(A + B \varepsilon_{AB}^n \right) \left(1 + C \ln \left(\frac{\dot{\varepsilon}_{AB}}{\dot{\varepsilon}_0} \right) \right) \\ & \times \left(\frac{-m}{T_m - T_0} \left(\frac{T_{AB} - T_0}{T_m - T_0} \right)^{m-1} \right) \left(\frac{\partial T}{\partial \gamma} \right) \end{aligned} \quad (3.13)$$

This expression represents the effect of material properties on the calculation angle θ which is related to hydrostatic pressure distribution on the primary shear zone. In Eq.

(3.13) the derivation $\frac{\partial T}{\partial \gamma}$ can be computed numerically. The constant C_0 can be found by

using the relation given in Eq. (3.14) (Adibi-Sedeh et al. (2003)):

$$C_0 = \frac{P_A - P_B}{k_u - k_l} \quad (3.14)$$

where k_u is the shear stress at upper boundary (EF in Fig. 3.1) and k_l shear stress at lower boundary (CD in Fig. 3.1) of the primary shear zone. In order to find k_u , strain at EF can

be approximated by Eq. (3.15) and strain rate can be assumed to be constant all along the primary shear zone (Adibi-Sedeh et al. (2003)),

$$\varepsilon_{EF} = 2\varepsilon_{AB} \quad (3.15)$$

and T_{EF} can be calculated analytically from its coordinates in the chip. Forces acting on the shear plane and the tool with assumed resultant stress distributions on the tool rake face are given in Fig. 3.2.

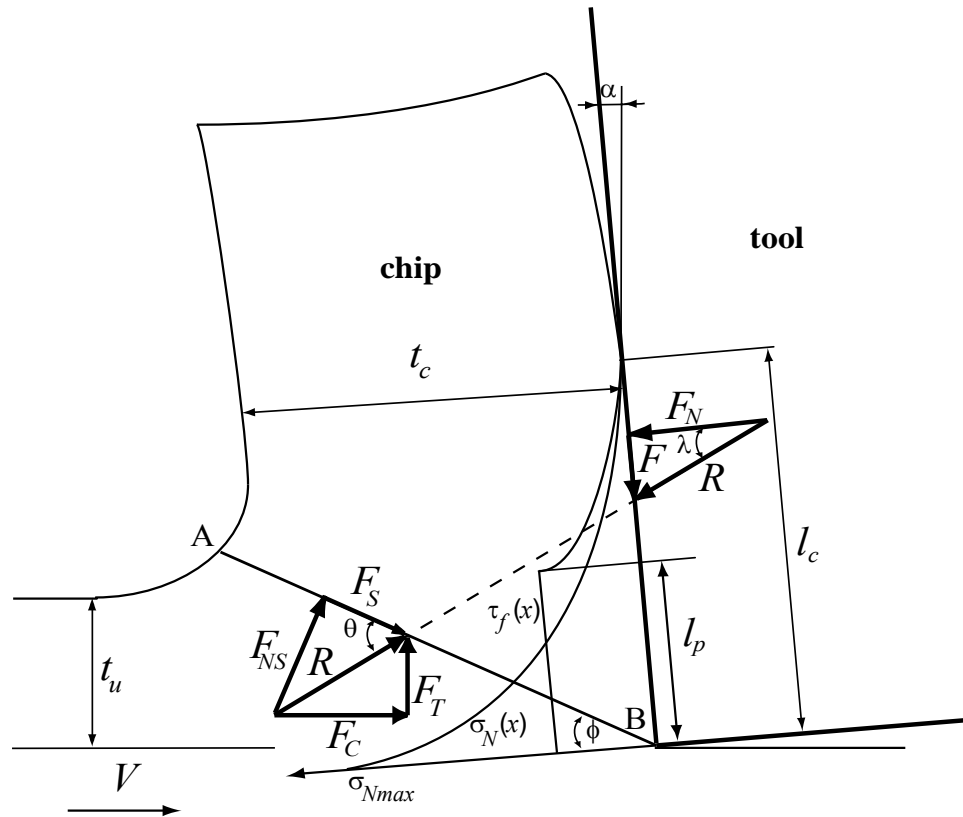


Figure 3.2 Forces acting on the shear plane and the tool with resultant stress distributions on the tool rake face

The distance between point B and the point where R cuts the shear the plane, X_{sh} , can be found by taking moments about the cutting edge of the normal stresses on the shear plane AB

$$X_{sh} = \frac{l_{AB}(2p_A + p_B)}{3(p_A + p_B)} \quad (3.16)$$

and the distance from the cutting edge to the point where the resultant force R intersects the tool cutting face, X_{fr} , can be found from geometry as given in Li (1997):

$$X_{fr} = \frac{\sin \theta}{\sin \left(\frac{\pi}{2} + \phi - (\theta + \alpha) \right)} X_{sh} \quad (3.17)$$

The normal (F_N) and tangential (F) components of the resultant cutting force (R) on the tool rake face, cutting force F_c and thrust force F_t can be obtained.

$$\begin{aligned} F_N &= R \cdot \cos(\theta - \phi + \alpha), F = R \cdot \sin(\theta - \phi + \alpha) \\ F_c &= R \cdot \cos(\theta - \phi), F_t = R \cdot \sin(\theta - \phi) \end{aligned} \quad (3.18)$$

Interfacial friction on the tool rake face is not continuous but a function of the normal and frictional stress distributions. According to Zorev (1963), the normal stress is greatest at the tool tip and gradually decreases to zero at the point where the chip separates from the rake face as shown in Fig. 3.2. The frictional shearing stress distribution is more complicated. Over the portion of the tool-chip contact area near the cutting edge, sticking friction occurs, and the frictional shearing stress, τ_{int} is equal to the average shear flow stress at tool-chip interface, k_{chip} . Over the remainder of the tool-chip contact area, sliding friction occurs, and the frictional shearing stress can be calculated using the coefficient of friction μ_e . The normal stress distribution on the tool rake face according to our assumed distribution can be described by Eq. (3.19)

$$\sigma_N(x) = \sigma_{N_{\max}} \left[1 - \left(\frac{x}{l_c} \right)^a \right] \quad (3.19)$$

where $\sigma_{N_{\max}}$ is given by Oxley (1989) as

$$\sigma_{N_{\max}} = p_B + 2k_{AB}(\phi - \alpha) \quad (3.20)$$

Unknowns in Eq. (3.19) are tool-chip contact length (l_c) and a , which require two equations to be solved. Integrating the normal stress along the entire tool-chip contact length yields the relation in Eq. (3.21), which is equal to normal force on the tool rake face.

$$F_N = \int_0^{l_c} w \sigma_N(x) dx = \int_0^{l_c} w \sigma_{N_{\max}} \left[1 - \left(\frac{x}{l_c} \right)^a \right] dx \quad (3.21)$$

Also taking the moment according to point B :

$$F_N X_{fr} = \int_0^{l_c} w \sigma_N(x) x dx = \int_0^{l_c} w \sigma_{N_{\max}} \left[1 - \left(\frac{x}{l_c} \right)^a \right] x dx \quad (3.22)$$

and denoting,

$$\mathbf{I} = \frac{\sigma_{N_{\max}} X_{fr} w}{F_N} \quad (3.23)$$

From Eq. (3.21) and (3.22), the contact length along the tool-chip interface, l_c , and the exponent a can be obtained as:

$$a = -1 + \frac{\sqrt{16\mathbf{I}^2 - 8\mathbf{I}}}{4\mathbf{I} - 2} \quad (3.24)$$

$$l_c = \frac{F_N \cdot (a+1)}{a w \sigma_{N_{\max}}} \quad (3.25)$$

As explained, the shear stress distribution on the tool rake face illustrated in Fig. 3.2 can be represented in two distinct regions: (a) in the sticking region $\tau_{\text{int}}(x) = k_{\text{chip}}$ and when $\mu_e \sigma_N(x) \geq k_{\text{chip}}, 0 < x \leq l_P$, (b) in the sliding region $\tau_{\text{int}}(x) = \mu_e \sigma_N(x)$ and when $\mu_e \sigma_N(x) < k_{\text{chip}}, l_P < x \leq l_c$. Here τ_{int} is the shear stress of the material at the tool-chip interface, and it is related to the frictional force between the chip and the tool, F_F , as

$$F_F = \int_0^{l_P} w \tau_{\text{int}} dx + \int_{l_P}^{l_c} w \mu_e \sigma_N(x) dx \quad (3.26)$$

The relation between the average coefficient of friction in the sliding region μ_e and τ_{int} is also given in Eq. (3.27):

$$\mu_e = \frac{\tau_{\text{int}}}{\sigma_N(l_P)} \quad (3.27)$$

Combining Eq. (3.26) and (3.27) leads to the expression for τ_{int} as shown in Eq. (3.28):

$$\tau_{\text{int}} = \frac{F_F}{wl_P + \frac{w}{\sigma_N(l_P)} \int_{l_P}^{l_c} \sigma_N(x) dx} \quad (3.28)$$

The chip velocity can be calculated as:

$$V_c = \frac{V \sin \phi}{\cos(\phi - \alpha)} \quad (3.29)$$

According to Oxley (1989), the average shear strain rate and shear strain at the tool chip interface are considered constant and can be estimated from Eq. (3.30) and (3.31).

$$\dot{\gamma}_{\text{int}} = \frac{V_c}{\delta t_c} \quad (3.30)$$

$$\gamma_{\text{int}} = \frac{l_P}{\delta t_c} \quad (3.31)$$

$$l_P = \frac{\delta.t_c}{\sin(\phi - \alpha)} \quad (3.32)$$

The flow stress at tool chip interface k_{chip} can be found by utilizing Eq. (3.1).

$$k_{chip} = \frac{1}{\sqrt{3}} \left[A + B(\bar{\epsilon})^n \right] \left[1 + C \ln \left(\frac{\dot{\bar{\epsilon}}}{\dot{\bar{\epsilon}}_0} \right) \right] \left[1 - \left(\frac{T_{intstiction} - T_0}{T_m - T_0} \right)^m \right] \quad (3.33)$$

where J-C material model is again utilized. Above given equations requires the temperature information at specific locations at the cutting zone. In the next chapter, an analytical thermal model proposed for machining will be explained. The analytical thermal model will allow us to calculate temperatures at any point in the cutting zone.

3.3. Analytical Thermal Modeling of the Cutting Process

Thermal modeling of metal cutting is highly important since it directly affects the process variables such as the cutting forces and the contact length both of which are required to model wear mechanisms. The analytical modeling of steady state temperature in metal cutting presented by Hahn (1951) is based on the heat source method of Jaeger (1942). Recently, Komanduri and Hou (2001 a,b,c) modified Hahn's (1951) solution for an oblique band heat source in a semi-infinite medium. Primary shear plane is modeled as a moving heat source in a semi-infinite medium and shown in Fig. 3.3.

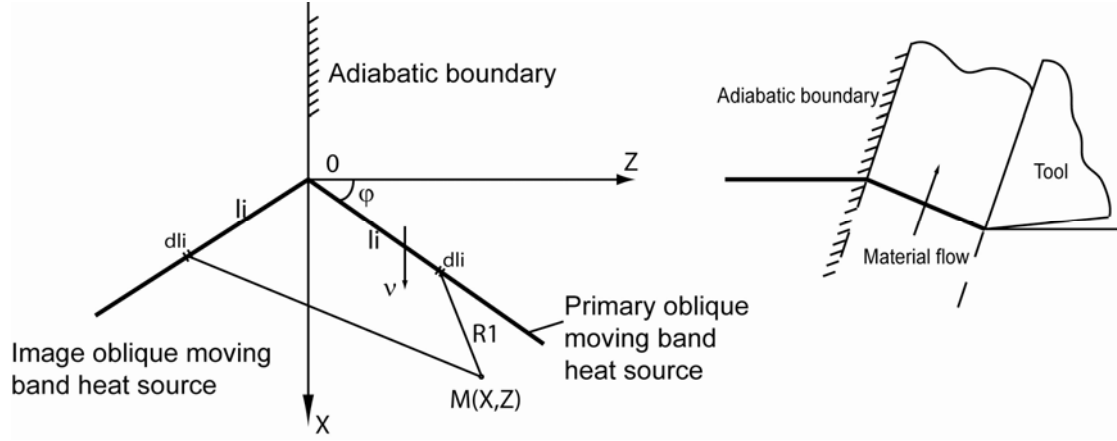


Figure 3.3 Modified Hahn's model for an oblique band heat source in a semi-infinite medium

In this model primary shear zone is modeled as a heat source is considered to be moving with chip. The temperature rise at any point $M(X, Z)$ caused by the moving line heat source is due to the combined effect of the primary and image heat sources and can be calculated using Eq. (3.34).

$$T_{M_{shear}}(X, Z) = \frac{q_{shear}}{2\pi\lambda_c} \int_{l_i=0}^{l_{AB}} e^{-\frac{(X-l_i \sin \phi) V_c}{2a_c}} \times \left\{ K_0 \left[\frac{V_c}{2a_c} \sqrt{(X-l_i \sin \phi)^2 + (Z-l_i \cos \phi)^2} \right] + \left[K_0 \left[\frac{V_c}{2a_c} \sqrt{(X-l_i \sin \phi)^2 + (Z+l_i \cos \phi)^2} \right] \right] \right\} dl_i \quad (3.34)$$

Heat intensity at primary shear zone due to shearing can be modeled uniformly as:

$$q_{shear} = \frac{F_s V_s}{l_{AB} w} \quad (3.35)$$

Eq. (3.34) and (3.35) will allow the calculation of average temperature in the primary shear zone which is required by J-C workpiece material model to calculate shear flow stress at the primary shear zone.

The secondary heat source is modeled by considering tool-chip interaction. Because of the presence of plastic and elastic zones along tool chip contact length, secondary heat source cannot be assumed as uniform. Recently, Huang and Liang (2003) used the non-uniform heat intensity along tool-chip interface in their model. They converted uniform shear stress distribution given in Oxley's theory to a non uniform distribution by assuming the length of sticking zone is half of the tool chip contact length. Non-linear heat intensity of the secondary heat source, which is dependent on shear stress distribution on the tool-chip interface, is calculated analytically in this study as explained above (Fig. 3.4). This approach is the refinement on Komanduri and Hou's (2001 a, b, c) model in this study where uniform heat source was used in their study. Calculation of the shear stress distribution and the lengths of sticking and sliding zones is a part stress distributions and force modeling.

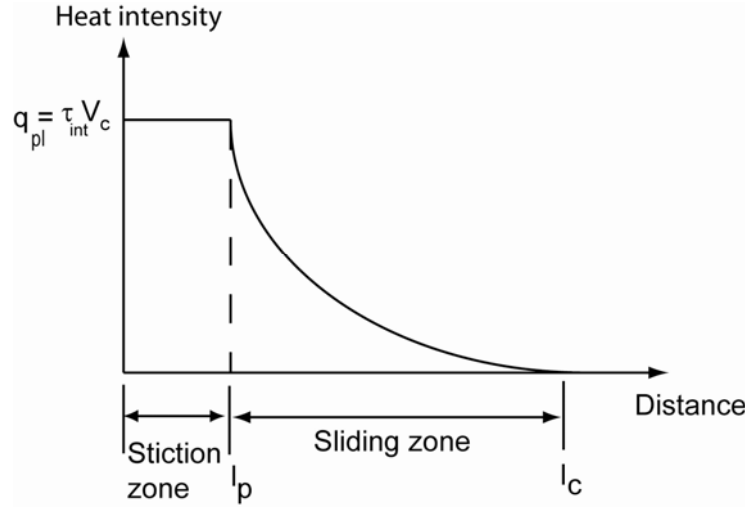


Figure 3.4 Heat intensity model along the rake face of the tool

The frictional heat source relative to the tool is a stationary rectangular heat source since cutting tool is not moving. The tool clearance face is also considered to be adiabatic. Considering the heat partition fraction for the chip $[1 - B(x)]$, the heat liberation rate $[1 - B(x)] q_{pl}(x)$ of the heat source is considered to be transferred into the tool. The temperature rise at any point $M (X, Y, Z)$ in the tool caused by the frictional stationary heat source including its image heat source, given as:

$$T_{M_{tool-friction}}(X, Z) = \frac{1}{2\pi\lambda_t} \int_{y_i=-w/2}^{w/2} \int_{x_i=0}^{l_c} [1 - B(x_i)] q_{pl}(x_i) \times \left(\frac{1}{R_i} + \frac{1}{R'_i} \right) dx_i dy_i \quad (3.36)$$

Using the above equations, the local temperature rise at each point along the tool-chip interface can be calculated. Since the temperature rise on both sides at the contacting

interface should be the same, the distribution of heat partition ratio can be calculated by matching the temperature distribution curves on the tool and chip sides as in Komanduri and Hou (2001 a, b, c).

3.4 Solution of the Combined Thermal and Analytical Modeling of the Cutting Process

For the proposed orthogonal machining model, cutting conditions and the material properties of the workpiece are the inputs. The outputs are process related variables, such as shear angle, contact length, cutting forces, tool stress distributions and temperature distribution in the chip and along the tool-chip interface. The shear angle, strain rate constant and the ratio of thickness of the tool-chip interface plastic zone to chip thickness are selected based on the minimum force principle. As discussed above, the temperature rise along shear zone (X, Z) can be calculated as given in Eq. (3.34). The average temperature in primary shear zone can be found by integrating Eq. (3.34) along the shear length, given as:

$$T_{AB} = \frac{\int_0^{l_{AB}} T_{M_{shear}}(X, Z) dl_i}{l_{AB}} + T_0 \quad (3.37)$$

The heat partition ratio expression, $B(X)$, is adopted from Komanduri and Hou (2001 b, c) and given in Eq. (3.38).

$$\begin{aligned}
 B(x) &= (B_{chip} - \Delta B_1) + 2\Delta B_1 \left(\frac{x}{l_c} \right)^{m_1} \\
 1 - B(x) &= (B_{tool} + \Delta B_1) - 2\Delta B_1 \left(\frac{x}{l_c} \right)^{m_1}
 \end{aligned}
 \tag{3.38}$$

In this expression, the coefficients B_{chip} , ΔB_1 , and m_1 should be calculated by matching the temperature distribution curves along the tool-chip interface. The discussions about this expression are given in Komanduri and Hou (2001 b, c). Once the $B(x)$ expression is calculated, the average temperature on the tool chip interface can be found as:

$$T_{int} = \frac{\int_0^{l_c} T_{M_{shear}}(X, 0) + T_{M_{chip-friction}}(X, 0, 0) dl_i}{l_c} + T_0
 \tag{3.39}$$

The thermal conductivity (λ_c) and thermal diffusivity (a_c) coefficients of the workpiece are usually considered to be constant, but in fact they also depend on temperature. An iterative approach is used in calculation of the temperatures. For example, an average temperature for the primary shear zone is predicted, thermal conductivity and diffusivity at that predicted average temperature are found and actual average temperature is calculated by using these constants. The iteration continues until the predicted and average temperature calculations are close, as shown in the flow chart given in Fig. 3.5.

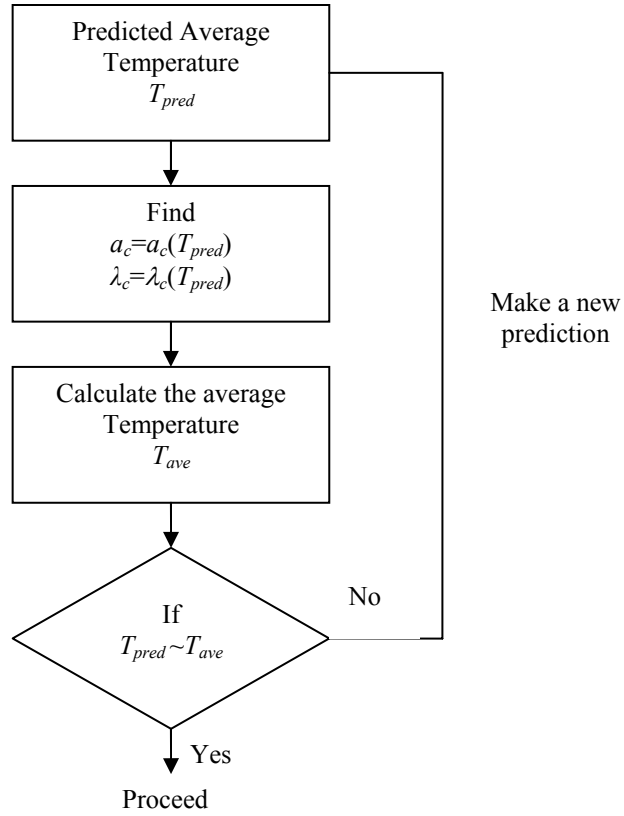


Figure 3.5. Flow chart for computing average temperatures

The shear angle ϕ is determined such that the tool-chip interface shear stress τ_{int} caused by the resultant cutting force for a given set of cutting conditions must be equal to the chip material flow stress k_{chip} at the sticking region, which is the function of strain, strain-rate and temperature at the interface for the same cutting condition. Since heat intensity is required to obtain temperature distribution in the primary shear zone, shear force is found through trial and error until assumed and calculated shear forces are identical. The search for the true value of ϕ will go through iterations until the calculated interface shear stress and the material shear flow stress are equal. If there is more than one shear angle that satisfies the above condition, the highest angle is chosen. Reasonable

values of C_0 and δ are also searched iteratively at the same time to simultaneously satisfy the conditions. The flow chart of this approach is summarized in Fig. 3.6.

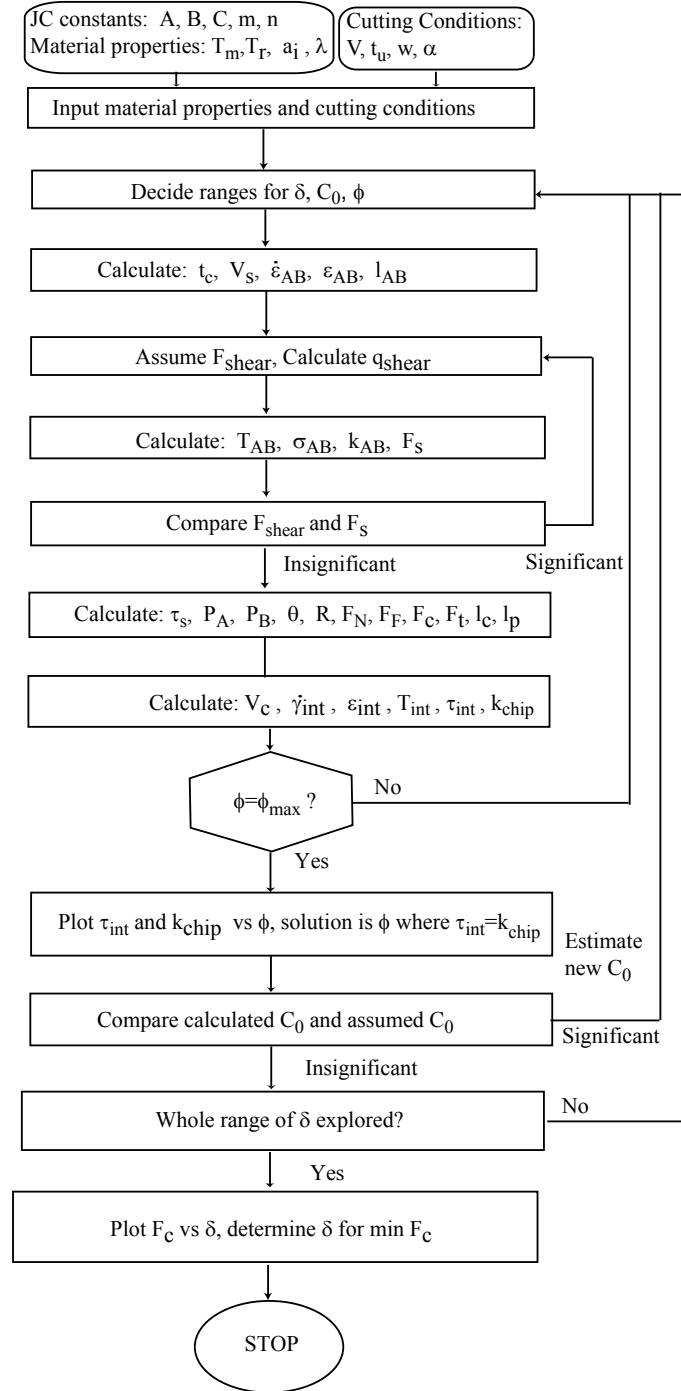


Figure 3.6. Flow chart of the computational algorithm

3.5. Model Validation and Results

In order to validate the predictive thermal and analytical modeling approach for metal cutting processes presented in this study, a set of orthogonal cutting experiments for machining AISI 1045 steel (Ivester et al. (2000)) is utilized. Experimental data include measured cutting and thrust forces and average temperatures on the shear plane and at the tool-chip interface. The cutting conditions for machining of AISI 1045 are given in Table 3.1. In these cutting conditions, machining with both a negative (-7 deg.) and a positive rake (5 deg.) angle were tested. Chip thickness and shear angle were calculated as presented in Table 3.2. The predicted temperatures are compared with experimental values in Table 3.3. The measured temperatures and the predicted temperatures at the tool-chip interface in machining of AISI 1045 steel indicate agreements for Test # 1, 2 and 4. However, more refined measurements of temperature distributions during the cutting process are needed to validate predicted temperature distributions and heat partitions. Such measurements for machining of AISI 1045 steel were performed by Davies et al. (2005). Fig. 3.7 shows the cutting and thrust force predictions of the proposed model under test conditions from literature (Ivester et al. (2000)). For the cases presented, the predicted forces are in good agreement with the experimental values and always remain within upper and lower limits. In addition, the predictions for normal stress distribution on the tool rake face for machining AISI 1045 steel are given in Table 3.3 and Fig. 3.8. The predicted normal stress distributions depict that the power law exponent a is less than 1 for machining at negative rake angles and greater than 1 for machining at positive rake angles. This behavior affects temperature

predictions since non-uniform heat partition at the tool-chip interface is obtained from normal stress distributions on the tool rake face.

Table 3.1 Cutting conditions for AISI 1045 steel ($w=2$) (Ivester et al. (2000))

(* model predictions)

Test	V (m/min)	α (deg)	t_u (mm)	t_c (mm)*	ϕ (deg.) *
1	200	-7	0.150	0.33	22
2	200	+5	0.150	0.33	25
3	200	-7	0.300	0.6	24
4	200	+5	0.300	0.6	27
5	300	-7	0.150	0.31	24
6	300	+5	0.150	0.31	26
7	300	-7	0.300	0.58	25
8	300	+5	0.300	0.56	29

Table 3.2 Force and temperature predictions for AISI 1045 steel.

Test	Predicted F_C (N)	Predicted F_T (N)	Predicted T_{AB}	Predicted $\max(T_{int})$	Measured $\max(T_{int})$
1	662	466	370	1080	1120
2	596	324	332	1125	1250
3	1206	728	369	1170	1100
4	1097	509	319	1158	1220
5	613	371	370	1241	1310
6	576	288	330	1227	1300
7	1174	671	365	1329	1305
8	1046	430	311	1310	1300

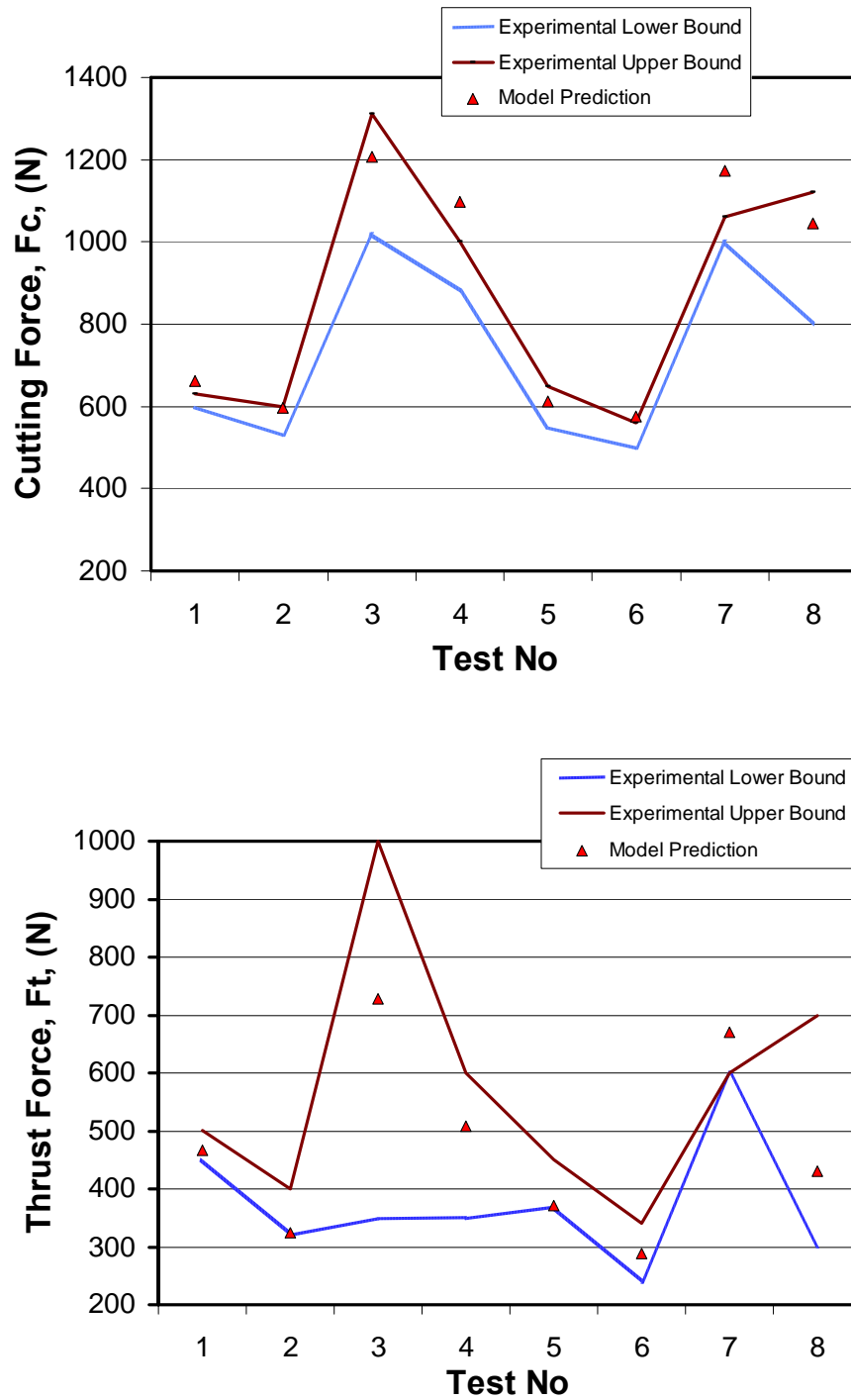


Figure 3.7. Comparison of the predictions of the cutting force (a), and thrust force (b) with experimental data from (Ivester et al. (2000))

Table 3.3 Predicted normal stress distribution parameters for machining AISI 1045 steel

Test	σ_{Nmax} (N/mm ²)	l_p (mm)	l_c (mm)	a
1	1380	0.12	0.6	0.75
2	992	0.11	0.54	1.1
3	1305	0.13	1.04	0.89
4	1007	0.28	0.91	1.3
5	1308	0.07	0.52	0.9
6	970	0.11	0.56	1.3
7	1325	0.14	0.98	0.91
8	1039	0.28	0.82	1.4

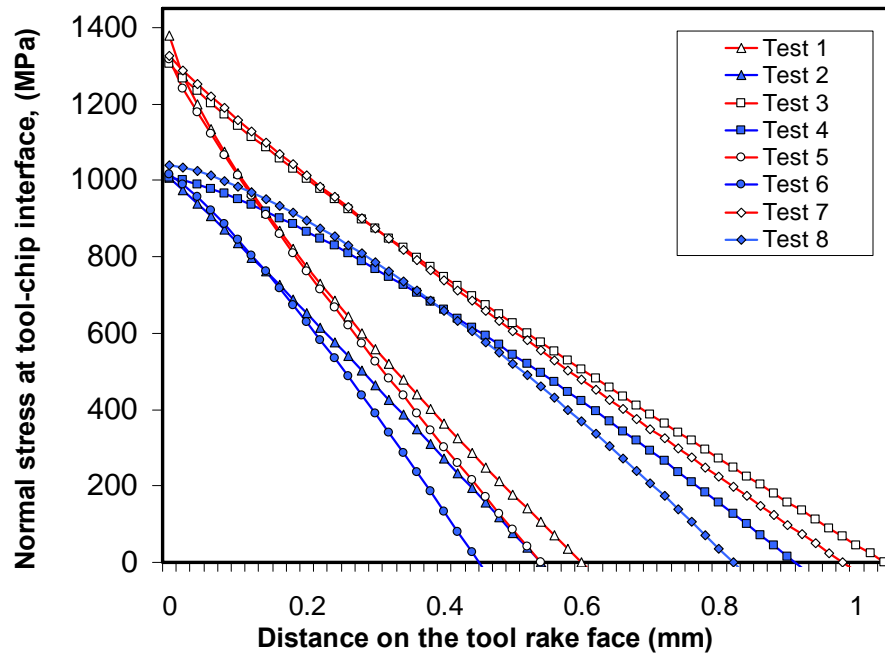


Figure 3.8. Predicted stress distributions on the tool rake face for machining AISI 1045 steel.

The temperature distributions in the tool, chip and workpiece can be obtained by dividing the tool, chip and workpiece into small increments and calculating the temperature rise at every point. Fig. 3.9 shows the temperature distributions in the chip, tool and workpiece.

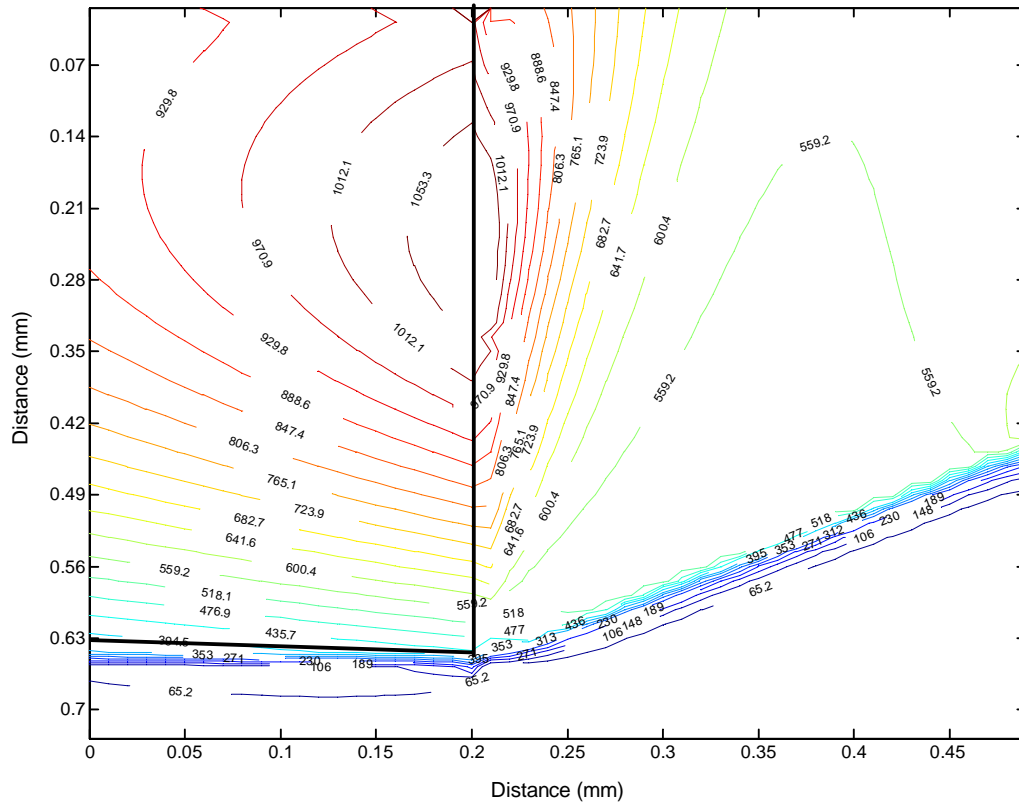


Figure 3.9. Temperature distributions for AISI 1045 at conditions in Test #1

When uniform heat intensity is used in thermal modeling maximum temperature is obtained close to the end of the tool-chip interface. Due to nonlinear heat intensity modeling, where the length of the sticking zone is considered, the location of maximum temperature gets closer to the middle of the tool chip interface. The temperature rise distribution along the tool-chip interface for chip and tool side is shown in Fig. 3.10. Variation of heat partition ratio along tool-chip interface is shown in Fig. 3.11. The

discrepancy between temperature rise curves can be reduced by using a heat partition expression, which has higher power terms.

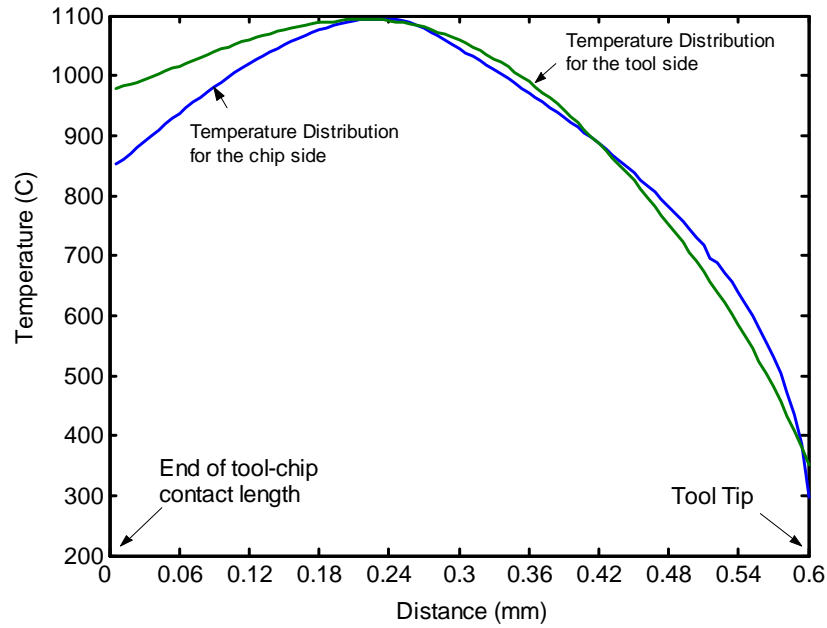


Figure 3.10. Temperatures along the tool-chip interface for test condition #1 for AISI

1045

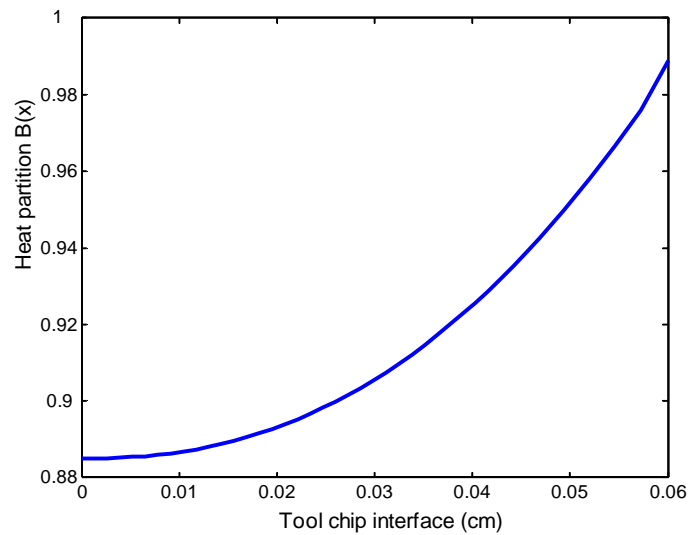
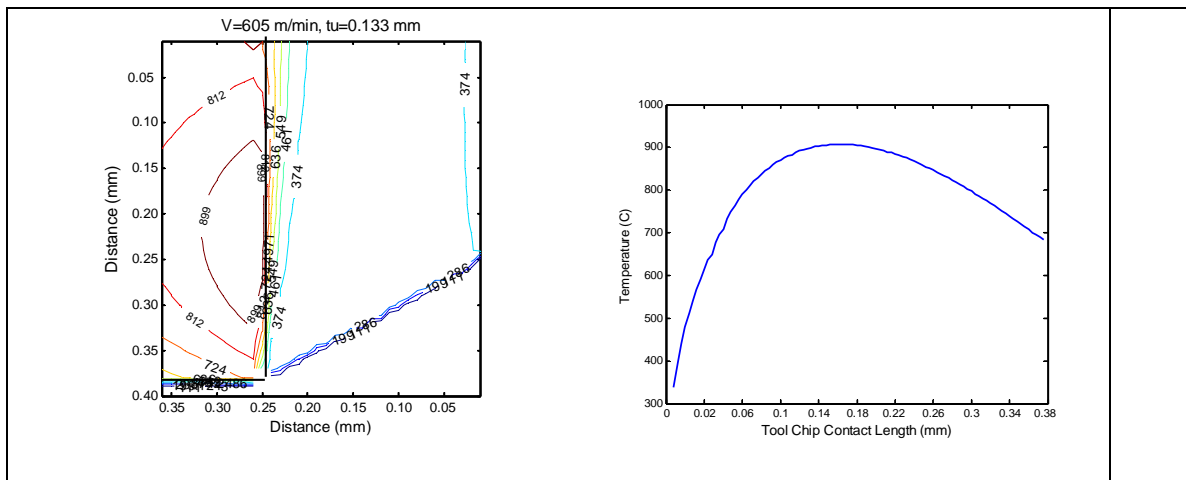


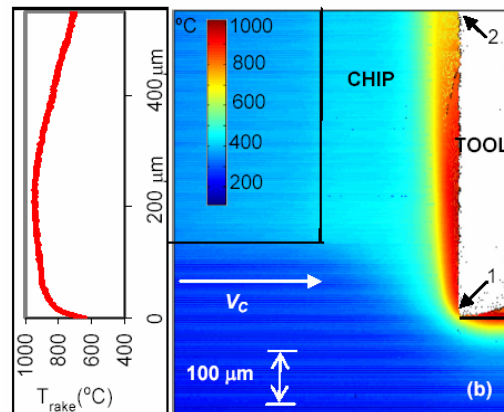
Figure 3.11. Heat partition ratio along the tool chip interface for test condition #1 for

AISI 1045

Measuring temperature during metal cutting is extremely difficult since the thickness of the primary shear zone is very narrow; chips scatter around during machining, different materials have different emissivities, and there is a relative motion between tool and chip in secondary shear zone. Recently, Davies et al. (2005) attempted to measure temperature distributions in an AISI 1045 workpiece by using a thermal microscope. The comparison of measured temperature distributions and predictions of our model is given in Fig 3.12.



(a)



(b) (Davies et al., 2005)

Figure 3.12. Comparison of temperature distributions (a) Predicted (b) Measured

3.6 Effect of Tool Flank Wear On Tool Forces, Stresses and Temperature Distributions

In this section, predictive modeling of cutting forces, stress and temperature distributions on tool rake and flank faces in the presence of tool flank wear are presented. The analytical and thermal modeling of orthogonal cutting is extended for worn tool case in order to study the effect of flank wear. Work material constitutive model based formulations of tool forces and stress distributions at tool rake and worn flank faces are utilized in calculating non-uniform heat intensities and heat partition ratios induced by shearing, tool-chip interface friction and tool flank face-workpiece interface contacts. In order to model forces and stress distributions under the flank wear zone, a worn tool force model is adapted from Waldorf (1996).

Forces acting on the shear plane and the tool with assumed resultant stress distributions on the tool rake face are given in Fig. 3.13. When it is assumed that the worn flank face is parallel to the cutting direction, the actual (measured) cutting forces in the cutting and thrust directions F_C and F_T during machining are the superposition of the wear forces and the cutting forces from shearing. These forces can be expressed as in Eq. (3.40) as suggested by Thomsen et al. (1962).

$$\begin{aligned} F_C &= F_{Cs} + F_{Cw} \\ F_T &= F_{Ts} + F_{Tw} \end{aligned} \tag{3.40}$$

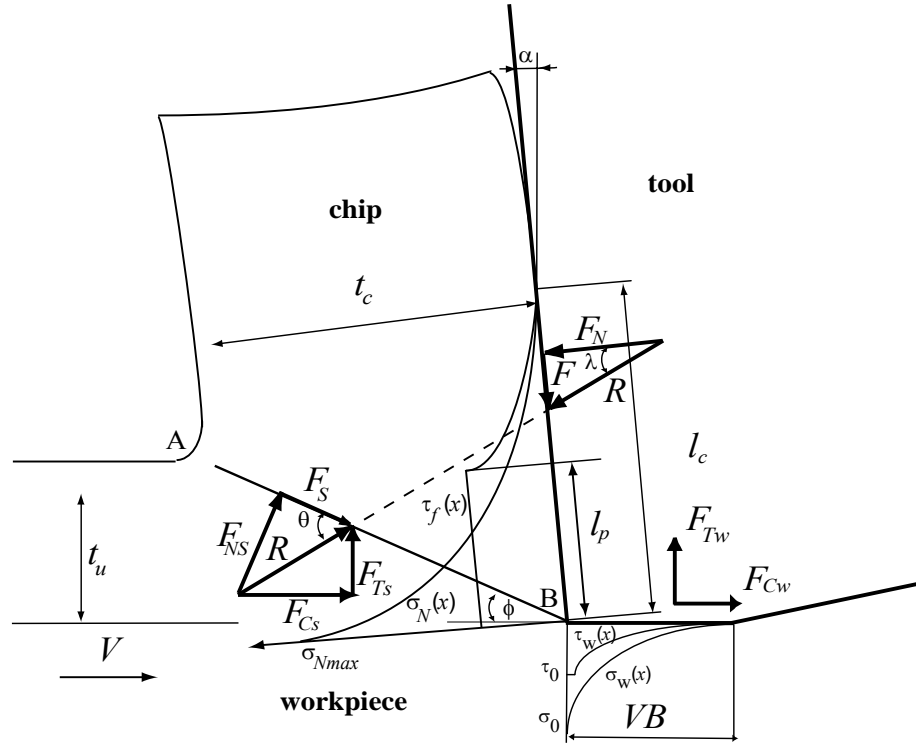


Figure 3.13. Forces acting on the shear plane, the rake and on the worn faces of the tool.

Thomsen et al. (1962) reported significant plastic flow below worn tool flank when a negative clearance angle exists but for zero clearance angle wear land does not affect the shearing mechanism. Later, Waldorf (1996) combined the model of Shi and Ramalingam (1991) with the findings of Thomsen et al. (1962) related to the worn flank face may becoming parallel to the cutting direction and extended to round edge tools that form sharp-like edges after stable build up. Waldorf's approach is used by many other researchers such as Huang and Liang (2003), Smithey et al. (2001) and Song (2003). In this study, we adapted Waldorf's (1996) model to obtain stress distributions under the flank wear area which determine non-uniform heat intensities between the flank and workpiece interface.

The cutting forces due to tool flank wear can be found by integrating σ_w and τ_w over the tool flank wear land as in Eq. (3.41).

$$\begin{aligned} F_{Tw} &= w \cdot \int_0^{VB} \sigma_w(x) dx \\ F_{Cw} &= w \cdot \int_0^{VB} \tau_w(x) dx \end{aligned} \quad (3.41)$$

where w is width of cut; VB is length of wear land and x is the distance from tool tip. In Waldorf's (1996) model, the stresses at flank face are defined according to the length of the wear land, and for small values of flank wear, elastic contact between tool and workpiece exists. In this state, the stresses are modeled to have a polynomial shaped distribution as shown in Fig. 3.13. However, when the flank wear reaches critical wear land length (VB^*) at which the plastic flow begins, the stress distributions take another form. Therefore, if $VB < VB^*$ then elastic contact is present, but if $VB > VB^*$ then plastic flow of the workpiece will be present at the front edge of the wear land, and elastic contact will be present at the back of the wear land. Determination of this critical tool wear value requires experimental observations. The tool tip stresses σ_0 and τ_0 required to define $\sigma_w(x)$ and $\tau_w(x)$ are shown in Fig. 3.13. For elastic contact ($VB < VB^*$) and $VB \neq 0$, the stresses at the tool flank face are given by

$$\begin{aligned}
\sigma_w(x) &= \sigma_0 \left(\frac{VB-x}{VB} \right)^2 \\
\tau_w(x) &= \tau_0 \text{ for } 0 < x < VB \left(1 - \sqrt{\frac{\tau_0}{\sigma_0}} \right) \\
\tau_w(x) &= \mu \sigma_w(x) \text{ for } VB \left(1 - \sqrt{\frac{\tau_0}{\sigma_0}} \right) < x < VB
\end{aligned} \tag{3.42}$$

where,

$$\begin{aligned}
\sigma_0 &= k \left[1 + \frac{\pi}{2} - 2\rho - 2\phi + 2\gamma + \sin(2\gamma - 2\phi) \right] \\
\tau_0 &= k \cos(2\gamma - 2\phi) \\
\gamma &= \eta_p + \phi - \sin^{-1} \left(\sqrt{2} \sin(\rho) \sin(\eta_p) \right) \\
\eta_p &= 0.5 \cos^{-1} (m_p)
\end{aligned} \tag{3.43}$$

were determined from the slip-line field given in Waldorf (1996). η_p is the slip-line angle for friction on worn area. The friction factor, m_p , is the ratio between the shear stress on the tool flank face and the shear flow stress of the workpiece k , which is found by using work material constitutive equation as explained earlier. The variable ρ is the prow angle, which is the inclination of uncut workpiece surface. When plastic flow is present ($VB > VB^*$), the stresses at flank face are as follows

$$\begin{aligned}
\sigma_w(x) &= \begin{cases} \sigma_0 & \text{for } 0 < x < VB - VB^* \\ \sigma_0 \left(\frac{VB-x}{VB^*} \right)^2 & \text{for } VB - VB^* < x < VB \end{cases} \\
\tau_w(x) &= \begin{cases} \tau_0 & \text{for } 0 < x < VB - VB^* \sqrt{\frac{\tau_0}{\sigma_0}} \\ \mu \sigma_w(x) & \text{for } VB - VB^* \sqrt{\frac{\tau_0}{\sigma_0}} < x < VB \end{cases}
\end{aligned} \tag{3.44}$$

where

$$\begin{aligned}
\sigma_0 &= k \left[1 + \frac{\pi}{2} - 2\rho + 2\eta_w + \sin(2\eta_w) \right] \\
\tau_0 &= k \cos(2\gamma - \eta_w) \\
\eta_w &= 0.5 \cos^{-1}(m_w)
\end{aligned} \tag{3.45}$$

where η_w is the slip-line field angle. The friction factor m_w , under plastic contact conditions at the flank face, is close to unity. If the tool flank stresses σ_w and τ_w in Eq. (3.42) and (3.44) are substituted into Eq. (3.41), the cutting forces due to flank wear can be predicted for known values of shear flow stress and shear angle. Consequently, the stress distributions given in Fig. 3.13 are multiplied with cutting velocity and are used to determine non-uniform rubbing heat intensities at the flank-workpiece interface.

3.7. Thermal Modeling of the Cutting Process for Worn Tools

In this section, thermal modeling of orthogonal cutting with a sharp tool has been extended to worn tools in order to determine forces, stresses and temperature distributions which may enable us to further examine the effects of worn tools on workpiece surface integrity. Along with shear zone and frictional heat sources, a third heat source stemming from rubbing between tool and workpiece is added to the model as shown in Fig 3.14.

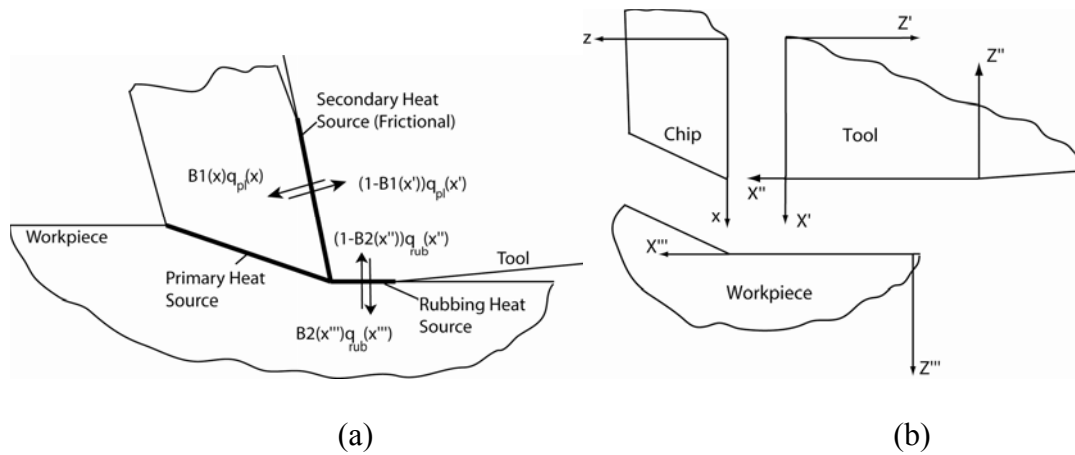


Figure 3.14. (a) Heat sources in worn tool thermal modeling and (b) coordinate systems for chip, tool and workpiece.

Primary shear zone is modeled as a uniform moving oblique band heat source; secondary shear zone, a frictional heat source, is treated as a non-uniform moving band heat source within a semi-infinite medium on the chip side and as a non-uniform stationary rectangular heat source within a semi-infinite medium on the tool side. Rubbing heat source is modeled as a non-uniform moving band heat source on the workpiece side and a non-uniform stationary rectangular heat source on the tool side.

Although many studies have been devoted to thermal modeling of machining, few studies have been conducted on worn tools. Worn tool thermal modeling studies started with Chao et al. (1961), but in their study the effect of primary shear zone was not considered. Recently, Wang and Liu (1999) and Chou and Evans (1999) studied the micro-structural changes on the workpiece caused by tool wear by using analytical thermal modeling to predict the detrimental effects of tool wear on surface integrity properties of the workpiece. Huang and Liang (2003) studied the effect of machining

conditions on tool wear and proposed a thermal model based on Carslaw and Jaeger's (1959) work. In their model the lower surface (in contact with tool) and upper surface of the chip are considered adiabatic. Komanduri (2001a) pointed out the importance of heat transfer from the lower surface of the chip to the tool and this effect is modeled as induced stationary heat intensity on the tool rake face. It has been shown that the temperature in the primary shear zone and its induced temperature rise effect on the tool-chip interface can reach 200-300 °C. In this study, the effect of primary shear zone on the flank face of the tool will again be considered as an induced stationary heat source on the tool flank face.

The objective of extending our model to machining with worn tool case is to obtain temperature distributions in the workpiece, chip and tool under the effect of tool flank wear. It is assumed that: (1) The temperature distributions on the interfaces are the same, which enables the calculation of the heat partition ratios. (2) The upper surface of the chip, the uncut surface of the workpiece, the tool side of tool-chip interface and the tool side of tool-workpiece interface are considered adiabatic. (3) The temperature distributions are in steady state. (4) Heat losses along tool-chip and tool-workpiece interfaces are omitted and it is assumed that all the deformation energy in the primary shear zone is converted into heat energy. (5) All the heat sources are plane heat sources and possible crater wear at the secondary shear zone does not affect the temperature distribution. (6) Heat intensities and heat partitions are modeled as non-uniform and as a function of distance on the interfaces. (7) The angle between tool flank and rake face is taken as 90° in formulations.

3.7.1 Modeling of Temperature Rise in the Chip

The thermal modeling of the primary shear zone and tool-chip interface is similar to sharp tool thermal modeling. The temperature rise at any point in the chip can be found by Eq. (3.46) with the addition of room temperature T_0 .

$$T_{M_{chip}}(X, Z) = T_{M_{chip-shear}}(X, Z) + T_{M_{chip-friction}}(X, Z) + T_0 \quad (3.46)$$

3.7.2. Modeling of Temperature Rise in the Tool

The tool side of the secondary heat source is modeled as a non-uniform stationary rectangular heat source. The flank surface of the tool is modeled as adiabatic. The temperature rise on the tool side can be written as in Eq. (3.47).

$$T_{M_{tool-friction}}(X', Y', Z') = \frac{1}{2\pi\lambda_t} \int_{y_i=-w/2}^{w/2} \int_{x_i=0}^{l_c} (1 - B_1(x'_i)) q_{pl}(x'_i) \left(\frac{1}{R_i} + \frac{1}{R'_i} \right) dx'_i dy'_i \quad (3.47)$$

$$R_i = \sqrt{(X' - x')^2 + (Y' - y')^2 + Z'^2}, R'_i = \sqrt{(X' - 2l_c + x')^2 + (Y' - y')^2 + Z'^2}$$

where λ_t is the thermal conductivity of the tool material. Since the lower surface of the chip is not adiabatic and in order to maintain continuity, the heating effect of the primary shear zone on the tool rake face should be included in thermal model. The heating effect

According to the coordinate system given in Fig. 3.15, the temperature rise at any point on the tool due to the rubbing heat source can be written as in Huang and Liang (2003).

$$T_{M_{tool-rubbing}}(X'', Y'', Z'') = \frac{1}{2\pi\lambda_t} \int_0^{VB} \int_{-w/2}^{w/2} [1 - B_2(X'')] q_{rub}(X'') \left(\frac{1}{R_i} + \frac{1}{R'_i} \right) dy'' dx'' \quad (3.49)$$

where

$$R_i = \sqrt{(X'' - x'')^2 + (Y'' - y'')^2 + Z''^2}, R'_i = \sqrt{(2VB - X'' - x'')^2 + (Y'' - y'')^2 + Z''^2}$$

and VB is the length of the flank wear. The heat intensity of the rubbing heat source is modeled as nonlinear by multiplying the cutting velocity and shear stress distribution found from Waldorf's worn tool model. Since the machined surface of the workpiece is not adiabatic, there is a heat transfer in this area. Similar to the tool rake face, a stationary uniform rectangular induced heat source is modeled on the tool flank face. The heat intensity of the induced heat source is found by matching the known average temperature rise under the flank face of the tool caused by primary shear zone with the average temperature rise caused by induced stationary heat source. The induced heat partition parameters are adjusted to maintain continuity on the tool-workpiece interface.

$$\bar{T}_{tool-workpiece} = \frac{1}{VB} \frac{q_{induced-flank}}{2\pi\lambda_t} \int_{y_i=-w/2}^{w/2} \int_{x_i=0}^{VB} (1 - B_{induced_flank}(x_i)) \left(\frac{1}{R_i} + \frac{1}{R'_i} \right) dx_i'' dy_i'' \quad (3.50)$$

where

$$\bar{T}_{tool-workpiece} = \frac{1}{VB} \int_0^{VB} T_{M_{workpiece-shear}} dx''$$

The coordinate systems used for Eqs. (3.47) - (3.48) and, (3.49) - (3.50) are different; therefore, in order to find the temperature rise at any point in the tool, a coordinate transformation is required. If the angle between flank and rake face is assumed to be 90 degrees, the temperature rise at any point on the tool-chip interface can be written as

$$T_{M_{rake}}(X', 0, 0) = T_{M_{tool-friction}}(X', 0, 0) + T_{M_{induced-rake}}(X', 0, 0) \\ + T_{M_{tool-rubbing}}(VB, 0, l_c - X') + T_{M_{induced-flank}}(VB, 0, l_c - X') \quad (3.51)$$

Similarly, the temperature rise at any point on the tool-workpiece interface can be written as

$$T_{M_{flank}}(X'', 0, 0) = T_{M_{tool-friction}}(l_c, 0, VB - X'') + T_{M_{induced-flank}}(l_c, 0, VB - X'') \\ + T_{M_{tool-rubbing}}(X'', 0, 0) + T_{M_{induced-rake}}(X'', 0, 0) \quad (3.52)$$

3.7.3 Modeling of Temperature Rise on the Workpiece

In order to model temperature rise on the workpiece, primary heat source is modeled again as an oblique moving band heat source which moves under the workpiece surface with cutting velocity as given in Komanduri and Hou (2001a). In their model, which is shown in Fig. 3.16, the uncut workpiece surface is considered as adiabatic. The origin of the coordinate system in this model is assumed to be the end of flank wear width.

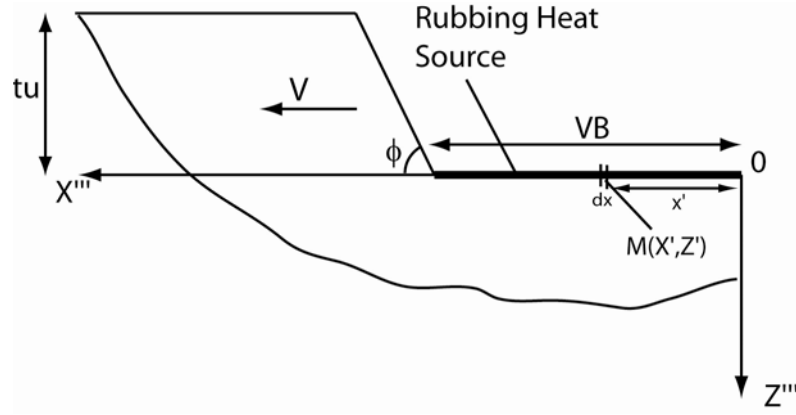


Figure 3.17. Thermal modeling of rubbing heat source on the workpiece side

The temperature rise on the workpiece can be written as

$$T_{M_{workpiece-rubbing}}(X''', Z''') = \frac{1}{\pi \lambda_c} \int_0^{VB} B_2(X''') q_{rub}(X''') e^{\frac{(X''' - x'')V}{2a_c}} \left[K_0 \left(\frac{V}{2a_c} \sqrt{(X''' - x'')^2 + Z'''^2} \right) \right] dx'' \quad (3.54)$$

Thus, the temperature rise at any point in the workpiece can be written as:

$$T_{M_{workpiece}}(X''', Z''') = T_{M_{workpiece-shear}}(X''', Z''') + T_{M_{workpiece-rubbing}}(X''', Z''') + T_0 \quad (3.55)$$

3.8 Solution for Temperature Distributions

In a similar study, Huang and Liang (2003) used numerical analysis to calculate heat partition ratios which resulted in computed temperature distribution only on the tool rake and flank interfaces, but numerical analysis cannot provide a full temperature distribution in the chip, tool and workpiece. Therefore, we aim to obtain a solution for temperature distribution at any given point in the cutting zone and in the tool. Heat partition ratios $B_1(x)$ and $B_2(x)$ indicate the energy going into the chip and workpiece respectively and can be calculated through equilibrium conditions along adiabatic tool-chip and tool-workpiece interfaces. The necessary equilibrium conditions which should be satisfied simultaneously to calculate heat partition ratios $B_1(x)$ and $B_2(x)$ are given in Eq. (3.56).

$$\begin{aligned}
 T_{M_{chip-shear}} + T_{M_{chip-friction}} &= T_{M_{tool-friction}} + T'_{M_{tool-rubbing}} + T_{M_{induced-rake}} + T'_{M_{induced-flank}} \\
 T_{M_{workpiece-shear}} + T_{M_{workpiece-rubbing}} &= T_{M_{tool-rubbing}} + T'_{M_{tool-friction}} + T_{M_{induced-flank}} + T'_{M_{induced-rake}}
 \end{aligned} \tag{3.56}$$

The subscript denotes the temperature rise at that region and prime as superscript shows the necessity for a coordinate transformation to make calculations compatible. The heat partition ratio expressions, $B_1(x)$ for the heat exchange at the tool rake face and chip interface, and $B_2(x)$ for the heat exchange between tool flank face and workpiece interface, are adapted from Komanduri and Hou (2001b, c) and given in Eq. (3.57) and Eq. (3.58).

$$\begin{aligned}
 B_1(x) &= (B_{chip} - \Delta B_1) + 2\Delta B_1 \left(\frac{x}{l_c} \right)^{m_1} + C_1 \Delta B_1 \left(\frac{x}{l_c} \right)^{k_1} \\
 1 - B_1(x) &= (B_{tool_rake} + \Delta B_1) - 2\Delta B_1 \left(\frac{x}{l_c} \right)^{m_1} - C_1 \Delta B_1 \left(\frac{x}{l_c} \right)^{k_1}
 \end{aligned} \tag{3.57}$$

$$\begin{aligned}
 B_2(x) &= (B_{workpiece} - \Delta B_2) + 2\Delta B_2 \left(\frac{x}{VB} \right)^{m_2} + C_2 \Delta B_2 \left(\frac{x}{VB} \right)^{k_2} \\
 1 - B_2(x) &= (B_{tool_flank} + \Delta B_2) - 2\Delta B_2 \left(\frac{x}{VB} \right)^{m_2} - C_2 \Delta B_2 \left(\frac{x}{VB} \right)^{k_2}
 \end{aligned} \tag{3.58}$$

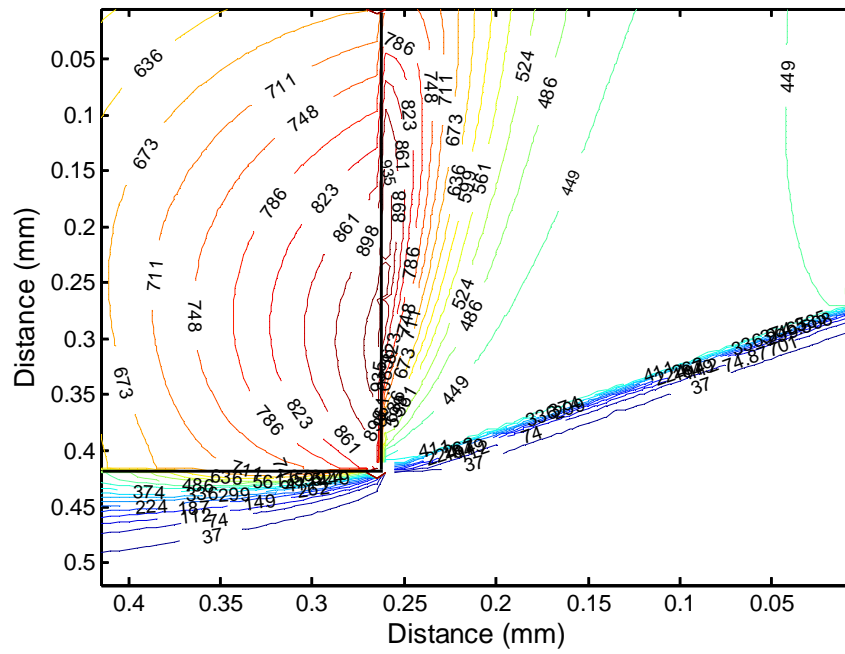
The constants B_{chip} , ΔB_1 , m_1 , k_1 , C_1 , $B_{workpiece}$, ΔB_2 , m_2 , k_2 , C_2 which have a unique effect on the temperature distribution curves at the interfaces should be calculated by matching the temperature distributions along tool-chip and tool-workpiece interfaces by using equilibrium conditions given in Eq. (3.56). In Komanduri and Hou's (2001c) work, where only the tool-chip interface is considered, matching the temperature distributions on both sides of the tool-chip interface is achieved by a simple computer code. In the case of worn tools, simultaneous solution of the heat partition ratio expressions $B_1(x)$ and $B_2(x)$ poses a two-objective optimization problem, which necessitates an extensive computation effort. An additional concern is that, for a better fit in temperature distribution curves, more parameters in Eq. (3.57) and (3.58) may be needed at the cost of increasing computational complexity. As a first step, in order to simplify the calculations, average heat partition ratios at the interfaces are calculated by matching average temperatures at the interfaces. Next, the heat partition equation parameters of Eq. 3.57 and 3.58 are solved and nonlinear heat partition ratios along interfaces are found.

3.9. Prediction of Temperature Distributions

In order to demonstrate the effects of tool wear on temperature distributions and other predictions AISI 1045 steel is chosen as work material. The cutting conditions are $V=200$ m/min, $t_u=0.15$ mm, $\alpha=0^\circ$ with various flank wear width values. Thermal properties of AISI-1045 steel are taken as constants where the thermal conductivity is 0.3 J/cm s $^\circ\text{C}$ and the thermal diffusivity is 0.1 cm²/s. The chosen cutting tool is carbide with constant thermal conductivity 0.4 J/cm s $^\circ\text{C}$.

3.9.1 Effect of Tool Flank Wear on Temperature Distributions

For the cutting condition given, under the assumption of constant heat partition ratios, temperature distributions in tool, chip and workpiece in machining AISI-1045 steel for flank wear width of 0.15 mm and for 0.3 mm are shown in Figure 3.18. The temperature distributions given in Fig 6 (a) and (b) reveal that as width of flank wear increases the location of the maximum temperature at the tool-chip interface approaches the tool tip because of the combined effect of two heat sources.



The investigation of variation of heat partition ratios with flank wear shown in Fig. 3.19 reveals that, in AISI-1045 steel, for small values of flank wear, all the heat generated at the tool-workpiece interface and some energy from tool-chip interface is transferred into the workpiece whereas when the flank wear becomes large, some fraction of the rubbing heat is transferred into the tool and chip. These results show that for AISI-1045, increasing flank wear values affects the direction of heat transfer hence temperature distributions in the chip, tool and workpiece. The maximum temperatures calculated at the interfaces for AISI-1045 is shown in Fig. 3.20. While the tool-workpiece interface temperature increases quickly with increasing flank wear length, the tool-chip interface temperature increases slowly.

The results shown in Fig. 3.19 and 3.20 are similar to the findings of Wang and Liu (1999). The temperature distributions at the tool-chip and tool-workpiece interface are given in Fig. 3.21. The temperature distributions at the interfaces are matched by calculating suitable parameters of expressions given in Eq. (3.57) and (3.58).

A closer match of temperature distributions could have been obtained by adding additional terms to heat partition ratio expressions. The distribution of the heat partition ratio for both interfaces is shown in Fig. 3.22. The predicted temperature distribution isotherms under a non-linear heat partition assumption is computed and given in Fig. 3.23.

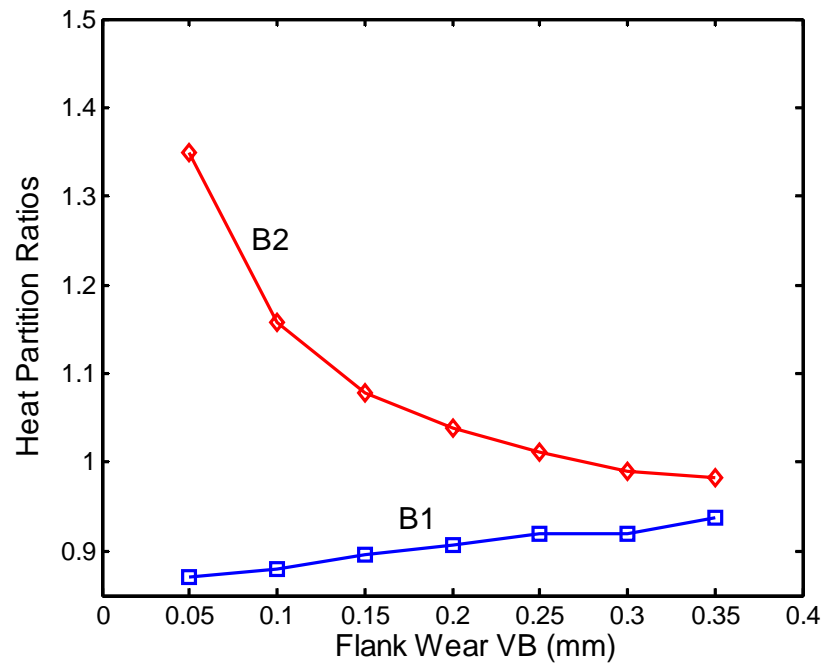


Figure 3.19 Change in the heat partition coefficients B_1 and B_2 with increasing flank wear.

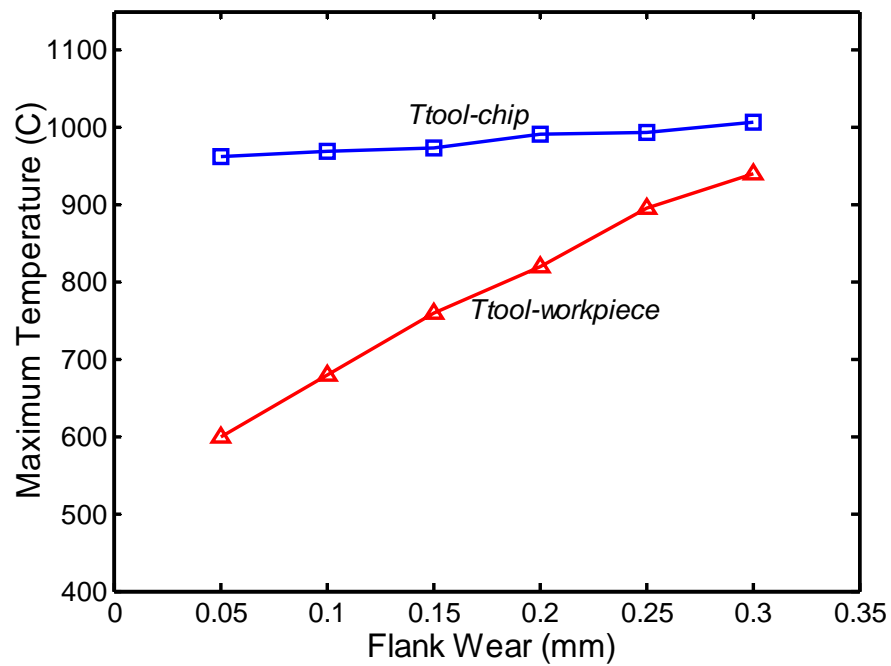
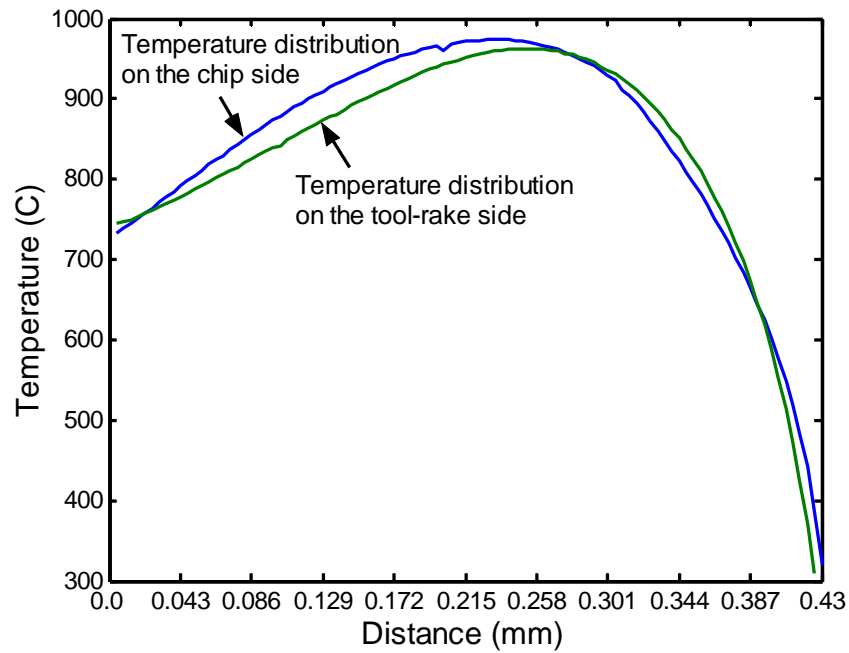
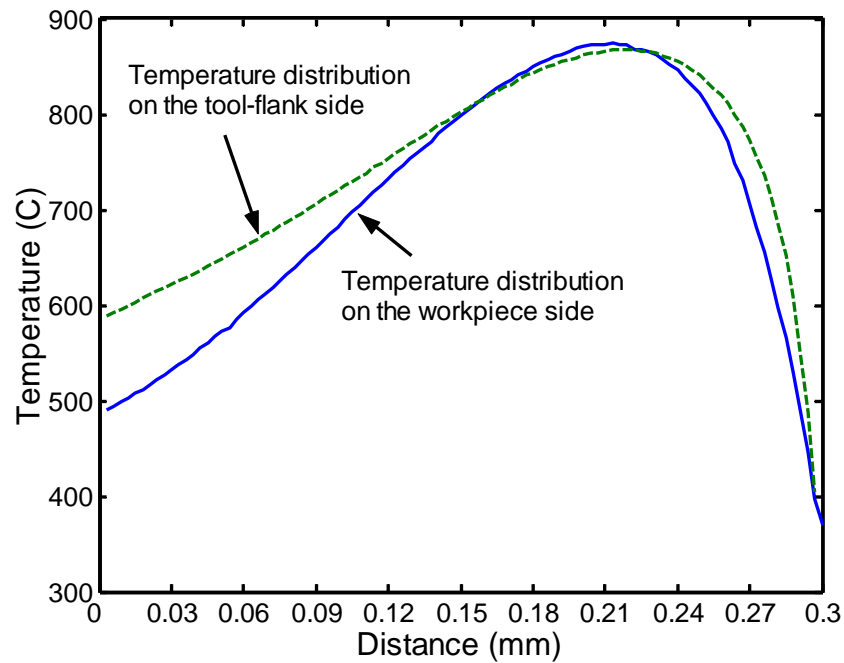


Figure 3.20 Change in the maximum temperatures with increasing flank wear.

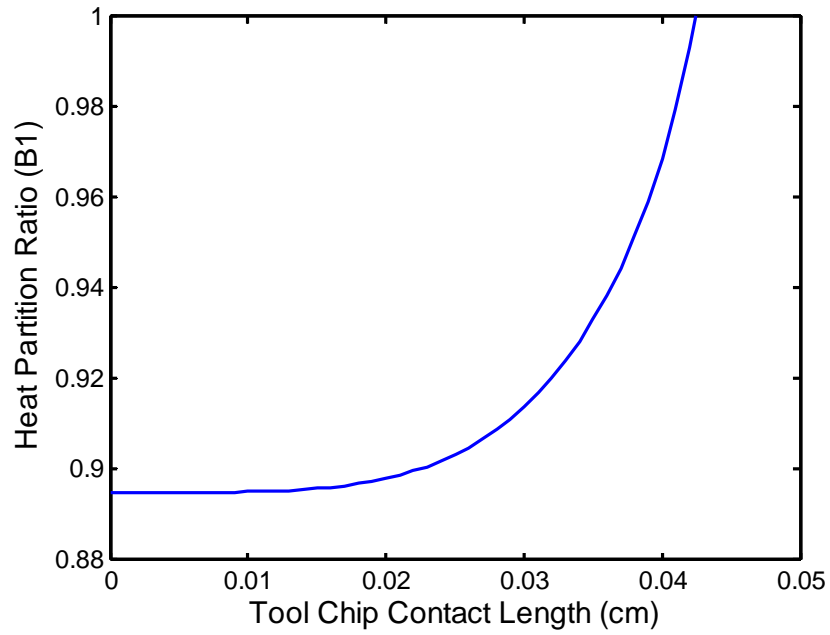


(a)

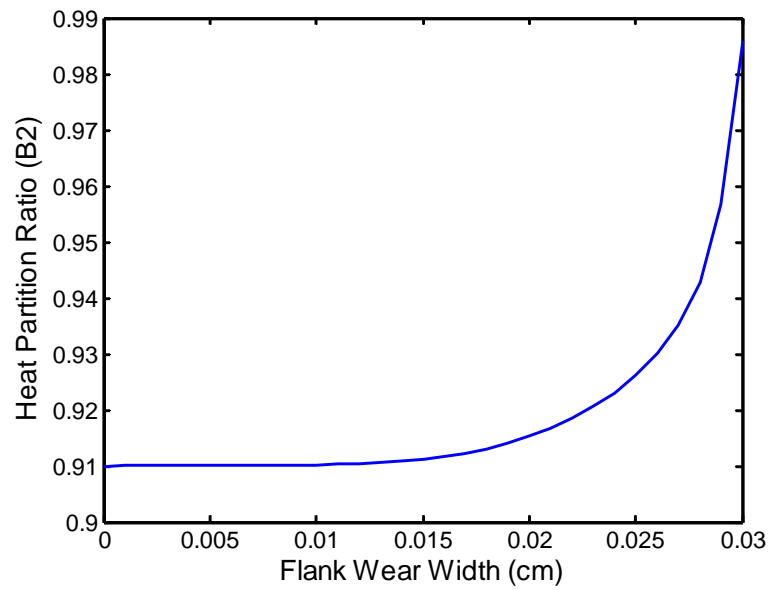


(b)

Figure 3.21. (a) Temperature distributions along the tool-chip interface, (b) temperature distributions along the tool-workpiece interface for AISI 1045 steel.



(a)



(b)

Figure 3.22. (a) Heat partition ratio along the tool-chip interface, (b) Heat partition ratio along the tool-workpiece interface for AISI-1045 steel.

3.10 Conclusions

This study combines oblique moving band heat source theory with non-uniform heat intensity at tool chip interface and Oxley's parallel shear zone theory to predict cutting forces, stress and temperature distributions. As a major contribution, the methodology proposed here integrates force and temperature prediction models in a single predictive model. In addition to that, predictive model which determines forces, stresses and temperature distributions in machining with worn tools is introduced. The

proposed technique has been applied to machining of AISI 1045 steel, and promising results have been obtained. The results have helped explain the heat partition behavior of the tool-chip and tool-workpiece interfaces as width of flank wear increases.

The temperature distribution in the workpiece can be employed in residual stress prediction models. The proposed model also provides significant advantages from the tool wear modeling point of view. By using this methodology, tool life can be predicted by integrating the outputs of the model into tool wear rate models for orthogonal cutting case.

CHAPTER 4

ANALYTICAL AND THERMAL MODELING OF HIGH-SPEED MACHINING WITH CHAMFERED TOOLS

4.1 Introduction

Chamfered tools with negative rake angle, first proposed by Hitomi (1961), are generally used to increase edge strength for machining hard materials. The negative rake angle helps trap the work material in front of the chamfered face, which acts as a cutting edge, protects the tool from rapid wear, and increases the strength of the edge. A stable trapped work material zone as shown in Fig. 4.1 was observed by many researchers, e.g. Kita et al. (1982), Hirao et al. (1982), Jacobson and Wallen (1988), and Zhang et al. (1991), when machining steel and often referred as dead metal zone (DMZ). Early research was mostly experimental and aimed at classifying the types of dead metal zones under different cutting conditions and chamfered tool designs. Dead metal zone differs from built-up-edge (BUE), which is mostly observed in machining softer materials such as aluminum alloys, because it does not disappear with an increased cutting speed (Zhang et al. 1991). Recently, some analytical models have been proposed to better understand dead metal zone phenomena and predict cutting forces. Zhang et al. (1991) proposed a cutting model for chamfered tools by utilizing the minimum energy method. They observed that the dead metal zone is stationary and its presence does not depend on cutting speed and chamfer angle. Ren and Altintas (2000) proposed a similar model which utilizes Oxley's (1989) predictive machining model. Movaheddy et al. (2002)

proposed a thermo-mechanical arbitrary Lagrangian Eulerian finite element formulation to simulate the chip formation process in orthogonal cutting with chamfered tools. In their study, the zone of stagnant material is identified from the velocity profile around the cutting edge. They concluded that chip formation is not affected by chamfer angle because of the dead metal zone formed under the chamfer. Long and Huang (2005) extended the models previously proposed by Zhang et al. (1991) and Ren and Altintas (2000) and considered that the inclination of the dead metal zone under chamfer is not equal to the shear angle as assumed in earlier models (Zhang et al. (1991) and Ren and Altintas (2000)). However they did not study how dead metal zone angle changes under different cutting conditions. Fang (2005) extended Lee and Shaffer's model (1951) to study the effect of large negative tool rake angle and cutting speed on the tool-chip friction and the shape of stagnation zone and showed that the size of the stagnation zone decreases with increasing cutting speed. Fang (2005) assumed that stagnant zone is parallel to workpiece surface and sticking conditions occurs on the stagnant zone. Fang and Wu (2005) proposed a slip-line model for positive rake angle chamfered tools without dead metal zone formation in front of the chamfer face and validated their model on aluminum alloys. Choudhury et al. (2005) studied the effects of chamfer height and chamfer angle on cutting forces and observed that chamfer height and angle mainly affect thrust (feed) force. In a similar study, Zhou et al. (2003) observed the influence of chamfer angle on the tool life of polycrystalline cubic boron nitride (PCBN) tools by investigating the relation between cutting forces and tool wear and found the optimum chamfer angle as negative 15° for the given cutting condition. Yen et al. (2004) studied the effects of various tool edge geometries on chip formation, cutting forces, and process

variables by using finite element analysis. For chamfered tools, they also observed increasing thrust forces with increasing chamfer angle and increasing thrust and cutting forces with increasing chamfer width.

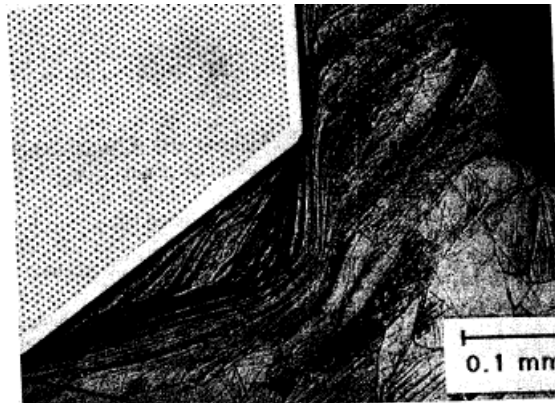


Figure 4.1 Dead metal zone when machining austenitic stainless steel with a chamfered tool with 60° rake angle at cutting speed 45 m/min (Zhang et al. (1991)).

The objective of this work is to study machining with negative rake angle chamfered tools in the presence of dead metal zone. Slip line field analysis will be used to deduce information about the geometry of the dead metal zone and to determine friction factors at the contact interfaces. An analytical thermal model proposed in an earlier study (Karpal and Özel (2006 a, b)) will be extended to calculate temperature fields in the tool-chip and tool-workpiece interfaces. Analytical thermal model for machining with chamfered tools will utilize heat intensities generated at the primary deformation zone due to shearing, tool-chip and dead metal zone-workpiece interfaces due to friction. The influence of cutting conditions on the tool and workpiece temperature distributions will be investigated in machining with chamfered tools.

Proposed approach is believed to further explain the mechanics of machining with chamfered tools and temperature generation in the machined workpiece.

Numerous studies on analytical thermal modeling of metal cutting have been undertaken since the pioneering studies of Hahn (1951), Jaeger (1942) and many others. Recently, Komanduri and Hou (2001a, b) predicted the temperature distributions in the chip, tool and workpiece by extending Hahn's solution. An extensive literature survey on thermal modeling in machining can also be found in Komanduri and Hou (2001b). The authors have also recently introduced analytical thermal modeling by determining non-linear heat intensities and partitions for cutting with sharp and worn tools (Karpas and Özel (2006a, b)).

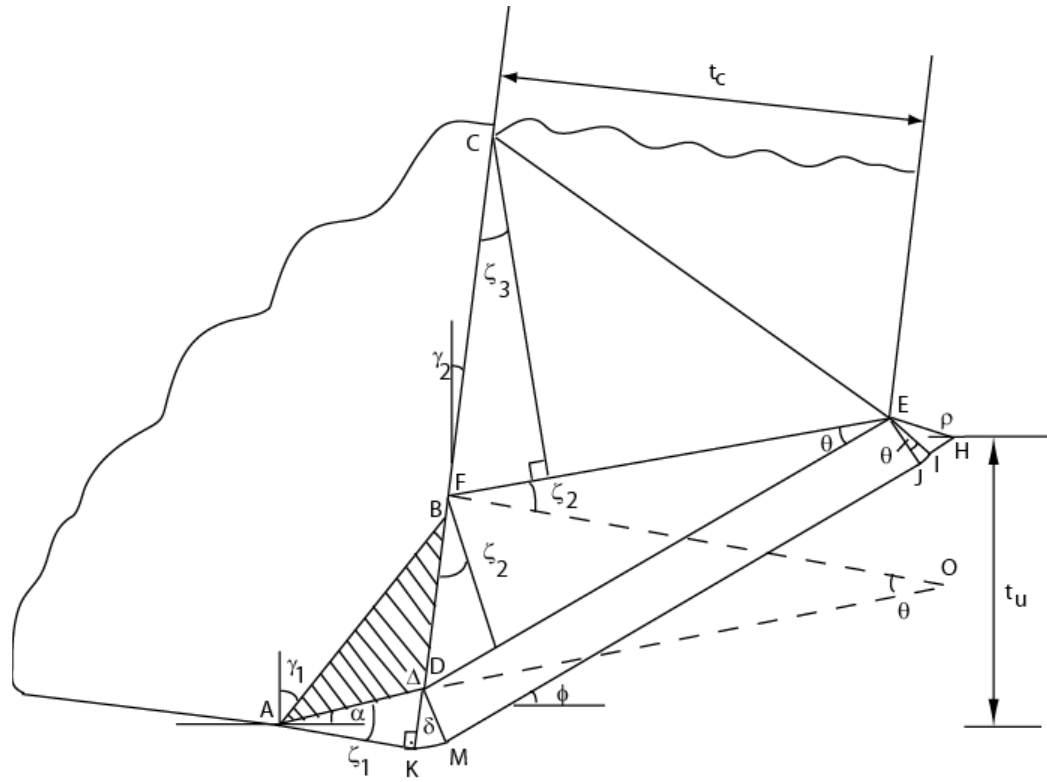
In this chapter, first the slip-line model proposed for machining with chamfered tools will be presented. Slip-line angles and therefore tool-chip friction will be calculated by using the slip-line model and orthogonal cutting tests. Subsequently, thermal modeling of chamfered tools will be presented. The heat transfer model for chamfered tools is obtained by extending the thermal modeling of sharp and worn tools by Karpas and Özel (2006 a, b). Preliminary work on slip line field analysis and analytical thermal modeling of chamfered tools was presented in Karpas and Özel (2006c).

4.2. Slip-Line Modeling for Machining with Chamfered Tools Considering Dead Metal Zone

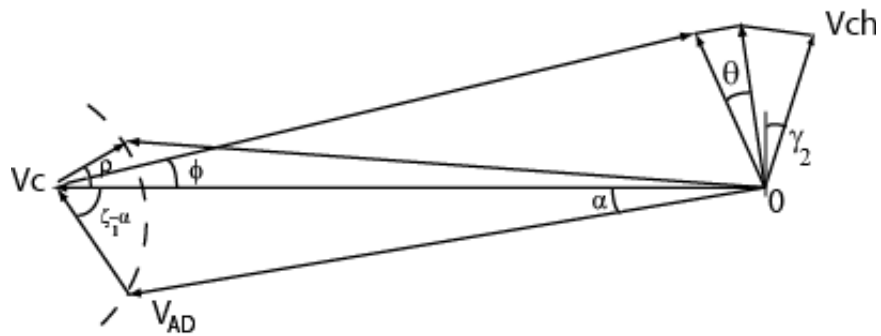
Modeling of machining by using plasticity theory based slip line field analysis has been a research subject for a long time. Based on Ernst and Merchant's (1941) model, Lee and Shaffer (1951) applied slip-line field analysis by assuming uniform shear flow stress throughout the slip-line field. Kudo (1965) suggested several slip-line models by replacing straight slip-lines with curved slip lines in Lee and Shaffer (1951) model. Shi and Ramalingam (1991) proposed a slip-line model for worn cutting tools which considered a flank wear land not parallel to the machined surface based on findings of Thomsen et al. (1962) which stated that material flow beneath flank wear would not be plastic if flank wear was parallel to the machined surface. Abebe and Appl (1981) proposed a slip-line field model for machining with large negative rake angle tools by considering stagnant metal zone in front of the cutting tool. Waldorf (1996) developed a slip-line model to study ploughing and tool wear mechanisms in round edged cutting tools. Fang et al. (2001) proposed a universal slip-line model for machining with restricted contact tools. Their proposed model reduces to previously suggested slip-line fields under special cases therefore can be used to explain mechanics of machining under various cutting conditions. Fang and Jawahir (2002) integrated their universal slip-line field with Oxley's predictive machining theory to investigate the effects of strains, strain rates and temperatures in machining with grooved tools.

Whilst slip-line field analysis considers work material as rigid, perfectly plastic, it provides average friction information at the tool-chip, and tool-workpiece interfaces. However, the mechanics of cutting cannot be fully explained by using slip-line field analysis since material characteristics such as strain hardening, strain rate effects and thermal softening are neglected and non-uniform stress distributions at the interfaces cannot be calculated without violating mass continuity conditions (Childs et al. 2000). Recently, Childs (2006) compared results of slip-line field analysis with finite element simulations for various materials and concluded that slip-line field analysis provides a legitimate framework for the machining process and yet cannot predict a unique solution for the chip flow. The slip-line model and its associated hodograph are illustrated in Fig. 4.2. The chip is assumed to be straight in order to simplify the model. The slip-line angles ζ_1 , ζ_2 , and ζ_3 denote the friction conditions on the surfaces AD , DF and FC where the tool rake face is in contact with the chip at FC . The shear angle is represented by (ϕ) . The angle formed by bottom surface of the DMZ and the cutting direction is named as DMZ angle (α) .

It is assumed that stagnant and strain hardened DMZ adjacent to the chamfer face acts as part of the cutting edge. Hence the work material flow separates at point D . The work material above point D flows upward into the chip, and the work material under point D flows downward into the workpiece.



(a)



(b)

Figure 4.2. The slip-line model (a) and its hodograph (b).

The inclination of the workpiece material ahead of the tool is also included in the model and shown by prow angle (ρ) which can be calculated by utilizing the requirement that the height of point E from the uncut workpiece surface should be the same as the height

of point D from cut workpiece surface due to velocity continuity as given in Eq. (4.1) (Shi and Ramalingam, (1991)).

$$\rho = \sin^{-1} \left(\frac{\sin(\alpha)}{\sqrt{2} \sin(\zeta_1)} \right) \quad (4.1)$$

In this slip-line model, cut chip thickness (t_c) and cutting forces (F_c and F_t) can be calculated according to uncut chip thickness (t_u), tool-chip friction factor under DMZ ($m_1 = \tau_{AD}/k$), shear angle (ϕ), dead metal zone angle (α), and tool geometry (height of the chamfer (h), rake angles (γ_1) and (γ_2)). The variable τ denotes frictional shear stress and k is the material shear flow stress. The value of friction factor (τ/k) varies between 0 and 1 where a value of zero means no friction occurs, a value of one means sticking conditions occur. The following expressions can be written from slip-line theory as:

$$\zeta_1 = \frac{1}{2} \cos^{-1} \left(\frac{\tau_{AD}}{k} \right) \quad (4.2)$$

$$\zeta_2 = \frac{1}{2} \cos^{-1} \left(\frac{\tau_{FD}}{k} \right) \quad (4.3)$$

$$\zeta_3 = \frac{1}{2} \cos^{-1} \left(\frac{\tau_{FC}}{k} \right) \quad (4.4)$$

$$p_E = k \left(1 + 2 \left(\frac{\pi}{4} - \phi - \rho \right) \right) \quad (4.5)$$

where the expression in the parenthesis in Eq (4.5) is equal to slip line field angle θ ;

$$\theta = \frac{\pi}{4} - \phi - \rho \quad (4.6)$$

and central fan angle (δ), the angle ADF (Δ) can be calculated as:

$$\delta = \phi + \zeta_1 - \alpha \quad (4.7)$$

$$\Delta = \frac{\pi}{2} + \frac{\theta}{2} + \zeta_1 + \zeta_2 - \delta \quad (4.8)$$

In order to simplify the problem, the dead metal zone is assumed to be extending from the rake face which enables us to relate slip line angle ζ_1 to slip line angles ζ_2 and ζ_3 as in Eq. (4.9) and (4.10).

$$\zeta_2 = \zeta_1 + \gamma_2 + \frac{\phi}{2} + \frac{\rho}{2} - \frac{\pi}{8} \quad (4.9)$$

$$\zeta_3 = \phi - \theta + \gamma_2 \quad (4.10)$$

The cut chip thickness (t_c) can be calculated as:

$$t_c = DE \sin(\pi/2 - \phi - \gamma_2) \quad (4.11)$$

where

$$DE = \frac{t_u}{\sin(\phi)} \quad (4.12)$$

It should be noted that absolute values of negative chamfer and rake angles are used in above given expressions. In an admissible slip-line field, the angles in Eqs. (4.7) and (4.8) should be equal to or greater than zero. The cutting force and thrust force are written as:

$$\begin{aligned} F_c &= kw \left\{ DE \left[\cos(\phi) + (1 + 2\theta) \sin(\phi) \right] + AD \left[\cos(\alpha) \cos(2\zeta_1) + (1 + 2\theta + 2\delta + \sin(2\zeta_1)) \sin(\alpha) \right] \right\} \\ F_t &= kw \left\{ DE \left[(1 + 2\theta) \cos(\phi) - \sin(\phi) \right] + AD \left[(1 + 2\theta + 2\delta + \sin(2\zeta_1)) \cos(\alpha) - \sin(\alpha) \cos(2\zeta_1) \right] \right\} \end{aligned} \quad (4.13)$$

where, w is the width of cut. The ratio of cutting force to thrust force (F_c/F_t) can be calculated from Eq. (4.13) without necessarily knowing shear flow stress (k) at the primary shear zone. In Eq. (4.13), the first term on the right hand side represents shearing and the second term represents ploughing forces due to DMZ.

Identification of the unknown slip line angle (θ), DMZ angle (α) and friction factors are performed by utilizing orthogonal cutting tests where cutting forces and chip thicknesses that are measured for various cutting conditions and matching those with slip line field calculations by using a Matlab code. The unknown slip-line angle pair (θ, α) are solved as a set of possible solutions depending on the tolerance value allowed between measured and calculated force (F_c/F_t) and chip ratios (t_c/t_u) as given in Eq. (4.14) for a known friction factor m_l .

$$\Delta E = \sqrt{\left[\left(\frac{F_c}{F_t} \right)_{ex} - \left(\frac{F_c}{F_t} \right)_{calc} \right]^2 + \left[\left(\frac{t_c}{t_u} \right)_{ex} - \left(\frac{t_c}{t_u} \right)_{calc} \right]^2} \leq Tol \quad (4.14)$$

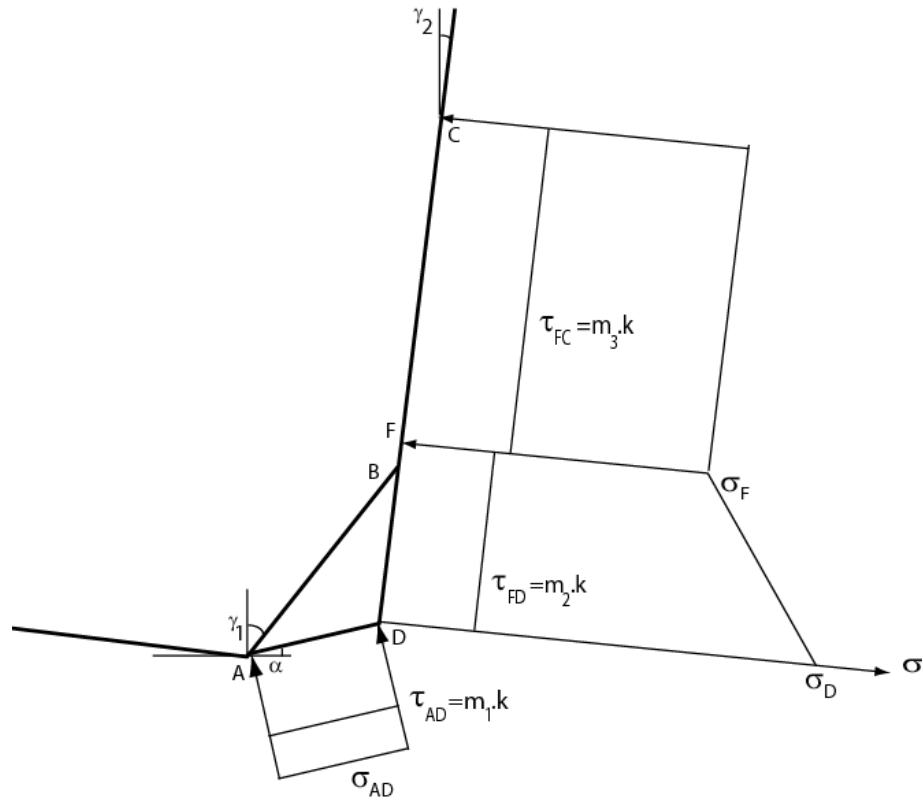
It must be noted that there is a range of m_l values which will satisfy Eq. (4.14) depending on the selected tolerance value due to the non-unique nature of slip-line field model adopted. In this work, a tolerance value of 0.001 has been chosen to narrow the range of m_l value. Once all of the slip lines angles are calculated, the shear flow stress (k) corresponding to that cutting condition can be calculated by using experimentally measured cutting forces.

According to above given slip-line field model, normal stresses at points A , D , F and C can be calculated. This yields to the stress distributions on the rake face, front and bottom interfaces of the dead metal zone as shown in Fig. 4.3(a). Frictional shear stresses (τ_{AD} , τ_{FD} and τ_{FC}) on AD , FD and FC respectively are calculated from the solved slip-line angles. Normal stresses at point D and F can be calculated by rotating slip-lines ED and EF normal to the rake face as in Eq. (4.15).

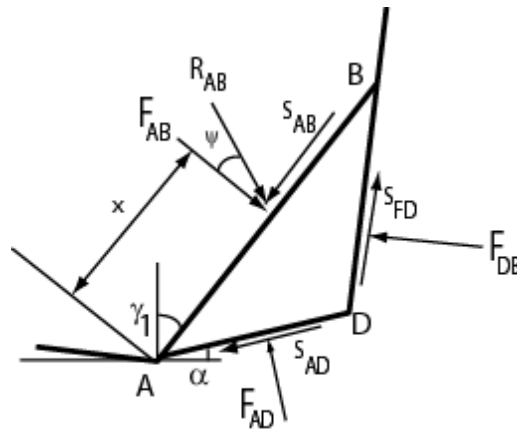
$$\begin{aligned}
 \sigma_D &= P_E + 2k(\phi + \gamma_2) \\
 \sigma_F &= k[1 + 2(\phi - \theta + \gamma_2)] \\
 \tau_{AD} &= m_1 k \\
 \tau_{DF} &= m_2 k \\
 \tau_{FC} &= m_3 k
 \end{aligned} \tag{4.15}$$

where m_2 ($m_2 = \cos(2\zeta_2)$) and m_3 ($m_3 = \cos(2\zeta_3)$) are the friction factors on DF and FC , respectively. The forces acting on the chamfer tool are given in Eq. (4.16) and shown in Fig. 4.3(b).

Once the slip-line angles are calculated, resultant force (R_{AB}) acting on the chamfer face of the tool can be calculated by subtracting rake face forces from total cutting forces. The point of application (x) of the resultant force can be found by considering moment equilibrium around point D . In order for dead metal zone to stay stagnant at AB , the shear stress on AB must be equal or less than shear flow stress ($\tau_{AB} \leq k$).



(a)



(b)

Figure 4.3 (a) Normal and shear stress distribution on the chamfer tool, (b) Force equilibrium at the chamfer face.

4.3 Experimental Setup and Results

Orthogonal turning of thin webs (2.5-2.8 mm) were performed on annealed AISI 4340 steel using CBN cutting tool inserts (TNG-423) with chamfered edge design (0.1 mm chamfer land, 20° chamfer angle) in a rigid CNC turning center as illustrated in Fig. 4.4. The tool holder provided a negative 7° rake angle; hence a negative 27° angle is formed at the chamfer face. The image of the chamfered edge preparation of the CBN insert taken by field emission scanning electron microscopy (FESEM) is given in Fig. 4.5. In the experiments straight edges of triangular inserts were used (see Fig. 4.4). Forces were measured with a Kistler ® turret type force dynamometer, a PC-based DAQ system and Kistler® DynoWare software, and cut chip thicknesses were measured by using a toolmaker's microscope.

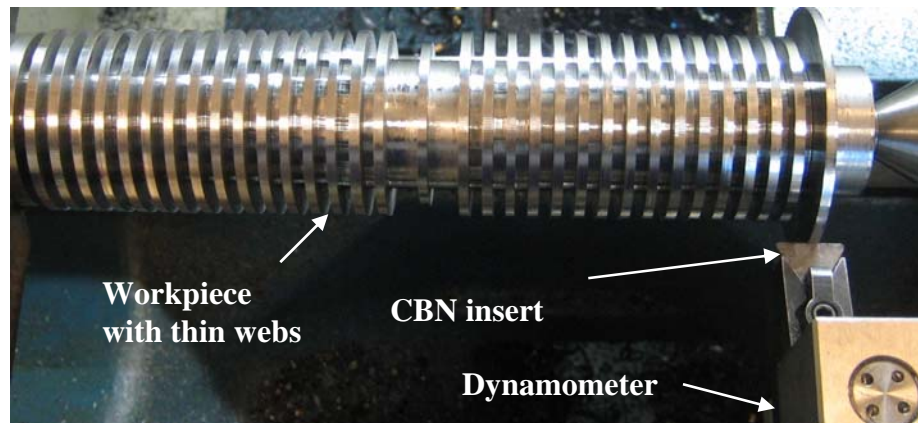


Figure 4.4 Experimental set-up for orthogonal turning.

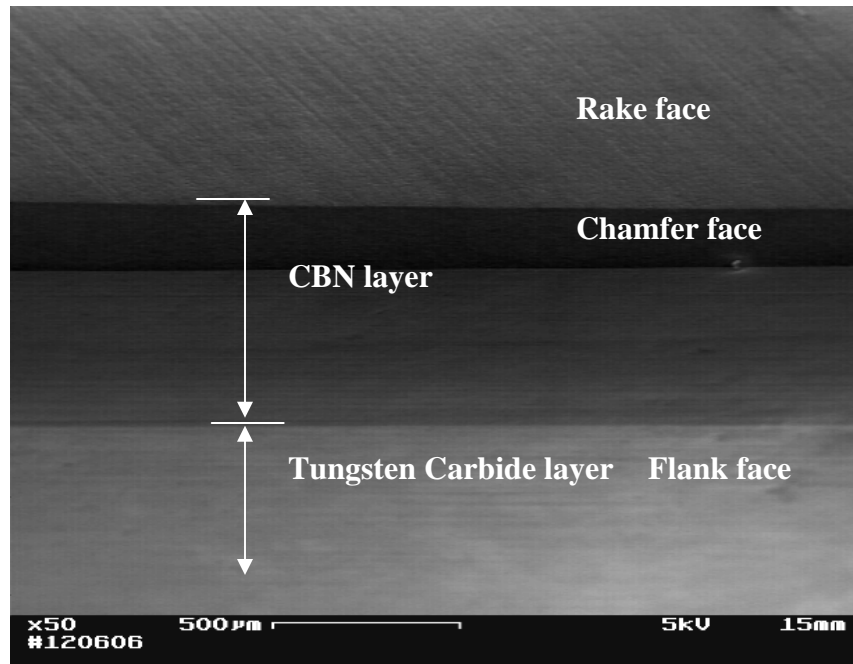
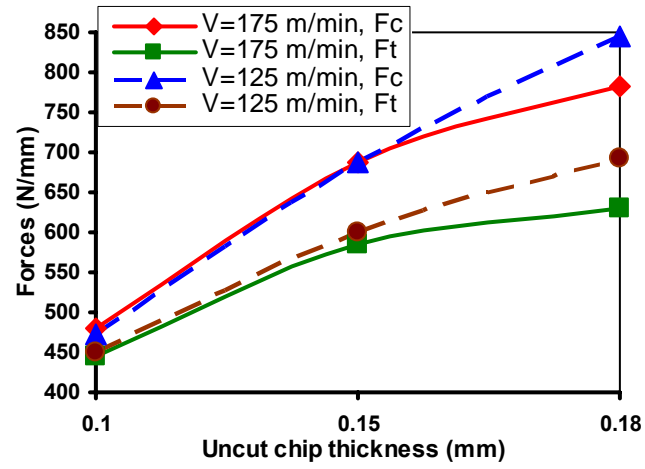
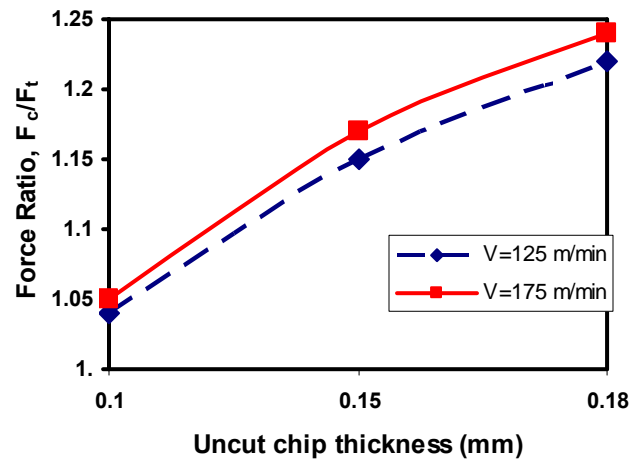


Figure 4.5 SEM image of the chamfered insert at 50 times magnification.

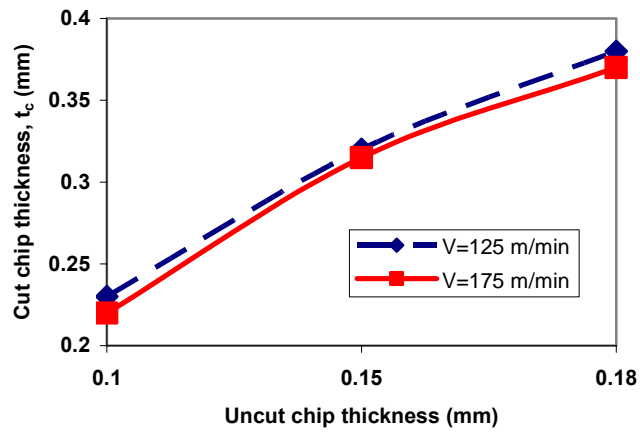
The experiments were conducted under various combinations of three different uncut chip thickness values (0.1, 0.15 and 0.18 mm) and two different cutting speeds (125, and 175 m/min). Measured and calculated force ratios and chip thickness values are shown in Fig. 4.6. According to experimental results (Fig. (4.6)): a) force ratio decreases as uncut chip thickness decreases, b) force ratio decreases as cutting speed increases, and c) cut chip thickness decreases as cutting speed increases, which are in agreement with general orthogonal machining observations.



(a)



(b)



(c)

Figure 4.6 Measured: (a) forces, (b) force ratio, (c) cut chip thickness.

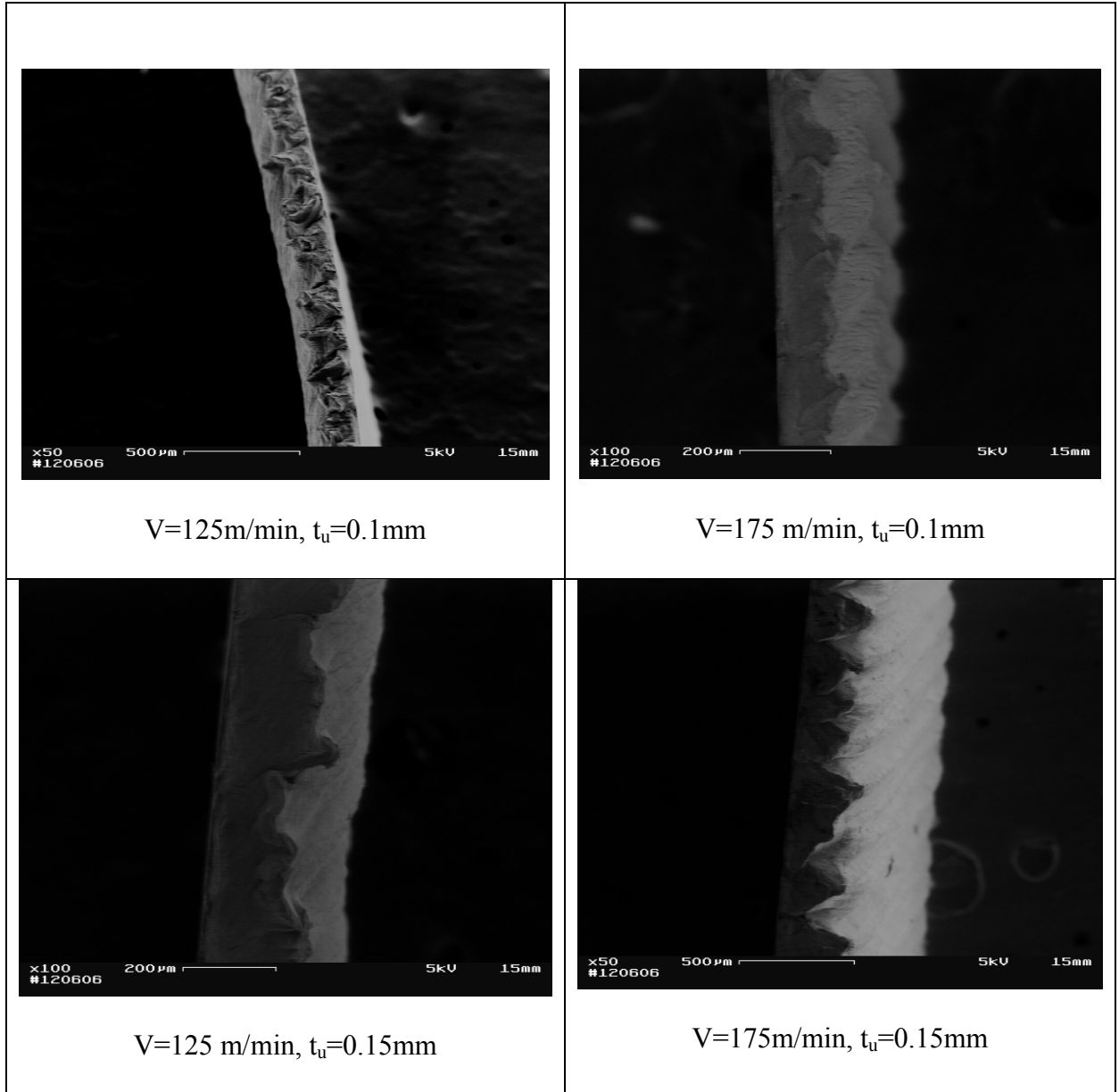


Figure 4.7 SEM images of the chips collected during experiments.

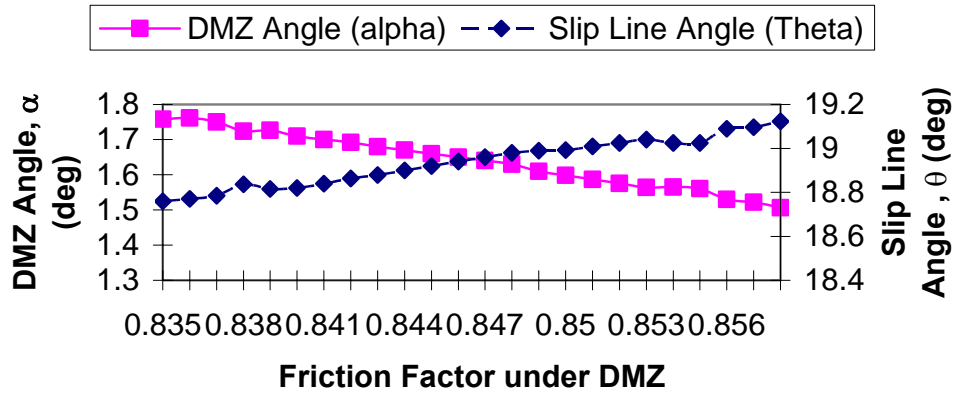
The SEM images of the chips produced under various cutting conditions are shown in Fig 4.7. For cutting speed $V=125\text{ m/min}$ continuous chips were obtained for all uncut chip thickness values. When cutting speed was increased formation of serrated chips were observed. Chip thickness is measured as an average for the serrated types of chips.

4.4 Identification of Slip-Line Angles and Friction Factors

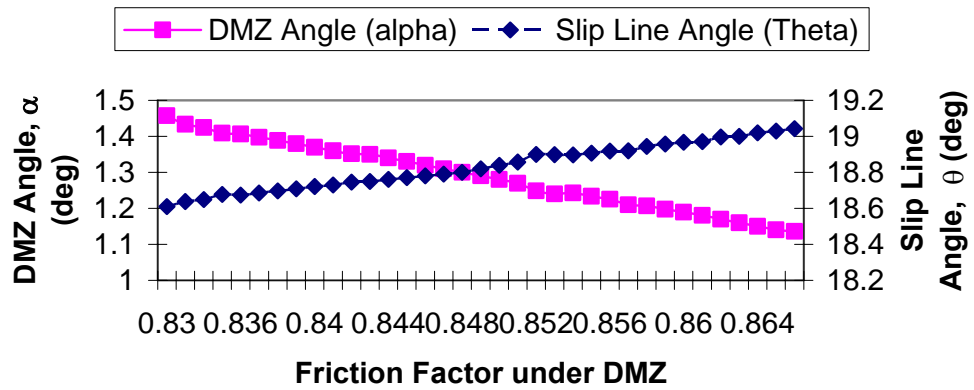
The slip-line field angle (θ) and DMZ angle (α) are identified for various cutting conditions by using measured force and chip thickness ratios given in Fig. 4.6. A range of friction factors (m_I) which satisfies the tolerance term given in Eq. (4.14) is obtained. The number of solutions can be further reduced by decreasing the tolerance value in Eq. (4.14). However, a wide range solution allows us to observe the effects of friction factor under DMZ (m_I) on the slip-line angles.

These identified slip-line angles are shown in Fig. 4.8(a, b, c) for the cutting speed of $V=125$ m/min. From the identified slip-line angles, the following observations can be made:

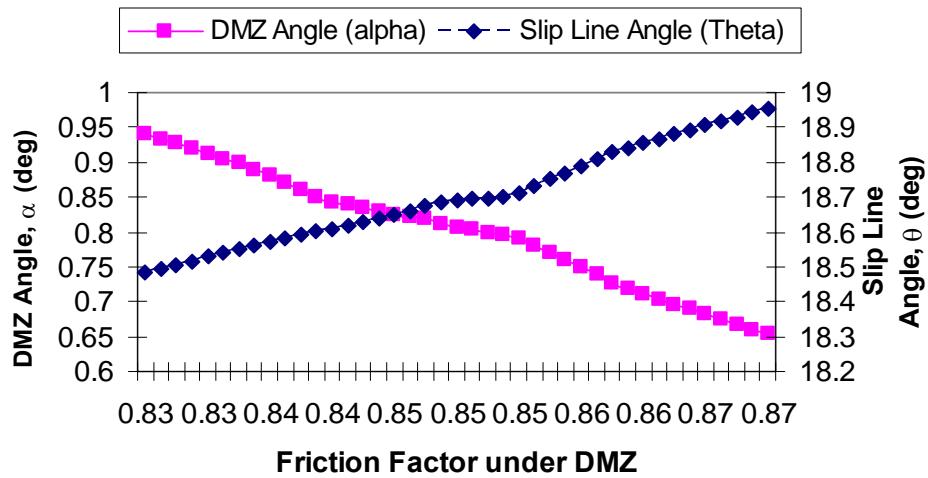
- As friction factor under DMZ (m_I) increases, DMZ angle (α) decreases and slip-line field angle (θ) increases. This implies that friction factor under the DMZ affects the shape of the primary deformation zone.
- Increased friction factor under DMZ (m_I) and resulting decreased DMZ angle change primarily thrust force. This implies that friction conditions on the front of dead metal zone (DF) and rake face slightly decreases in order to satisfy constant force ratio.
- DMZ angle (α) decreases as uncut chip thickness increases and increases as cutting speed increases.
- Slip-line field angle (θ) decreases with increasing cutting speed and decreases with increasing uncut chip thickness.



(a)



(b)



(c)

Figure 4.8 Identified dead metal zone angle (α) and Slip Line Field Angle (θ) for

$V=125\text{ m/min}$ (a) $t_u=0.1\text{mm}$, (b) $t_u=0.15\text{ mm}$, (c) $t_u=0.18\text{mm}$.

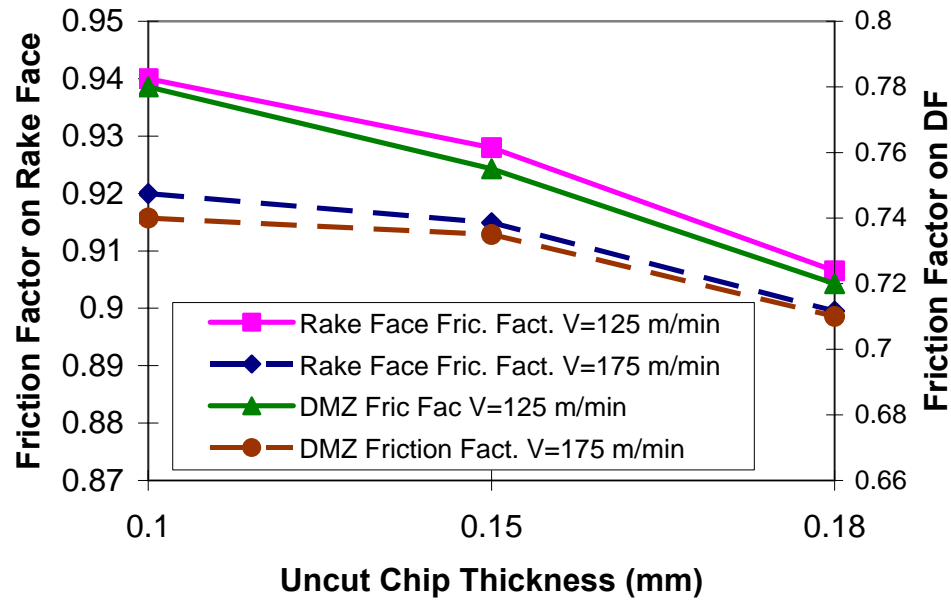


Figure 4.9 Variation of rake face friction factor with uncut chip thickness and cutting speed.

Friction factor calculated on the front boundary of the dead metal zone (m_2) and on the rake face are given in Fig.4.9 for various cutting conditions. Friction factors on DF and rake face are slightly decreasing with increasing uncut chip thickness and increasing with increasing cutting speed. However, friction factors are found not to be so sensitive to the changes in experimental cutting conditions.

The temperatures at the dead metal zone are expected to increase with increasing uncut chip thickness since decreasing dead metal zone angle will result in higher heat intensity at the bottom surface of the DMZ. This will also result in temperature rise and decreasing friction factor on the front of the DMZ. Due to thermal softening property of

steels, machining under these conditions becomes more favorable. This further justifies usage of chamfered tools in roughing operations where large depths of cuts are taken.

The distribution of normal stresses along DC extended from the frond end of the DMZ to rake face of the chamfered tool is shown in Fig 4.10. Normal stress at point D is found to be around 2.5 or 3 times of the shear flow stress of work material which is in agreement with observation by Childs et al. (2000). Due to increased chip load, normal stresses applied to the rake face increase with the increase in uncut chip thickness as expected. However, shear stress applied to the rake face, hence, the friction factor slightly decreases.

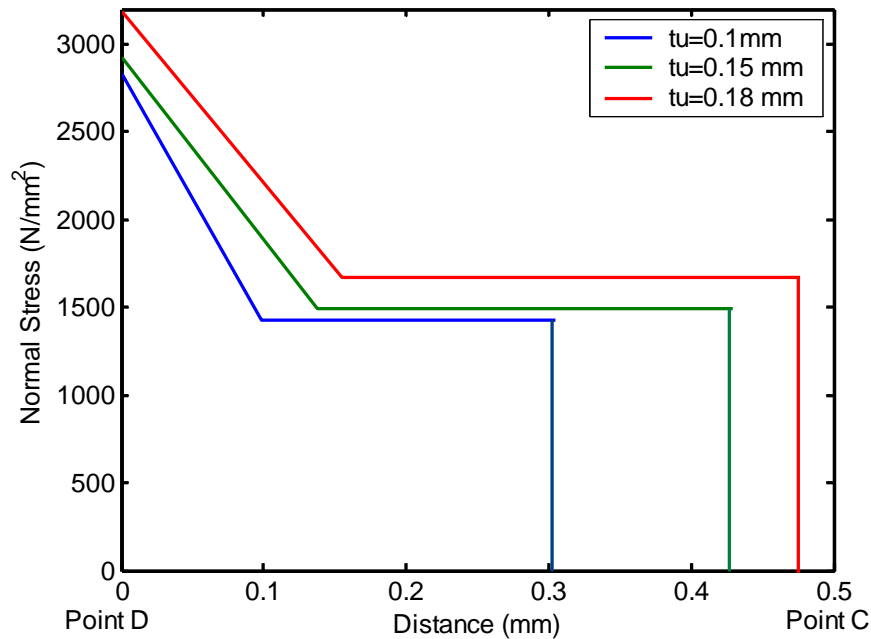


Figure 4.10 Distribution of normal stresses for $V=125$ m/min on the rake face of the tool.

The stress distributions can be further utilized to calculate the force partition on the chamfered and rake faces of the cutting tool. As uncut chip thickness increase 80% from 0.1 to 0.18 mm/rev, percentage of the resultant force exerted on the chamfered face decreases from 45% to 31% and the percentage of the resultant force exerted on rake face increases from 55% to 69%. Fig. 4.11 illustrates the changes in percentage of resultant force on the chamfer face. This indicates that slip-line field model can be beneficial in investigating the effects chamfer angle and chamfer height on the mechanics of cutting and proper selection of cutting tool for a given cutting condition.

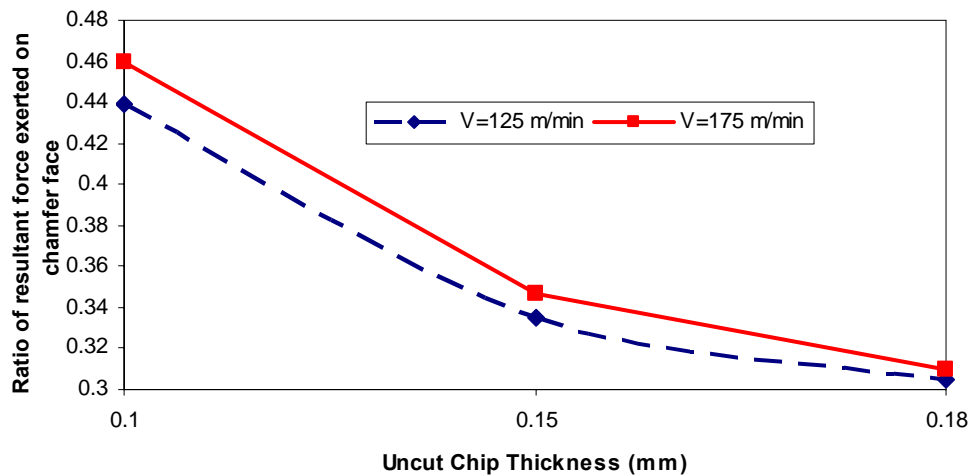


Figure 4.11 Percentage of resultant force exerted on the chamfer face

In order to be able to investigate the effects of cutting conditions on tool temperature distributions, an analytical thermal model is proposed for orthogonal machining with chamfered tools. Proposed analytical thermal model utilizes identified friction factors, velocities, shear angle, length of primary shear zone, DMZ geometry, tool-chip contact

length and stress distributions at the interfaces to calculate the heat intensities and obtaining temperature distributions in the tool and cutting zone.

4.5 Thermal Modeling of Chamfered Tools for Orthogonal Machining

The heat sources considered in analytical thermal model and the regions affected by these heat sources are shown in Fig. 4.12. Shear plane heat source is considered as a uniform oblique moving band heat source. The heat intensity of the frictional heat source is modeled as a non-uniform moving band heat source on the chip side and a stationary heat source on the tool side. The frictional heat intensity on BD is neglected considering the low heat intensity at that region as a result of low chip velocity. Frictional heat source under dead metal zone is also modeled as a moving band heat source. This heat source is considered to heat up workpiece and dead metal zone. In order to satisfy continuity conditions, the heating effect of the shear plane heat source on the tool will be modeled as an induced stationary heat source on the chamfered and rake faces. Analytical thermal model yields steady state temperatures at the cutting zone in a very short amount of time. It allows the investigation of heat partitioning between chip and tool. In analytical thermal model, it is assumed that: (i) the temperature distributions on the interfaces are the same, which enables the calculation of the heat partition ratios on the rake and chamfer faces. (ii) The upper surface of the chip, the uncut surface of the workpiece and the tool side of tool-chip interface are considered adiabatic. (iii) The temperature distributions are in steady state. (iv) Heat loss along the tool-chip interface is omitted and

it is assumed that all the deformation energy in the primary shear zone is converted into heat energy. (v) All the heat sources are plane heat sources.

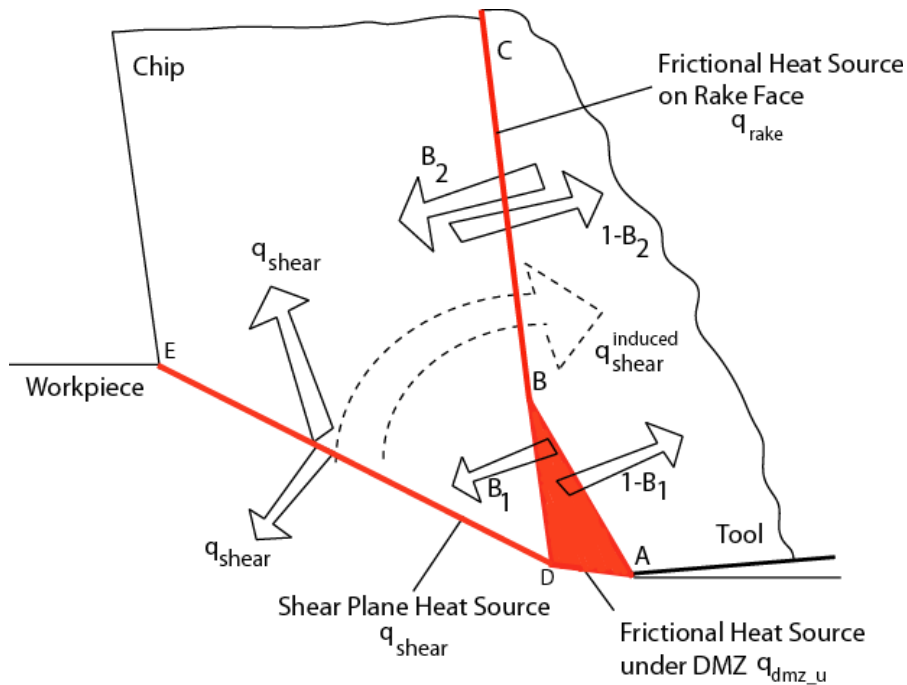


Figure 4.12 Heat sources in thermal modeling of orthogonal cutting with a chamfered tool

4.5.1 Modeling of Temperature Rise in the Chip Due to Shear Plane Heat Source

The analytical modeling of steady state temperature in metal cutting presented by Hahn (1951) was based on the heat source method of Jaeger (1942). Komanduri and Hou (2001 a, b, c) modified Hahn's infinite medium oblique band heat source solution and obtained a semi-infinite medium oblique band heat source solution by considering the upper surface of the chip as adiabatic and adding an appropriate image heat source as

As for the workpiece side of the thermal modeling, primary heat source is modeled again as an oblique moving band heat source which moves with cutting velocity as given in Komanduri and Hou (2001a, b, c). The uncut workpiece surface is considered as adiabatic. Assuming the origin of the coordinate system to be at point A, following expressions can be derived.

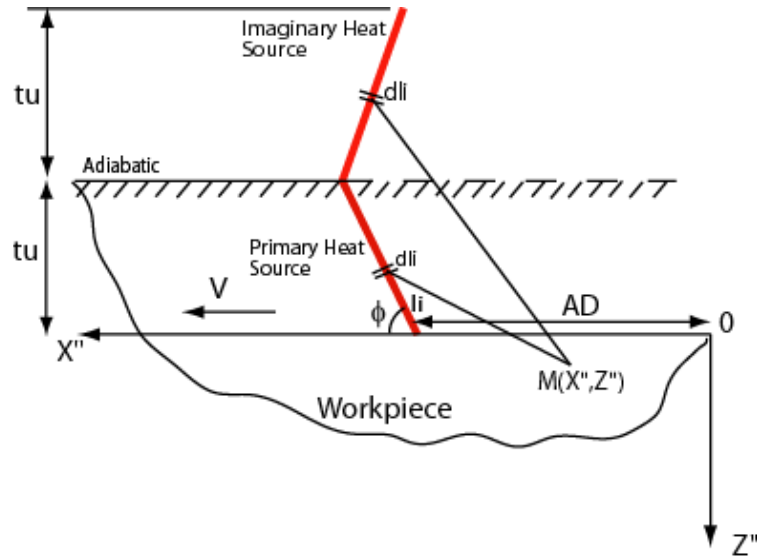


Figure 4.14 Thermal modeling of primary heat source on the workpiece side

$$T_{M_{workpiece-shear}}(X'', Z'') = \frac{q_{shear}}{2\pi\lambda_c} \int_{l_i=0}^{DE} e^{\frac{(X''-l_i \cos \phi - AD)V}{2a_c}} \left\{ K_0 \left[\frac{V}{2a_c} \sqrt{(AD + l_i \cos \phi - X'')^2 + (Z'' + l_i \sin \phi)^2} \right] + \right. \\ \left. K_0 \left[\frac{V}{2a_c} \sqrt{(AD + l_i \cos \phi - X'')^2 + (2t_u + Z'' - l_i \sin \phi)^2} \right] \right\} dli \quad (4.17)$$

The frictional heat source under the dead metal zone due to rubbing is modeled as a band heat source moving along the tool-workpiece surface with cutting velocity as in Carslaw

and Jaeger (1959). Since the heat source does not move obliquely it coincides with its imaginary heat source as shown in Fig 4.15.

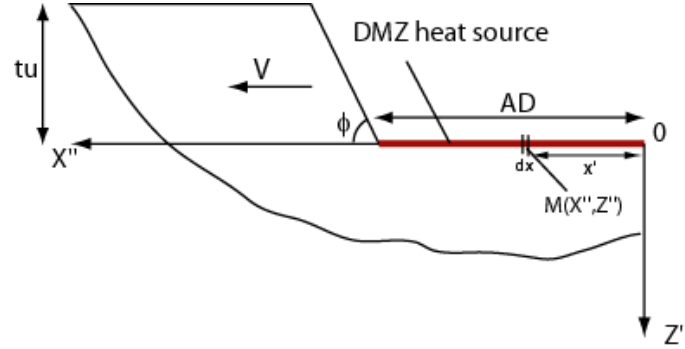


Figure 4.15 Thermal modeling of DMZ heat source on the workpiece side

The temperature rise at any point in the workpiece due to DMZ heat source can be written as;

$$T_{M_{dmz}}(X'', Z'') = \frac{q_{dmz-u}}{\pi\lambda_c} \int_0^{AD} (1-\psi) e^{\frac{(X''-x'')V_{dmz}}{2a_c}} \left[K_0 \left(\frac{V_{dmz}}{2a_c} \sqrt{(X''-x'')^2 + Z''^2} \right) \right] dx'' \quad (4.18)$$

4.5.2 Modeling of Temperature Rise in the Chip Due to Frictional Heat Sources

The effect of frictional heat source along tool-chip interface on the chip side is modeled as a non-uniform moving band heat source and the temperature rise at any point in the chip due to these heat sources can be calculated with Eq. (4.19). The tool rake face and upper surface of the chip are considered to be adiabatic as shown in Fig. 4.16. Since

$$\begin{aligned}
T_{M_{chip-friction}}(X, Z) &= \frac{B_2}{\pi \lambda_c} \int_{l_i=0}^{\overline{CF}} q_{rake}(l_i) e^{-\frac{(X-l_i)V_{ch}}{2a_c}} \left[K_0 \left(R_1 \frac{V_{ch}}{2a_c} \right) + K_0 \left(R_1' \frac{V_{ch}}{2a_c} \right) \right] dl_i \\
R_1 &= \sqrt{(X-l_i)^2 + (Z)^2} \\
R_1' &= \sqrt{(X-l_i)^2 + (2t_c - Z)^2} \\
q_{rake}(l_i) &= \tau_{CF} V_{ch}(l_i)
\end{aligned}
\tag{4.19}$$

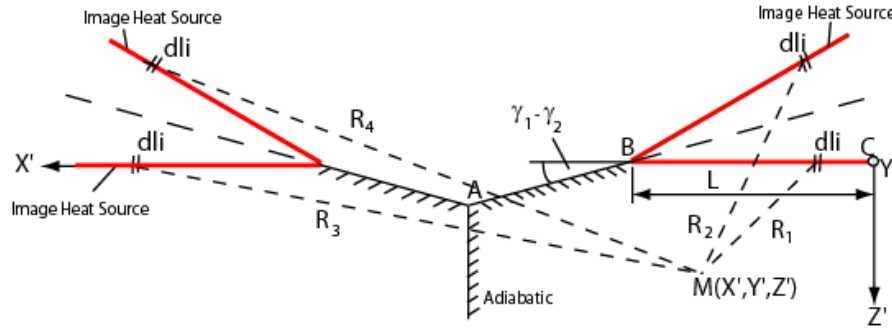
where B_2 denotes the heat partition ratio.

4.5.3 Modeling of Temperature Rise in the Tool Due to Stationary Heat Sources

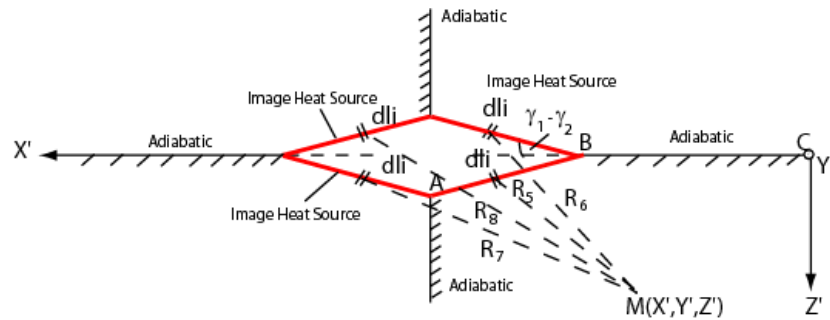
The tool side of the frictional heat source is modeled as a stationary rectangular heat source on the rake face. The image heat sources are added to satisfy adiabatic boundary conditions on the rake, chamfer and clearance faces are shown in Fig. 4. 17. The temperature rise on the tool side can be written with the expressions given in Eq. (4.20)

$$\begin{aligned}
T_{M_{sta-rake}}(X', Y', Z') &= \frac{(1-B_2)}{4\pi\lambda_t} \left[\int_{-w/2}^{w/2} \int_{l_i=0}^{\overline{BC}} q_{rake}(l_i) \left(\frac{1}{R_1} + \frac{1}{R_3} \right) dl_i dy_i + \int_{-w/2}^{w/2} \int_{l_i=0}^{\overline{BC}} q_{rake}(l_i) \left(\frac{1}{R_2} + \frac{1}{R_4} \right) dl_i dy_i \right] \\
T_{M_{sta-cham}}(X', Y', Z') &= \frac{(1-B_1)wq_{dmz=u}}{4\pi\lambda_t} \left[\int_{-w/2}^{w/2} \int_{h_i=0}^{\overline{AB}} \left(\frac{1}{R_5} + \frac{1}{R_7} \right) dh_i dy_i + \int_{-w/2}^{w/2} \int_{h_i=0}^{\overline{AB}} \left(\frac{1}{R_6} + \frac{1}{R_8} \right) dh_i dy_i \right]
\end{aligned}$$

$$\begin{aligned}
R_1 &= \sqrt{(X' - l_i)^2 + Z'^2 + (Y' - y_i)^2} \\
R_3 &= \sqrt{(2\overline{BC} + 2\overline{AB}\cos(\chi) - X' - l_i)^2 + Z'^2 + (Y' - y_i)^2} \\
R_2 &= \sqrt{(X' - (\overline{BC} - l_i)\cos(2\chi) - \overline{BC})^2 + (Z' + (\overline{BC} - l_i)\sin(2\chi))^2 + (Y' - y_i)^2} \\
R_4 &= \sqrt{(\overline{BC} + 2\overline{AB}\cos(\chi) + \overline{BC}\cos(2\chi) - l_i\cos(2\chi) - X')^2 + (Z' + (\overline{BC} - l_i)\sin(2\chi))^2 + (Y' - y_i)^2} \\
R_5 &= \sqrt{(\overline{BC} + h_i\cos(\chi) - X')^2 + (Z' - h_i\sin(\chi))^2 + (Y' - y_i)^2} \\
R_6 &= \sqrt{(\overline{BC} + h_i\cos(\chi) - X')^2 + (Z' + h_i\sin(\chi))^2 + (Y'' - y_i)^2} \\
R_7 &= \sqrt{(\overline{BC} + 2\overline{AB}\cos(\chi) - h_i\cos(\lambda) - X')^2 + (Z' - h_i\sin(\chi))^2 + (Y' - y_i)^2} \\
R_8 &= \sqrt{(\overline{BC} + 2\overline{AB}\cos(\chi) - h_i\cos(\lambda) - X')^2 + (Z' + h_i\sin(\chi))^2 + (Y' - y_i)^2} \quad (4.20) \\
\chi &= \gamma_1 - \gamma_2 \\
q_{dmz} \rightarrow u &= \tau_{AD} V_{dmz}
\end{aligned}$$



(a)



(b)

Figure 4.17 Thermal modeling on the tool side; (a) rake face, (b) chamfer face.

If $\gamma_1 - \gamma_2$ is taken as 90 degrees, Eq. (4.20) yields the tool side of the worn tool thermal model proposed in (Karpas and Ozel 2006b). The heating effect of the frictional heat source under the dead metal zone on the chamfer face of the tool is modeled by multiplying the heat intensity (q_{dmz_u}) with a heat partition factor (ψ) as shown in Eq. (4.18, 4.20). Considering most of the heat generated at this heat source will be transferred into the workpiece, heat partition factor is taken as 0.2 in this study. The heat partition ratios (B_1) and (B_2) can be found numerically by matching the temperature distributions on the chip and the tool side for both rake and chamfer faces. The thermal equilibrium is represented by Eq. (4.21).

$$T_{M_{chip-shear}}(X, 0) + T_{M_{chip-friction}}(X, 0) = T_{M_{sta-cham}}(X, 0) + T_{M_{sta-rake}}(X, 0) + T_{M_{induced}}(X, 0) \quad (4.21)$$

The intensity of the induced heat source, heating effect of shear plane heat source in the tool, can be calculated in a similar fashion as explained in (Karpas and Özel 2006 a, b, c).

4.6. Results and Model Validation

The solution for the analytical thermal model is performed via computer programs developed in Matlab®. The solution has been performed either by solving the temperature equilibrium given in Eq. (4.21) numerically along the tool-chip interface in a discrete fashion or simply by solving the equilibrium of the average temperatures in the

chip and the tool side. Temperature rise in any point in shear zone and workpiece underneath the dead metal zone can also be calculated from Eqs. (4.17) and (4.18). The calculated heat intensities are given in Table 4.1. The temperature distributions and isotherms obtained from these solutions are given below.

Table 4.1. Heat intensities at various locations around cutting zone.

Cutting Speed	Uncut Chip Thickness	q_{shear} (J/mm ² s)	q_{rake} (J/mm ² s)	q_{DMZ_u} (J/mm ² s)
$V=125$ m/min	0.1 mm	2500	884	1680
$V=175$ m/min	0.1 mm	3730	1363	2590

4.6.1 Temperature Distributions along the Tool Chamfer and Rake Face

The temperature distributions along the rake and chamfer face are computed under various cutting conditions. Fig. 4.18 shows the effect of cutting speed on tool-chip interface temperatures for a given uncut chip thickness.

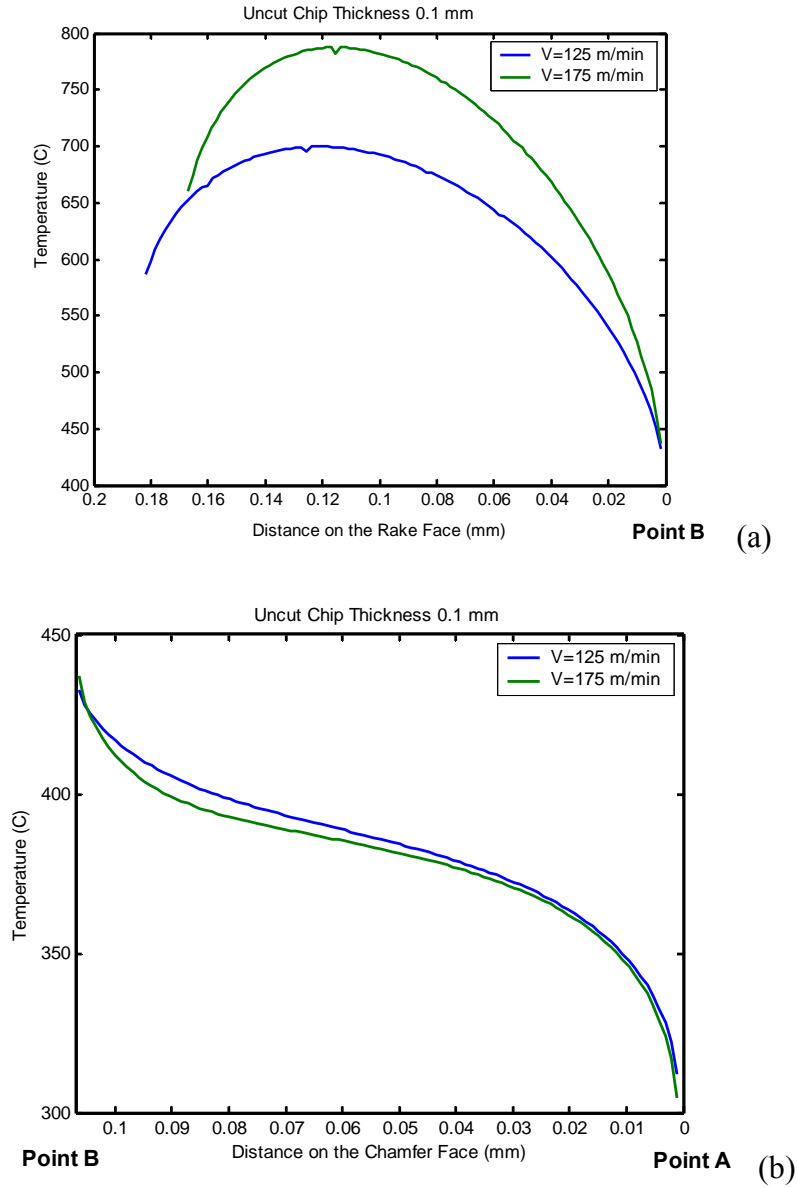


Figure 4.18. Temperature distribution at the (a) rake and (b) chamfer interfaces for $t_u=0.1$ mm

As cutting speed increases, rake face temperatures increase. Temperature distributions along the chamfer face seem to be the same for both cutting speeds. Increasing the uncut chip thickness also increases the temperatures at the rake face. In Fig. 4.19, the effect of increasing uncut chip thickness on the temperature distributions at the interfaces is shown.

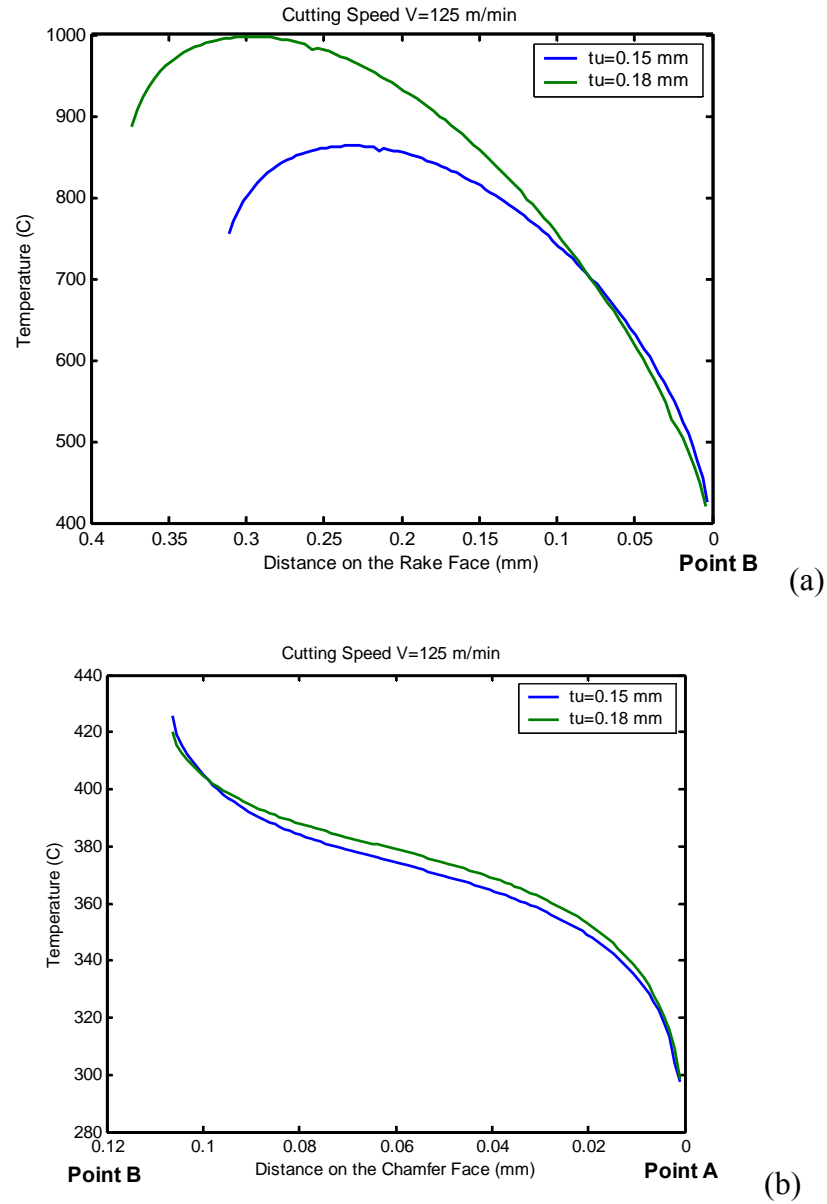


Figure 4.19 Temperature distribution along the (a) rake and (b) chamfer interfaces for $V=125$ m/min and various uncut chip thickness values.

Fig. 4.20 shows the temperature distributions along the rake and chamfer interfaces for $V=175$ m/min and different uncut chip thickness values. In Fig. 4.20a, increasing uncut chip thickness resulted in only a slight increase on the maximum temperature at the rake face however slightly lower temperatures on the chamfer face.

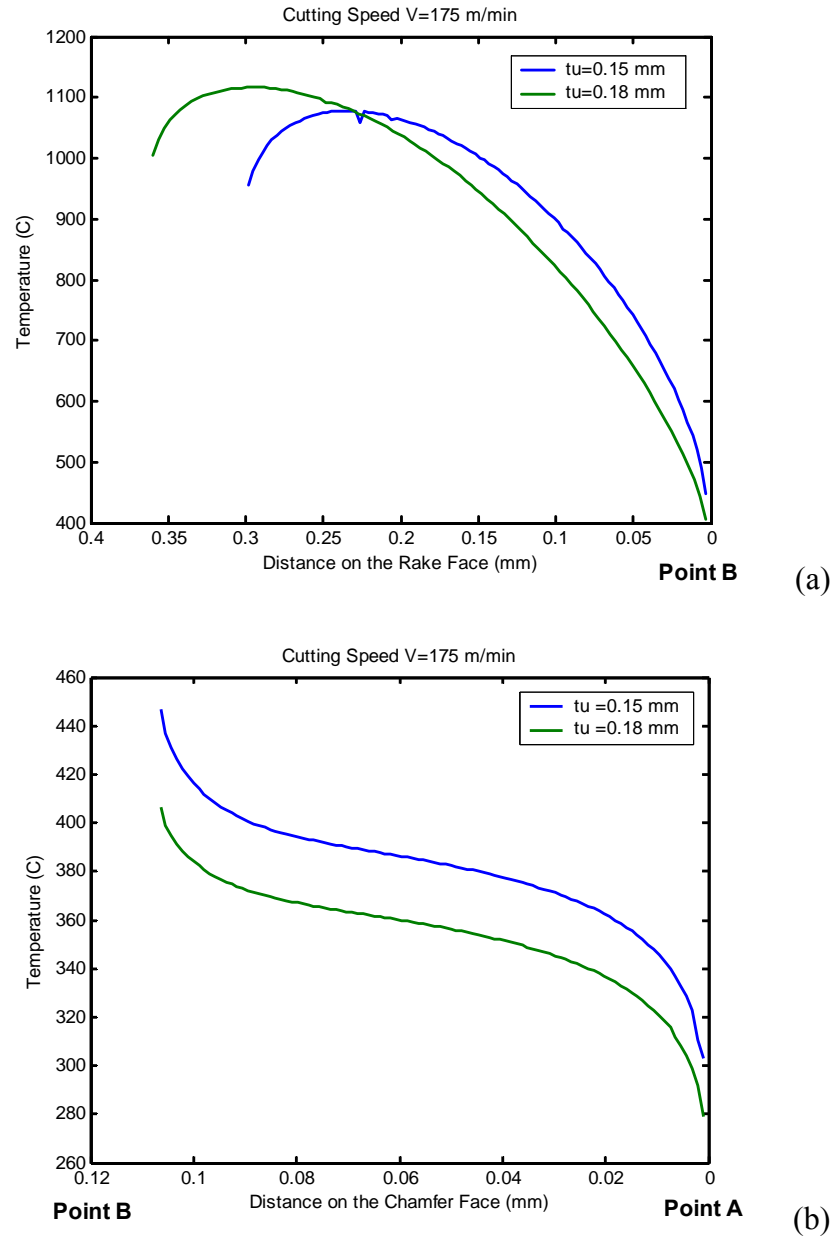


Figure 4.20 Temperature distribution along the (a) rake and (b) chamfer interfaces for $V=175$ m/min and various uncut chip thickness values

It must be noted that when cutting speed increased, lower temperature rises take place at the chamfered face. In order to explain why lower temperatures at chamfer face are

obtained for increasing uncut chip thickness values at higher cutting speeds, the non-uniform heat partitions along the rake face are calculated as given in Fig. 4.21.

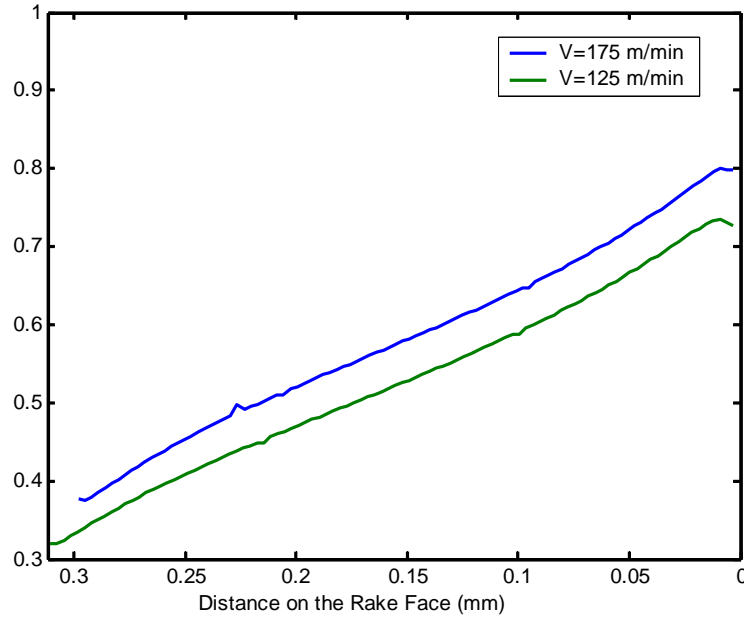


Figure 4.21 Heat Partition along Rake Face for $t_u=0.15$ mm.

It is clear from Fig. 4.21, the local heat partition along the rake face increases. It indicates a steady temperature rise in the chip as the chip travels along the rake face and leaves the contact at a higher temperature. Most of the heat energy is carried away within the chips when cutting speed increases, which is the original premise of high speed cutting. Hence, this observation is a self-evident validation of the proposed thermal model and its solution.

4.6.2 Comparison of Calculated Temperature Fields with FEA

In order to compare the temperature distributions computed using the analytical thermal model for machining with chamfered tools, finite element (FE) simulations were performed under the same cutting conditions using commercial software DEFORM-2D®. Identified rake face friction factors through slip-line field analysis are used in these simulations. Workpiece is modeled as rigid, perfectly plastic material. Johnson-Cook (1983) material model parameters for AISI 4340 steel are adapted from Gray et al. (1994). In their study, Gray et al. investigated the JC parameters for various materials by using split Hopkinson bar test and calculated most suitable JC parameters for AISI 4340 steel as $A=1504$ MPa, $B=569$ MPa, $n=0.22$, $C=0.003$, $m=0.9$. In order to allow serrated chip formation in the finite element simulations, Cockcroft-Latham (1966) damage criteria is utilized. By utilizing experimental chip shapes, the critical damage value was selected with trial and error to be around 290 MPa for annealed AISI 4340 steel. Simulated chip thicknesses are found to be in agreement with the measured values as shown in Fig. 4. 22.

A stagnant metal zone can be seen in FE simulations, when velocity field is plotted as shown in Fig. 4.23. In this figure, the triangular area adjacent to chamfer face with a very low velocity value may indicate the possible dead metal zone formation. The temperature fields in the tool are calculated for two different cutting conditions and compared with FE simulations as shown in Fig. 4.24.

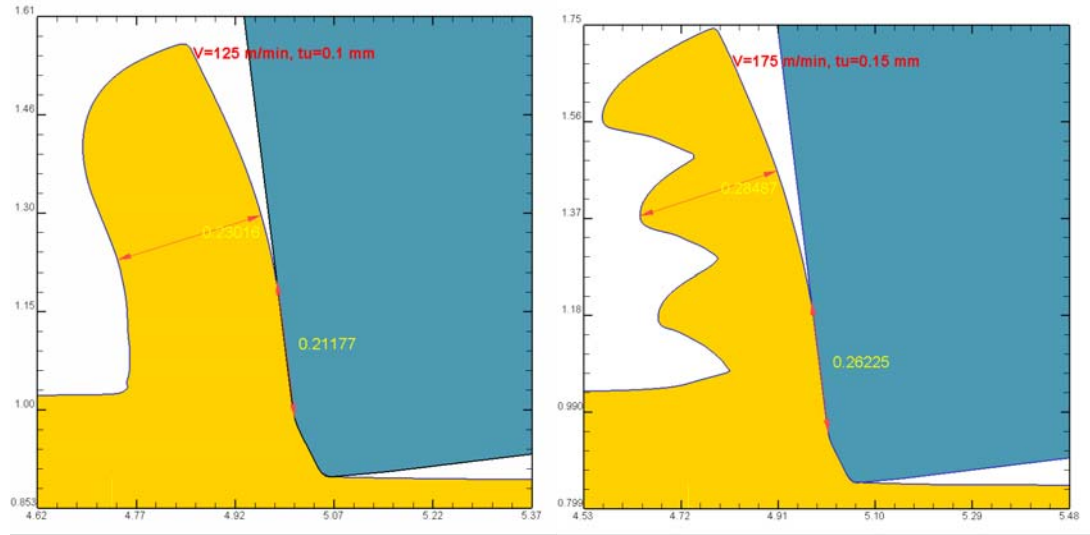


Figure 4.22. Simulated chip formation for the cutting conditions of $V=125$ m/min, $t_u=0.1$ mm and $V=175$ m/min, $t_u=0.15$ mm.

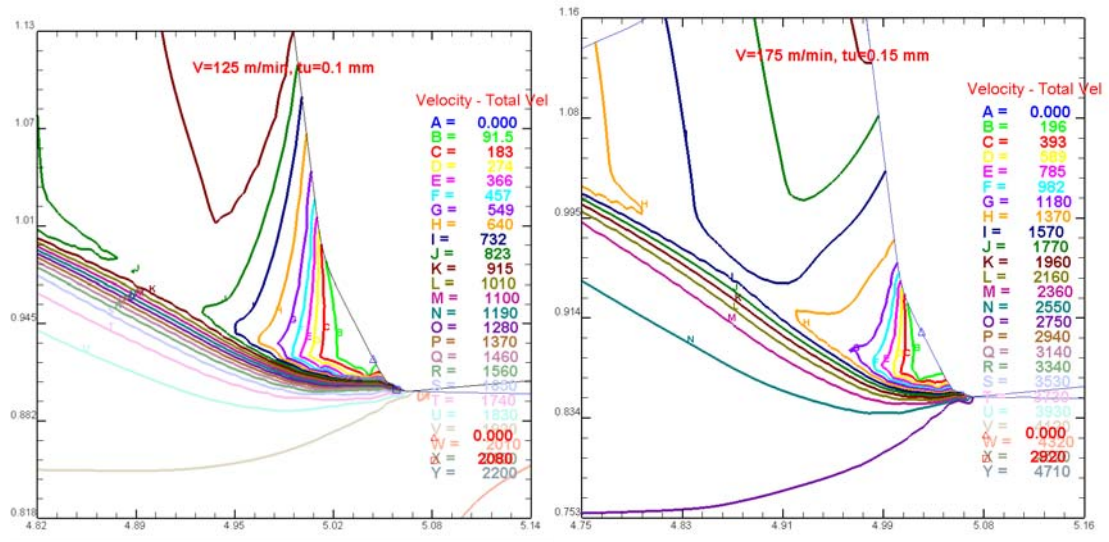
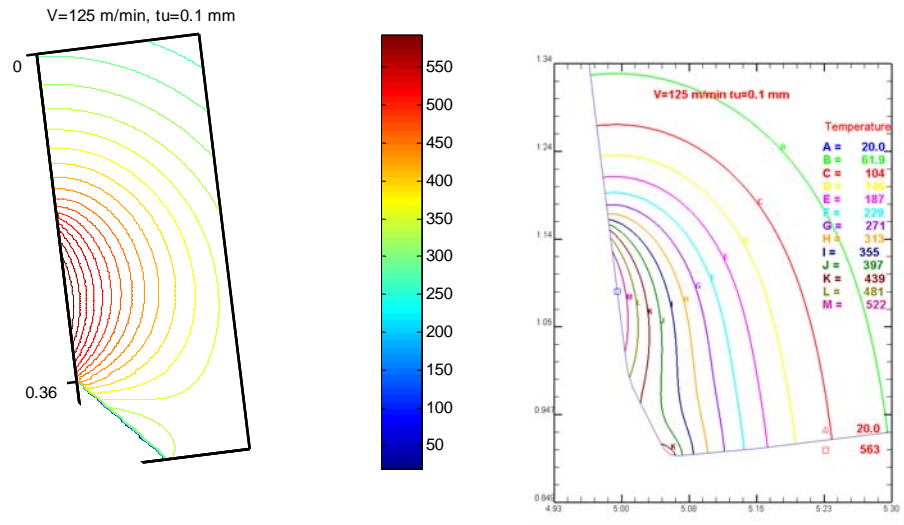


Figure 4.23. Velocity field for the cutting conditions of $V=125$ m/min, $t_u=0.1$ mm and $V=175$ m/min, $t_u=0.15$ mm.

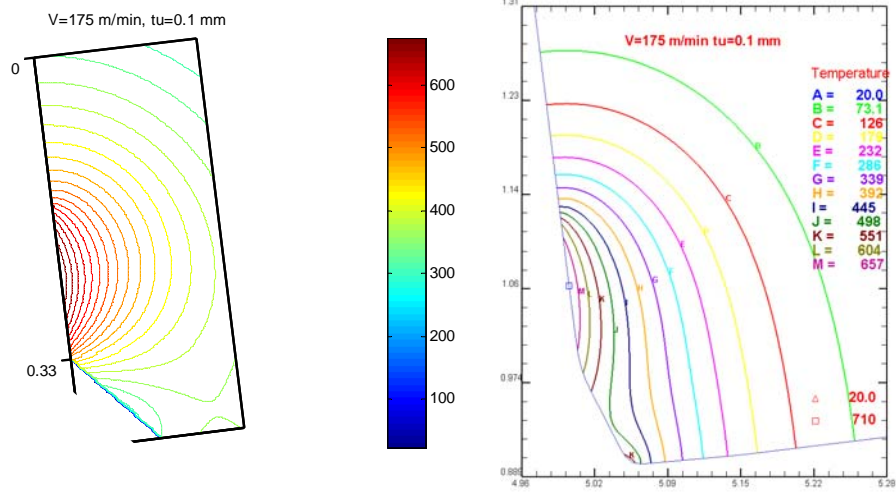
The temperature fields in the shear zone and in the workpiece are also calculated for six different cutting conditions as given in Fig. 4.25-4.27. These temperature fields reveal the temperature rise effects of the deformation zones that workpiece undergoes in the primary shear zone and underneath the DMZ. According to these isotherms, the maximum temperature location in the workpiece is seen to be at the tip of the chamfer face in both analytical thermal calculations and FE simulations. Temperature isotherms calculated from both approaches are also found to be in close agreements.

In machining at the low cutting speed, temperatures diffused deeper into the workpiece than machining at the higher cutting speed as it can be seen from Figs. 4.25-4.27. Higher temperature gradients should be expected in the workpiece for machining at higher cutting speeds.

In analytical thermal modeling approach, heat intensity at the primary shear zone is mainly calculated from the work material shear flow stress whereas frictional heat source under DMZ is calculated both from shear flow stress and friction factor. Therefore, additional temperature rise caused by the frictional heat source under DMZ will reduce shear flow stress. In conjunction with decreasing friction factor under DMZ, lower heat intensities and lower temperatures may be generated as a result in certain cutting conditions. For instance at the cutting speed of $V=175$ m/min, as uncut chip thickness increases average temperature under DMZ has decreased as shown in Fig. 4.28. However, average temperature under DMZ for the cutting speed of $V=125$ m/min has been found increasing with increasing uncut chip thickness.

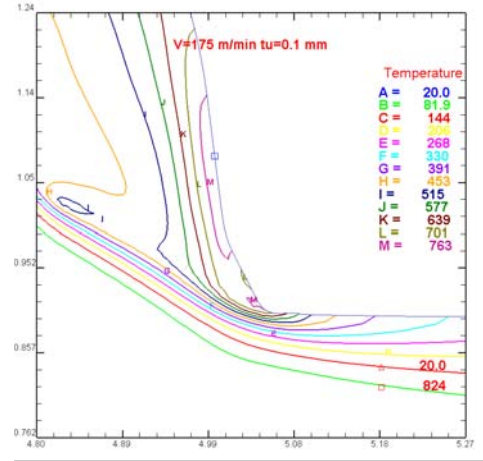
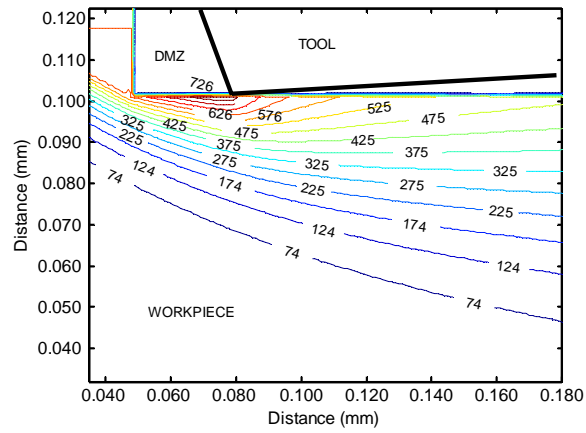


(a)

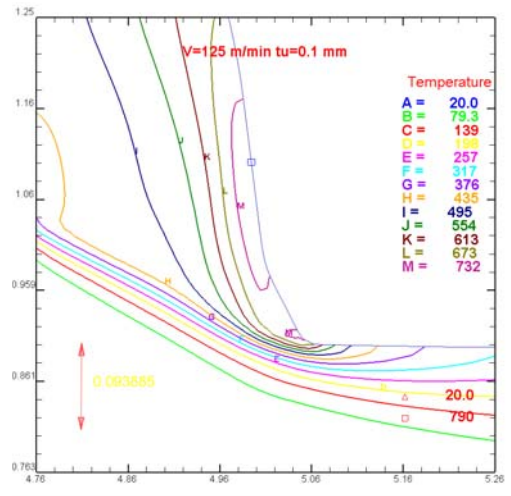
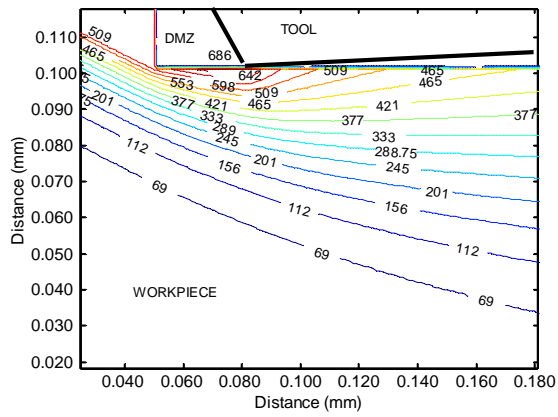


(b)

Figure 4.24. Isotherms obtained from analytical method for (a) $V=125$ m/min, $t_u=0.1$ mm, and (b) $V=175$ m/min, $t_u=0.1$ mm. (All temperatures are in °C)



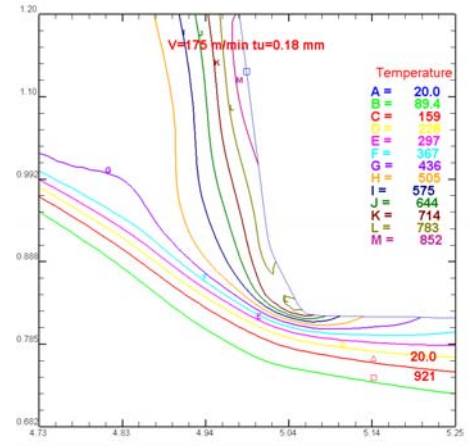
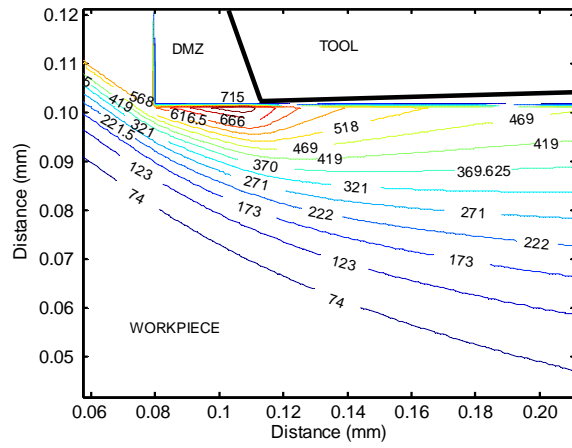
(a)



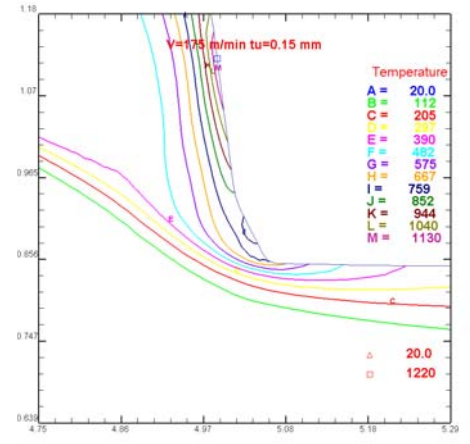
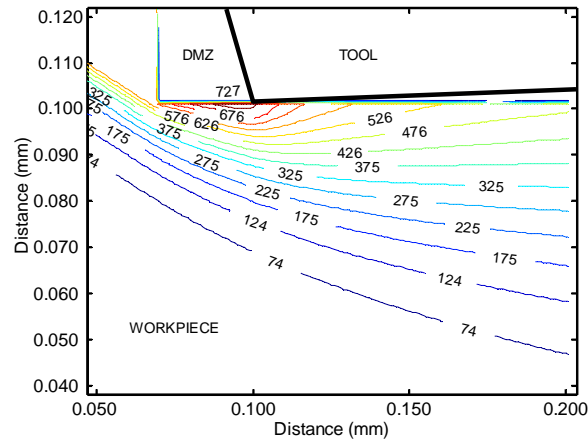
(b)

Figure 4.25. Temperature distributions in the workpiece (a) $V=175$ m/min, $t_u=0.1$ mm (b)

$V=125$ m/min, $t_u=0.1$ mm. (All temperatures are in $^{\circ}\text{C}$)

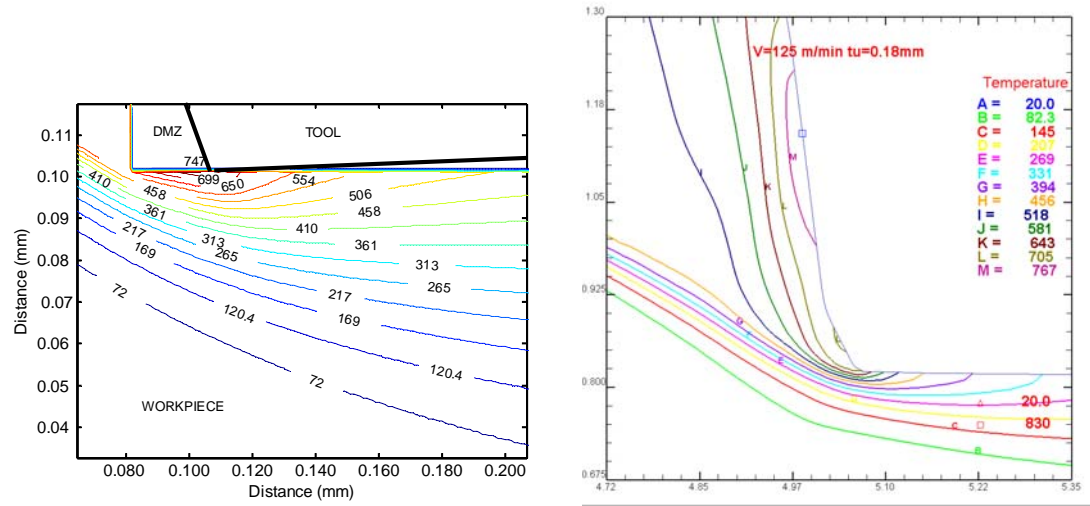


(a)

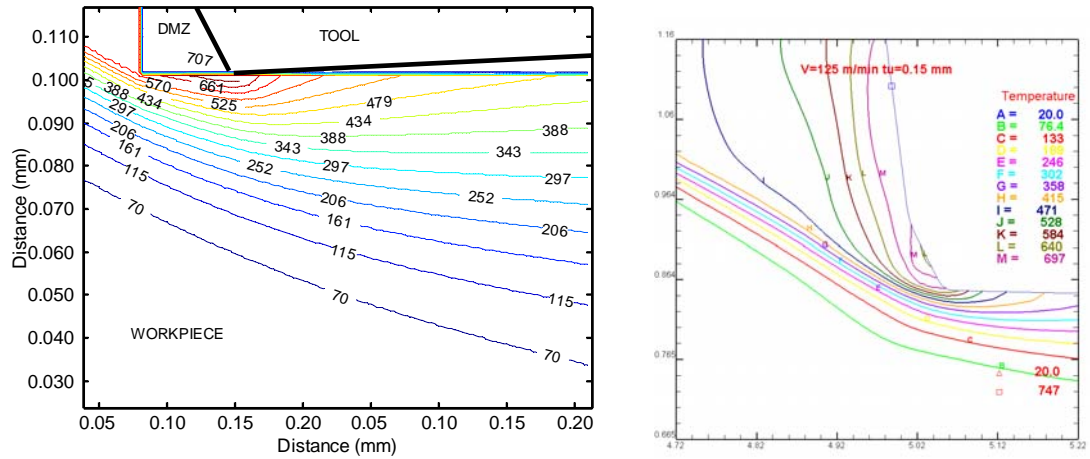


(b)

Figure 4.26. Temperature distributions in the workpiece (a) $V=175$ m/min, $t_u=0.18$ mm and (b) $V=175$ m/min, $t_u=0.15$ mm. (All temperatures are in $^{\circ}\text{C}$)



(a)



(b)

Figure 4.27. Temperature distributions in the workpiece (a) $V=125$ m/min, $t_u=0.18$ mm and (b) $V=125$ m/min, $t_u=0.15$ mm. (All temperatures are in °C)

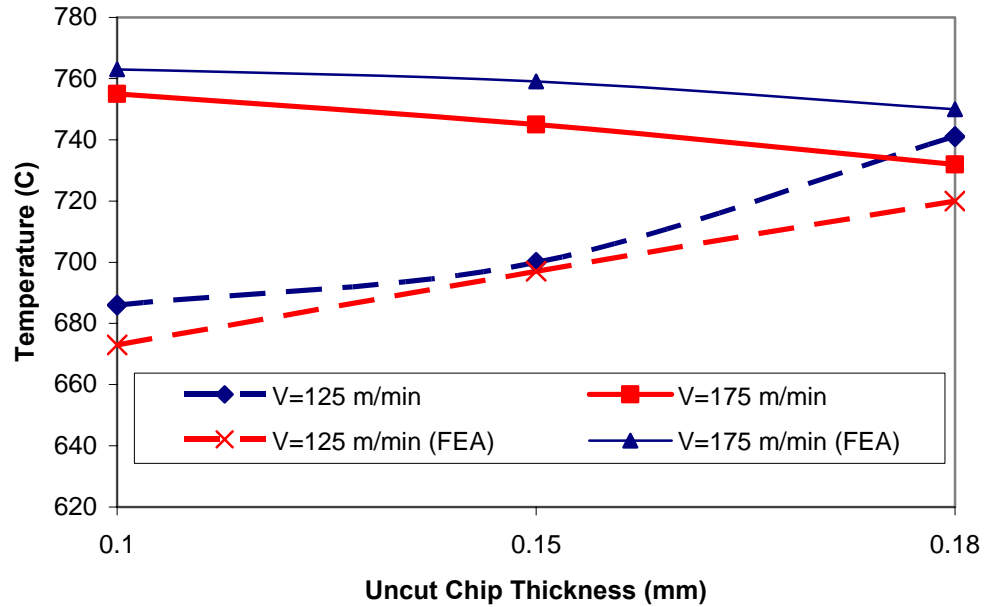


Figure 4.28. Maximum temperatures under the dead metal zone T_{AD} .

4.7 Conclusions

In this chapter, mechanics of high-speed machining with chamfered tools is investigated. A slip-line field model is presented to explain material flow in the cutting zone during orthogonal cutting with chamfered tools. The model considers that a dead metal zone is formed adjacent to the chamfer face of the tool edge during cutting. The slip-line angles and friction factors are identified by using experimental orthogonal cutting force data. An analytical thermal model for orthogonal cutting with chamfered tools is also introduced. The heat sources considered in this model are: (a) primary heat source due to shearing, (b) frictional heat source at the tool-chip interface and (c) frictional heat source under DMZ. Intensities of these heat sources are calculated by

utilizing slip-line field analysis. The temperature rises in the cutting tool and workpiece are computed and compared with finite element simulations. In addition, influence of cutting conditions i.e cutting speed and uncut chip thickness on the temperature distributions along the chamfer and rake faces are explored.

The results indicate that a combined slip-line field analysis and analytical thermal modeling approach can be used in studying the influence of dead metal zone on the mechanics of high-speed cutting. According to above given results, it is seen that dead metal zone primarily affects the temperature distributions around the tip of the tool and eases the material flow due to thermal softening with increased temperatures. Since the size of the dead metal zone is mainly determined by chamfer angle, rake angle and chamfer height, the selection of correct chamfered tool design for a given cutting process is important. Increasing chamfer angle will result in increased thrust forces and higher temperatures around DMZ which may reach to a level to damage workpiece machined surface and high tool tip temperatures. These models can be utilized to design and optimize chamfered tools for high-speed machining of steels.

CHAPTER 5

MECHANICS OF HIGH SPEED CUTTING WITH CURVILINEAR EDGE TOOLS

5.1 Introduction

Emerging machining techniques such as hard turning, hard milling and micro mechanical machining where the uncut chip thickness and the tool edge dimension are in the same order of magnitude require cutting edges which can withstand high mechanical and thermal stresses, hence wear, for a prolonged machining time. It is known that sharp tools are not suitable for such machining operations therefore, tool manufacturers introduced different types of tool edge preparations such as chamfered, double chamfered, chamfer + hone, honed, and waterfall hone (oval-like) edge designs. The influence of cutting edge geometry on machining performance has been a research topic in metal cutting for a long time. It has been reported by many researchers that design of the cutting edge design affects the outcome of the machining processes in terms of cutting forces, surface integrity and tool life. Chamfered tools are usually used in roughing and interrupted turning. The stable trapped material (dead metal zone or cap) in front of the chamfered cutting edge increases the strength of the tool tip at the cost of increased cutting forces. Honed tools are employed in finish turning operations because application of hone increases the impact resistance. Waterfall hone edge geometry combines the appropriate characteristics of chamfered and honed tools such as increased

tool tip strength and increased rake angle due to its oval-like geometry eases the flow of work material in front of the tool.

The proper selection of edge preparation (edge radius, chamfer angle and height) can be possible once the behavior of material flow around the cutting edge is well understood. The effect of edge preparation on the mechanics of cutting has been investigated by many researchers by using various methods such as analytical (Albrecht, (1960); Zhang et al., (1991); Endres et al., (1995); Waldorf et al., (1998); Manjunathaiah et al., (2000); Ren, and Altintas, (2000); Fang, (2003)), computational (Kim et al., (1997); Movaheddy et al., (2002); Özel, (2003); Yen et al., (2004); Chen et al., (2006)) and experimental (Abdel-Moneim et al., (1974); Jacobson et al., (1988); Thiele et al., (1999); Shimmel et al., (2002)) methods. The initial motivation of studying the effects of edge preparation was to understand the ploughing phenomena (Albrecht, (1960); Palmer et al., (1963); Abdel-Moneim et al., (1974)). A tertiary shear zone at the tool-workpiece interface was believed to be responsible for additional cutting forces. In an early study, Mayer and Stauffer (1973) compared the performance of the honed and chamfer tool inserts with sharp tools during non-interrupted machining of AISI 1045 steel. They found that the increasing hone radius and chamfer width and angle results in increased forces and decreased tool life.

In order to model in the mechanics of cutting in that zone by using analytical techniques, two major approaches have been proposed. The first approach is based on the existence of a stagnation point on the tool round edge where the material flow is diverted upwards and downwards (Manjunathaiah et al., (2000); Fang, (2003)). The second

approach considers a stable build up of material in front of the tool edge like a dead metal zone which diverts material flow (Waldorf et al., (1998)). Waldorf (1996) compared these two approaches for AL 6061-T6 aluminum and AISI 4340 steel, and concluded that the model with stable build up describes experimental results better than the other hypothesis. The stable trapped work material zone formation was observed by Kountanya et al. (2001) for honed tools. As for stagnation point based approaches, Manjunathaiah et al. (2000) utilized equivalent chamfer geometry for the honed tool by identifying the stagnation point on the tool. Fang (2003) presented a detailed slip-line field analysis for rounded-edge tools based on stagnation point assumption. In this study, dead metal zone assumption is adopted due to the fact that negative rake tools are used. All the work mentioned above, especially the ones based on stagnation point assumption, considered cutting tools with positive rake angle. In this study, a stagnant metal zone is assumed in front of the cutting tool. Recently, Ranganath et al. (2007) investigated the effects of edge radius for machining of cast iron. Honed cutting tools with various edge radii and rake angles were tested. Proposed mechanistic model successfully captured the effect of hone radius on cutting forces during cutting with positive rake angle tools, however increased prediction errors were observed at zero and negative rake angle cutting conditions.

In order to model extremely complex material flow around honed tools, especially in finish machining conditions, finite element modeling (FEM) techniques are very popular. In FEM models, workpiece material properties and the edge geometry of the cutting tool can be defined and process variables such as forces, temperature distributions, stresses, etc. can be obtained. Kim et al. (1999) studied the effects of honed

edge preparation on the forces and temperatures in orthogonal cutting by using finite element analysis and showed that tool edge radius influences field variables such as temperature distributions and strain rate. They observed increasing cutting forces and temperatures, decreasing maximum effective strain rate with increasing edge radius. In another finite element simulation based study, Yen et al. (2004) observed the effect of various tool edge geometries on the field variables. They also observed increasing average rake face temperature in the tool, increasing effective strain distribution in the chip and workpiece with increasing edge radius. Recently Chen et. al. (2006) investigated the performance of honed and chamfered PCBN cutting tools for hard turning of AISI 52100 steel. They concluded that the optimum selection of edge preparation depends on machining parameters.

It must also be noted that the correct definition of friction conditions are crucial in order to obtain meaningful results from the finite element models. Sartkulvanich and Altan (2005) performed a sensitivity analysis and showed the effect of friction and flow stress models on the outputs of 2D cutting finite element simulations. Özel (2006) investigated tool-chip interfacial frictional models by using FEM and concluded that when frictional properties and workpiece material behavior are properly modeled, FEM models can offer accurate and viable predictions.

The goal of this chapter is to understand the mechanics of cutting edge for various rounded edge designs by utilizing slip-line analysis. Similar to previous chapter, orthogonal cutting tests will be performed in order to identify slip-line angles and friction

factors. Obtained friction factor information will be used in finite element simulations. Honed and waterfall hone type of edge preparations will be compared in terms of measured cutting forces, and simulated cutting temperatures, strain and stress distributions. The findings will constitute a base for edge design in 3D cutting. The geometrical comparison of honed, and waterfall hone edge preparation is given in Fig. 5.1. The FESEM pictures of honed and waterfall edge preparations are shown in Fig 5.2. The ratio of the top of the edge to its side is usually taken as 2:1.

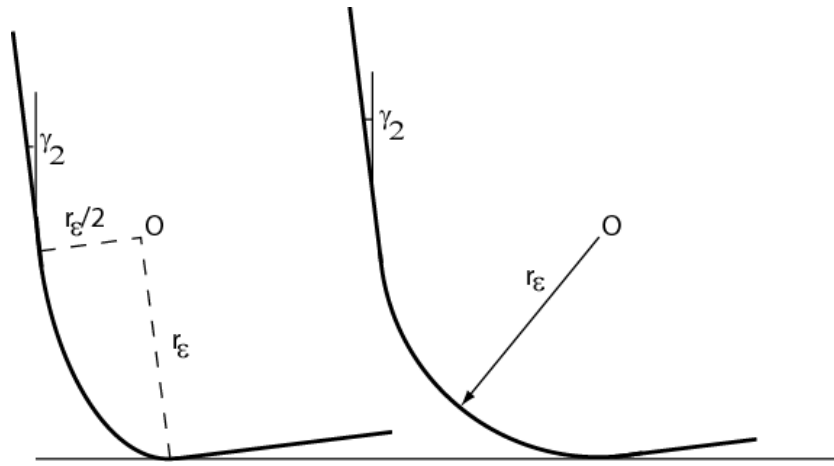


Figure 5.1. Waterfall hone ($r_{\epsilon}/2$ - r_{ϵ}) and honed (r_{ϵ}) type of edge preparations.

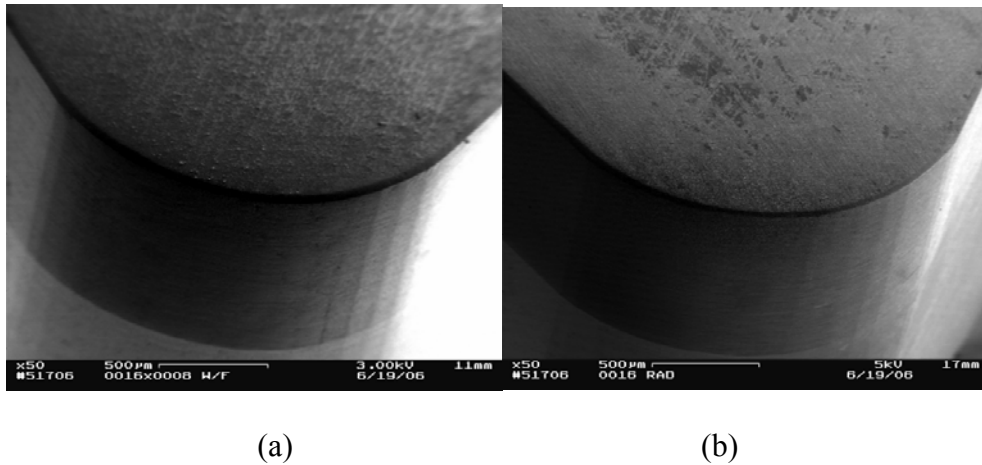


Figure 5.2. SEM images of (a) waterfall hone and (b) honed edge preparations.

Figure 5.3. Slip-line model for machining with (a) honed and (b) waterfall hone type of edge preparations.

The geometry of dead metal zone (DMZ) will be calculated according to honed (r_ϵ) or waterfall hone ($r_\epsilon - r_\epsilon/2$) radii instead of chamfer angle and chamfer height. The rest of the formulation will be identical to chamfered tool slip-line field formulation. As in chamfered tool slip-line model, the chip is assumed to be straight. The shear angle is represented with (ϕ), the angle formed by the bottom boundary of the DMZ with the cutting direction is DMZ angle (α), cut chip thickness (t_c), tool-chip contact length on the rake face (FC), tool-chip friction at the rake face ($m_3 = \tau_{BC} / k$), and friction factor on the front boundary of DMZ ($m_2 = \tau_{DF} / k$) are calculated according to given uncut chip thickness (t_u), friction factor under DMZ on AD ($m_1 = \tau_{AD} / k$), hydrostatic pressure at point E (P_E) and tool geometry (hone radius r_ϵ or waterfall $r_\epsilon - r_\epsilon/2$, negative rake angle γ_2).

For honed edge preparation, the distances AD and DF can be expressed as:

$$AD = \frac{r_\epsilon [\cos(\alpha) - \sin(\gamma_2)\cos(\alpha) - \sin(\alpha)\cos(\gamma_2)]}{\cos(\alpha + \gamma_2)}$$

$$DF = \frac{r_\epsilon (1 - \sin \gamma_2)}{\cos(\alpha + \gamma_2)}$$
(5.1)

For waterfall hone edge preparation, the distances AD and DF can be expressed as:

$$AD = \frac{(r_\epsilon / 2)}{\cos(\alpha + \gamma_2)}$$

$$DF = r_\epsilon [2 - \tan(\alpha + \gamma_2)]$$
(5.2)

It must be noted that, absolute value of negative rake angle is used in above given expressions. By using the same identification procedure as explained in Chapter 4,

friction factors on tool-chip interface, slip-line angle (θ), friction factor on the rake face (m_l) and DMZ angle (α) were identified

5.3 Experimental Plan

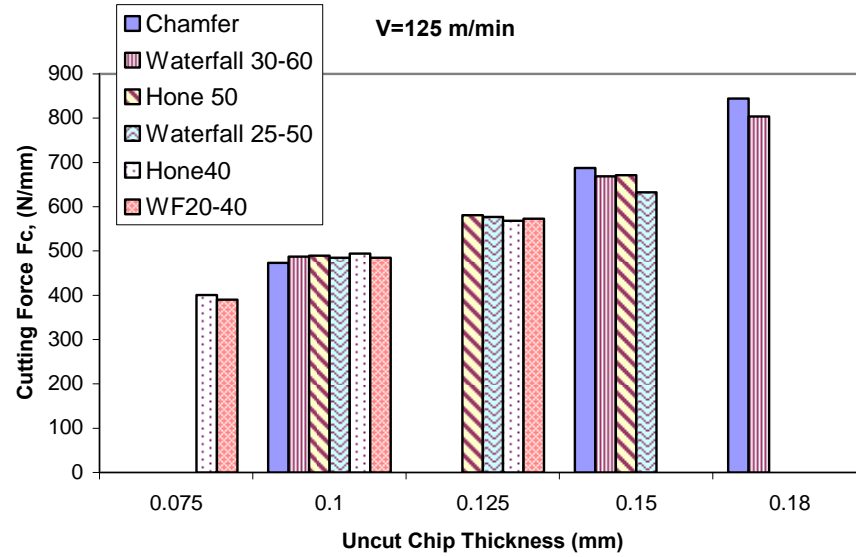
Orthogonal turning of thin webs (2.5-2.8 mm) were performed on AISI 4340 steel using CBN cutting tool inserts (TNG-423) with various honed and waterfall hone edge designs in a CNC turning center. The cutting conditions are summarized in Table 5.1. Forces were measured with a Kistler ® turret type force dynamometer, a PC-based DAQ system and Kistler® DynoWare software.

Table 5.1 Cutting conditions used in experiments and simulations (marked by **X**)

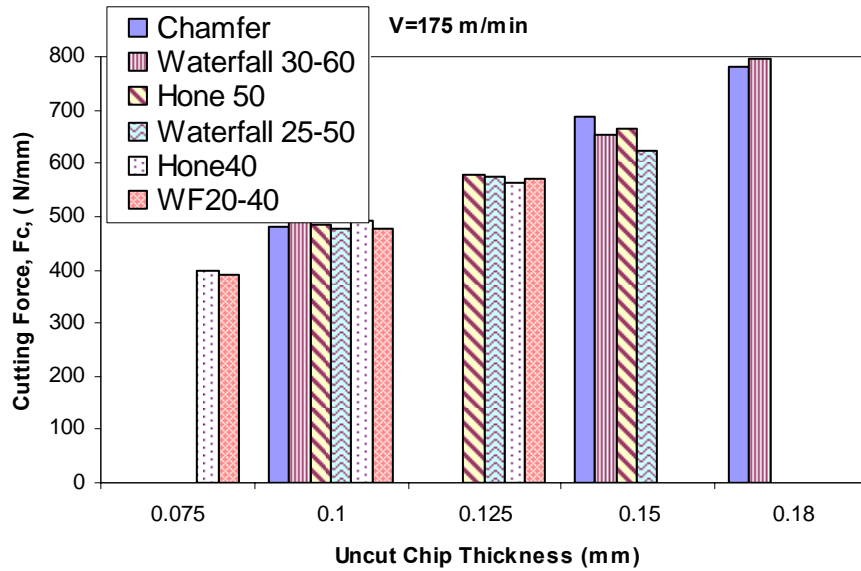
Uncut Chip Thickness(mm)	Tool Type				
	Honed $r_\epsilon=40\ \mu\text{m}$	Honed $r_\epsilon=50\ \mu\text{m}$	Waterfall 20-40 μm	Waterfall 25-50 μm	Waterfall 30-60 μm
0.075					
0.1	X	X	X	X	X
0.125	X				
0.15	X	X	X	X	X
0.18					

In cutting tests, two different cutting speeds are selected as 125 m/min and 175 m/min. Experiments are replicated two times. Uncut chip thickness values used in the experiments are selected in accordance with edge radius of the cutting tool. The thrust

and cutting force measurements are shown in Fig. 5.4. Orthogonal cutting forces obtained from chamfered tools are also included in the figures.



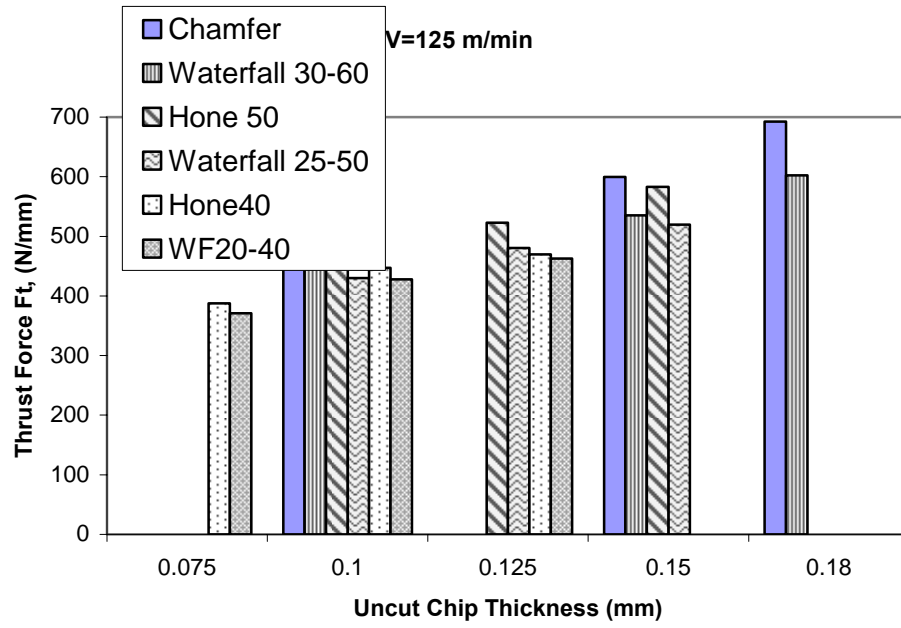
(a)



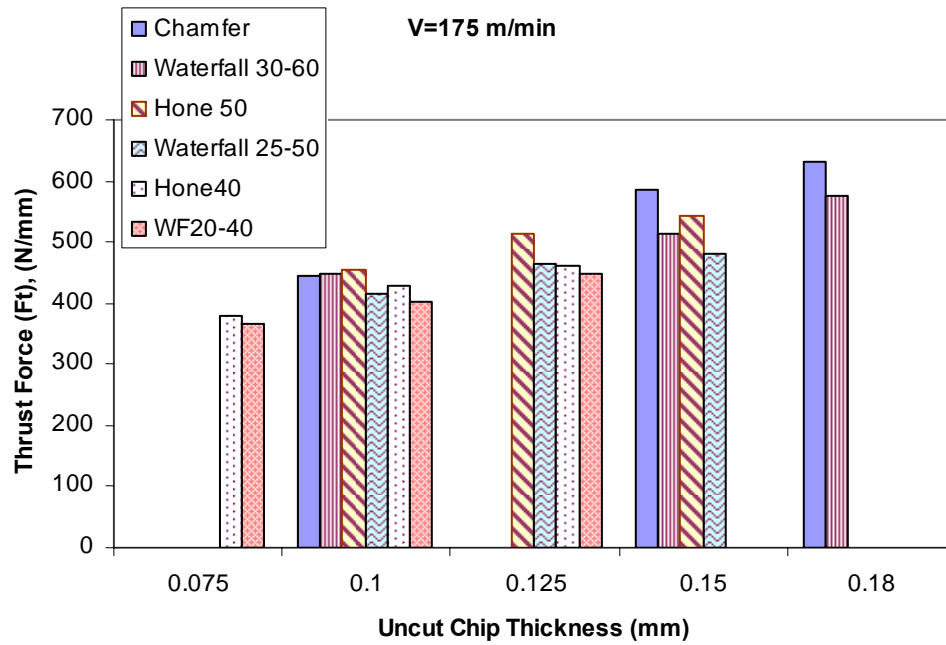
(b)

Figure 5.4(a, b) Measured cutting (F_c) and thrust forces (F_t):

(a) $V=125$ m/min F_c , (b) $V=175$ m/min F_c



(c)

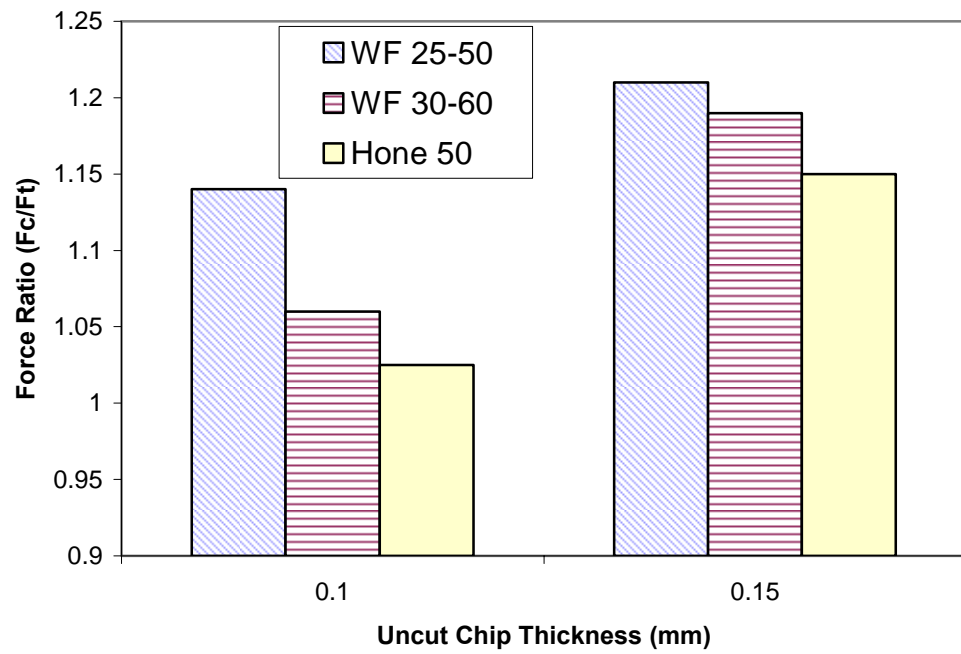


(d)

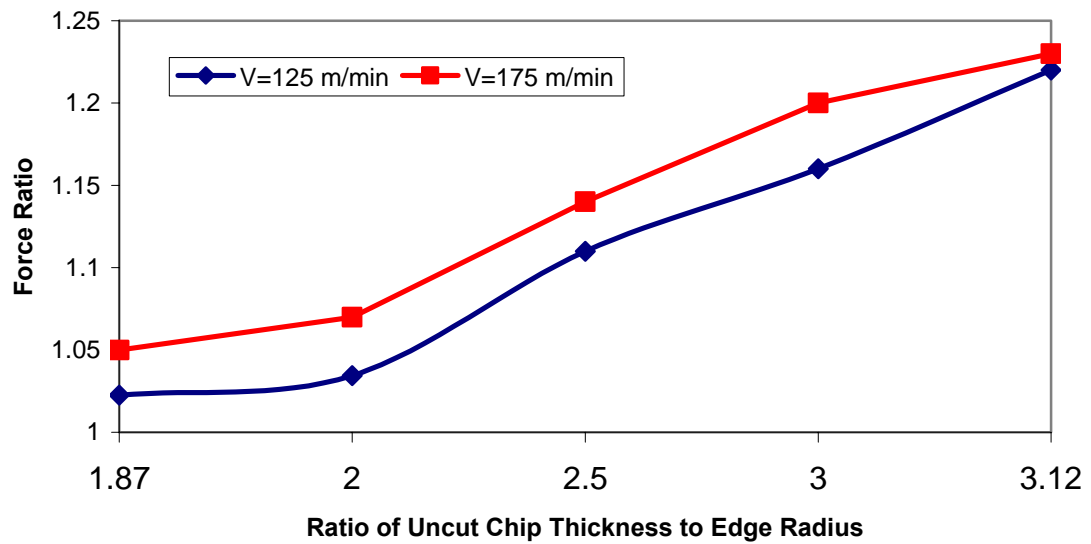
Figure 5.4(c, d) Measured cutting (F_c) and thrust forces (F_t):(c) $V=125$ m/min F_t , (d) $V=175$ m/min F_t .

The results have revealed the relationship between edge radius and cutting forces. The effect of edge preparation on cutting forces, especially on thrust forces, becomes more noticeable when uncut chip thickness is increased. In terms of measured cutting forces, waterfall hone tools yielded lower than honed and chamfered tools. Waterfall hone with 20-40 μm edge dimension yielded the lowest thrust forces. It is clear from the experimental results that as edge radius increases, thrust forces increase.

Increasing cutting speed resulted in slightly decreasing cutting forces. Fig 5.5(a) represents the variation of force ratio with respect to uncut chip thickness for honed and waterfall hone edge preparations with 50 μm , 25-50, and 30-60 μm edge radius, respectively. Due to lower thrust force measurements, waterfall hone tools have greater force ratios under the same cutting conditions. Increasing cutting speed increased the force ratio because of further decreasing thrust forces. In order to investigate the relationship between the uncut chip thickness and the edge radius, the force ratio (F_c/F_t) is plotted against the ratio of uncut chip thickness to edge radius in Fig. 5.5 (b) for two different cutting speeds. According to these results, as the ratio of uncut chip thickness to edge radius decreases, force ratio (F_c/F_t) becomes closer to unity.



(a)



(b)

Fig 5.5 (a) Comparison of force ratio for waterfall and honed edge preparations (b) Force ratio (F_c/F_t) versus ratio of uncut chip thickness to edge radius

By using the same friction factor identification procedure as explained in Chapter 4, rake face friction factor (m_3), dead metal zone angle (α), dead metal zone friction factor (m_1), and slip-line angle (θ) can be determined. Fig 5.6 shows the relationship between the ratios of uncut chip thickness to edge radius to the rake face friction factors for different cutting speeds. According to these results, as the ratio of uncut chip thickness to edge radius increases, friction factor on the rake face decreases. As cutting speed increases, rake face friction factor decreases.

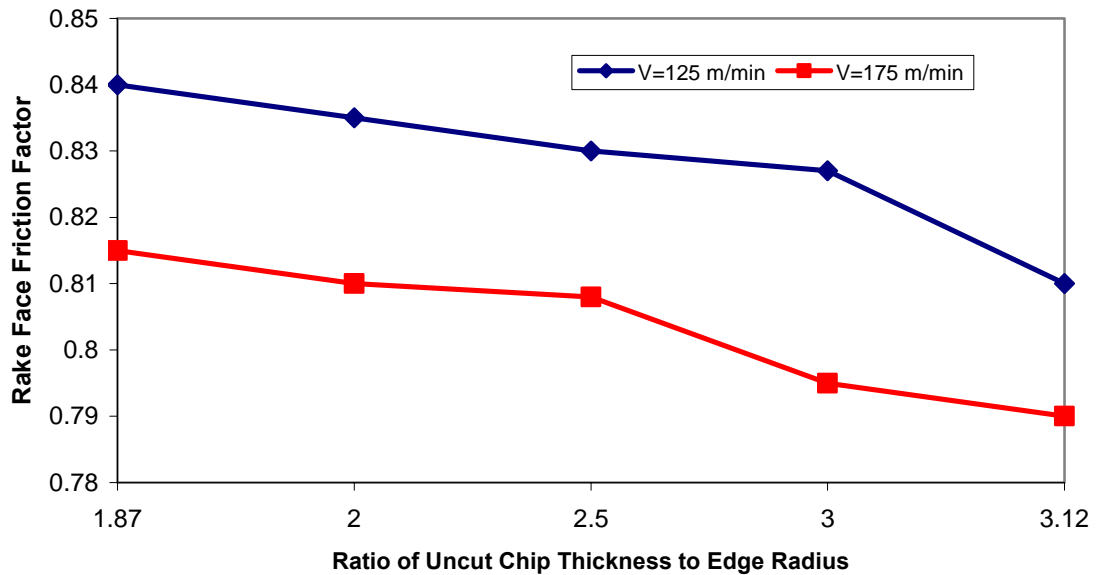


Figure 5.6 Variation of rake face friction factors with respect to ratio of uncut chip thickness to edge radius.

Table 5.2 and 5.3 shows the identified slip-line angles for all cutting conditions. These results reveal that, waterfall hone tools exhibited higher rake face friction factors

(m_3) than honed tools. Similar friction factors on the front boundary of the dead metal zone (m_2) were obtained.

Table 5.2 Comparison of identified slip-line angles of honed and waterfall hone edge preparations for $V=125$ m/min

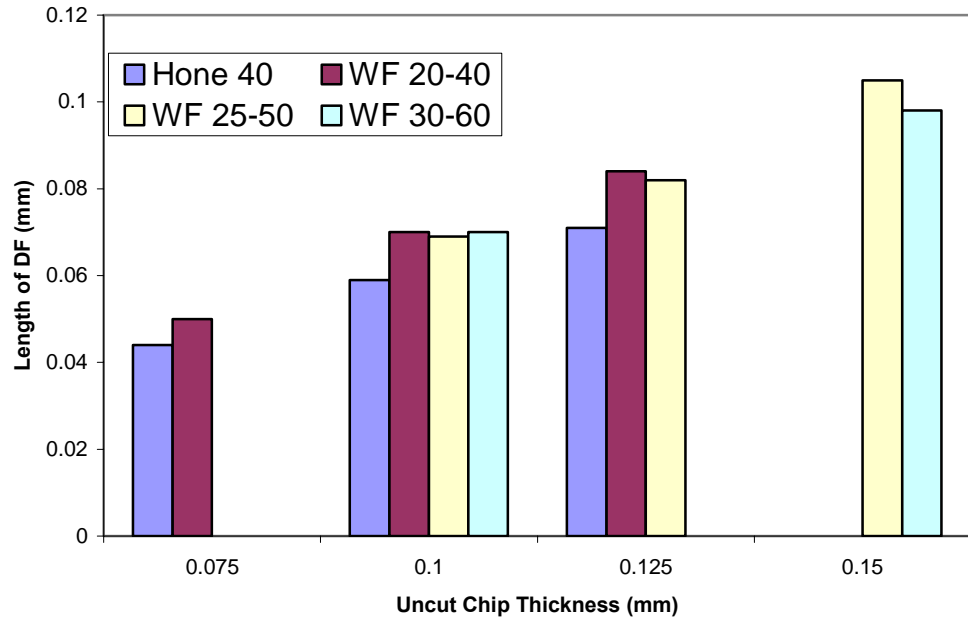
		t_u (mm)	α	θ	m_1	m_2	m_3	t_c
V=125 m/min	Hone 40	0.075	5.73	13.51	0.525	0.68	0.836	0.165
		0.1	5.4	13.49	0.573	0.68	0.834	0.22
		0.125	5.17	13.11	0.581	0.66	0.813	0.265
	Hone 50	0.1	6.07	13.83	0.423	0.688	0.84	0.22
		0.125	5.68	13.51	0.49	0.675	0.829	0.27
		0.15	5.84	13.7	0.397	0.671	0.827	0.32
	WF 20-40	0.075	4.65	16.11	0.32	0.71	0.88	0.165
		0.1	4.68	15.54	0.448	0.7	0.87	0.22
		0.125	4.43	15.36	0.4	0.69	0.85	0.265
	WF 25-50	0.1	4.316	15.21	0.57	0.7	0.86	0.22
		0.125	3.85	15.2	0.6	0.69	0.85	0.26
		0.15	3.52	14.73	0.7	0.68	0.84	0.305
	WF 30-60	0.1	4.674	15.51	0.455	0.7	0.87	0.22
		0.15	3.55	14.71	0.635	0.668	0.835	0.31
		0.18	2.92	14.22	0.745	0.654	0.82	0.365

Table 5.3 Comparison of identified slip-line angles of honed and waterfall hone edge preparations for $V=175$ m/min.

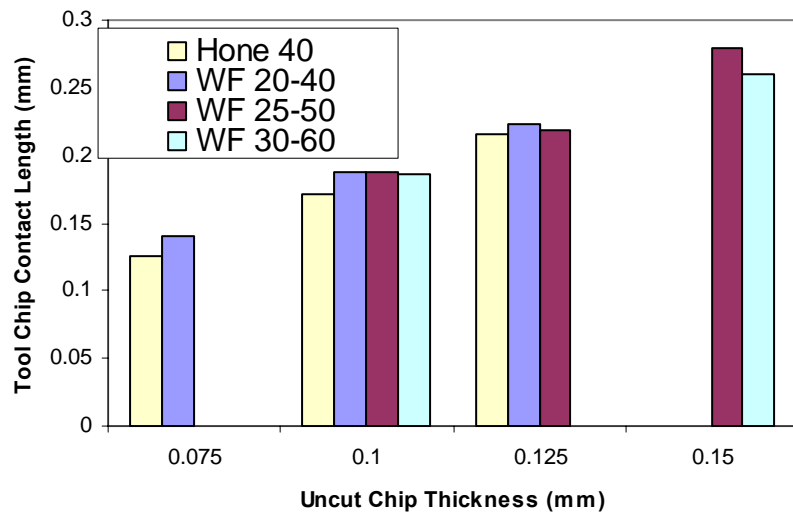
		t_u (mm)	α	θ	m_1	m_2	m_3	t_c
V=175 m/min	Hone 40	0.075	5.14	13.09	0.6	0.66	0.815	0.16
		0.1	5.05	13.03	0.589	0.654	0.808	0.21
		0.125	4.88	12.91	0.6	0.647	0.8	0.26
	Hone 50	0.1	5.1	13.06	0.577	0.655	0.808	0.21
		0.125	5.27	13.19	0.51	0.65	0.807	0.26
		0.15	4.61	12.76	0.652	0.642	0.795	0.31
	WF 20-40	0.075	3.85	15	0.3	0.64	0.82	0.15
		0.1	4.27	15.22	0.438	0.68	0.85	0.21
		0.125	3.95	14.97	0.457	0.66	0.83	0.255
	WF 25-50	0.1	4.06	15.03	0.523	0.68	0.847	0.2
		0.125	3.72	14.81	0.544	0.66	0.832	0.25
		0.15	3.53	14.664	0.55	0.649	0.82	0.3
	WF 30-60	0.1	4.13	15.083	0.557	0.69	0.855	0.21
		0.15	3.25	14.547	0.635	0.648	0.81	0.31
		0.18	2.25	14.227	0.845	0.644	0.81	0.36

Dead metal zone angle (α) is found to be lower in waterfall hone tools. Slip-line angle (θ) in waterfall hone tools are identified as greater than honed tools, which indicate a greater tool-chip contact length in waterfall hone tools. Fig 5.7 shows the variation of the tool-chip contact length and the length of front surface of the DMZ (DF in Fig 5.3b) with

respect to uncut chip thickness at cutting speed $V=125$ m/min. These results show that waterfall hone tools have longer tool-chip contact length both on the rake face and on the DMZ. Tool-chip contact length is a little less than 2 times of the uncut chip thickness.



(a)



(b)

Figure 5.7 Length of front surface of the DMZ and tool chip contact length for various uncut chip thickness values at $V=125$ m/min.

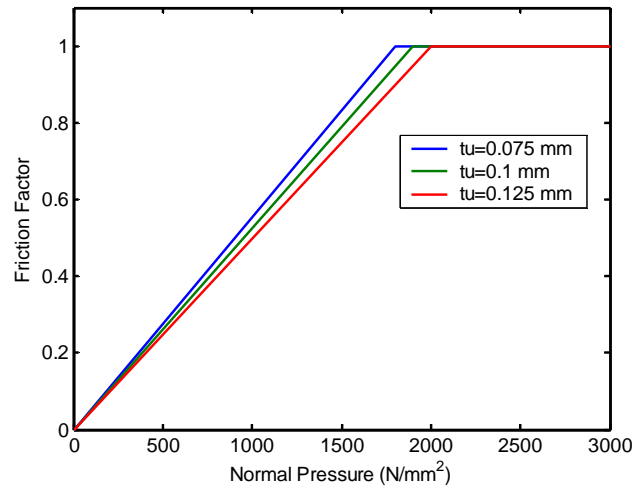
Above given results suggest that oval-like design of waterfall hone edge preparation helps transferring the loads acting on the tip of the tool towards the rake face of the tool. Dead metal zone covers a greater range of the tool tip which protects the cutting tip. According to the identified slip-line angles given in Table 5.2 and 5.3, honed tool with 40 μm edge radius and waterfall hone with 20-40 μm edge dimensions yielded different results. This implies that waterfall hone equivalent of honed tools must have greater edge dimensions.

Investigation of the influence of various edge preparations on field variables such as temperatures, effective stresses, and strains, is performed by finite element simulations. The details of finite element simulations are explained in the next section.

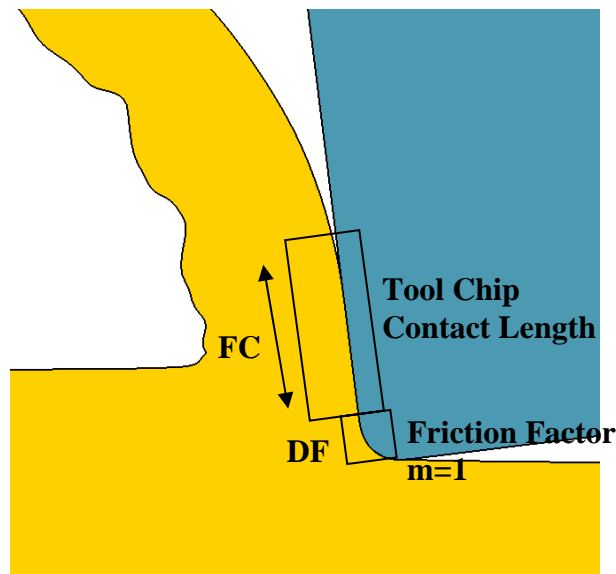
5.4 Finite Element Analysis

In order to compare field variables such as temperature distributions, strains, and maximum effective stresses in the tool, finite element simulations were performed by using commercial software DEFORM-2D®. Work material constitutive constants for AISI-4340 steel ($A=1504$ MPa, $B=569$ MPa, $n=0.22$, $C=0.003$, $m=1.17$) was adapted from Grey et al. (1994) and used in simulations under rigid-plastic material deformation conditions. As mentioned before, friction definition is crucial in order to obtain reasonable simulations in finite element analysis. Fig. 5.8 (a) shows how the friction factors are defined as a function of normal pressure at the tool-chip interface for various uncut chip thickness values in this study. In Fig. 5.8 (b), DF represents the region where

the friction factor will be equal to one (sticking zone) and FC denotes the tool chip contact length where the friction factor will decrease with decreasing normal pressure on the tool rake face (Fig. 5.8a). It must be noted that, normal stress distribution on the rake face is function of tool edge geometry and cutting conditions. It can be calculated from identified slip-line angles and shear flow stress as shown in Chapter 4.



(a)



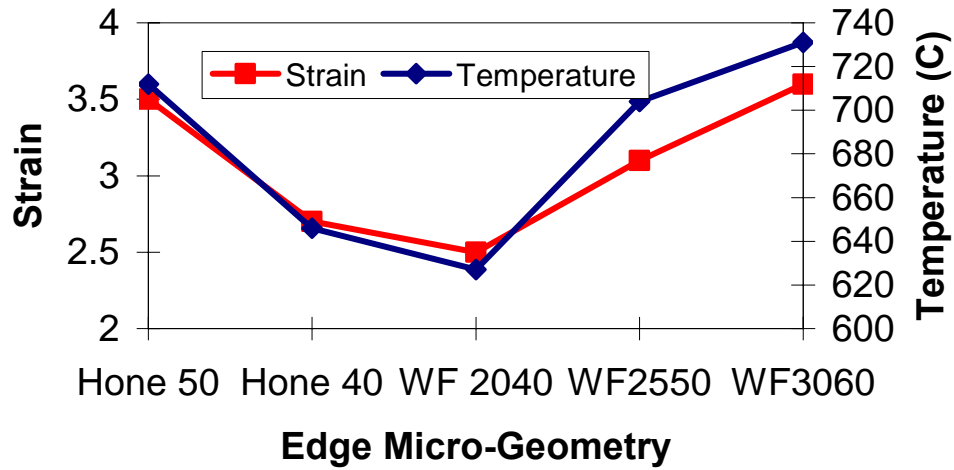
(b)

Figure 5.8 Friction definition used in finite element simulations.

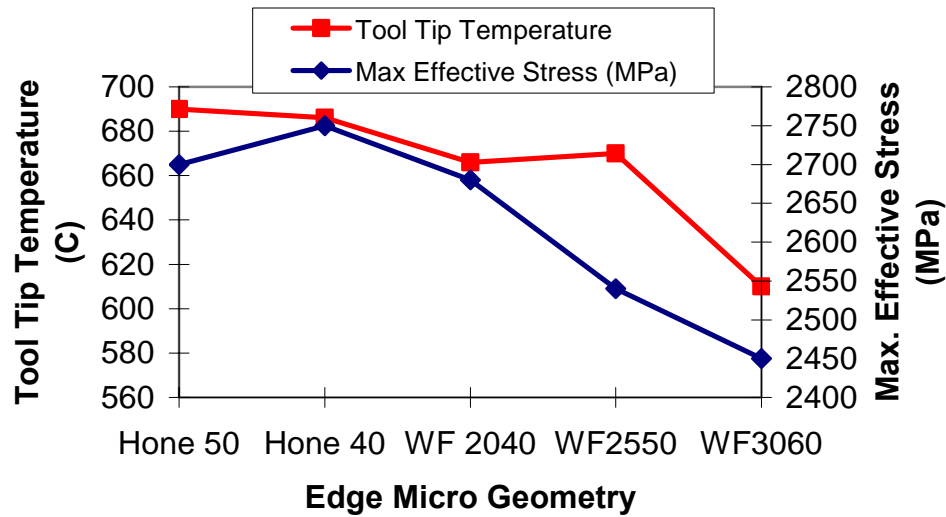
In order to simulate serrated chips which were observed during large uncut chip thickness experiments, a damage model proposed by Cockcroft and Latham (1966) is employed. The critical damage coefficient is determined by trial and error and kept constant in all simulations.

Fig. 5.9 (a) illustrates the variation of the strains and temperatures on the machined workpiece surface for various edge preparations at the cutting condition $V=175$ m/min and $t_u=0.15$ mm. Fig. 5.9 (b) demonstrates the variation of maximum effective stresses on the tool and tool tip temperatures at the same cutting condition. It can be seen from these results that as edge radius increases, strains and temperatures on the machined surface increases. Surface integrity of workpiece, i.e. residual stresses and surface roughness, is directly related to strains and temperature distributions on the machined workpiece surface. There are certain advantages of using small hone radius in terms of obtaining good surface roughness; however, using relatively larger edge radius may produce compressive residual stresses on the workpiece. Tool tip temperatures tend to decrease with increasing edge radius. The reason for decreasing tool tip temperatures may be explained with increased surface area for heat transfer as edge radius increases. However, when edge radius is not selected according to uncut chip thickness i.e. machining a small uncut chip thickness with a large hone; temperatures are localized at the tip of the tool which leads to rapid tool wear. According to the results given in Fig 5.9 (a) and (b), waterfall hone with 20-40 μm edge dimension seems like the most suitable edge preparation among other edge preparations when only workpiece is considered. Waterfall hone with 30-60 μm edge dimensions can be selected when only cutting tool is

considered. For all edge preparations, rake face temperatures were found to be around 800 °C. Fig. 5.10 shows the finite element simulation results of temperature distributions in the cutting tool.



(a)



(b)

Figure 5.9 (a) Strains and temperatures on the machined workpiece surface, (b) Tool tip temperatures and maximum effective stresses at the cutting condition $V=175$ m/min,

$$t_u=0.15 \text{ mm.}$$

In Fig. 5.10, it can be seen that rake face temperature distributions are distributed more evenly in waterfall hone tools than honed tools because of longer tool-chip contact. The lowest tool tip temperature obtained in waterfall hone 30-60 μm edge dimension tool. Larger tool tip surface area helps distribution of heat energy around the tool tip. Fig. 5.11 represents the distribution of effective stresses on the tool. The effect of the edge shape on effective stress distributions can be clearly seen in this figure. The locations of maximum stresses are found to be closer to the tool tip for waterfall hone tools. Fig. 5.12 shows the chip shape and strain distributions for all edge preparations. As mentioned before, serrated chips were observed at high uncut chip thicknesses. The simulated chip shapes are in good agreement with the SEM images obtained from chips collected during machining tests (Fig. 5.18-21). It is obvious from these images that, as edge radius increases the degree of serration also increases under the same cutting condition. Increasing edge radius works like increasing negative rake angle which causes further plastic deformations on the chip yields more serration. Because of its cyclic nature, serrated chips produce fluctuations in forces depending on the degree of serration. Fluctuating forces are known to cause vibrations and which may yield poor surface finish. In order to investigate the effect of decreasing cutting speed and decreasing uncut chip thickness, finite element simulations were performed at the cutting condition of $V=125$ m/min and $t_u=0.1$ mm. Fig 5.13 shows that waterfall hone with 20-40 μm edge dimensions yielded favorable temperature distributions compared to others. Fig 5.14 represents the stress distributions at the cutting condition of $V=125$ m/min and $t_u=0.1$ mm. The stress distributions are similar to those obtained for $V=175$ m/min and $t_u=0.15$ mm with lower stress values. In a more detailed analysis, the stress distributions in the

honed tool for various uncut chip thicknesses are shown in Fig. 5.16. As expected, the effective stresses increase with increasing uncut chip thickness. Fig. 5.15 illustrates the simulated chip shapes for low uncut chip thickness cutting condition where the degree of serration is less than large uncut chip thickness machining case. Stagnant metal zone is illustrated by plotting velocity profiles of finite element simulations for different cutting conditions in Fig. 5.17. Stagnant metal zone covers the tool tip in all cutting cases.

Finally, the comparison of measured and predicted cutting forces and chip thicknesses are given in Table 5.3. Finite element simulations yielded very good predictions in terms of cutting forces (F_c) and cut chip thickness (t_c) values, however thrust forces (F_t) were under predicted by the finite element software.

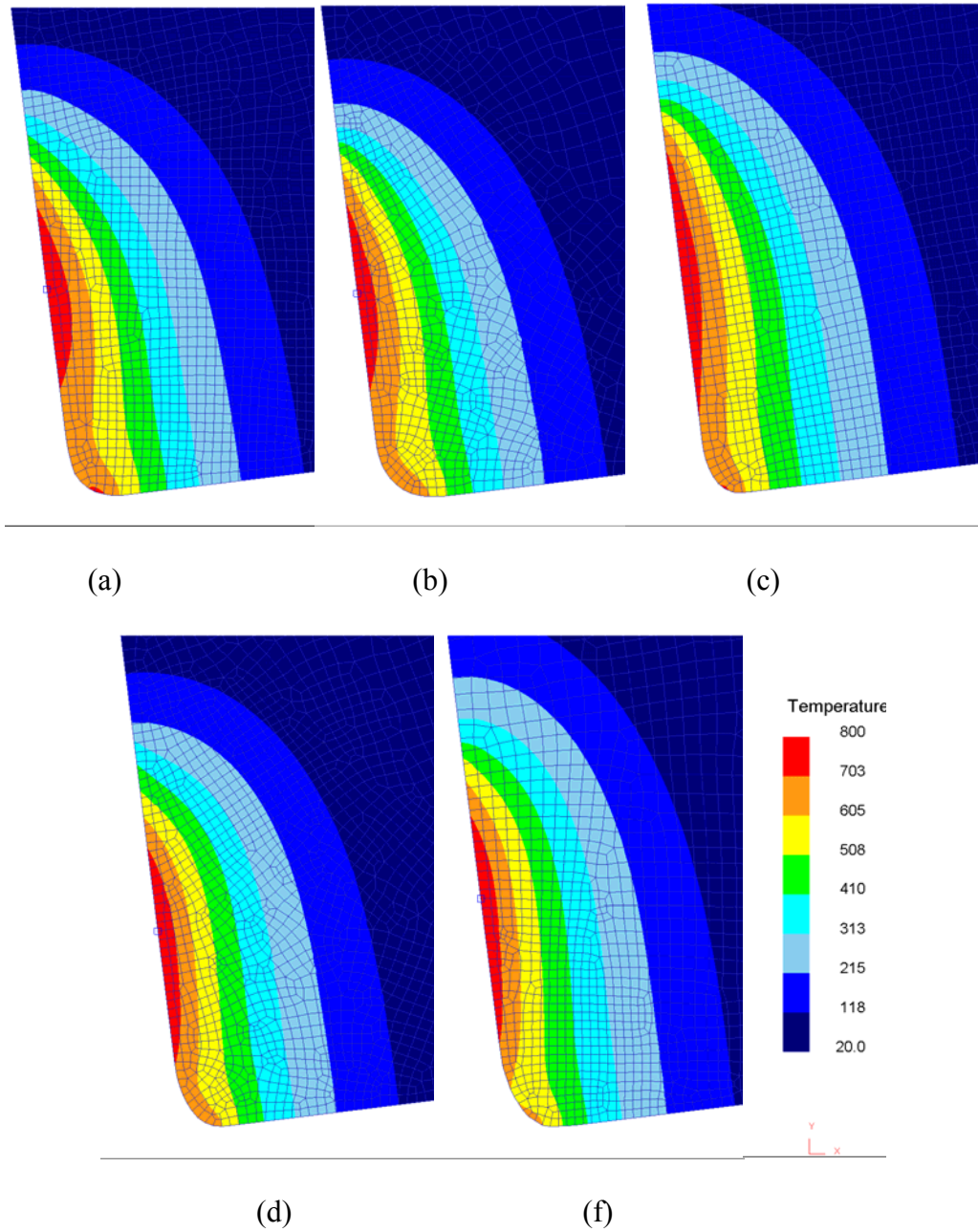


Figure 5.10 Tool temperature distributions for $V=175$ m/min, $t_u=0.15$ mm: (a) Hone 40 μm , (b) Hone 50 μm , (c) WF 20-40 μm , (d) WF-25-50 μm , (e) WF 30-60 μm .

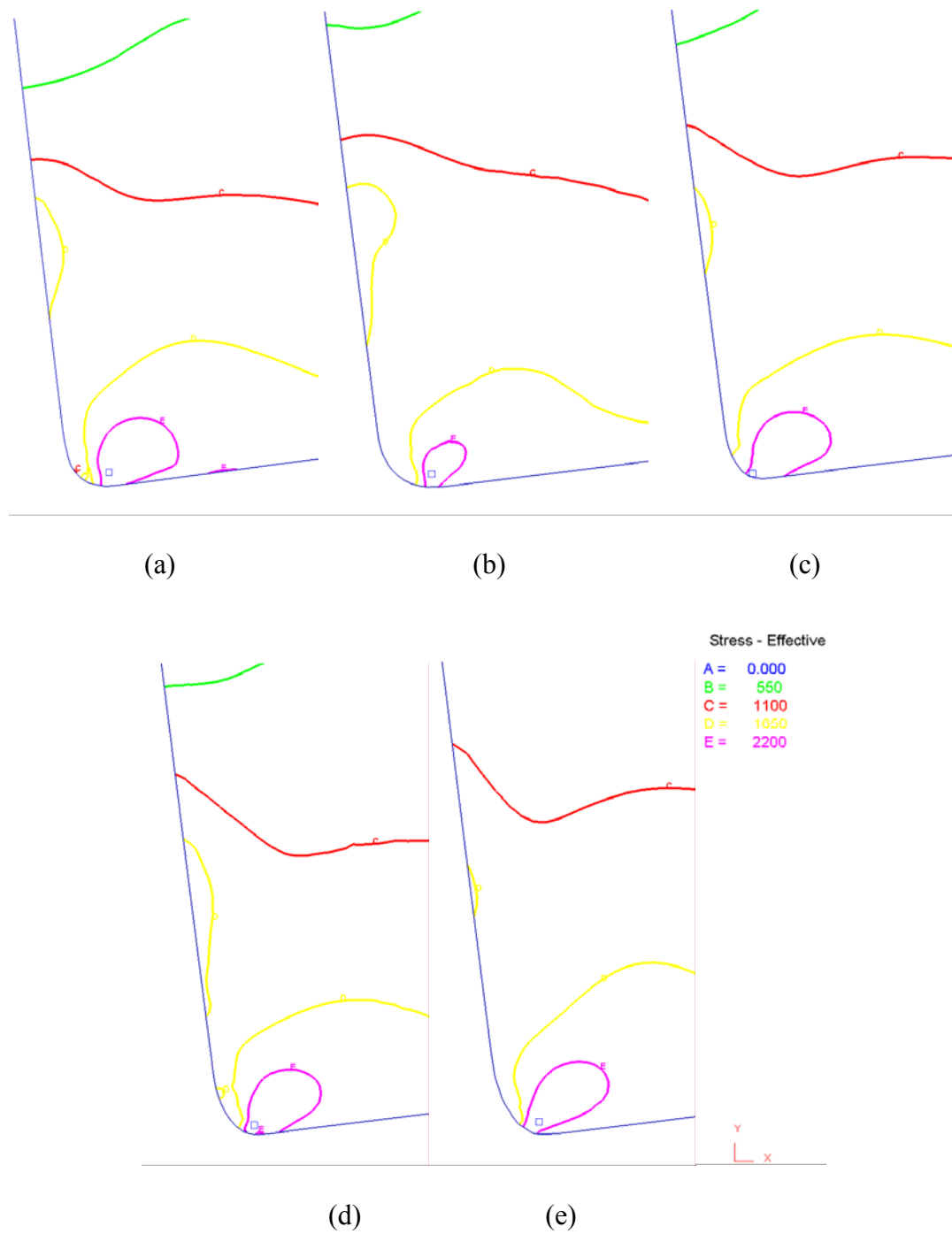


Figure 5.11 Effective stress distributions in honed and waterfall hone tools for $V=175$ m/min, $t_u=0.15$ mm: (a) Hone 40 μm , (b) Hone 50 μm , (c) WF 20-40 μm , (d) WF-25-50 μm , (e) WF 30-60 μm .

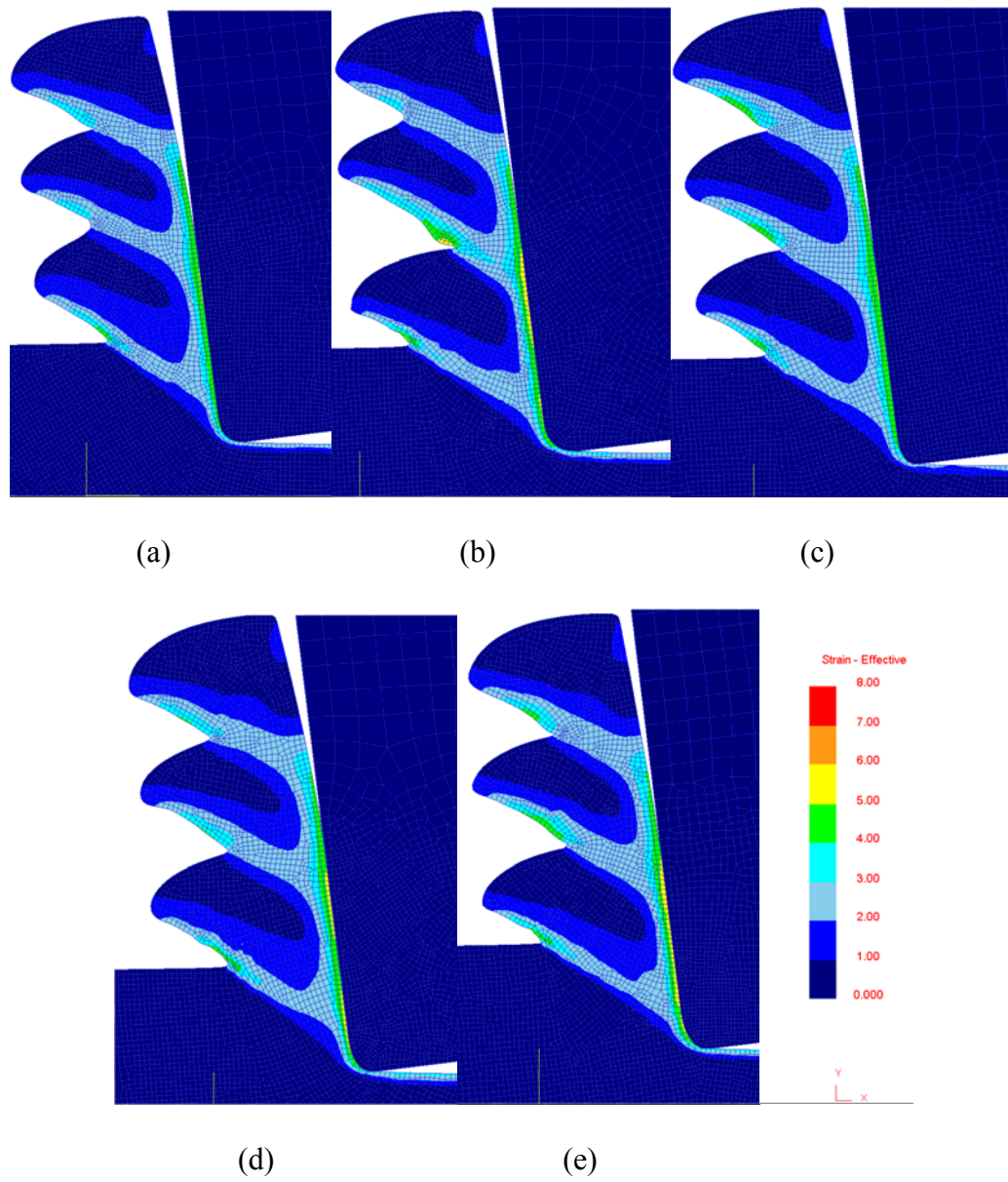


Figure 5.12 Strain distributions in honed and waterfall hone tools for $V=175$ m/min, $t_u=0.15$ mm: (a) Hone 40 μm , (b) Hone 50 μm , (c) WF 20-40 μm , (d) WF-25-50 μm , (e) WF 30-60 μm .

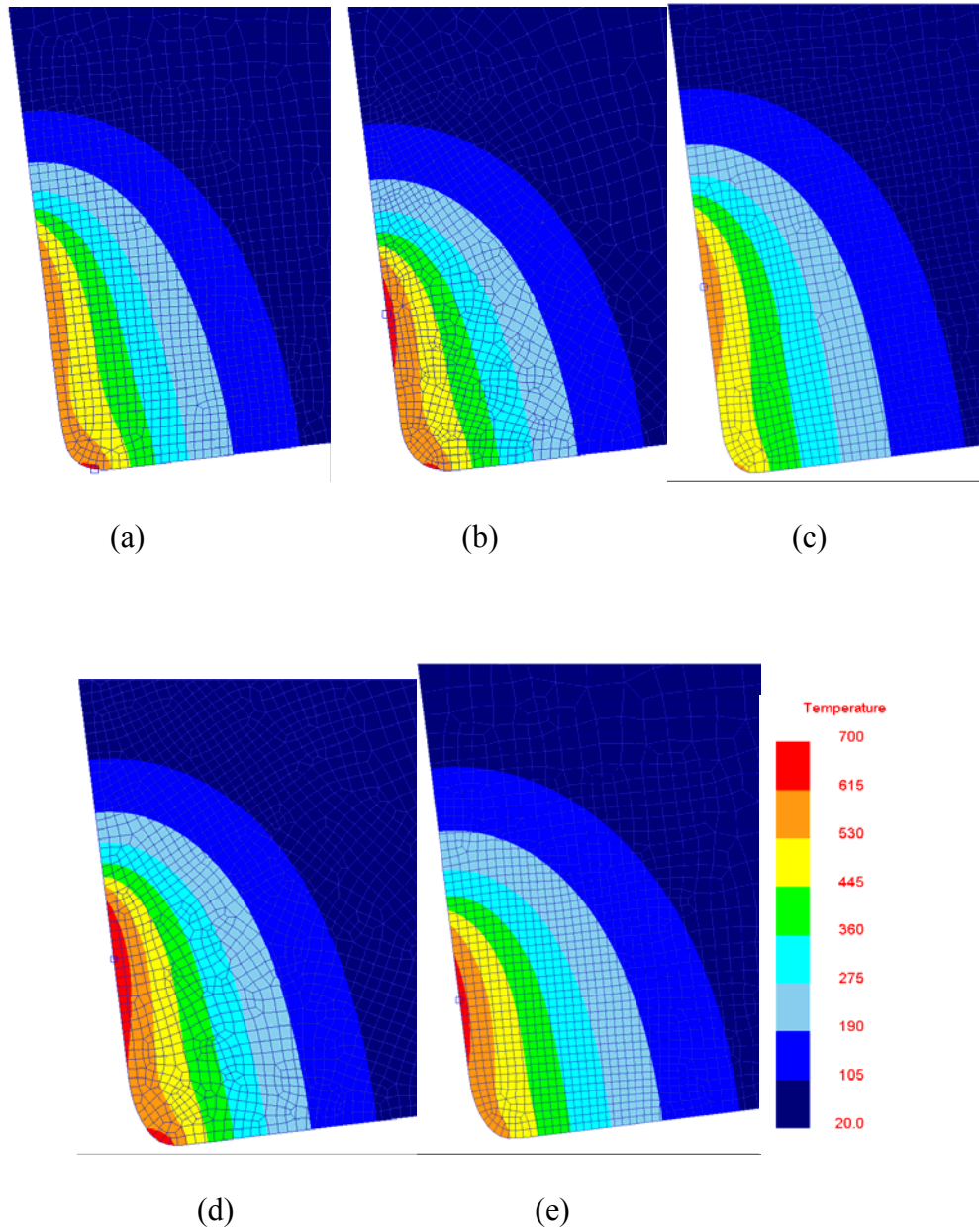


Figure 5.13 Tool temperature distributions for $V=125$ m/min, $t_u=0.1$ mm:

(a) Hone 40 μm , (b) Hone 50 μm , (c) WF 20-40 μm , (d) WF-25-50 μm , (e) WF 30-60 μm .

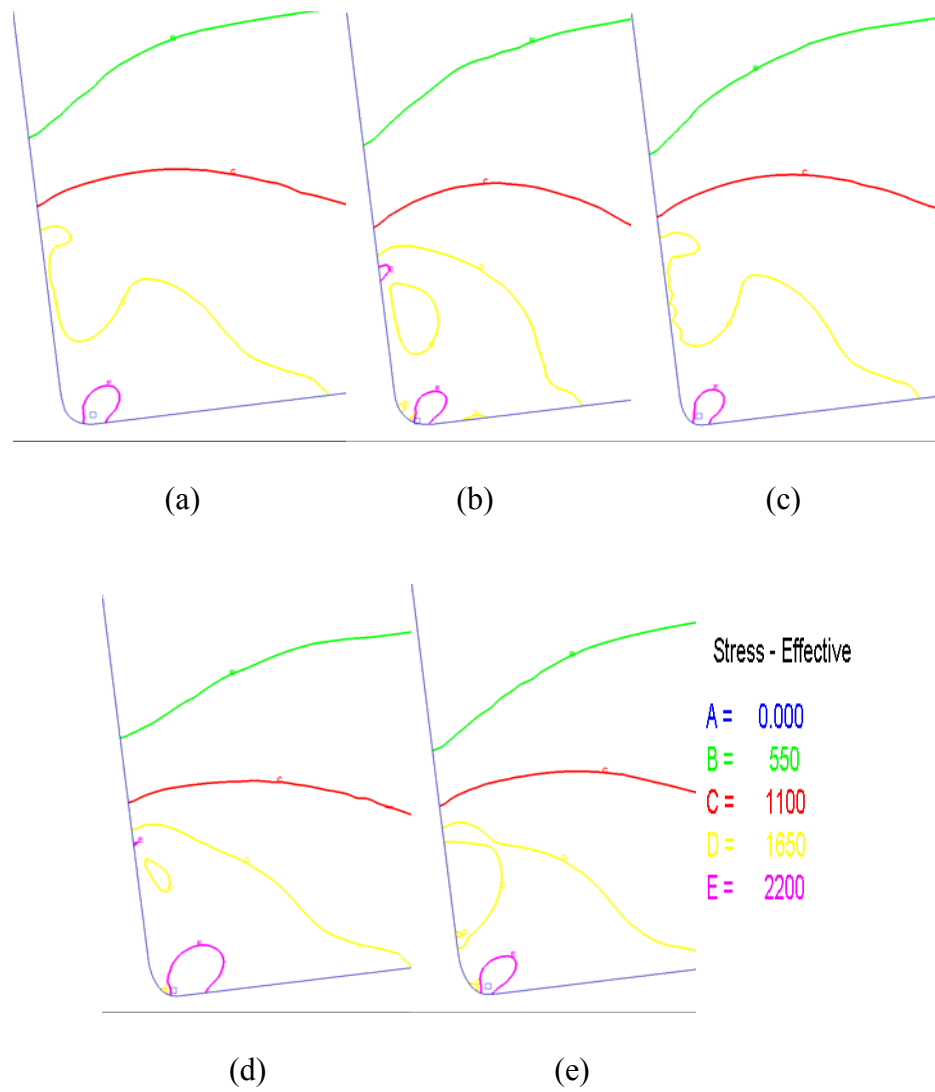


Figure 5.14 Effective stress distributions in honed and waterfall hone tools for $V=125$

m/min, $t_u=0.1$ mm: (a) Hone 40 μm , (b) Hone 50 μm , (c) WF 20-40 μm ,

(d) WF-25-50 μm , (e) WF 30-60 μm .

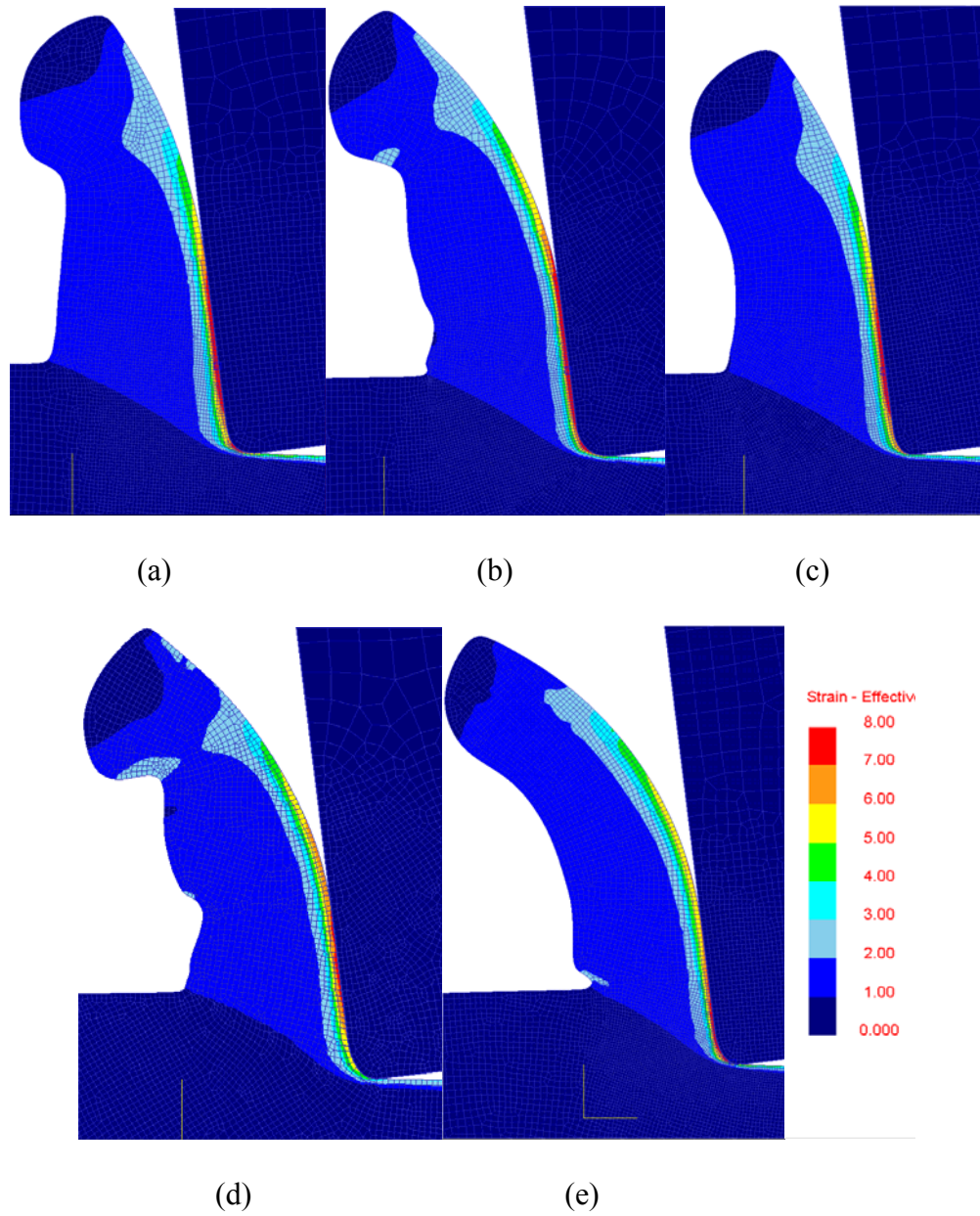


Figure 5.15 Strain distributions in honed and waterfall hone tools for $V=125$ m/min, $t_u=0.1$ mm: (a) Hone 40 μm , (b) Hone 50 μm , (c) WF 20-40 μm , (d) WF-25-50 μm , (e) WF 30-60 μm .

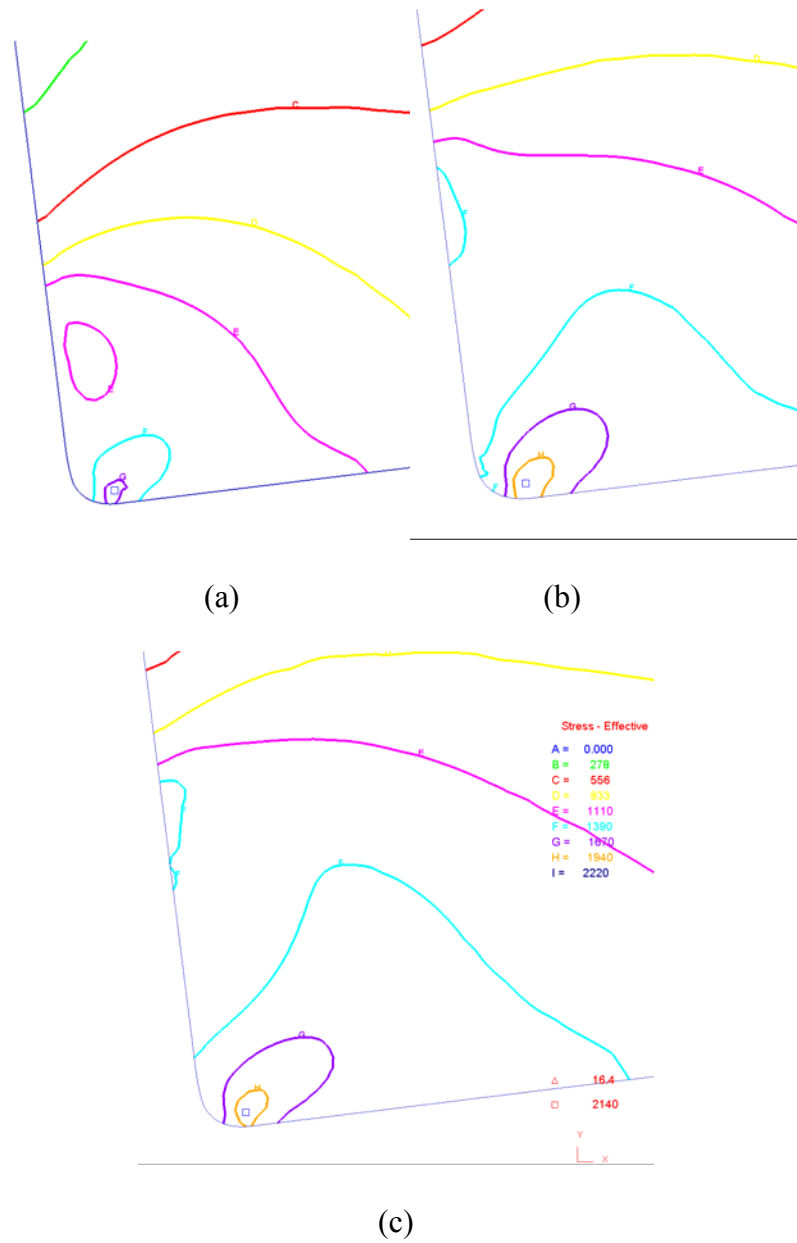


Figure 5.16 Effective stress distributions in honed tool 40 μm at $V=125$ m/min:

(a) $t_u=0.075$ mm, (b) $t_u=0.1$ mm, (c) $t_u=0.125$ mm.

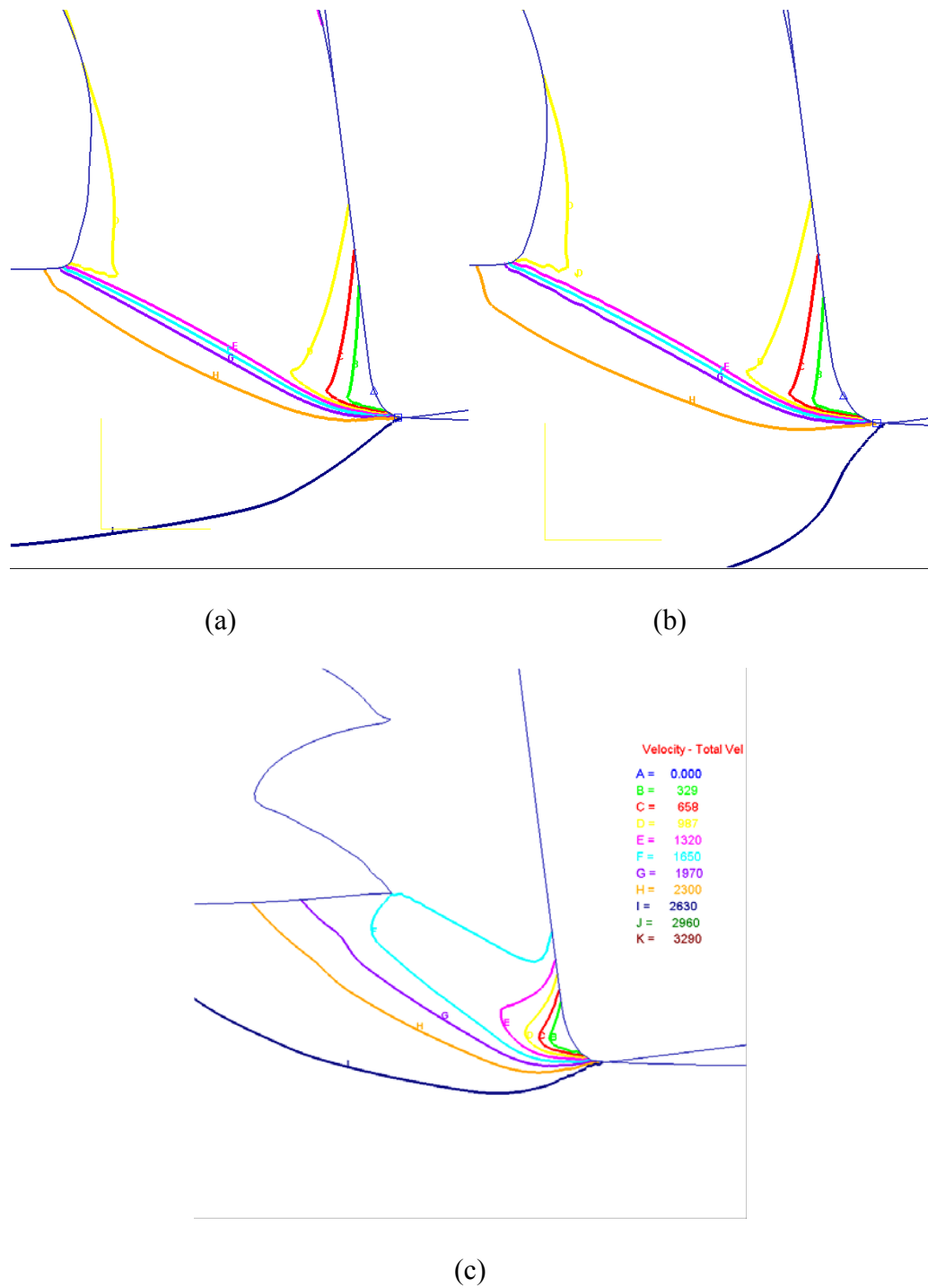


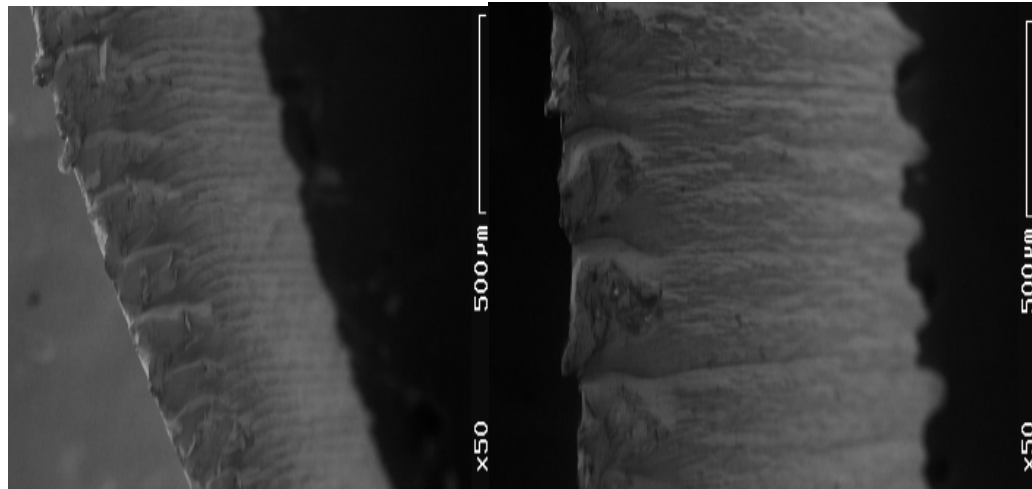
Figure 5.17 Dead metal zone formation for honed and waterfall edge preparations:

(a) Hone 40 μm , $V=125$ m/min, $t_u=0.1$ mm, (b) WF 30-60 μm , $V=125$ m/min, $t_u=0.1$ mm,

(c) WF 30-60 μm , $V=175$ m/min, $t_u=0.15$ mm

Table 5.4 Predicted and measured cutting forces and chip thicknesses

Insert Type	Cutting Speed (m/min)	Uncut Chip Thickness	Measured Cutting Force	Measured Thrust force Ft	Predicted Cutting Force	Predicted Thrust Force	Error % Fc	Error % Ft	Measured Chip Thick.	Predicted Cut Chip Thickness
Hone 40	125	0.1	493	444	512	370	3.8	16.6	0.22	0.22
Hone 50	125	0.1	489	478	485	355	0.8	25.7	0.22	0.23
WF 20-40	125	0.1	484	435	491	330	1.4	24	0.22	0.23
WF 25-50	125	0.1	484	423	480	340	0.8	19	0.23	0.23
WF 30-60	125	0.1	487	457	486	325	0.2	28	0.23	0.23
Hone 50	175	0.15	666	543	660	430	0.9	20	0.31	0.3
WF 25-50	175	0.15	624	481	632	400	1.28	16	0.29	0.3
WF 30-60	175	0.15	653	515	641	405	1.8	21	0.3	0.3

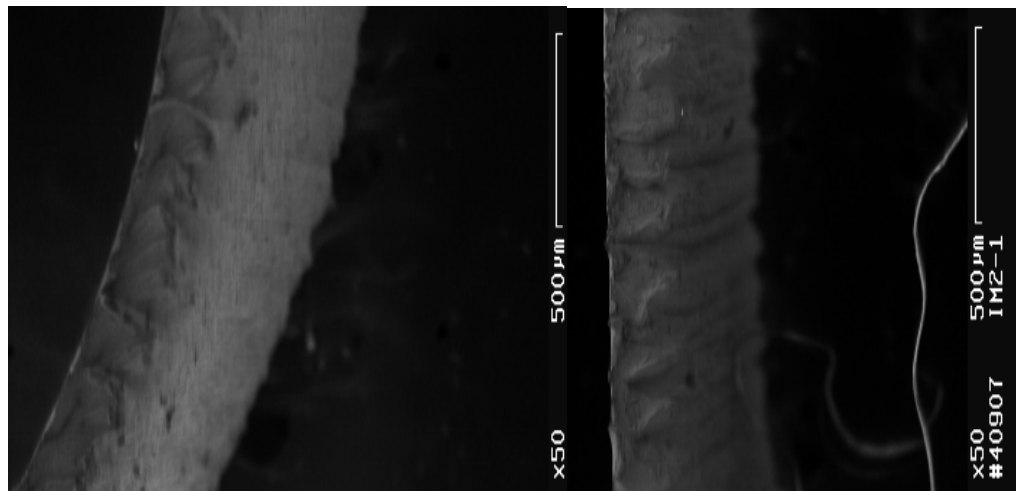


(a)

(b)

Figure 5.18 Chip formation for honed edge preparations for $V=125$ m/min, $t_u=0.1$ mm:

(a) Hone $40\ \mu\text{m}$, (b) Hone $50\ \mu\text{m}$



(a)

(b)

Figure 5.19 Chip formation for waterfall hone edge preparations for $V=125$ m/min, $t_u=0.1$

mm: (a) WF $20\text{-}40\ \mu\text{m}$, (b) WF $25\text{-}50\ \mu\text{m}$

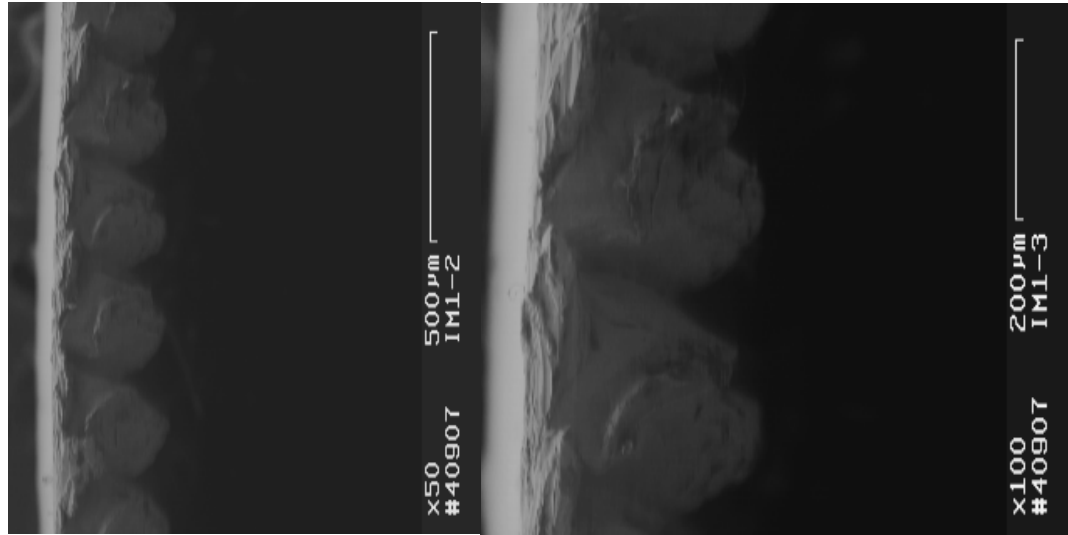


Figure 5.20 Chip formation for WF 30-60 μm edge preparation for $V=125\text{ m/min}$, $t_u=0.1\text{ mm}$ with two magnification levels

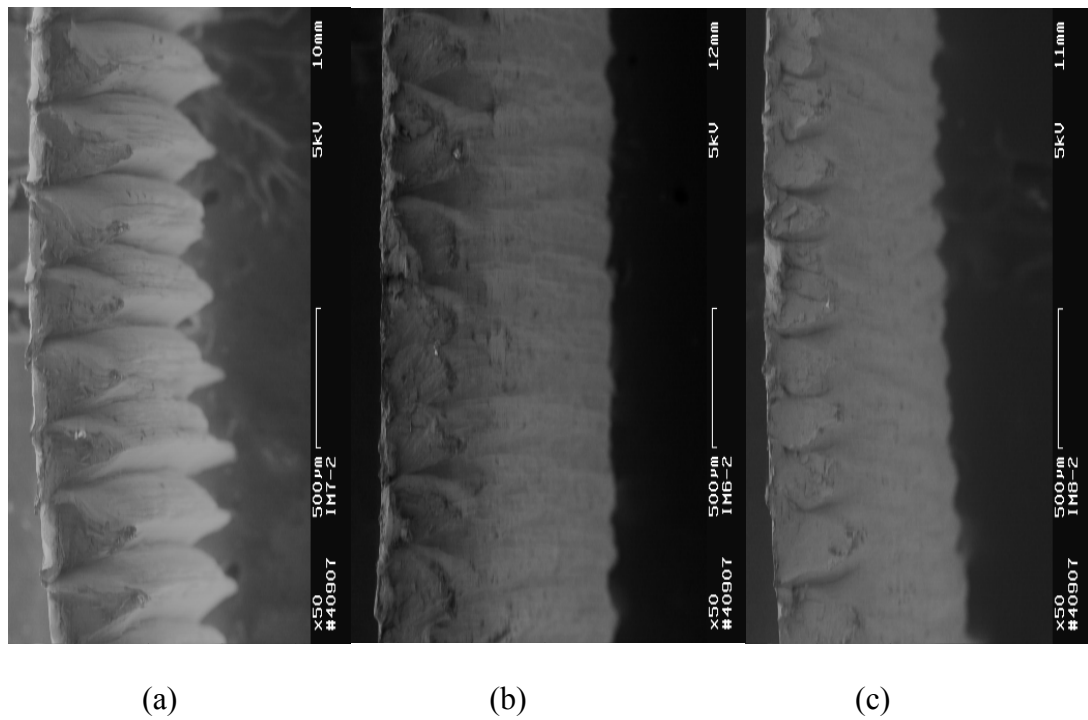


Figure 5.21 Chip formation for honed and waterfall edge preparations for $V=175\text{ m/min}$, $t_u=0.15\text{ mm}$: (a) Hone 50 μm , (b) WF 25-50 μm , (c) WF 30-60 μm

5.5 Conclusions

In this chapter, the tool-chip friction characteristics of curvilinear edge tools are investigated by utilizing orthogonal cutting tests, slip-line field analysis, and finite element simulations. Orthogonal cutting tests were used to identify slip-line angles which yielded tool-chip friction characteristics of curvilinear edge cutting tools. Finite element simulations, which make use of the friction factor findings of the slip-line field analysis, are used to study temperature, strain, and stress distributions in the cutting tools. Proposed approach introduces a scientific approach to model friction in finite element simulations and yielded good results in terms of simulated cutting forces and chip shapes. It has been shown that;

- (a) Size of edge radius is an important factor and it affects the mechanics of high speed cutting,
- (b) Edge radius must be selected according to cutting conditions, large edge radius is not suitable for machining low uncut chip thickness,
- (c) The ratio of uncut chip thickness to edge radius around 3 seems to be an appropriate ratio for edge preparations used in the cutting tests. There must be an upper limit on this value which considers the rupture strength of the edge preparation. However, due to experimental limitations this upper limit was not studied.
- (d) There is always a trade-off when it comes to edge radius selection. The purpose of using cutting tools with curvilinear edges is to protect the cutting edge from

chipping, to improve its impact resistance, to increase surface area for heat transfer from the cutting zone. However, if the edge radius is not selected carefully, that may result in increased cutting forces, poor surface workpiece quality and short tool lives. When selecting edge radius for a given cutting condition, both machined workpiece surface and cutting tool must be considered.

- (e) The observation of collected chip shapes revealed that edge preparation affects chip formation mechanism due to increased cyclical plastic deformations along the face of the curvilinear edge.

CHAPTER 6

DESIGN AND ANALYSIS OF VARIABLE MICRO-GEOMETRY CUTTING TOOLS

6.1. Introduction

Metal cutting operations represent the largest class of manufacturing operations where turning is the most commonly employed material removal process. Although the mechanics of metal cutting is studied in orthogonal or 2-D, vast majority of practical turning operations are in 3-D. The goal of this chapter is to investigate the influence of various edge preparations on the mechanics of 3-D machining by using experimental data and finite element simulations. The findings of Chapter 5 are utilized in finite element simulations. The effect of different definitions of friction factor on the field variables is investigated. Finally, a methodology for advanced cutting tool micro geometry (variable micro-geometry) design in 3-D cutting is proposed.

In recent years, 3-D finite element analysis (FEA) has become available to calculate and simulate the process variables such as cutting forces, temperature and stress distributions, etc. during machining. There are numerous studies on finite element analysis of orthogonal machining which provide essential information about the mechanics of cutting, yet the studies on 3-D finite element modeling of machining is limited. 3-D FEA based process models is needed to study practical machining operations. Ceretti et al. (2000) developed a 3-D FEA model for turning to predict cutting

forces, temperature and stress distributions for the machining of aluminum alloys and low-carbon steels under orthogonal and oblique cutting configurations. Guo and Dornfeld (1998) presented a 3-D FEA model to simulate burr formation when drilling stainless steel. They emphasized the importance of proper definition of work material properties and friction conditions. Guo and Liu (2002) proposed a 3-D FEA model for hard turning of AISI 52100 steel using PCBN tools. Their model was used to predict the temperature distribution over the cutting edge, the residual stress distribution on the machined surface and cutting forces. They stressed that there is a need for a method which yields rake face friction factor or coefficient of friction values. In a recent study, Liu and Shih (2006) compared the predictions of a 3-D FEA model with experimental measurements for turning of titanium. They also investigated the effects of edge preparations on process variables and observed that increasing cutting speed increases tool temperature, decreases cutting forces; increasing edge radius, decreases tool temperatures and increases cutting forces. In their simulations they were also able to demonstrate serrated chip formation in machining of titanium.

6.2. Mechanics of 3-D Turning

A general schematic of 3-D turning is given in Fig 6.1 where the cutting process is defined by the cutting speed (V), feed rate (f) and depth of cut (d). The resulting cutting forces, namely cutting force (F_c), thrust force (F_t), and feed forces (F_z) with their directions are also shown in Fig. 6.1.

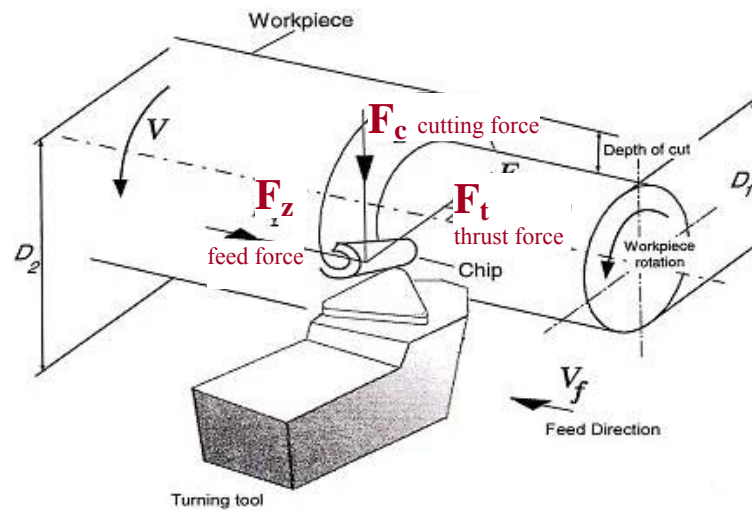


Figure 6.1 Mechanics of 3-D turning. (Altintas (2000))

The detailed interaction of the cutting tool and workpiece is explained in Fig. 6.2. It can be seen that chip load is a function of depth of cut, feed rate, and tool corner radius. In this figure it is important to observe that the thickness of the chip, which is shown as the hatched area, varies along tool corner radius.

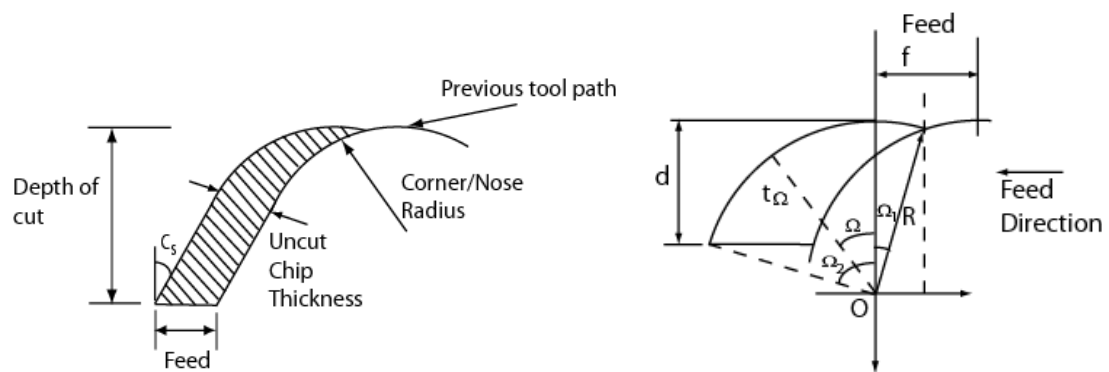


Figure 6.2 Chip load in typical turning operation with a corner radius tool

Assuming rake and inclination angles introduced by the tool holder are zero, maximum uncut chip thickness and the variation of chip thickness along the chip can be calculated as follows

$$\begin{aligned}
 \Omega_1 &= -\sin^{-1}\left(\frac{f}{2R}\right) \\
 \Omega_2 &= \cos^{-1}\left(\frac{R-d}{R}\right) \\
 t_\Omega &= R + f \sin \Omega - \sqrt{R^2 - f^2 \cos^2 \Omega} \quad \text{when} \quad \Omega \leq \tan^{-1}\left(\frac{R \sin \Omega_2 - f}{R-d}\right) \\
 t_\Omega &= R - \frac{R-d}{\cos \Omega} \quad \text{when} \quad \Omega > \tan^{-1}\left(\frac{R \sin \Omega_2 - f}{R-d}\right)
 \end{aligned} \tag{6.1}$$

Fig. 6.3 shows the chip thickness with respect to sweep angle Ω for a given cutting condition. The distribution of chip loads on the insert can be determined as a function of angle Ω along corner radius of the tool. As shown in Fig. 6.3, the chip thickness becomes very small for a considerable range of angle Ω along corner radius.

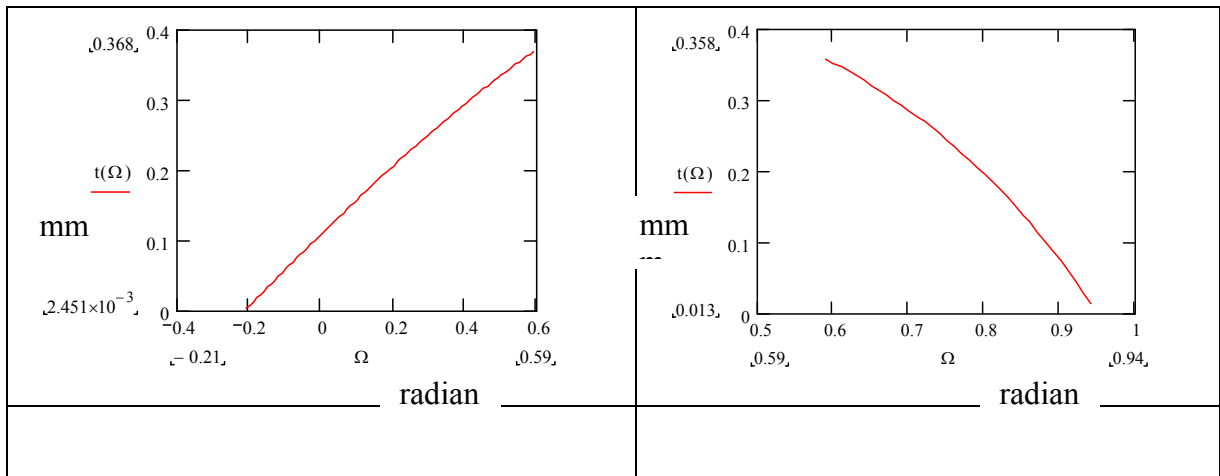


Figure 6.3 Variation of uncut chip thickness

In previous chapter, we showed that a ratio of uncut chip thickness to edge radius around 3 is suitable for machining AISI 4340 steel with curvilinear edge CBN cutting tools. In a similar study this ratio is found to be around 2 by Endres and Koutanya (2002) after tool wear tests for a different workpiece-tool material. However, it is clear from Fig. 6.3 that the ratio does not stay constant along the tool corner radius and decreases continuously towards the end of contact point if uniform edge design cutting tools are employed. It is believed that if a proper ratio of edge preparation to uncut chip thickness can be maintained along tool corner radius, significant advantages such as prolonged tool life and superior surface finish can be obtained. This is explained in the next section.

6.3 Advanced Cutting Tool Micro-Geometry Design

Edge preparation enhances tool life but at the same time makes cutting less efficient especially when the ratio of uncut chip thickness to tool edge radius decreases. In Chapter 5, it has been shown that friction factor increases with decreasing uncut chip thickness to edge radius ratio. Due to trapped work material at the trailing edge of the cutting tool, cutting cannot be performed efficiently which results in increased strains at that region and high temperatures. In order to explain this in detail, let us reconsider Fig. 6.2 which demonstrates the chip load during 3-D machining. As explained before, the thickness of the chip varies from a maximum equal to the feed rate to a minimum on the tool's corner radius. If a uniform edge radius applied along the corner radius of the cutting tool, cutting efficiency will be low due to small ratio of uncut chip thickness to tool edge radius around the trailing edge. Large edge radius will not be able to machine

that area but rub it against the workpiece. Three critical sections A-A, B-B and C-C are demonstrated in Fig.6.4. In Section A-A which is leading cutting edge, uncut chip thickness is greater than the edge radius which indicates regular cutting. In Section B-B, at the end of the leading edge, the uncut chip thickness is equal to the edge radius where the rubbing action becomes more dominant than shearing. In Section C-C, at the trailing edge, the edge radius is larger than the thickness of the uncut chip and work material is rubbed against the workpiece. This rubbing action which results in increased temperatures on the tool and workpiece surfaces is believed to hinder the performance of the tool.

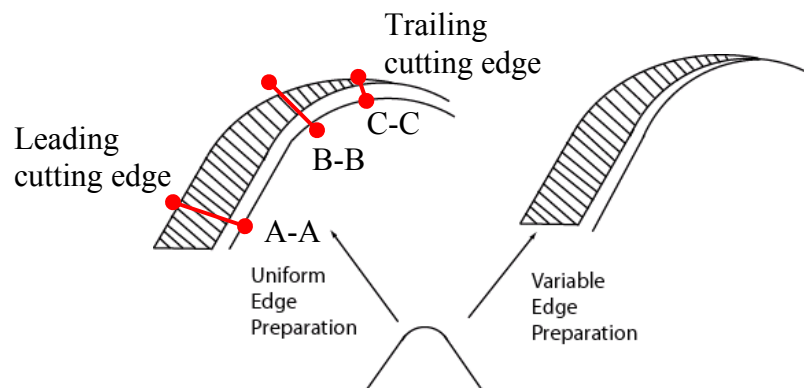


Figure 6.4 Uniform vs. variable edge design on a tool insert

Computer controlled honing devices enable the production of cutting tools with “engineered” micro-geometry or cutting tools with variable edge preparation where the edge radius along the corner radius of the cutting tool changes as a function of the thickness of the chip (Conicity Technologies, 2006). A CAD model of a variable edge

design tool insert is given in Fig. 6.5. This figure shows the tip of a cutting tool with variable edge preparation ($r_{\varepsilon}(\varrho)$). The edge radii at point A and B are 0.05 mm and 0.01 mm respectively where $r_{\varepsilon A} > \dots > r_{\varepsilon B}$.

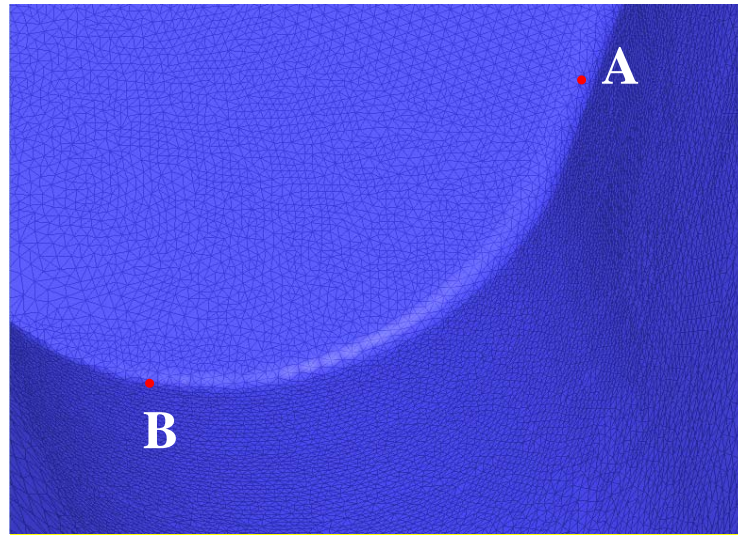


Fig. 6.5. The tip of the variable hone micro-geometry insert.

The purpose of this design is to eliminate the rubbing action at trailing edge of the tool by decreasing the edge radius towards the tip of the tool. This will reduce the unwanted excessive heat generation at the trailing zone and increase the performance of the tool. Proper tool edge design for the process in hand can be made only when tool-chip friction and heat generation mechanisms at the tool-chip and tool-workpiece interfaces are understood.

In variable edge design, the key parameter is the ratio of uncut chip thickness to edge radius ($\lambda = t(\varrho) / r_{\varepsilon}(\varrho)$). As mentioned earlier, the proper ratio is believed to around 3. If this ratio is known, for a particular cutting condition a variable cutting edge

can be designed. Variable edge preparation is not limited to honed micro-geometry inserts. Chamfered and waterfall type micro-geometry inserts can also have variable edge preparation. As for variable chamfered edge design, the goal will be to calculate optimum chamfer angle and chamfer height for given uncut chip thickness along the cutting edge as detailed in Klocke and Kratz (2005). The purpose of continuously changing the chamfer angle along the corner radius is to alter the locations of high temperature zones and reduce the possibility of a crater wear formation.

A methodology is proposed for advanced cutting tool micro-geometry design as shown in the flowchart in Fig 6.6. For a given cutting condition values of suggested tool corner radius (R) can be obtained from tool manufacturers. Tool edge radius (r_e) must be selected in accordance with tool corner radius. It should be noted that the friction identification method for micro-geometry tools proposed in Chapter 5 is at the core of this design methodology. Cutting conditions and workpiece material affects the friction conditions and this information is built into 3-D finite element model. The field variables obtained from 3-D process simulations such as temperature and stress distributions, tool wear, cutting forces etc. are utilized in assessing the performance of cutting tools or selecting cutting conditions for a given edge preparation.

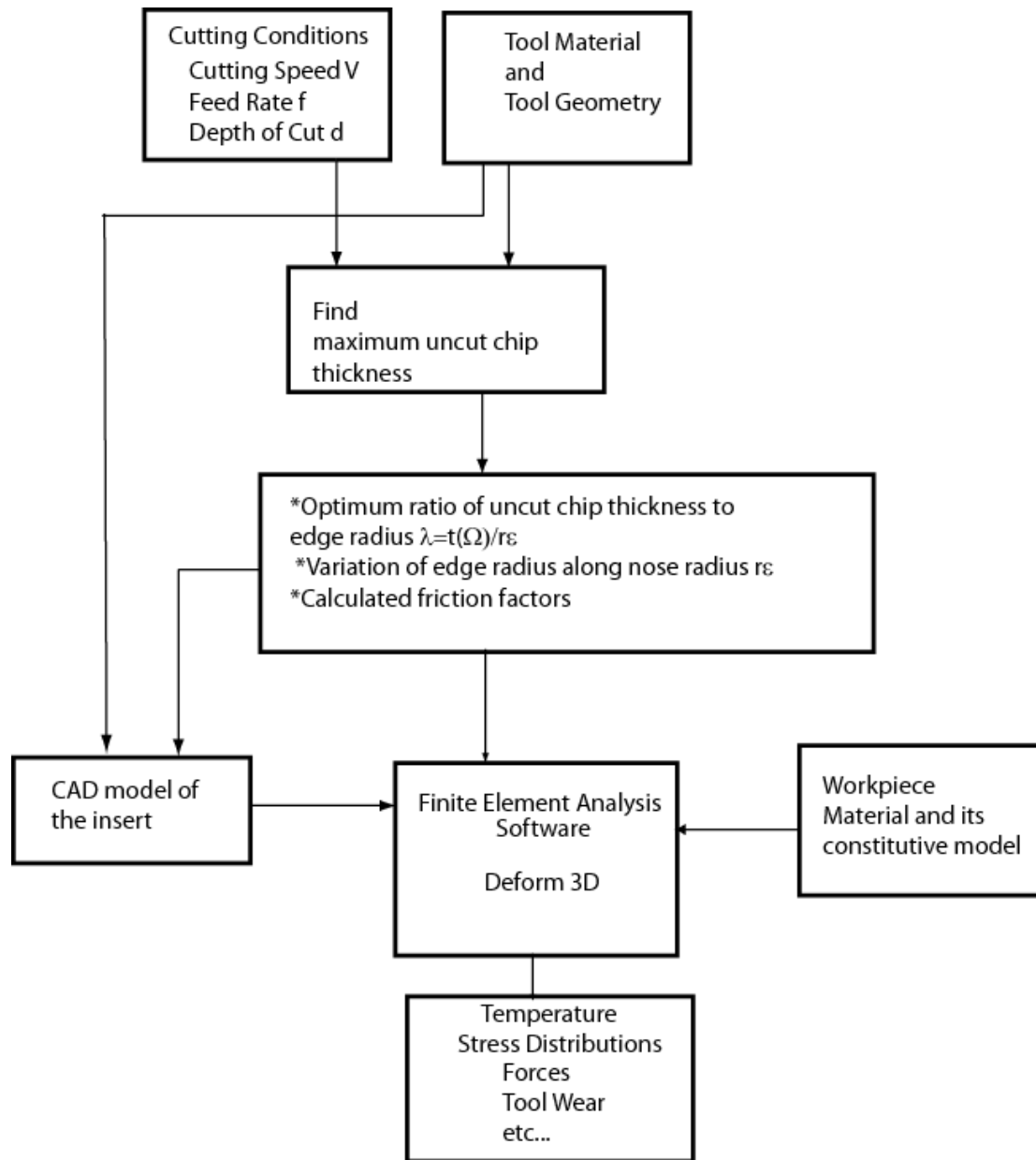


Figure 6.6 Flowchart of advanced cutting tool micro-geometry design.

In order to investigate the performance of cutting tools with various edge preparations, tools with uniform and variable edge preparations provided by Conicity Technologies have been used in machining tests. The experimental procedure is explained in the next section.

6.4 Experimental Procedure

In this study, turning of AISI 4340 steel using PCBN inserts with nine different micro-geometries (uniform chamfer with 0.1 mm chamfer height and 20° angle, uniform hone with 50 μm edge radius, uniform hone with 40 μm edge radius, uniform waterfall hone with 20-40 μm edge dimensions, uniform waterfall hone with 25-50 μm edge dimensions, uniform waterfall hone with 30-60 μm edge dimensions, variable hone with $r_A=50\ \mu\text{m}$, $r_B=10\ \mu\text{m}$ edge radii, variable waterfall hone with $r_A=25-50\ \mu\text{m}$, $r_B=10\ \mu\text{m}$ edge radii, and variable hone with $r_A=30-60\ \mu\text{m}$ $r_B=10\ \mu\text{m}$ edge radii was considered. SEM images of some edge preparations are shown in Fig. 6.7.

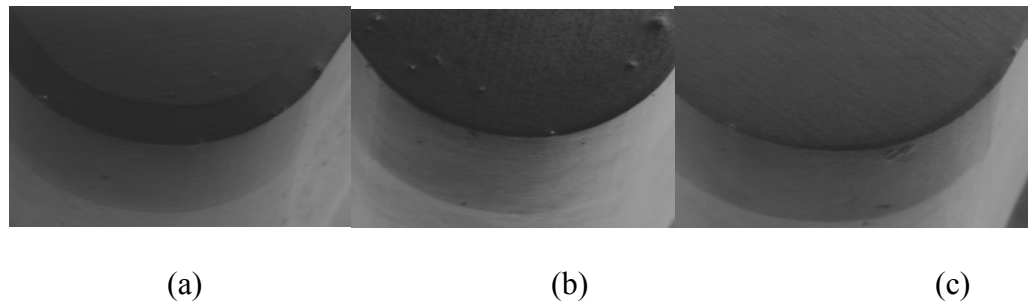


Figure 6.7 Images of PCBN inserts at 50 times magnification obtained with scanning electron microscopy: a) chamfered, b) uniform honed with 0.05 mm radius, c) variable hone with 0.01 to 0.05 mm edge dimensions.

Bar turning experiments were conducted using a cylindrical bar specimen with a diameter of 2.8 inches (71 mm) and length of 12 inches (305 mm). Solid top PCBN inserts (TNG-423) were used with a Kennametal MTG NR-123B right hand tool holder that provided 0° lead, -5° side rake, and -5° back rake angles. The cutting forces were measured with a three-component force dynamometer (Kistler Type 9121) mounted on the turret disk of

the CNC lathe. The charge signal generated at the dynamometer was amplified using charge amplifiers (Kistler Type 5814B1), acquired and sampled by using data acquisition PCMCIA card and Kistler DynoWare software on a laptop computer. Table 6.1 summarizes the experimental cutting conditions.

Table 6.1 Cutting conditions used in experiments and simulations (marked by **X**)

Cutting Conditions	Tool Type								
	Hone 40	Hone 50	WF 20-40	WF 25-50	WF 30-60	Var Hone 50	Var WF 25-50	Var WF 3060	Chamfered
V=125 m/min, f=0.15 mm, d=1 mm		X				X			X
V=125 m/min, f=0.1 mm, d=1 mm									
V=175 m/min, f=0.1 mm, d=1 mm									
V=175 m/min, f=0.15 mm, d=0.5 mm									
V=175 m/min, f=0.1 mm, d=0.5 mm									

The cutting force measurements were replicated three times. The averages of the cutting forces are shown in Fig. 6.8-6.12. Similar to the results of orthogonal cutting, the effect of edge preparation became apparent on thrust force (F_t) measurements. The cutting force measurements obtained from various edge preparation tools are again found to be similar. For the cutting condition of $V=125$ m/min, $f=0.15$ mm/rev, $d=1$ mm, variable waterfall

hone edge with 25-50 μm edge dimension yielded the lowest thrust forces followed by variable hone 50 μm edge radius. These two variable edge preparations produced higher cutting forces (F_c) than other edge preparations as shown in Fig 6.8. This result may imply that more efficient cutting due to variable edge preparation results in lower thrust forces but slightly higher cutting forces. It must be noted that the ratio of feed to tool edge radius is 3 in that cutting condition.

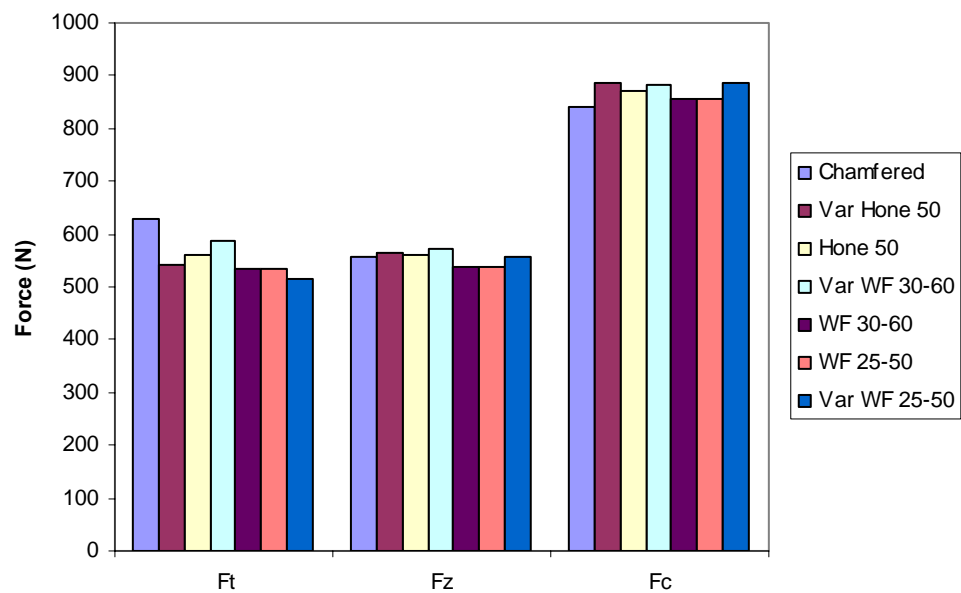


Figure 6.8 Measured cutting forces at the cutting condition of

$$V=125 \text{ m/min}, f=0.15 \text{ mm/rev}, d=1 \text{ mm}$$

Fig. 6.9 shows the force measurements for the cutting condition of $V=125 \text{ m/min}$, $f=0.1 \text{ mm/rev}$, $d=1 \text{ mm}$ where the feed rate is decreased compared to previous cutting condition. Decreasing feed rate resulted in lower cutting forces. In this cutting condition, honed tool with 40 microns edge radius yielded the lowest thrust force. This result

supports our finding when feed rate is decreased, the edge radius must be decreased.

Variable edge designs again performed well under this cutting condition.

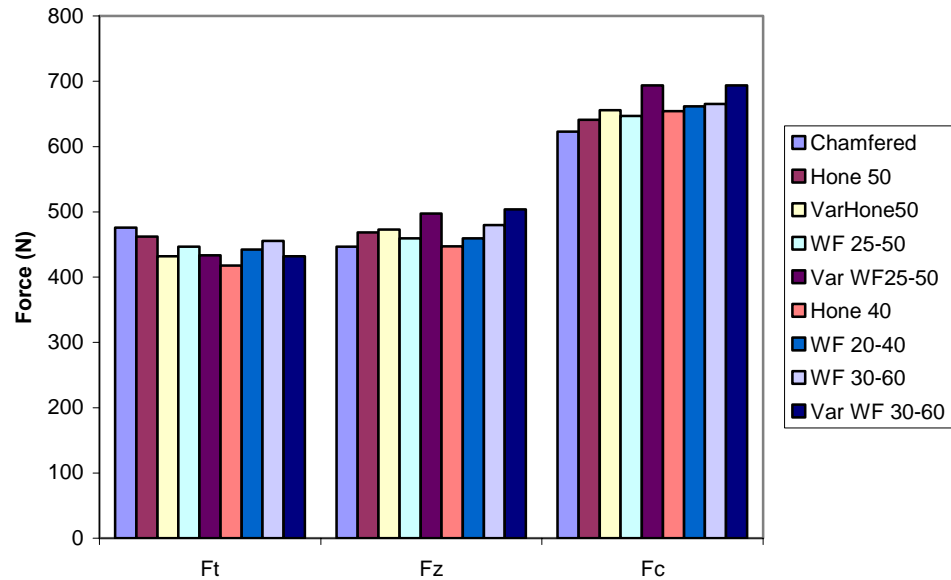


Figure 6.9 Measured cutting forces at the cutting condition of

$V=125$ m/min, $f=0.1$ mm/rev, $d=1$ mm.

Figure 6.10 shows the cutting force measurement when cutting speed is increased to $V=175$ m/min where the variable waterfall hone with 25-50 μ m edge preparation performed far better than other edge preparations. Variable edge preparations again outperformed the uniform edge preparations. Increasing cutting speed resulted in decreased cutting forces as expected.

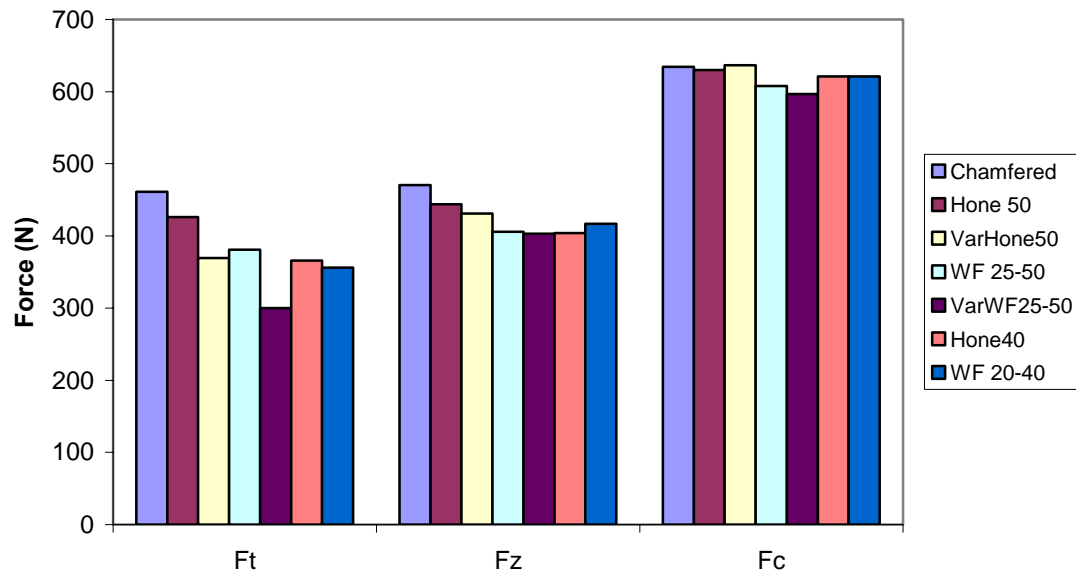


Figure 6.10 Measured cutting forces at the cutting condition of

$$V=175 \text{ m/min}, f=0.1 \text{ mm/rev}, d=1 \text{ mm}$$

Fig 6.11 and 6.12 demonstrate the cutting force measurements when depth of cut is decreased to 0.5 mm. It must be noted that the corner radius of the cutting tools used in our experiments are $R=1.2 \text{ mm}$ which means that the cutting will be performed by the tip of the tool ($d < R$). As expected, the rubbing effects are expected to be dominant in this cutting condition case which is evident from thrust forces nearly equal to cutting forces. Variable edge preparations yielded the lowest cutting forces.

It must be noted that, in this study, no attempts were made to validate edge preparation dimensions. It is known that the dimensions may vary from tool to tool due to inaccuracies during edge preparation process. As an example, variable waterfall hone

with 30-60 microns edge dimension yielded unexpectedly high force measurements in Fig 6.11 probably due to above mentioned reasons.

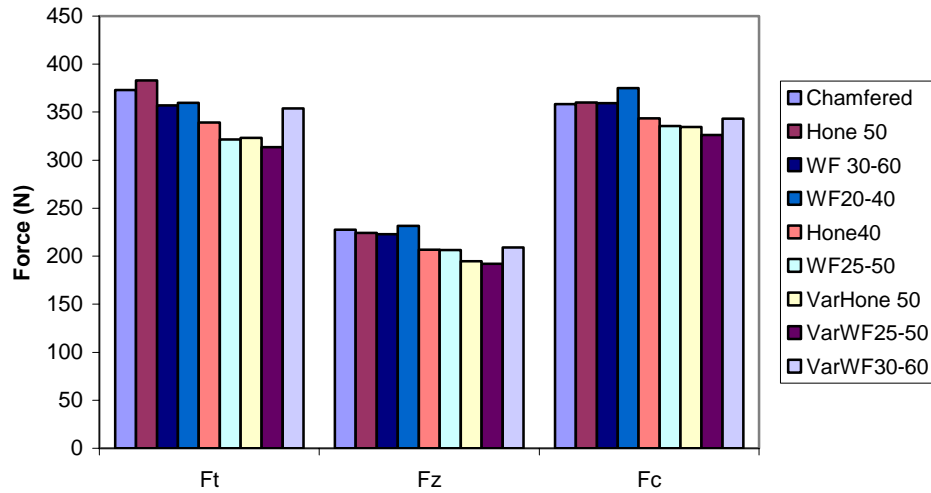


Figure 6.11 Measured cutting forces at the cutting condition of

$V=175\text{m/min}$, $f=0.1\text{ mm/rev}$, $d=0.5\text{mm}$

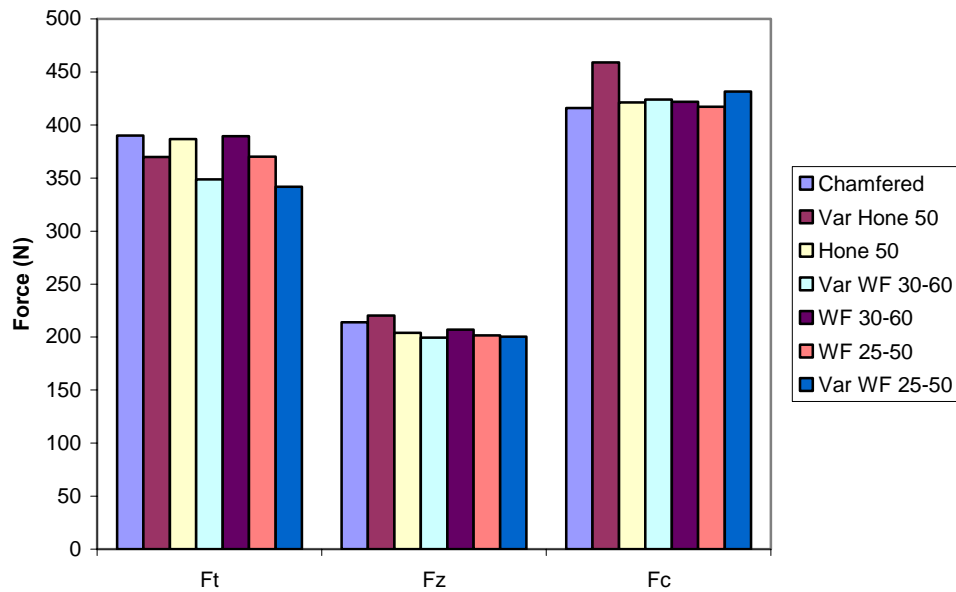


Figure 6.12 Measured cutting forces at the cutting condition of

$V=175\text{m/min}$, $f=0.15\text{ mm/rev}$, $d=0.5\text{mm}$

6.5 3D Finite Element Analysis

In this study, a Finite Element Analysis (FEA) software (Deform 3D) is used to study the effects of uniform chamfered, uniform honed and variable honed edge preparations.

The workpiece is modeled as rigid-perfectly plastic material where the material constitutive model of this deformable body is represented with Johnson-Cook (1983) material model where $A=1504$ MPa, $B=569$ MPa, $n=0.22$, $C=0.003$, $m=0.9$ are the parameters for AISI 4340 steel as given by Grey et al. (1994). Workpiece is represented by a curved model with 70 mm diameter which is consistent with the experimental conditions. Only a segment (15 degrees) of the workpiece was modeled in order to keep the size of mesh elements small. Workpiece model includes 140000 elements. The bottom surface of the workpiece is fixed in all directions. The cutting tool is modeled as a rigid body which moves at the specified cutting speed by using 100000 elements. Thermal boundary conditions are defined accordingly in order to allow heat transfer from workpiece to cutting tool. The FEM software DEFORM 3D is based on an implicit Lagrangian computational routine with continuous adaptive remeshing. A very fine mesh density is defined at the tip of the tool and at the cutting zone to obtain fine process output distributions. The minimum element size for the workpiece mesh was set to 0.015 mm. All simulations were run at the same cutting condition (cutting speed of $V=125$ m/min, feed rate of $f=0.15$ mm/rev, and depth of cut of $d=1$ mm). A workpiece material damage model proposed by Cockcroft-Latham (1966) was also used in simulations.

As discussed earlier, finite element simulations are very sensitive to friction model used at the tool/chip-workpiece interface. Usually a constant friction factor or coefficient of friction is used to define friction model. It has been shown in Chapter 5 that friction modeling is more complex than that and requires the information of sticking and sliding regions. However, definition of these regions in 3D cutting is not as straightforward as orthogonal 2D cutting since chip load varies on the rake face of the tool. In order to investigate the effect of friction factor on finite simulation outputs, a sensitivity analysis is performed. The effect of three different friction factors on the process outputs such as predicted cutting forces and maximum tool temperatures are shown for honed and variable hone cutting tools in Table 6.2.

Table 6.2 The effect of friction factor on process outputs

	Variable Hone 50				Uniform Hone 50			
Friction Factor	Ft (N)	Fc (N)	Fz (N)	Tool Temp, C	Ft (N)	Fc (N)	Fz (N)	Tool Temp, C
0.4	220	635	220	545	278	820	390	630
0.7	260	785	270	656	362	900	500	760
0.85	380	820	390	690	440	939	515	775

According to these results, as friction factor increases, cutting forces and tool temperatures increase as expected. Decreasing friction factor results in thinner and curled chips. Fig. 6.13 represents the simulated and measured cutting forces, it can be seen that finite element simulation tends to under predict the thrust and feed forces while cutting

force prediction is agreement with measured forces. In obtaining results given in Fig. 6.13, friction factors of 0.9, 0.92, and 0.85 are found to be the most suitable for the simulations with uniform chamfered, uniform honed and variable honed inserts respectively. The reason honed tools have lower friction factor may be related to its blunter edge compared to variable hone and chamfered tools. The FEM software DEFORM 3D version 5.0 does not allow users to define friction windows where sliding and sticking regions can be defined. It allows the definition of friction factor as a function of normal pressure however it also did not improve thrust and feed force predictions and yielded similar results to constant friction factor definition of interface friction between tool and workpiece. It must be noted that even though a higher friction factor used in simulations, variable hone force predictions are still lower than honed and chamfered tools.

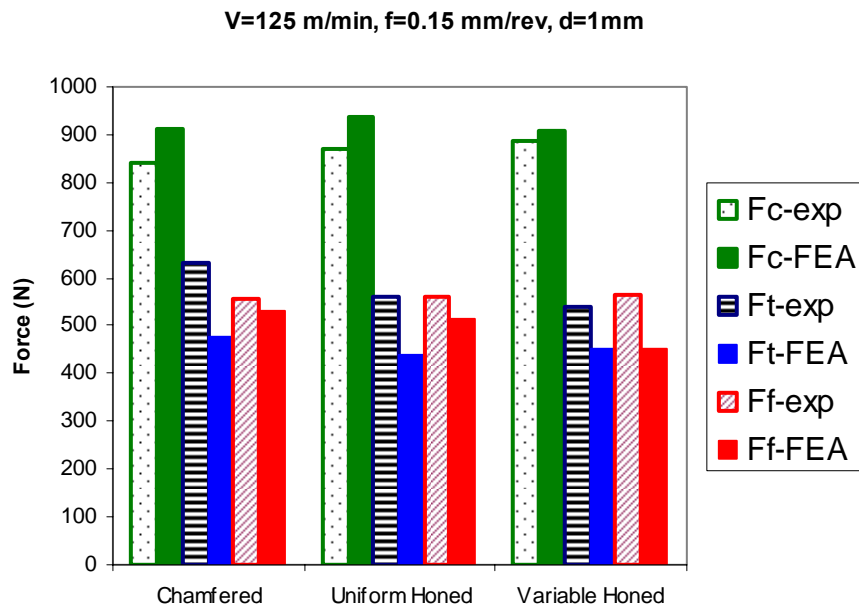
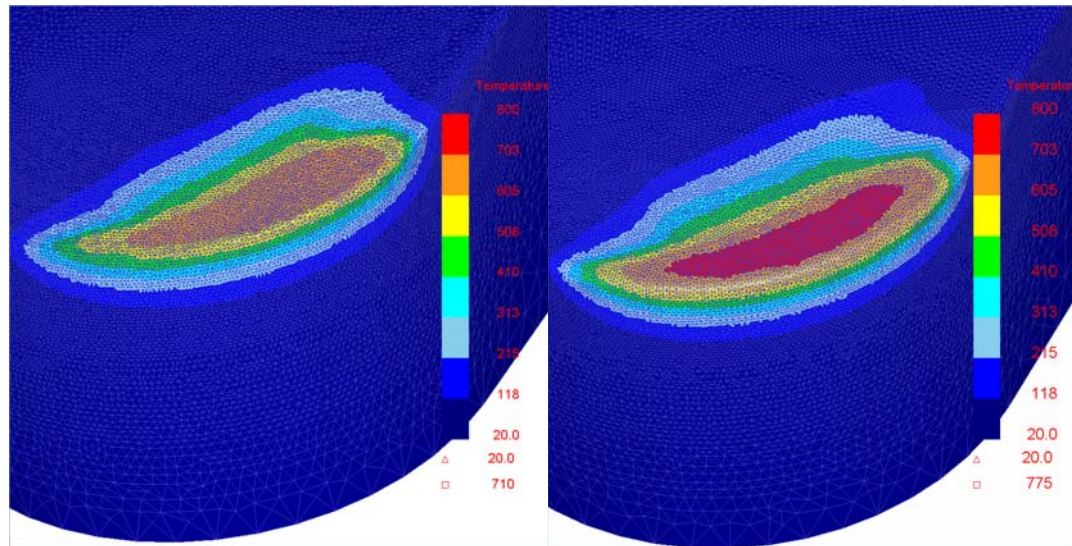


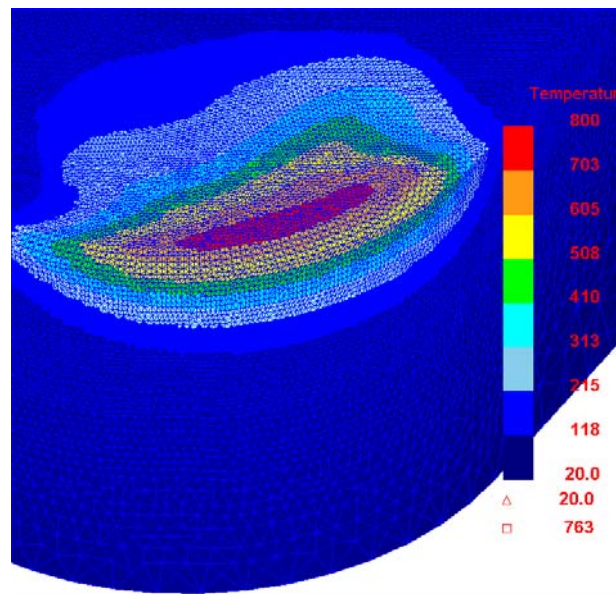
Figure 6.13 Comparison of measured and simulated forces for various micro-geometry inserts

Predicted temperature distributions on the tool are shown in Fig. 6.14 for three different edge preparation inserts.



(a)

(b)



(c)

Figure 6.14 Temperature distributions simulated for machining with
(a) variable honed, (b) uniform honed, and (c) uniform chamfered inserts

Temperature distributions in Fig 6.14 depict that smallest hot zone formed on the variable honed tool and maximum temperatures of 710 °C, 775 °C and 763 °C were predicted for variable honed, uniform honed and, uniform chamfered inserts respectively.

According to our findings in Chapter 5, friction factor must increase at the trailing edge of the cutting tool. This increase is also believed to affect the chip morphology. In order to investigate the effects of various edge preparations on chip morphology, the photographs of collected chips (cutting speed of $V=125$ m/min, feed rate of $f = 0.15$ mm/rev, and depth of cut of $d=1$ mm) are shown in Fig 6.15 and measurements of chip curling (diameter and pitch) taken from chips are listed on Table 6.3

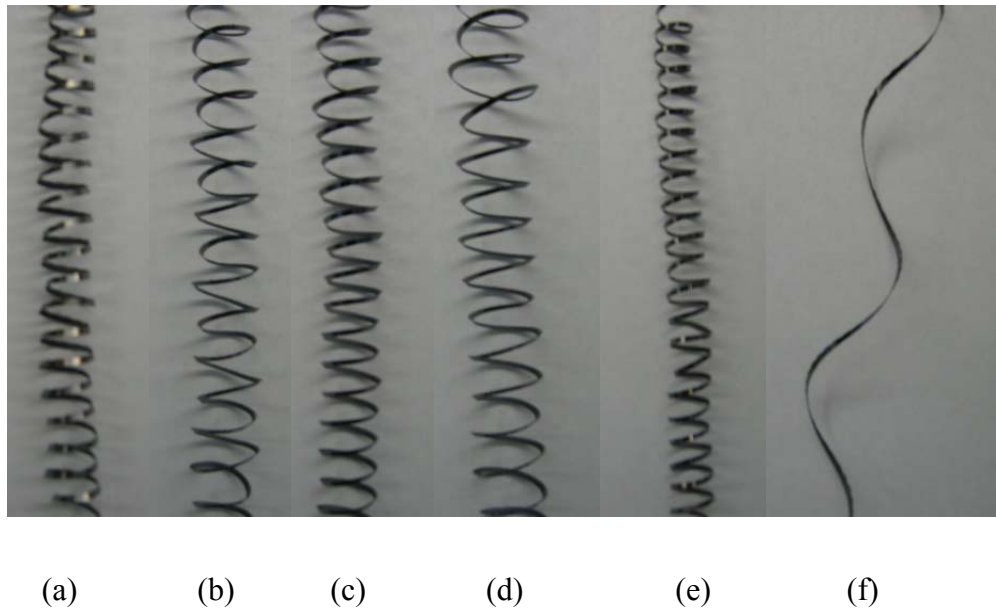


Figure 6.15 Photographs of collected chips: (a) Uni. Hone 50μm, (b) Var Hone 50 μm, (c) Uni. Waterfall Hone 25:50 μm, (d) Variable Waterfall 25:50 μm, (e) Uni. Waterfall Hone 30:60 μm, (f) Chamfered.

Table 6.3 Chip diameter and pitch measurements

	Chip Diameter (mm)	Pitch (mm)
Uniform Hone 50 μm	12.7	6.35
Variable Hone 50 μm	19.05	12
Uni. Waterfall Hone 25:50 μm	15.87	9.52
Variable Waterfall 25:50 μm	19	11.1
Uni. Waterfall Hone 30:60 μm	13	7.95

It is observed that, uniform edge preparations resulted in chips smaller in diameter and pitch than variable edge preparations. The chips produced by uniform hone 50 μm and uniform waterfall 30:60 μm are quite similar. Chamfered tool produced long and straight chips which are not desirable in practical cutting conditions since they tend to accumulate around the cutting edge and scratch the surface.

Temperature distributions in the chip and workpiece for uniform chamfered, uniform honed, and variable hone obtained from finite element simulations are shown in Fig. 6.16. Workpiece temperatures are observed to be higher when machining with chamfered tools. Fig. 6.17 demonstrates the effectiveness of using variable hone edge preparation. Effective strains at the root of the chip are found to be lower in variable edge design which confirms the basic premise of variable edge design. Low strains, which mean less rubbing action, are believed to decrease cutting temperatures at the trailing edge of the cutting tool. SEM images of the chips produced by these edge preparations are shown in Fig. 6.18 where continuous chips were obtained with a little serration.

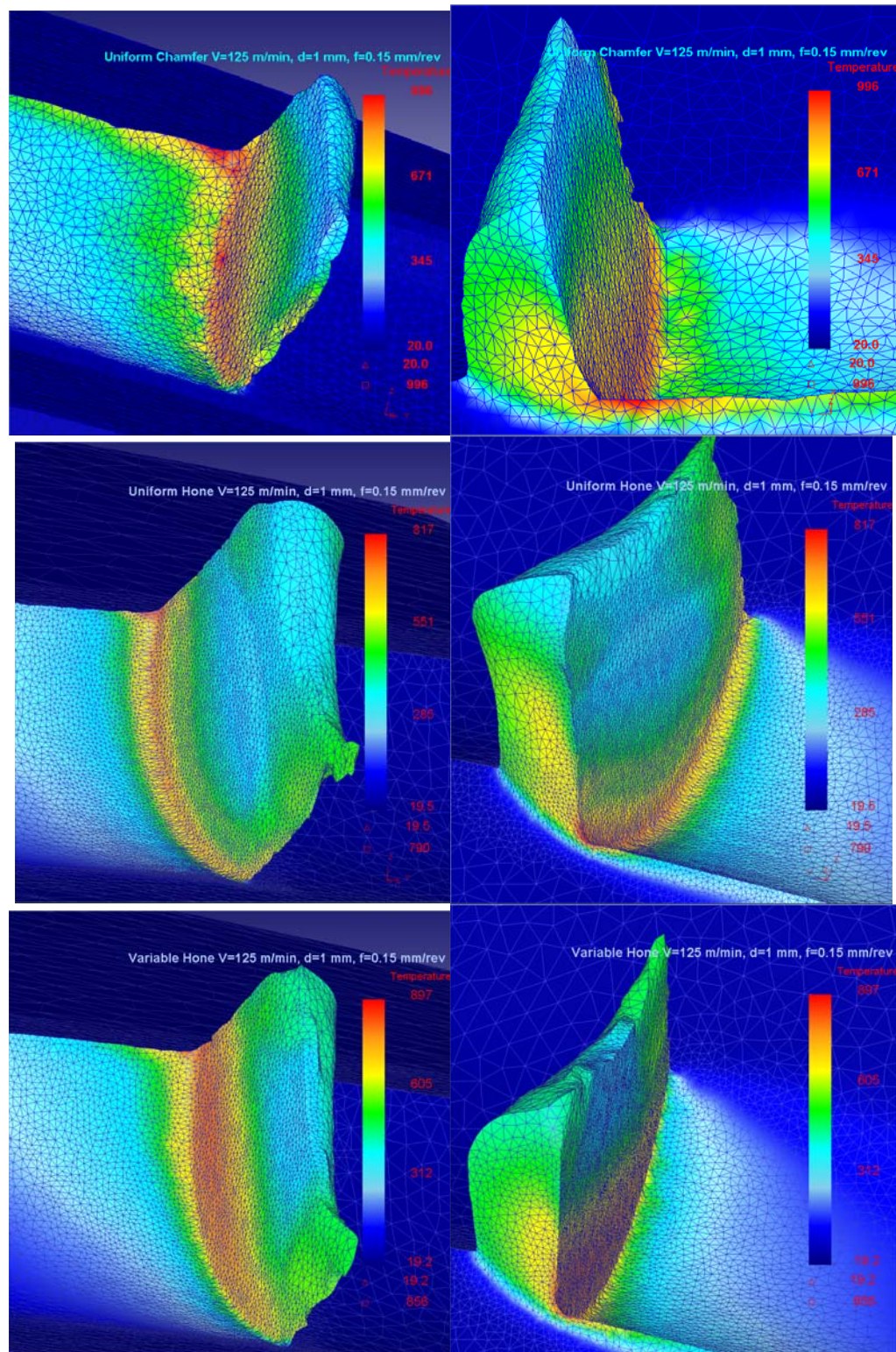


Figure 6.16 Temperature distributions in the chip and workpiece

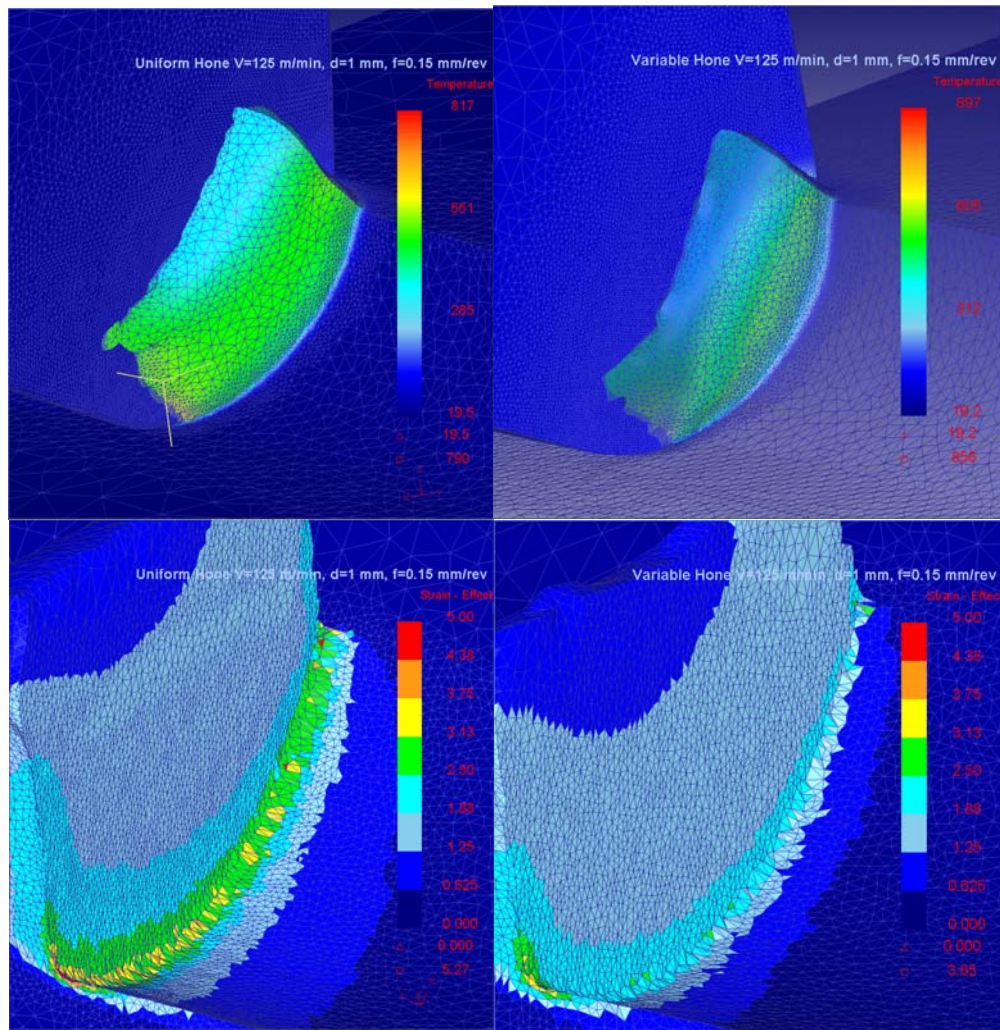
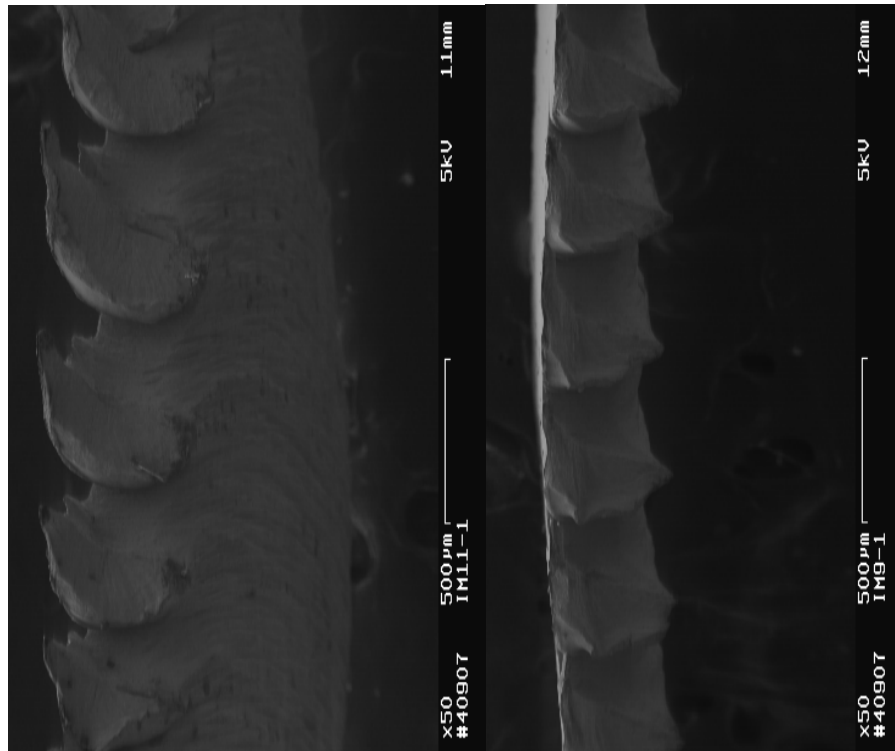
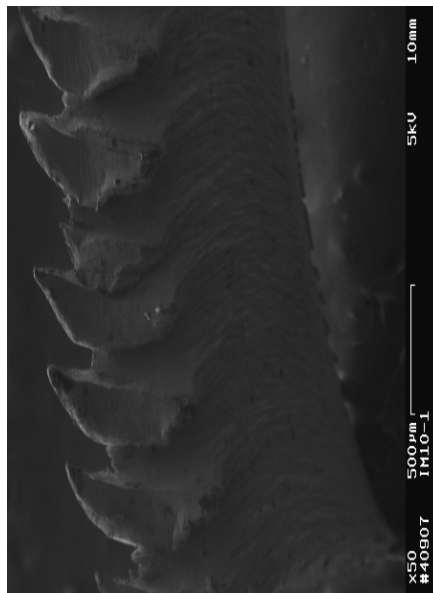


Figure 6.17 Effective strain distributions at the cutting zone for uniform honed and variable honed inserts.



(a)

(b)



(c)

Figure 6.18 SEM images of chip shapes produced by (a) uniform chamfered, (b) uniform honed and (c) variable hone inserts.

6.6 Tool Wear Analysis Using 3-D FEA

Finite element simulations can also be utilized to predict tool wear. The distributions of the process variables such as effective stresses, temperatures and sliding velocities allows the simulation of the tool wear on the tool rake and flank faces when combined with a tool wear model. The important factors affecting tool wear are: (i) the workpiece material and its physical properties, (ii) the tool-chip and tool-workpiece interface conditions (lubricated or dry cutting), (iii) the cutting tool properties such as tool material, coatings, and edge preparation, (iv) the dynamic characteristics of the machining process such as chatter.

The tool wear rate models describe the rate of volume loss on the tool rake and flank faces per unit area per unit time. There are many different tool wear rate models proposed in literature depending on the type of tool wear i.e. adhesive, diffusive, etc. The tool wear rate model based on the adhesive wear proposed by Usui et al. (1978) is adapted in this study. Usui tool wear rate model, as given in Eq. (6.2), uses interface temperature (T), normal stress (σ), and sliding velocity (V_s) at the contact surfaces as inputs and yields tool wear rate (flank or crater) for a given location on the tool surface.

$$\frac{dVB}{dt} = c_1 \sigma_n V_s e^{(-c_2/T)} \quad (6.2)$$

The tool wear rate models usually have unknown coefficients (c_1 and c_2 in Usui tool wear model) that need to be calibrated depending on the workpiece and tool

materials. In this study, unknown coefficients in Eq (6.2) is taken from literature as $c_1=1\text{e-}6$ and $c_2=900$ and used in finite element simulations. Fig. 6.18 shows the simulated tool wear zones on the tool for uniform chamfered, uniform honed, and variable honed cutting tools.

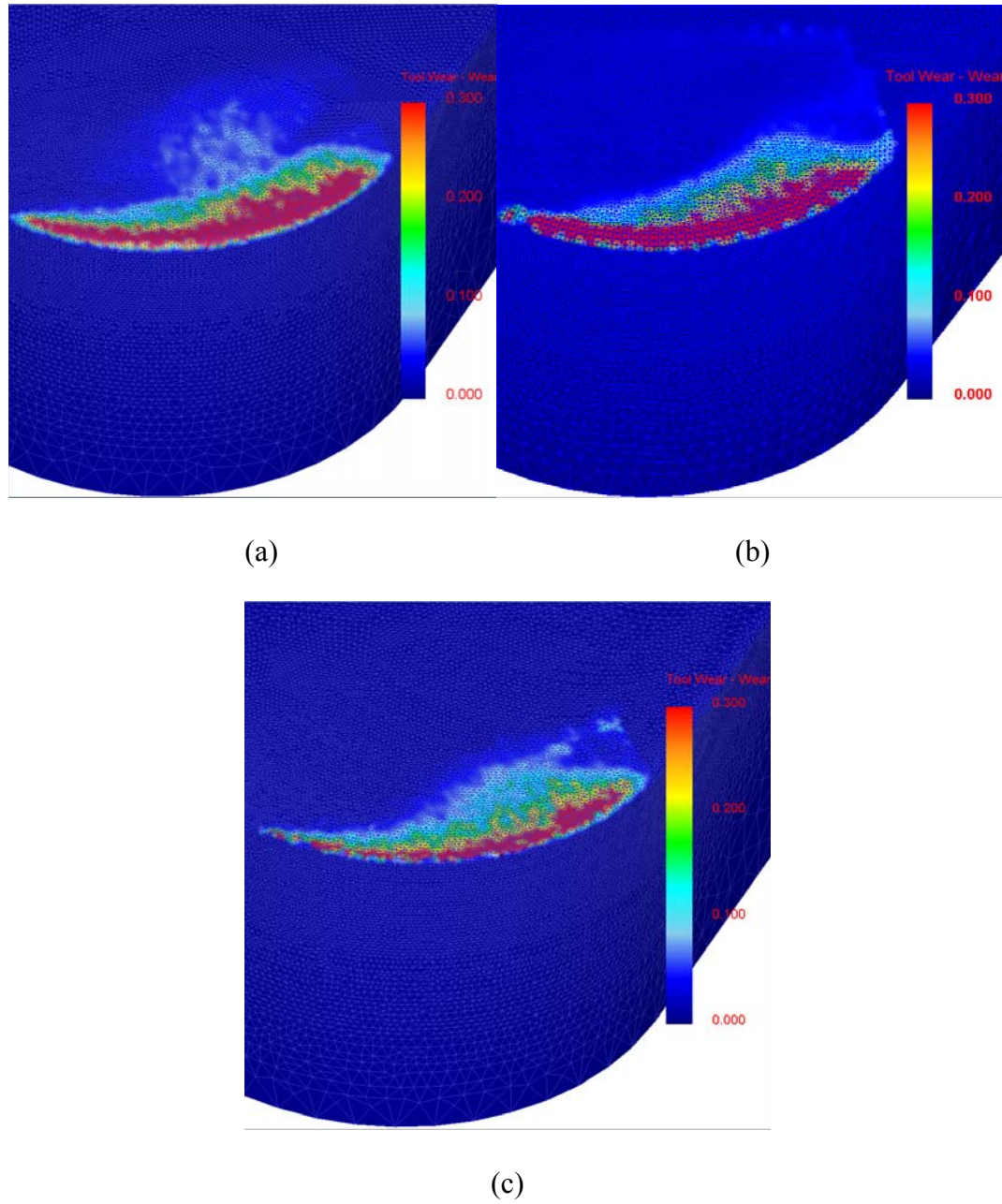


Figure 6.19 Tool wear simulations for machining with (a) honed inserts, (b) uniform chamfered and (c) variable honed.

It must be noted that different tool wear constants for different cutting edges might be obtained if experimental tool wear data were used to calibrate tool wear rate constants c_1 and c_2 . This approach is performed to observe the combined effect of normal stresses and temperatures on the cutting tools.

6. 7 Conclusions

In this chapter, a methodology is proposed for variable cutting tool micro-geometry design. Bar turning experiments and 3-D finite element analysis are performed to compare uniform and variable edge preparations. These results revealed that the variable edge preparation inserts perform better than uniform edge preparation counterparts if the variable edge is properly designed for the given cutting conditions. 3-D FEA based process simulations are utilized for predicting forces, stresses, and tool wear. Tool wear simulations are considered to represent combined effect of normal stress and temperatures which clearly demonstrated the effectiveness of variable edge preparations. The effect of edge preparation on chip formation is investigated. Preliminary findings suggest that variable edge preparations result in curled chips larger in diameter than uniform edge preparations.

CHAPTER 7

ACHIEVEMENTS AND FUTURE WORK

This dissertation is motivated by the need of understanding the influence of edge preparations on the mechanics of metal cutting. The ultimate goal in current metal cutting research is to select optimum cutting tool micro-geometry and cutting conditions for a given process by using analytical and computational methods. The objectives of this study were; to improve existing analytical predictive modeling techniques, to combine favorable aspects of analytical methods and finite element analysis to study cutting tool micro-geometry, and to optimize cutting conditions in hard turning. Physics-based analytical predictive models and computational finite element simulations were performed to investigate machining with sharp, worn, chamfered, honed, and waterfall hone cutting tools. Modeling of tool life, tool wear, and surface roughness are very difficult to model by using analytical and computational methods. Therefore, an experimental method which uses neural network modeling and evolutionary algorithm is proposed to obtain optimum cutting conditions in hard turning for given experimental data. Main achievements of this study towards the above mentioned objectives are listed as follows:

1. Experimental Modeling and Optimization of Cutting Conditions in Hard Turning (Chapter 2)

- A modular neural network model is used to predict tool wear and surface roughness for a given cutting condition. In neural network model, the effect of tool wear on surface roughness is considered due to experimental observations of decreasing surface roughness with increasing tool wear. Increasing tool wear has a sharpening effect on the tool edge which results in improved surface on the workpiece for a while. (Ozel and Karpaz (2005))
- Swarm Intelligent Neural Network System (SINNS) is proposed and employed to calculate optimum cutting conditions in hard turning for given experimental data. The effectiveness of the proposed approach is demonstrated on several case studies. According to authors' best knowledge; it is the first study where multi objective optimization is applied to machining optimization. (Karpaz and Ozel (2007b))

2. Analytical and Thermal Modeling of Orthogonal Cutting Process (Chapter 3)

- Oxley's (1986) predictive machining model is improved by integrating Zorev (1963) friction model to the secondary shear zone. Integrated friction model together with Johnson-Cook (1983) material constitutive model allowed the calculation of sticking and sliding zones and non-linear heat intensity on the secondary shear zone which in turn yielded more accurate and reasonable temperature distributions at the cutting zone. Non-linear heat partition at the

tool-chip interface is calculated. The effect of rake angle on the normal stress at the tool-chip interface is demonstrated. (Karpata and Ozel (2006a))

- Oxley's (1986) model is extended for worn tool case. Worn tool model helped explaining the heat partition phenomenon between workpiece and worn tool flank face (Karpata and Ozel (2006b))

3. Analytical and Thermal Modeling of High Speed Machining with Chamfered Tools (Chapter 4)

- A slip-line field adopted from literature and experimental cutting tests are employed to investigate the behavior of dead metal zone which was overlooked by many previous studies.
- An analytical thermal model is proposed for machining with chamfered tools and the effect of dead metal zone on the temperature distributions at the cutting zone is studied. Analytical thermal model uses identified friction factors and yielded temperature distributions similar to those obtained from finite element simulations. The analytical thermal model simulates the temperature distributions in a very short time. According to authors' best knowledge, it is the first study to model analytical temperature distributions in chamfered cutting tools. (Karpata and Ozel (2006c))

4. Mechanics of High Speed Cutting With Curvilinear Edge Tools (Chapter 5)

- Slip-line field analysis is conducted on various curvilinear edge tools to identify friction factors during orthogonal machining. Identified friction factors are used

in finite element simulations to compare the machining characteristics of these edge preparations. Proposed methodology offers a science based way of defining friction factor and reduces the guesswork in finite element simulations.

- The effect of various edge preparations on chip formation is studied. SEM pictures of chips clearly revealed the effect of edge preparation on chip formation.

5. Design and Analysis of Variable Micro-Geometry Cutting Tools (Chapter 6)

- Bar turning experiments were conducted by using cutting tools with uniform and variable edge preparations. The findings of Chapters 4 and 5 are used to explain the mechanics of cutting with variable micro-geometry cutting tools. A design methodology for variable micro-geometry is proposed. This chapter is believed to be the first study on variable micro-geometry cutting tools in literature. (Karpat et al. (2007c))

Some future work directions based on the topics studied in this dissertation are listed below:

1. The analytical thermal model given in Chapter 2 and 3 for machining with sharp, worn and chamfered tools can be modified for minimum quantity lubrication (MQL) machining conditions. One of the advantages of using hard turning is eliminate cutting fluid. However, there are certain advantages of using cutting fluids such as decreasing friction at the interfaces. MQL offers a way to minimize

the cutting fluid consumption during machining since cutting fluid is sprayed to certain locations on the cutting tool.

2. The chamfered too model can be extended to calculate/predict residual stresses in the workpiece. All the necessary information such as stress distribution at the tool-workpiece interface, and temperature distributions in the workpiece are already available from chamfered tool slip-line and analytical thermal model.
3. Although slip-line models explain the mechanics of cutting, they require orthogonal cutting information. Therefore they cannot be fully utilized as predictive models as they are. By implementing minimum energy method as in Oxley's model cutting forces etc. can be predicted. The effect of dead metal zone angle must be considered in the analysis.
4. In order to investigate the cutting conditions where the uncut chip thickness is very small and edge radius of the cutting tool is larger than uncut chip thickness (micromachining), multi-scale finite element analysis which consider the micro-structure of the workpiece can be studied. Fracture mechanisms must be considered since it becomes equally important as shearing in micro scale.
5. In practice, complex surfaces are machined where the chip load on the cutting tool changes depending on the workpiece design features. Methodology proposed in this dissertation can be further extended for these cases.
6. The effect tool coating on process outputs can be easily integrated to proposed analytical and computational models. The combined effect of edge preparation and coating may result in drastic increases in tool life and productivity.

APPENDIX

EXPERIMENTAL TOOL WEAR AND SURFACE ROUGHNESS

DATA

Hardness HRc	Edge* Prep.	Cutting Speed m/min	Feed Rate mm/rev	Cutting Distance in.	Tool Wear mm	Surface Roughness μm
51.3	100	100	0.1	2	0.04	0.385
51.3	100	100	0.1	3	0.05	0.45
51.3	100	100	0.1	4	0.06	0.35
51.3	100	100	0.1	5	0.07	0.3625
51.3	100	100	0.1	6	0.075	0.3675
51.3	100	100	0.1	7	0.1	0.385
51.3	100	100	0.1	8	0.1125	0.37
51.3	10	100	0.2	2	0.044444	1.1825
51.3	10	100	0.2	3	0.05	1.2975
51.3	10	100	0.2	4	0.055556	1.0575
51.3	10	100	0.2	5	0.066667	1.2825
51.3	10	100	0.2	6	0.072222	1.1325
51.3	10	100	0.2	7	0.072222	1.24
51.3	10	100	0.2	8	0.077778	1.2375
51.3	10	100	0.2	9	0.077778	1.2325
51.3	10	100	0.2	10	0.083333	1.185
51.3	10	100	0.2	11	0.088889	1.17
51.3	10	100	0.2	12	0.088889	1.3425
51.3	10	100	0.2	13	0.094444	1.2525
51.3	10	100	0.2	14	0.094444	1.3275
51.3	10	100	0.2	15	0.094444	1.4
51.3	10	100	0.2	16	0.1	1.3275
51.3	10	200	0.2	1	0.044444	0.9625
51.3	10	200	0.2	2	0.044444	0.565
51.3	10	200	0.2	3	0.05	0.19
51.3	10	200	0.2	4	0.055556	0.19
51.3	10	200	0.2	5	0.066667	0.1725
51.3	10	200	0.2	6	0.077778	0.16
51.3	10	200	0.2	7	0.088889	0.16
51.3	10	200	0.1	1	0.044444	0.78
51.3	10	200	0.1	2	0.044444	0.56
51.3	10	200	0.1	3	0.055556	0.545
51.3	10	200	0.1	5	0.055556	0.655

51.3	10	200	0.1	6	0.066667	0.66
51.3	10	200	0.1	7	0.072222	0.68
51.3	10	200	0.1	8	0.072222	0.405
51.3	10	200	0.1	9	0.088889	0.3575
51.3	10	200	0.1	10	0.088889	0.37
51.3	10	200	0.1	11	0.088889	0.3425
51.3	10	200	0.1	12	0.088889	0.32
51.3	10	200	0.1	13	0.094444	0.3475
51.3	10	200	0.1	14	0.094444	0.3325
51.3	10	200	0.1	15	0.094444	0.26
51.3	10	200	0.1	16	0.094444	0.2925
51.3	10	100	0.1	1	0.05625	0.4725
51.3	10	100	0.1	2	0.0625	0.475
51.3	10	100	0.1	3	0.06875	0.485
51.3	10	100	0.1	4	0.06875	0.5025
51.3	10	100	0.1	5	0.10625	0.49375
51.3	10	100	0.1	6	0.13125	0.41
51.3	10	100	0.1	7	0.13125	0.405
51.3	10	100	0.1	8	0.1375	0.44
51.3	10	100	0.1	9	0.15	0.4425
51.3	10	100	0.1	10	0.15	0.47
51.3	10	100	0.1	11	0.15	0.3775
51.3	10	100	0.1	12	0.1625	0.405
51.3	10	100	0.1	13	0.1625	0.3575
51.3	10	100	0.1	14	0.16875	0.4
51.3	10	100	0.1	15	0.175	0.3
51.3	10	100	0.1	16	0.175	0.3725
51.3	100	200	0.1	1	0.0375	0.415
51.3	100	200	0.1	2	0.0625	0.385
51.3	100	200	0.1	3	0.075	0.385
51.3	100	200	0.1	4	0.08125	0.3875
51.3	100	200	0.1	5	0.1	0.355
51.3	100	200	0.1	6	0.125	0.3075
51.3	100	200	0.1	7	0.125	0.2725
51.3	100	200	0.1	8	0.125	0.2675
51.3	100	200	0.1	9	0.125	0.3875
51.3	100	200	0.1	10	0.13125	0.305
51.3	100	200	0.1	11	0.1375	0.3025
51.3	100	200	0.1	12	0.1625	0.2475
51.3	100	200	0.1	13	0.175	0.315
51.3	100	200	0.1	14	0.18125	0.3375
51.3	100	200	0.1	15	0.1875	0.255
51.3	100	200	0.1	16	0.2	0.285
51.3	100	100	0.2	1	0.05	1.2125
51.3	100	100	0.2	2	0.05625	1.2125
51.3	100	100	0.2	3	0.075	1.08
51.3	100	100	0.1	4	0.06	0.35
51.3	100	100	0.2	5	0.08125	1.4
51.3	100	100	0.2	6	0.08125	1.4225

51.3	100	100	0.2	7	0.08125	1.57
51.3	100	100	0.2	8	0.08125	1.5275
51.3	100	100	0.2	9	0.0875	1.46
51.3	100	100	0.2	10	0.09375	1.395
51.3	100	100	0.2	11	0.09375	1.5575
51.3	100	100	0.2	12	0.09375	1.6725
51.3	100	100	0.2	13	0.09375	1.635
51.3	100	100	0.2	14	0.1	1.5925
51.3	100	100	0.2	15	0.1	1.71
51.3	100	100	0.2	16	0.1	1.76
54.7	100	100	0.1	1	0.0625	0.485
54.7	100	100	0.1	2	0.0875	0.4675
54.7	100	100	0.1	3	0.1	0.55
54.7	100	100	0.1	4	0.125	0.445
54.7	100	100	0.1	5	0.15	0.47
54.7	100	100	0.1	6	0.1625	0.4375
54.7	100	100	0.1	7	0.15625	0.6075
54.7	100	100	0.1	8	0.1625	0.62
54.7	100	100	0.1	9	0.16875	0.64
54.7	100	100	0.1	10	0.175	0.5725
54.7	100	100	0.1	11	0.18125	0.5
54.7	100	100	0.1	12	0.1875	0.5875
54.7	100	100	0.1	13	0.19375	0.5375
54.7	100	100	0.1	14	0.19375	0.6925
54.7	100	100	0.1	15	0.2	0.7025
54.7	100	100	0.1	16	0.2	1.05875
54.7	100	200	0.1	1	0.075	0.39
54.7	100	200	0.1	2	0.0875	0.5275
54.7	100	200	0.1	3	0.1	0.5925
54.7	100	200	0.1	4	0.11875	0.54
54.7	100	200	0.1	5	0.1375	0.6075
54.7	100	200	0.1	6	0.15625	0.555
54.7	100	200	0.1	7	0.18125	0.5925
54.7	100	200	0.1	8	0.2	0.6075
54.7	100	200	0.1	9	0.2125	0.505125
54.7	100	200	0.1	10	0.225	0.5075
54.7	100	200	0.1	11	0.225	0.4825
54.7	100	200	0.1	12	0.2375	0.4925
54.7	100	200	0.1	13	0.24375	0.385
54.7	100	200	0.1	14	0.25	1.1375
54.7	100	200	0.1	15	0.25	0.4725
54.7	100	200	0.1	16	0.25	0.43
54.7	100	100	0.2	1	0.0375	1.24
54.7	100	100	0.2	2	0.0375	1.0825
54.7	100	100	0.2	3	0.04375	1.2775
54.7	100	100	0.2	4	0.05	1.4275
54.7	100	100	0.2	5	0.05625	1.5175
54.7	100	100	0.2	6	0.0625	1.2175
54.7	100	100	0.2	7	0.0625	1.70375

54.7	100	200	0.2	1	0.0375	1.23
54.7	100	200	0.2	2	0.05	1.1275
54.7	100	200	0.2	3	0.0875	1.1525
54.7	100	200	0.2	4	0.1	1.06
54.7	100	200	0.2	5	0.11875	1.07
54.7	100	200	0.2	6	0.125	1.0725
54.7	100	200	0.2	7	0.13125	1.2325
54.7	100	200	0.2	8	0.1375	1.1825
54.7	100	200	0.2	9	0.1375	1.095
54.7	100	200	0.2	10	0.25	0.8675
54.7	100	200	0.2	11	0.14375	1.04
54.7	100	200	0.2	12	0.14375	1.0625
54.7	100	200	0.2	13	0.14375	1.265
54.7	100	200	0.2	14	0.14375	1.1725
54.7	100	200	0.2	15	0.15	1.1325
54.7	100	200	0.2	16	0.15	1.1475
54.7	10	100	0.1	2	0.05	0.28125
54.7	10	100	0.1	3	0.06875	0.315
54.7	10	100	0.1	5	0.125	0.4825
54.7	10	100	0.1	6	0.125	0.4475
54.7	10	100	0.1	7	0.13125	0.43125
54.7	10	100	0.1	8	0.13125	0.35
54.7	10	100	0.1	9	0.35	0.2875
54.7	10	200	0.1	2	0.0125	0.29625
54.7	10	200	0.1	3	0.05	0.30625
54.7	10	200	0.1	4	0.06875	0.30125
54.7	10	200	0.1	5	0.0875	0.31625
54.7	10	200	0.1	6	0.1	0.33
54.7	10	200	0.1	7	0.125	0.32125
54.7	10	200	0.1	8	0.125	0.345
54.7	10	200	0.1	9	0.15	0.36125
54.7	10	200	0.1	10	0.1375	0.34875
54.7	10	200	0.1	11	0.14375	0.37125
54.7	10	200	0.1	12	0.15	0.37625
54.7	10	200	0.1	13	0.1625	0.3375
54.7	10	200	0.1	14	0.1625	0.33
54.7	10	200	0.1	15	0.1625	0.35
54.7	10	200	0.1	16	0.1625	0.38875
54.7	10	100	0.2	1	0.046512	0.34125
54.7	10	100	0.2	2	0.046512	0.3825
54.7	10	100	0.2	3	0.081395	0.42375
54.7	10	100	0.2	4	0.081395	0.4725
54.7	10	100	0.2	5	0.093023	0.515
54.7	10	100	0.2	6	0.116279	0.4475
54.7	10	100	0.2	7	0.116279	0.43125
54.7	10	100	0.2	8	0.116279	0.48875
54.7	10	100	0.2	9	0.116279	0.56875
54.7	10	100	0.2	10	0.127907	0.5525

54.7	10	100	0.2	11	0.127907	0.5425
54.7	10	100	0.2	12	0.127907	0.54
54.7	10	100	0.2	13	0.127907	0.51875
54.7	10	100	0.2	14	0.127907	0.5275
54.7	10	100	0.2	15	0.127907	0.5275
54.7	10	100	0.2	16	0.133721	0.51
54.7	10	200	0.2	1	0.034884	1.06125
54.7	10	200	0.2	2	0.046512	1.0675
54.7	10	200	0.2	3	0.05814	1.06125
54.7	10	200	0.2	4	0.05814	1.025
54.7	10	200	0.2	5	0.069767	1.06375
54.7	10	200	0.2	6	0.081395	1.03875
54.7	10	200	0.2	7	0.081395	1.0125
54.7	10	200	0.2	8	0.093023	1.02625
54.7	10	200	0.2	9	0.093023	1.03625
54.7	10	200	0.2	10	0.093023	1.0875
54.7	10	200	0.2	11	0.104651	0.97875
54.7	10	200	0.2	12	0.104651	0.96125
54.7	10	200	0.2	13	0.110465	0.9375
54.7	10	200	0.2	14	0.110465	0.935
54.7	10	200	0.2	15	0.116279	0.91
54.7	10	200	0.2	16	0.122093	0.8475
54.7	10	200	0.05	1	0.023256	0.19125
54.7	10	200	0.05	2	0.034884	0.175
54.7	10	200	0.05	3	0.063953	0.22875
54.7	10	200	0.05	4	0.069767	0.26875
54.7	10	200	0.05	5	0.093023	0.27625
54.7	10	200	0.05	6	0.098837	0.26125
54.7	10	200	0.05	7	0.098837	0.245
54.7	10	200	0.05	8	0.104651	0.23

*Edge Prep 10: Honed tool, Edge Prep. 100: Chamfered tool

REFERENCES

- Abdel-Moneim M. Es., R.F. Scrutton, (1974), "Tool Edge Roundness and Stable Built-Up Formation in Finish Machining", *ASME Journal of Engineering for Industry*, pp. 1258-1267.
- Abebe M., and Appl F.C., 1981 "A Slip Line Solution For Negative Rake Angle Cutting", *Transactions of NAMRI/SME*, Vol. 19, pp 341-348.
- Adibi-Sedeh A.H., V. Madhavan, B. Bahr, (2003), "Extension of Oxley's analysis of machining to use different material models", *ASME Journal of Manufacturing Science and Engineering*, Vol 125, pp. 656-666.
- Albrecht P., (1960), "New Developments in Theory of the Metal Cutting Process in Metal Cutting", *ASME Journal of Engineering for Industry*, pp. 348-357.
- Altintas Y., (2000), "Metal Cutting Mechanics, Machine Tool Vibrations, and CNC Design", Cambridge University Press.
- Astakhov VP. (1999), Metal cutting mechanics. Boca Raton, FL: CRC Press.
- Atkins A.G., (2003), "Modelling metal cutting using modern ductile fracture mechanics: quantitative explanations for some longstanding problems", *International Journal of Mechanical Sciences*, Vol. 45, pp.373-396
- Azouzi R., M. Guillot, (1997), "On-line prediction of surface finish and dimensional deviation in turning using neural network based sensor fusion", *International Journal of Machine Tools and Manufacture*, Vol. 37, No 9, pp. 1201-1217.
- Barry J., G. Byrne, (2001) "Cutting tool wear in the machining of hardened steels, Part II: CBN cutting tool wear", *Wear*, Vol. 247, pp. 152-160.
- Benardos P.G, G.C. Vosniakos, (2003), "Predicting Surface Roughness in Machining: A Review", *International Journal of Machine Tools and Manufacture*, Vol. 43, 2003, pp. 833-844.
- Benitez J.E, R.M. Everson, J.E. Fieldsend, (2005), "A MOPSO Algorithm Based Exclusively on Pareto Dominance Concepts", *Evolutionary Multi-Criterion Optimization*, pp. 459-473.
- Boothroyd G., (1963), "Temperatures in orthogonal metal cutting", *Proc. Inst. Mech. Eng.*, 177, pp. 789-810.

Budak E., Y. Altintas, (1993), "Prediction of Milling Force Coefficients from Orthogonal Data", *ASME Journal of Manufacturing Science and Engineering*, Vol. 64, pp. 453-460.

Carslaw H.S, J.C. Jaeger, (1959), *Conduction of Heat in Solids*, Oxford University Press, Oxford.

Ceretti E., C. Lazzaroni, L. Menegardo, T. Altan, (2000), "Turning simulations using a three-dimensional FEM code", *Journal of Materials Processing Technology*, Vol. 98, pp. 99-103.

Childs T.H.C, Maekawa K., and Obikawa T., Yamane Y., (2000), "Metal Machining Theory and Applications". London. Butterworth-Heinemann, U.K.

Childs T.H.C., (2006), "Numerical experiments on the influence of material and other variables on plane strain continuous chip formation in metal machining", *International Journal of Mechanical Sciences*, Vol 48, pp. 307-322.

Chao B.T, K.J Trigger, (1953), "The significance of the thermal number in metal machining", *Transactions of ASME*, (1953), 75, 109-120.

Chao B.T, H.L. Li, K.J. Trigger, (1961), "An experimental investigation of temperature distribution at tool-flank surface", *Trans. ASME, J. Engineering for Industry*, 83 (4), 496-504.

Chen L., T.I. El-Wardany, M. Nasr, M.A. Elbestawi, (2006), "Effects of edge preparation and feed when hard turning a hot work die steel with polycrystalline cubic boron nitride tools," *Annals of the CIRP*, Vol. 55/1, pp. 89-92.

Chou Y.K, C. J. Evans, (1997), "Tool wear mechanism in continuous cutting of hardened tool steels", *Wear*, Vol. 212, pp.59-65.

Chou Y.K, C. J. Evans, (1999), "White layers and thermal modeling of hard turned surfaces", *Int. J. of Machine Tools and Manufacture*, Vol. 39, pp. 1863–1881.

Chou Y.K, C.J. Evans, M.M. Barash, (2002), "Experimental investigation on CBN turning of hardened AISI 52100 steel", *Journal of Materials Processing Technology*, Vol. 124, pp. 274-283.

Choudry S.K., G. Bartarya, (2003), "Role of temperature and surface finish in predicting tool wear using neural network and design of experiments", *International Journal of Machine Tools and Manufacture*, Vol. 43, pp 747-753.

Choudhury I. A, N.L. See, M. Zuhairi, (2005), "Machining with Chamfered Tools", *Journal of Materials Processing Technology*, Vol. 170, pp. 115-120.

Chryssolouris G., (1982), "Turning of hardened steels using CBN tools," *Journal of Applied Metal Working*, Vol. 2, pp. 100-106.

Cus F., J. Balic, (2003) "Optimization of cutting process by GA approach," *Robotics and Computer Integrated Manufacturing*, Vol. 19, pp. 113–121

Cockroft, M.G., and Latham, D.J., 1966, A Simple Criterion of Fracture for Ductile Metals, National Engineering Laboratory, Report 216.

Coello C.A., M.S. Lechuga, (2002) "MOPSO: A proposal for multiple-objective particle swarm optimization," *Proceedings of IEEE, World Congress on Computational Intelligence*, 2002, pp.1051-1056

Coello C.A, G. T. Pulido, M. S. Lechuga, (2004), "Handling Multiple Objectives With Particle Swarm Optimization", *IEEE Transactions on Evolutionary Computation*, Vol. 8, pp. 256-279.

Conicity Technologies, Cresco PA, USA. www.conicity.com

Davies M.A., A.L. Cooke, E.R. Larsen, (2005), "High Bandwidth Thermal Microscopy of Machining AISI 1045 Steel", *Annals of CIRP*, Vol 54/1. pp.63.

Dimla D.E, P.M. Lister, N.J Leighton, (1997), "Neural network solutions to the tool condition monitoring problem in metal cutting – A review critical review of methods", *International Journal of Machine Tools and Manufacture*, Vol. 39, pp 1219-1241

Eberhart R.C., J. Kennedy, (1995) "Particle swarm optimization", *Proceedings of IEEE International Conference on Neural Networks*, Piscataway, NJ, pp. 1942-1948

El-Mounayri H., Z. Dugla, H. Deng, (2003) "Prediction of surface roughness in end milling using swarm intelligence," *Proceedings of the 2003 IEEE Swarm Intelligence Symposium*, pp. 220-227.

Elanayar S., Y.C. Shin, (1995), "Robust tool wear estimation with radial basis function neural networks", *ASME Journal of Dynamic Systems, Measurement and Control*, Vol. 117, pp.459-467.

Endres W.J., R.E De Vor, , S. G. Kapoor, (1995), "A Dual Mechanism Approach to the Prediction of Machining Forces, Part I and 2, *ASME Journal of Engineering for Industry*, Vol. 117, pp. 526-541.

Endres W.J., R. Kountanya, (2002), "The effects of corner radius and edge radius on tool flank wear," *Transactions of North American Manufacturing Research Institute*, Vol. XXX pp. 401-407.

Ernst, H., Merchant M. E., (1941), "Chip Formation, Friction and High Quality Machined Surfaces, *Trans. ASME*, Vol 29, pp. 229-378.

Fang, N., Jawahir, I.S., Oxley, P.L.B., (2001), "A Universal Slip-Line Model with Non-Unique Solutions for Machining with Curled Chip Formation and a Restricted Contact Tool," *Int. J. Mech. Sci.* Vol. 43, pp. 557-580.

Fang, N., Jawahir, I.S., (2002), "An Analytical Predictive Model and Experimental Validation for Machining with Grooved Tools Incorporating the Effects of Strains, Strain-Rates, and Temperatures," *Annals of the CIRP* 51, pp. 83-86.

Fang N., (2003), "Slip Line Modeling of Machining with a Rounded-Edge Tool, Part I: New Model and Theory", *Journal of Mechanics and Physics of Solids*, Vol. 51, pp. 715-742.

Fang N., (2005), "Tool-Chip Friction in Machining with a Large Negative Rake Angle Tool", *Wear*, Vol.258, pp. 890-897.

Fang N., Q. Wu, (2005), "The Effects of Chamfered and Honed Tool Edge Geometry in Machining of Three Aluminum Alloys", *Int. J. of Mach. Tools and Manuf.*, Vol. 45, pp.1178-1187.

Fang X.D, H. Safi-Jahanshaki, (1997), "A new algorithm for developing a reference model for predicting surface roughness in finish machining of steels", *International Journal of Production Research*, Vol. 35, No.1, pp. 179-197 .

Feng C.X., X.F. Wang, (2002), "Development of Empirical Models for Surface Roughness Prediction in Finish Turning", *International Journal of Advanced Manufacturing Technology*, Vol. 20, pp. 348-356.

Feng C.X, X.F. Wang, (2003), "Surface roughness predictive modeling: neural networks versus regression, *IIE Transactions*, Vol. 35, pp. 11-27.

Fieldsend J.E., S. Singh, (2002), "A multi-objective algorithm based upon particle swarm optimization, an efficient data structure and turbulence," *Proceedings of the U.K. Workshop on Computational Intelligence*, pp. 1677-1681.

Fu H.J., R.E DeVor, S.G. Kapoor, (1984), "A Mechanistic Model for the Prediction of the force system in Face Milling Operation", *ASME Journal of Engineering for Industry*, Vol 106, pp. 81-88.

Ghasempoor A., J. Jeswiet, T.N. Moore, (1999), "Real time implementation of on-line tool condition monitoring in turning", *International Journal of Machine Tools and Manufacture*, Vol. 39, pp.1883-1902.

Gray G.T, S.R. Chen, W. Wright, M.F. Lopez, (1994), "Constitutive Equations for Annealed Metals under Compression at High Strain Rates and High Temperatures," *Los Alamos National Laboratory Report*, LA-12669-MS.

Guo Y., D.A. Dornfeld, (1998), "Finite element analysis of drilling burr minimization with a backup material," *Transactions of North American Manufacturing Research Institute*, Vol. XXVI, pp. 207-212.

Guo Y., C.R. Liu, (2002) "3D FEA modeling of hard turning," *ASME Journal of Manufacturing Science and Engineering*, Vol. 124, pp. 189-199.

Hahn R.S., (1951), "On the temperature developed at the shear plane in the metal cutting process" *In Proceedings of First US National Congress of Applied Mechanics*, pp. 661-666.

Hirao K., R. Tlustý, R. Sowerby, G. Chandra, (1982), "Chip Formation with Chamfered Tools", *Journal of Eng. for Industry*, Vol. 104, pp. 339-342.

Hitomi K., (1961), "Fundamental Machinability Research in Japan", *Journal of Eng. for Industry*, Vol. 83, pp. 531-544.

Hodgson T., P.H.H. Trendler, G. F. Michelletti, (1981), "Turning hardened tool steels with Cubic Boron Nitride inserts", *Annals of the CIRP*, Vol. 30/1, pp. 63-66.

Hu X., R. Eberhart, (2002), "Multiobjective optimization using dynamic neighborhood particle swarm optimization," *Proceedings of IEEE Swarm Intelligence Symposium*, 2002, pp.1404-1411.

Huang Y., S.Y. Liang, (2003), "Modelling of the cutting temperature distribution under the tool flank wear effect", *Proc. Instn Mech. Engrs, Part C: J. Mechanical Engineering Science*, 217, 1195-1208.

Ivester R.W, M. Kennedy, M. Davies, R. Stevenson, J. Thiele, R. Furness, S. Athavale, (2000), "Assessment of machining models: progress report", *Machining Science and Technology*, 4 (3), 511-538.

Jacobson S., P. Wallen, (1988), "A New Classification System For Dead Zones in Metal Cutting", *Int. J. Mach. Tools Manuf.*, Vol. 28, pp. 529-538.

Jaeger J.C., (1942), "Moving sources of heat and the temperatures at sliding contacts", Vol. 76, *Proc. R. Soc. NSW*, pp. 203-224.

Johnson G.R., W. H. Cook, (1983), "A constitutive model and data for metals subjected to large strains, high strain rates and high temperatures", *Proceedings of the 7th International Symposium on Ballistics, The Hague, The Netherlands*, pp. 541-547.

Karpat Y., and Özel T., (2006a), "Predictive Analytical and Thermal Modeling of Orthogonal Cutting Process. Part I: Predictions of Tool Forces, Stresses and Temperature Distributions," *ASME Journal of Manuf. Sci. & Engr.*, Vol. 128/2, pp. 435-444.

Karpat Y., and Özel T., (2006b), "Predictive Analytical and Thermal Modeling of Orthogonal Cutting Process. Part II: Effect of Tool Flank Wear On Tool Forces, Stresses and Temperature Distributions," *ASME Journal of Manuf. Sci. & Engr.*, Vol. 128/2, 445-453.

Karpat Y., and Özel, T., (2006c), "An Integrated Analytical Thermal Model for Orthogonal Cutting with Chamfered Tools", *Transactions of NAMRI/SME*, Vol. 34.

Karpat Y., T. Özel, (2007a) "3-D FEA of Hard Turning: Investigation of PCBN Cutting Tool Micro-Geometry Effects", *Transactions of NAMRI/SME*, in print.

Karpat Y., T. Özel, (2007b), "Multi-Objective Optimization For Turning Processes Using Neural Network Modeling And Dynamic-Neighborhood Particle Swarm Optimization," *International Journal of Advanced Manufacturing Technology*, in print.

Karpat Y., T. Özel, J. Sockman, W. Shaffer, (2007c) "Design and Analysis of Variable Micro-Geometry Tooling for Machining Using 3-D Process Simulations," *Proceedings of International Conference on Smart Machining Systems*, March 13-15, 2007 National Institute of Standards and Technology, Gaithersburg, Maryland, USA.

Kim K.W., Lee, W.Y., Sin, H., (1999), "A Finite Element Analysis for Machining with Tool Edge Considered", *Journal of Material Processing Technology*, Vol. 86, pp. 45-55.

Kita Y., M. Ido, N. Kawasaki, (1982), "A Study of Metal Flow Ahead of Tool Face with Large Negative Rake Angle", *Journal of Eng. for Industry*, Vol. 104, pp. 319-325.

Klocke F., Kratz, H., (2005), "Advanced Tool Edge Geometry for High Precision Hard Turning", *Annals of CIRP*, 54/1/2005, pp.47-50.

Kudo H., (1965), "Some New Slip Line Solutions for Two Dimensional Steady State", *Int. Journal of Mech. Sci.*, Vol 7, pp. 43-55.

Koenig W.A, R. Komanduri, H.K. Toenshoff, G. Ackeshott, (1984), "Machining of hard metals", *Annals of the CIRP*, Vol.33/2, pp. 417-427.

Komanduri R., Z. B. Hou, (2001a) "Thermal Modeling of Metal Cutting Process - Part I", *Int. J. of Mach. Sci.*, Vol. 42, pp. 1715-1752.

Komanduri R., Z. B. Hou, (2001b) "Thermal Modeling of Metal Cutting Process - Part II", *Int. J. of Mach. Sci.*, Vol. 43, pp. 57-88.

Komanduri R., Z. B. Hou, (2001c) "Thermal Modeling of Metal Cutting Process - Part III", *Int. J. of Mach. Sci.*, Vol. 43, pp. 89-107.

Kountanya, R.K., W. J. Endres, (2001), "A High Magnification Experimental Study of Orthogonal Cutting with Edge-Honed Radius", *Proceedings of 2001 ASME Int. Mech. Eng. Congress and Expo.*, New York.

Koutanya, R.K., W.J. Endres, (2004), "Flank Wear of Edge Radiused Cutting Tools Under Ideal Straight Edged Orthogonal Conditions", *Journal of Manufacturing Science and Engineering*, Vol 126, p.496-505.

Lee E.H, B.W. Shaffer, (1951), "The theory of plasticity applied to a problem of machining", *Journal of Applied Mechanics*, (1951), 18, 405-413.

Leone W.C., (1954), "Distribution of shear zone heat in metal cutting", *Transactions of ASME*, 76,121-125.

Leowen E.G., M.C. Shaw, (1954), "On the analysis of cutting tool temperatures", *Transactions of ASME*, 71, 217-231.

Li, X., (1997), "Development of a Predictive Model for Stress Distributions at the Tool-Chip Interface In Machining," *J. Mater. Process. Technol.*, Vol. 63, pp. 169–174.

Liu R., A. Shih, (2006), "Finite element modeling of 3D turning of titanium", *International Journal of Advanced Manufacturing Technology*, Vol. 29, No 3-4, pp. 253-261.

Liu Q., Y. Altintas, (1999), "On-line monitoring of flank wear in turning with multilayered feed-forward neural network", *International Journal of Machine Tools and Manufacture*, Vol. 39, pp. 1945-1959.

Long Y., Y. Huang, (2005), "Force Modeling Under Dead Metal Zone Effect In Orthogonal Cutting With Chamfered Tools", *Transactions of NAMRI/SME*, Vol. 33, pp. 573-580.

Marler R.T, Arora J.S, (2004) "Survey of multi-objective optimization methods for engineering". *Struct Multidisc Optimization*, Vol. 26, pp.369–395

Mamalis G., J. Kandrak, M. Horvath, (2005), "On a Novel Tool Life Relation for Precision Cutting Tools", *Journal of Manufacturing Science and Engineering*, Vol. 127, pp 328-332.

Mayer J.E., D.J. Staufer, (1973), "Effects of Tool Edge Hone and Chamfer on Wear Life", *SME Technical Paper*.

- Manjunathaiah J., W.J. Endres, (2000), "A New Model and Analysis of Orthogonal Machining With an Edge-Radiused Tool", *ASME Journal of Manufacturing Science and Engineering*, Vol. 122, pp. 384-390.
- Matsumoto Y., F. Hashimoto, G. Lahoti, (1999), "Surface integrity generated by precision hard turning", *Annals of the CIRP*, Vol.48/1, pp. 59-62.
- Merchant M.E., (1944), "Basic Mechanics of the Metal Cutting Process", *Journal of Applied Mechanics*, Vol 66, pp.168-175.
- Mostaghim S., J. Teich, (2003) "Strategies for finding good local guides in multi-objective particle swarm optimization," *Proceedings of IEEE 2003 Swarm Intelligence Symposium*, pp. 26-33.
- Movaheddy M. R., Y. Altintas, M. S. Gadala, (2002), "Numerical Analysis of Metal Cutting With Chamfered and Blunt Tools", *ASME Journal of Manuf. Sci.& Eng.*, Vol. 124, pp. 178-1888.
- Narutaki N., Y. Yamane, (1979), "Tool wear and cutting temperature of CBN tools in machining of hardened steels", *Annals of the CIRP*, Vol. 28/1, pp. 23-28.
- Ohbuchi Y., Obikawa, T., (2003), "Finite Element Modeling of Chip Formation in the Domain of Negative Rake Angle Cutting", *ASME Journal of Engineering Materials and Technology*, Vol. 125, pp. 324-332.
- Oxley P.L.B., (1989), *The Mechanics of Machining: An Analytical Approach to Assessing Machinability*, Ellis Horwood Limited, England.
- Özel T., T. Altan, (2000), Determination of workpiece flow stress and friction at the chip-tool contact for high-speed cutting, *Int. Journal of Machine Tools & Manufacture*, 40/1, 133-152.
- Özel T., A. Nadgir, (2002), "Prediction of flank wear by using back propagation neural network modeling when cutting hardened H-13 steel with chamfered and honed CBN tools", *International Journal of Machine Tools and Manufacture*, Vol. 42, pp. 287-297.
- Özel, (2003), "Modeling of Hard Part Machining: Effect of Insert Edge Preparation for CBN Cutting Tools", *Journal of Materials Processing Technology*, Vol.141, pp. 284-293.
- Özel T., T-K. Hsu, E. Zeren, (2003), "Effects of cutting edge geometry, workpiece hardness, feed rate and cutting speed on surface roughness and forces in finish turning of hardened AISI H13 steel, *International Journal of Advanced Manufacturing Technology*, Vol. 25, pp. 262-269.
- Özel T., Y. Karpat, (2005), "Predictive modeling of surface roughness and tool wear in hard turning using regression and neural networks", *International Journal of Machine Tools and Manufacturing*, Vol 45, pp. 467-479.

Özel, T., (2006), "Influence of Friction Models on Finite Element Simulations of Machining", *International Journal of Machine Tools and Manufacture*, Vol. 46, Issue 5, pp. 518-530.

Palmer, W.B., Yeo, R.C.K., (1963), "Metal Flow near the Tool Point during Orthogonal Cutting with a Blunt Tool", *Proc. 4th Int. MTDR Conf.*, pp.61-71.

Pareto V., (1906) "Manuale di Economica Politica", Societa Editrice Libreria. Milan; In: Schwier AS , Page AN (eds) translated to English by Schwier AS as Manual of Political Economy, Kelley, New York

Ranganath, S., Campbella, A. B., Gorkiewicz, D.W., (2007), "A model to calibrate and predict forces in machining with honed cutting tools or inserts", *International Journal of Machine Tools and Manufacture*, Volume 47, pp. 820-840.

Ren H., M.R. Altintas, (2000), "Mechanics of Machining with Chamfered Tools", *ASME Journal of Manuf. Sci. & Eng.* , Vol. 122, pp. 650-659.

Risbood K.A, U.S. Dixit, A.D. Sahasrabudhe, (2003), "Prediction of surface roughness and dimensional deviation by measuring cutting forces and vibrations in turning process" *Journal of Materials Processing Tech.*, Vol. 132, pp. 203-214.

Saravanan R., P. Asokan, M. Sachidanandam, (2002), "A multi-objective genetic algorithm (GA) approach for optimization of surface grinding operations," *International Journal of Machine Tools and Manufacture*, Vol. 42, pp. 1327-1334.

Sartkulvanich P., T. Altan, G. Abdullah, (2005), "Effects of flow stress and friction models in finite element simulation of orthogonal cutting – a sensitivity analysis," *Machining Science and Technology*, Vol. 9, pp. 1-26.

Scheffer C., H. Kratz, P.S Heyns, F. Klocke, (2003), "Development of a tool wear-monitoring system for hard turning", *International Journal of Machine Tools and Manufacture*, Vol. 43, pp. 973-985.

Shaw M.C., (1954), Metal cutting principles, 3rd ed. Cambridge, MA:MIT Press

Shi T., S. Ramalingam, (1991), "Slip-line solution for orthogonal cutting with a chip breaker and flank wear", *International Journal of Mechanical Sciences*. Vol. 33/9, pp. 689-704.

Shimmel, R., Endres, W., Stevenson, R., (2002), "Application of an Internally Consistent Material Model to Determine the Effect of Tool Edge Geometry in Orthogonal Machining", *ASME Journal of Manufacturing Science and Engineering*, Vol. 124, No. 4, pp. 536-543.

Sick B., (2002), "On-line and indirect tool wear monitoring in turning with artificial neural networks: A review of more than a decade of research", *Mechanical Systems and Signal Processing*, Vol. 16, pp. 487-546.

Smithey D.W, S.G. Kapoor, R.E. DeVor, (2001), "A new mechanistic model for predicting worn tool cutting forces", *Machining Science and Technology*, 5(1), 23-42.

Song H., (2003), "Thermal modeling for finish hard turning", Ph.D thesis, University of Alabama, 2003.

Tandon V., H. El-Mounayri, and H. Kishawy, (2002) "NC end milling optimization using evolutionary computation," *International Journal of Machine Tools and Manufacture*, Vol 42, pp. 595-605.

Thiele J.D, S.N. Melkote, (1999), "Effect of cutting edge geometry and workpiece hardness on surface generation in the finish hard turning of AISI 52100 steel", *Journal of Materials Processing Technology*, Vol. 94, pp. 216-226.

Thiele J.D, S.N. Melkote, R.A. Peascoe, T.R. Watkins, (2000), "Effect of cutting-edge geometry and workpiece hardness on surface residual stresses in finish hard turning of AISI 52100 steel", *ASME Journal of Manufacturing Science and Engineering*, Vol. 122, pp.642-649.

Thomsen E.G, A.G. MacDonald, S. Kobayashi, (1962), "Flank friction studies with carbide tool reveal sublayer plastic flow", *Transactions of the ASME Journal of Engineering for Industry*, 53-62.

Toenshoff H.K, H.G. Wobker, D. Brandt, (1995), "Hard turning influences on workpiece properties", *Transactions of the NAMRI/ SME*, Vol. 23, pp. 215-220.

Toenshoff H.K, C. Arendt, R. Ben-Amor, (2000), "Cutting hardened steel", *Annals of the CIRP*, Vol. 49/2, pp. 1-19.

Trigger K.J, B.T. Chao, (1951), "An analytical evaluation of metal cutting temperatures", *Transactions of ASME*, 73, 57-68.

Tsai K., P. Wang, (2001), "Predictions on surface finish in electrical discharge machining based upon neural network models", *International Journal of Machine Tools and Manufacture*, Vol. 41, pp 1385-1403.

Usui E., A. Hirota, M. Masuko, (1978), "Analytical prediction of three dimensional cutting process, Part 3:Cutting Temperature and crater wear of carbide tool", *Journal of Engineering for Industry*, Vol. 100, 236-243.

Villalobos-Arias M. A., G. T. Pulido, and C.A Coello, (2005), "A Proposal to Use Stripes to Maintain Diversity in a Multi-Objective Particle Swarm Optimizer", *IEEE Swarm Intelligence Symposium*, pp.22-29.

Waldorf D.J, (1996), "Shearing, ploughing, and wear in orthogonal machining". Ph.D. thesis, University of Illinois at Urbana-Champaign, IL.

Waldorf, D.J., De Vor, R.E., Kapoor, S.G., (1998), "A Slip-Line Field for Ploughing During Orthogonal Cutting", *ASME Journal of Manufacturing Science and Engineering*, Vol. 120, No. 4, pp. 693-699.

Wang J.Y, C.R. Liu, (1999), "Effect of tool flank wear on the heat transfer, thermal damage and cutting mechanics in finish hard turning", *CIRP Annals*, Vol. 48/1, 80-83.

Yen Y.C, A. Jain, T. Altan, (2004), "A finite element analysis of orthogonal machining using different tool edge geometries", *Journal of Materials Processing Technology*, Vol. 146, pp. 72-81

Zhang H.T., P.D. Liu, R.S. Hu, (1991), "A Three-Zone Model and Solution of Shear Angle in Orthogonal Machining", *Wear*, Vol 143, pp 29-43.

Zhou J.M., Walter H., Andersson M., Stahl J.E., (2003), "Effect of chamfer angle on wear of PCBN cutting tool", *International Journal of Machine Tools and Manufacture*, Vol. 43, pp. 301-305.

Zitzler E., M. Laumanns, S. Bleuler, (2003), "A tutorial on evolutionary multiobjective optimization," *Workshop on Multiple Objective Metaheuristics (MOMH 2002)*, Springer-Verlag, Berlin, Germany.

Zorev N.N, (1963), "Inter-relationship between shear processes occurring along tool face and shear plane in metal cutting", *International Research in Production Engineering*, ASME, New York, 42-49.

CURRICULUM VITA

YİĞİT KARPAT

09/92-06/96	B.S. Mechanical Engineering Dokuz Eylul University, Izmir Turkey
01/97-01/00	M. S., Mechanical Engineering Middle East Technical University, Ankara Turkey
01/03-10/07	Ph.D, Industrial and Systems Engineering Rutgers, The State University of New Jersey

PUBLICATIONS

1. Y. Karpata and T. Özel, "An Integrated Analytical Thermal Model For Orthogonal Cutting With Chamfered Tools", *Transactions of North American Manufacturing Research Institute* Vol. XXXIV, 2006.
2. Y. Karpata and T. Özel, "Swarm-Intelligent Neural Network System (SINNS) Based Multi-Objective Optimization of Hard Turning," *Transactions of North American Manufacturing Research Institute*, Vol. XXXIV, pp. 9-16, 2006.
3. Y. Karpata and T. Özel, "Predictive Analytical and Thermal Modeling of Orthogonal Cutting Process. Part II: Effect of Tool Flank Wear on Tool Forces, Stresses and Temperature Distributions, " *ASME Journal of Manufacturing Science and Engineering*, Vol 128, pp 435- 444, 2006
4. Y. Karpata and T. Özel, "Predictive Analytical and Thermal Modeling of Orthogonal Cutting Process. Part I: Predictions of Tool Forces, Stresses and

Temperature Distributions," *ASME Journal of Manufacturing Science and Engineering*, Vol 128, pp 445- 453, 2006

5. T. Ozel, Y. Karpat, "Predictive Modeling of Surface Roughness and Tool Wear in Hard Turning using Regression and Neural Networks", *International Journal of Machine Tools and Manufacture*, Vol 45, pp 467-479, 2005.